UNIVERSITAT POLITÈCNICA DE CATALUNYA
BARCELONATECH

Escola Tècnica Superior d'Enginyers de Camins, Canals i Ports de Barcelona

Doctorat en Anàlisi Estructural

PhD Thesis

Modeling of Droplet Dynamics in a Proton Exchange Fuel Cell Electrode Channel

Author:
Àlex Jarauta Arabí

Supervisor:
Pavel B. Ryzhakov
Co-Supervisor:
Jordi Pons i Prats
Internal Examiner:
Eugenio Oñate

February, 2016

Abstract

Fuel cells are promising alternatives to conventional energy conversion devices. Cells fueled with hydrogen are environmentally friendly and their efficiency is up to 3 times higher than that of high-temperature combustion devices. However, they are still expensive and their durability is limited. One of the key factors in fuel cell performance is the so-called *water management*. Water produced within the fuel cell is evacuated through the gas channels, but at high current densities water can block the channel, limiting the current density generated in the fuel cell and thus reducing its efficiency. Novel numerical analysis methods with feasible computational cost and high accuracy could help characterizing droplet transport in gas microchannels. In this work we focus on modeling and simulation of droplet emergence, deformation and detachment in fuel cell gas channels as this defines the most common mode of liquid transport in the problem at hand. However, methods presented could be applied to other problems involving a gas-liquid system, where liquid is found as small droplets or films.

A semi-analytical model of a water droplet emerging from a pore of the gas diffusion layer surface in a Polymer Electrolyte fuel cell channel is developed. The geometry of the static and deformed shape is characterized and the main geometric variables (i.e. radius, height, perimeter) are assumed to depend on the contact angles only. The forces acting on the droplet are the drag force of the air and the surface tension force, which acts as adhesion force. The analytical study solves the problem of a growing droplet in a gas flow channel to see the effects of: i) air velocity and liquid mass flow in droplet deformation and oscillation; and, ii) droplet height in frequency of oscillation. The predicted values for both drag and surface tension force are higher than the results found in literature. Higher air velocity values lead to more deformation of the droplet and oscillation with lower frequency but higher amplitude. Similar effects have been identified when the liquid mass flow is increased, leading to faster detachment of the droplet.

A continuum Lagrangian formulation for the simulation of droplet dynamics is proposed next. This model is developed in two and three dimensions. Using the Lagrangian framework, liquid surface can be accurately identified. The surface tension force is computed using the curvature defined by the boundary of the Lagrangian mesh. Special emphasis is given to the treatment of the surface tension term in the linearized version of governing equations. The corresponding tangent matrix allows for alleviating the severe time step size restrictions associated to the capillary wave scale. A dynamic contact angle condition is developed in order to include effects of rough surfaces in contact line evolution. Numerical examples of sessile drop in a horizontal surface and sessile drop in an inclined plane are compared to experimental results. Results show excellent agreement with experimental data. Numerical results are also compared the semi-analytical model previously developed by the authors in order to discuss the limitations of the semi-analytical approach.

An embedded formulation for the simulation of immiscible coupled gas-liquid problems is then presented. Previous model considered only the liquid domain, and airflow effects were not included at the continuum level. The embedded method is particularly designed for handling gas-liquid systems where liquid represents a small fraction of the total domain. Gas and liquid are modeled using the Eulerian and

the Lagrangian formulation, respectively. The Lagrangian domain (liquid) moves on top of the fixed Eulerian mesh. The location of the material interface is accurately defined by the position of the boundary mesh of the Lagrangian domain. The individual fluid problems are solved in a partitioned fashion and are coupled using a Dirichlet-Neumann algorithm. Neumann part of the coupling includes the entire stress tensor (normal and tangential components). Representation of the pressure discontinuity across the interface does not require any additional techniques being an intrinsic feature of the method. The proposed formulation is validated with several numerical examples and a convergence analysis is included as well.

Finally, the embedded formulation is used to model the problem of interest, which is the dynamics of a droplet in a PEFC electrode channel. Numerical examples include a time detachment analysis, where the droplet pins and detachment occurs when a threshold value of contact angle hysteresis is reached. Results show good agreement with experimental data available, and results using the semi-analytical method again show the limitations of this model. An extension to the previous example includes water injection into the gas channel in order to compare results with previous studies in literature.

Resumen

Las pilas de combustible son una alternativa prometedora a los dispositivos de conversión de energía convencionales. Las pilas alimentadas con hidrógeno son respetuosas con el medio ambiente y su eficiencia es hasta 3 veces mayor que la de los dispositivos de combustión de alta temperatura. Sin embargo, su precio todavía es elevado y su durabilidad es limitada. Uno de los factores clave en el rendimiento de las pilas de combustible es la denominada *gestión del agua*. El agua producida dentro de la pila es evacuada a través de los canales de gas, pero en condiciones de alta densidad de corriente, el agua puede bloquear el canal, limitando la densidad de corriente generada en la pila de combustible y reduciendo así su eficiencia. Nuevos métodos de análisis numérico con un coste computacional factible y una mayor precisión podrían ayudar a caracterizar el transporte de gotas en microcanales de gas. En este trabajo nos centramos en la formación de la gota, su deformación y posterior desprendimiento en los canales de gas de las pilas de combustible, ya que esto define el modo de transporte de la fase líquida más común en el problema analizado. Sin embargo, los métodos presentados podrían ser aplicados a otros problemas relacionados con un sistema gas-líquido, donde el líquido se encuentra como pequeñas gotas o películas.

En la presente tesis, se ha desarrollado un modelo semi-analítico de una gota de agua que emerge de un poro de la superficie de la capa de difusión en un canal de una pila de combustible tipo PEFC (Polymer Electrolyte fuel cell). La geometría de la gota estática y deformada se ha caracterizado y se ha supuesto que las principales variables geométricas (radio, altura, perímetro) sólo dependen de los ángulos de contacto. Las fuerzas que actúan sobre la gota son la fuerza de arrastre del aire y la fuerza de tensión superficial, que actúa como fuerza de adherencia. El estudio analítico resuelve el problema de una gota que crece en un canal de gas para ver los efectos de: i) la velocidad del aire y del caudal de líquido en la deformación de las gotas y su oscilación; y, ii) la altura de la gota en la frecuencia de oscilación. Los

valores predichos tanto para la fuerza de arrastre cómo para la tensión superficial son más altos que los resultados encontrados en la literatura. A mayor velocidad del aire, mayor es la deformación de la gota y sus oscilaciones tienen menor frecuencia pero mayor amplitud. Se han identificado efectos similares cuando se incrementa el caudal de líquido, dando lugar a un desprendimiento más rápido de la gota. Los valores de oscilación de frecuencia predichos son significativamente menores que los valores de la literatura, pero estos resultados han sido obtenidos en condiciones distintas de inyección de agua.

Como alternativa al modelo semi-analítico, se propone una formulación contínua Lagrangiana para la simulación de la dinámica de gotas. El modelo se ha desarrollado en dos y tres dimensiones. Utilizando el enfoque Lagrangiano, la superficie del líquido se puede identificar con precisión. La fuerza de tensión superficial se calcula utilizando la curvatura definida por el borde de la malla Lagrangiana. Se hace especial hincapié en el tratamiento del término de tensión superficial en la versión linealizada de las ecuaciones de gobierno. La matriz tangente correspondiente permite suavizar las restricciones de paso de tiempo asociadas a la escala de la onda capilar. Se ha incluido una condición de ángulo de contacto dinámico con el fin de incluir los efectos de las superficies rugosas en la evolución de la línea de contacto. Los resultados obtenidos en los ejemplos numéricos de una gota estática en una superficie horizontal y en un plano inclinado se han comparado con resultados experimentales. Los resultados muestran una excelente concordancia con los datos experimentales. También se han comparado los resultados numéricos con el modelo semi-analítico desarrollado previamente por los autores con el fin de discutir las limitaciones del enfoque semi-analítico.

Con el fin de incluir los efectos del aire sobre la gota, se presenta una formulación incrustada (*embedded* de su terminología en inglés) para la simulación de problemas de varios fluidos inmiscibles. El modelo anterior sólo considera el dominio de líquido, y los efectos del flujo de aire no se incluyen. El método está diseñado especialmente para la simulación de sistemas gas-líquido donde el líquido representa una pequeña fracción del dominio. El gas y el líquido se modelan mediante las formulaciones Euleriana y Lagrangiana, respectivamente. El dominio Lagrangiano (líquido) se mueve por encima de la malla Euleriana fija. La ubicación de la interfaz material se define exactamente por la posición del borde de la malla del dominio Lagrangiano. Los problemas de cada fluido se resuelven de una manera particionada y se acoplan mediante un algoritmo de Dirichlet-Neumann. La representación de la discontinuidad de la presión a través de la interfaz no requiere técnicas adicionales, ya que es una característica intrínseca del método. La formulación propuesta se valida con varios ejemplos numéricos y también se ha incluido un análisis de convergencia.

Finalmente, la formulación *embedded* se utiliza para modelar el problema objetivo, que es la dinámica de una gota en un canal de una pila PEFC. Los ejemplos numéricos incluyen un análisis del tiempo de desprendimiento, donde la línea de contacto de la gota se fija y el desprendimiento se produce cuando se alcanza un valor de umbral de la histéresis del ángulo de contacto. Los resultados concuerdan satisfactoriamente con los datos experimentales disponibles, y los resultados utilizando el modelo semi-analítico muestran de nuevo las limitaciones de este modelo. Finalmente el ejemplo anterior se extiende incluyendo la inyección de agua en el

canal de gas con el fin de comparar los resultados con estudios previos encontrados en la literatura.

Acknowledgments

I would like to thank Prof. Eugenio Oñate for giving me the opportunity of becoming a member of CIMNE. I would like to express my gratitude to him for being interested in fuel cell research.

I am very grateful to my supervisors Dr. Pavel Ryzhakov and Dr. Jordi Pons for their guidance and support during the writing of this thesis. Pavel, thank you for your endless support and patience during these years. I cannot put into words how much you have helped me growing as a scientist. Jordi, thanks again for your encouragement and support, and being interested in my research as much as I am.

I am also thankful to Dr. Marc Secanell for his useful comments and for his support and encouragement during all these years. Marc, thanks for giving me the opportunity of collaborating with you. Your interest in science and your endless energy are truly inspiring.

I would also like to express my gratitude to Dr. Riccardo Rossi, Prof. Sergio Idelsohn and Dr. Herbert Owen for reading the manuscript and and providing useful hints.

Many thanks to Dr. Jordi Cotela, Dr. Julio Marti, Mr. Guillermo Casas and Dr. Pablo Becker for their insightful discussions and their help. Also thanks to Dr. Pooyan Dadvand for his useful hints on the implementation of the code in Kratos and to Mr. Enrique Escolano for his technical support on GiD.

Thanks to all my friends and family, specially my parents, Eusebi and Adolfina, and my brother Eduard, for their love and support. I thank my parents for giving me the opportunity of study and showing me the importance of learning. Thanks for all your support, patience and encouragement.

Last but not least, I would like to thank my beloved wife Cristina for her love and patience, for helping me write this thesis and smiling when the screen was showing colorful plots of the droplet. Thank you for being by my side during all these wonderful years and making me a better person.

Thanks to all of you because I could not have written this thesis without your support.

This work has been supported by the FPI Research Grant BES-2011-047702 subject to the Spanish Project BIA2010-15880 from the Ministerio de Economía y Competitividad.

To my beloved wife Cristina

Table of Contents

Abstract **i**

Acknowledgments **v**

List of Figures **xi**

List of Tables **xvi**

1 Introduction **1**
1.1 Motivation . . . 1
1.2 Literature Review . . . 6
1.3 Objectives . . . 12
1.4 Structure of the Thesis . . . 13

2 A semi-analytical model for droplet dynamics on the GDL surface of a PEFC electrode **15**
2.1 Physical phenomena . . . 15
2.1.1 Interfacial energies and contact angles . . . 15
2.1.2 Flow regime characterization . . . 19
2.1.3 Adhesion force modeling . . . 21
2.2 Model description . . . 22
2.3 Droplet geometry model . . . 23
2.4 Droplet dynamics model . . . 25
2.4.1 Drag coefficient model . . . 25
2.4.2 Adhesion force model . . . 31
2.4.3 Boundary conditions . . . 31
2.4.4 Geometry and dynamic model integration . . . 33
2.5 Results and discussion . . . 33
2.5.1 Validation . . . 33
2.5.2 Evolution of the center of mass, hysteresis angle and forces . . . 36
2.5.3 Detachment time and force . . . 36
2.6 Conclusions . . . 38

3 A Lagrangian finite element model for droplets **41**
3.1 Governing equations . . . 43
3.2 FEM discretization . . . 45
3.2.1 Monolithic approach . . . 47

3.2.2 Fractional step approach . . . 50
3.3 Surface tension . . . 52
3.3.1 Curvature in two dimensions . . . 52
3.3.2 Curvature in three dimensions . . . 53
3.3.3 Implicit treatment of the surface tension term . . . 56
3.3.4 Dynamic contact angle condition and adhesion force . . . 60
3.4 Results and discussion . . . 62
3.4.1 Static drop . . . 63
3.4.2 Dynamic drop . . . 66
3.4.3 Sessile drop . . . 71
3.4.4 Sessile drop on an inclined plane . . . 75
3.5 Conclusions . . . 78

4 An embedded multiphase model 81
4.1 Multiphase flow modeling . . . 81
4.2 Numerical model . . . 85
4.2.1 Governing equations . . . 85
4.2.2 Finite Element formulation for the gas . . . 86
4.2.3 Finite Element formulation for the liquid . . . 89
4.2.4 Coupling strategy . . . 90
4.2.5 Solution algorithm . . . 96
4.3 Examples . . . 97
4.3.1 Static droplet . . . 97
4.3.2 Oscillation of a droplet levitated by an airflow . . . 99
4.3.3 Two-fluid sloshing . . . 103
4.4 Conclusions . . . 107

5 Analysis of droplet-gas interactions in a PEFC channel using an embedded formulation 109
5.1 Introduction . . . 109
5.2 Results and discussion . . . 111
5.2.1 Sessile droplet in a free space . . . 113
5.2.2 Sessile droplet in a channel . . . 119
5.2.3 Droplet injection in a channel . . . 124
5.3 Conclusions . . . 130

6 Conclusions and future work 141
6.1 Summary and conclusions . . . 141
6.2 Outcome . . . 143
6.3 Future work . . . 143

References 145

A Area ratio deduction 155

B Droplet Geometry Model **159**
B.1 Angles and distances . . . 159
B.1.1 Chord and height . . . 161
B.1.2 Perimeter . . . 162
B.2 Area . . . 163
B.2.1 Droplet area . . . 164
B.3 Equation to solve . . . 164
B.4 Center of Mass . . . 167
B.4.1 Circle . . . 167
B.5 Volume of the droplet . . . 174
B.5.1 Volume of the sphere . . . 174
B.5.2 Volume of the spherical cap . . . 175
B.5.3 Volume of the droplet . . . 176
B.5.4 Contact line . . . 176

C Newmark-Bossak integration scheme **179**

List of Figures

1.1 Schematic view of a Polymer Electrolyte fuel cell [1] 3
1.2 Exploded view of a Polymer Electrolyte fuel cell (top) and detailed view of gas channel with an emerging droplet (bottom) 4
1.3 Flow types that can be found in a PEFC cathode channel. Reproduced from reference [2] 5
1.4 Microscale picture of the GDL surface covered with Teflon. Courtesy of Marc Secanell, ESDLab, University of Alberta 11

2.1 Work of adhesion 16
2.2 Interfacial energy 16
2.3 Work of adhesion considering a third medium 17
2.4 Different paths of surface separation 17
2.5 Settling of a liquid droplet on a solid surface 18
2.6 Variables used for the adhesion force computation 21
2.7 Droplet emerging on the GDL surface subjected to the drag and adhesion forces 22
2.8 Static (left) and dynamic (right) droplet geometries used in the numerical analysis of the drag force 26
2.9 Computational domain of the gas channel used in the drag coefficient calculation 26
2.10 Drag coefficient and drag force according to White (solid red line) and semi-analytical model (dashed blue line) 27
2.11 Drag coefficient of the two deformed droplets compared to the static geometry 29
2.12 Drag coefficient representation as a function of the hysteresis angle and the Reynolds number for droplet heights less than 10% of channel height 30
2.13 Contact line of a deformed droplet 31
2.14 Flowchart of the algorithm to solve the dynamic problem 33
2.15 Droplet deformed shape representation at different time steps of the simulation 34
2.16 Validation results of the semi-analytical model 35
2.17 Evolution of the center of mass x-coordinate, contact angles and forces acting on the droplet 37

3.1 Schematic representation of a water droplet using an Eulerian formulation with the VOF method (left) and a Lagrangian formulation (right) 42

3.2 Schematic representation of the considered single-phase system 43
3.3 Discrete boundary 52
3.4 (a) Plane defined by normal vector to surface and tangent vector to the considered curve and (b) Infinitessimal area around a considered point, with normal vector $\mathbf{n}$ and principal directions $\mathbf{e}_1$ and $\mathbf{e}_2$ 54
3.5 (a)-(b) 1-ring neighborhood of node $\mathbf{x}_i$ with its Voronoi region (shaded area) and angles opposite to an edge, (c)-(d) Voronoi region for obtuse triangles 55
3.6 Interface domain, boundary and normal vector to the boundary . . . 59
3.7 TRIPLE_POINT flag used to identify the contact points 60
3.8 (a)-(b) Normal vector and contact angle at current and equilibrium configurations and (c) Normal vector at contact line node and its nearest neighbor to obtain the curvature at contact line 61
3.9 (a) Mesh used to discretize the domain, (b) pressure distribution inside the droplet and (c) pressure evolution at the central node 64
3.10 (a) Relative error vs number of nodes, (b) mesh with $h = 0.1$ m and (c) mesh with $h = 0.05$ m 65
3.11 Comparison among the solutions obtained using the coupled (monolithic) and the fractional step scheme in the liquid phase. 67
3.12 Domain evolution for two different initial configurations 68
3.13 Shape and y-displacement evolution of an elliptic droplet with different viscosities, in two and three dimensions 69
3.14 Domain evolution for an elliptic drop with $\mu = 10^{-5}$ Pa s 70
3.15 Droplet evolution for three different contact angles 72
3.16 Injection process of a droplet on a hydrophobic surface. All images have the same scale. 73
3.17 Comparison between modeled (in 2D and 3D) and experimental droplets with volumes from 3 to 30 μl using a scale in mm (top) and normalized (bottom), using pinning with variable contact angle 74
3.18 Experimental set-up to measure gravity effects on a sessile droplet . . 76
3.19 Resulting animation of the modeled droplet during deformation process 77
3.20 Comparison between the measured contact angle (square and diamond markers) and the modeled contact angle (solid and dashed lines) 77
3.21 Contact angle along the contact line as a function of coordinate x and the deformation parameter λ 78

4.1 Embedded setting 85
4.2 Embedded setting: real, fictitious and interface parts of the Eulerian domain 91
4.3 Explicit treatment of interface boundary condition for velocity. 92
4.4 Triangular element with linear velocity interpolation 94
4.5 Tetrahedron element with linear velocity interpolation 96
4.6 Pressure field at the final time step 98
4.7 Comparison between the fully Lagrangian formulation ([3]), the embedded method and the analytical solution. $p_E^{init} = 0$ Pa 98
4.8 Results for the non-zero initial pressure in the gas phase ($p_E^{init} = 10$ Pa) 99

4.9 Drop levitated by an airflow entering the domain with uniform velocity U_a . . . 100
4.10 Velocity field in the air domain . . . 100
4.11 Drop exposed to airflow . . . 101
4.12 Vertical and horizontal displacements of the droplet's surface . . . 102
4.13 Two-fluid sloshing model (in meters) . . . 103
4.14 Pressure field in the Lagrangian domain for the density ratio 1:1. Prior to the application of the coupling (left) and after applying the coupling (right). . . . 104
4.15 Error at $t = 0.5$ s against time step . . . 104
4.16 Pressure contours for two-fluid sloshing with density ratio 2:1 . . . 105
4.17 Pressure along the height (x=0.4 m) at time=0.5 s . . . 105
4.18 Liquid wave height at the left wall using different mesh sizes and time steps. Density ratio 2:1 . . . 106
4.19 Liquid wave height at the left wall compared to reference [4] . . . 106

5.1 (a) Exceeding water produced within the membrane diffuses through the GDL and emerges into the gas channel and (b) detailed view of gas channel with an emerging droplet and air flowing from left to right 110
5.2 Schematic representation of a water droplet in a PEFC gas channel in two (top) and three dimensions (bottom) . . . 112
5.3 (a) Mesh used to represent the PEFC gas channel, (b) detail of the finer mesh around the droplet and (c) mesh used to represent the 13 μl-volume droplet . . . 114
5.4 Frequency of oscillation in x and y directions for several air velocities 115
5.5 Evolution of the droplet deformation, pressure profile and velocity field within a PEFC channel . . . 116
5.6 Pressure profiles in air for the wind tunnel simulation . . . 117
5.7 Magnitude of the velocity profiles in air for the wind tunnel simulation 118
5.8 Velocity profile and streamlines on the wake side of the droplet . . . 118
5.9 Oscillation frequency versus the inverse of the square root of droplet volume, according to experiments (exp), numerical model (mod) and semi-analytical model (SA). Droplet volumes of 13, 30, 58 and 100 μl have been used to reproduce the results from reference [5] . . . 119
5.10 Critical air velocity for detachment as a function of droplet diameter obtained with analytical model from [6] (red line), experimental data from [7] (blue circle markers), the embedded model (green diamond markers) and the semi-analytical model (black triangle markers) . . . 120
5.11 Drop (blue solid line) and air velocity (red dashed line) profiles at detachment in a PEFC channel . . . 121
5.12 Advancing (blue dashed line) and receding (red solid line) angle evolution for the 0.7 mm-diameter droplet . . . 123
5.13 Deformation process of a 0.7 mm-diameter droplet subjected to airflow 123
5.14 Pressure profiles in air for a 1 mm-diameter droplet . . . 124
5.15 Magnitude of the velocity profiles in air for a 1 mm-diameter droplet 125
5.16 Mesh used for the droplet injection example . . . 126

5.17 Lagrangian inlet process in a channel 127
5.18 Experimental (left column) and simulated (right column) deformation process of an emerging droplet into a gas channel. Experimental results extracted from [8] 129
5.19 Advancing (blue diamond markers) and receding angles observed in [8] 130
5.20 Numerical results according to VOF model from [9] (left column) and embedded model (right column) of the deformation process of an emerging droplet into a gas channel. 131
5.21 Air pressure profile at $t = 0.4$ ms for a channel with a pore located at (a) 1.5 mm and (b) 0.25 mm from entrance. 132
5.22 Slug formation in a gas channel. Pressure profiles in air 133
5.23 Slug formation in a gas channel. Magnitude of velocity profiles in air 134
5.24 Pressure profiles in air 135
5.25 Velocity profiles in air 136
5.26 Pressure profiles in water 137
5.27 Velocity profiles in water 138

A.1 Characterization of a droplet with a spherical cap shape 155

B.1 Deformed droplet geometry. Air flows from right to left 159
B.2 Static droplet geometry 165
B.3 Computed θ_{R} versus fitted θ_{R} 166
B.4 Center of mass of a circular sector 167
B.5 Center of mass of the sector CT 169
B.6 Area of the ETB triangle depending on θ_{R} 171
B.7 Triangle ETB for values of $\theta_{\mathrm{R}} > \frac{\pi}{2}$ 171
B.8 Triangle ETB for values of $\theta_{\mathrm{R}} < \frac{\pi}{2}$ 172
B.9 Center of mass coordinates depending on θ_{A} 173
B.10 Center of mass coordinates depending on θ_{A} 174
B.11 Droplet contact line once it is deformed 177

List of Tables

1.1 Types of fuel cells depending on their electrolyte, reactant gases and working temperature [10] 2

2.1 Constants used in the fitting curve of the advancing and receding angles relationship 24
2.2 Parameters used in the simulation 32
2.3 Detachment time, height, width, and area covered for different water injection rates ($\dot{Q}$) and air velocities (u_{air}) 38

3.1 Input parameters used in the solver for monolithic scheme 63
3.2 Input parameters used in the velocity and pressure solvers for fractional step scheme 63
3.3 Prescribed (θ_s) and obtained (θ_{obs}) contact angles, and relative error (ϵ_θ) between these variables 71
3.4 Relative error between numerical and experimental results with respect to contact angle (ϵ_θ), height (ϵ_h) and chord (ϵ_h) for different droplet volumes (V), considering fixed (fix) and dynamic (dyn) contact angles 75

4.1 Summary of the frequencies and "chimney" heights obtained in scenarios 1-3. 101

5.1 Water and air properties used in the simulations, considering $T = 298$ K and $p = 1$ atm 113
5.2 Parameters used in the sessile droplet in a free space example 114
5.3 Parameters used in the sessile droplet in a channel example 120
5.4 Detachment time (t_{det}) and area covered (A_{cov}) for different droplet heights (h) according to current model and semi-analytical model presented in [11] 122
5.5 Parameters used in the droplet injection in a channel example 126

Chapter 1

Introduction

1.1 Motivation

Why fuel cells? Developing environmentally friendly energy converting devices is an emerging need in the modern world. Most conventional energy conversion devices used rely upon fossil fuels, such as oil or coal, which are limited and produce a huge amount of pollutants [10]. In the last decades, many alternatives have been proposed to decrease air pollution, namely solar energy, wind power, hydroelectric power and batteries. Among these alternatives, fuel cells have shown to be a promising energy conversion device for several important industrial applications due to their efficiency and high power density. Fuel cells is one of the leading candidates to replace internal combustion engines for vehicles, as they are the only presently available technology that can offer equivalent power density, range, and refueling times in a sustainable way. Cells fueled with hydrogen are environmentally friendly and their efficiency is up to 3 times higher than that of high-temperature combustion devices.

Apart from transportation, they can be used for portable electronics applications, such as laptops or even for stationary power sources in emergency cases. Fuel cells were invented more than 100 years ago, and they have been considerably improved recently [12]. However, despite their advantages, they are still expensive and their durability is limited to be commercialized at a large scale. There are still factors, such as material degradation and water management, that require further studies and design improvement. Intensive research is therefore required to reduce their cost and enhance their life cycle.

What is a fuel cell? A fuel cell is an electrochemical device that has the ability to turn the chemical energy in a fuel directly into electricity with high efficiency. Inside the fuel cell, oxidation and reduction electrochemical reactions take place producing low-voltage direct current (DC) and heat. The former is used to do useful work while the latter is wasted or can be used in cogeneration applications.

When a fuel cell is fed with pure hydrogen, its theoretical efficiency is approximately 83% [12]. This value is limited by the change in the free energy available and the thermal energy in the reaction involved. For other fuels (i.e. methane) the efficiency is lower. Other energy conversion devices, like reciprocating engines, are limited by the efficiency of the Carnot cycle, which depends on the temperatures of

Table 1.1: Types of fuel cells depending on their electrolyte, reactant gases and working temperature [10]

Type	Fuel	Electrolyte	Catalyst	Temperature [°C]	Max Efficiency [%]
Alkaline	H_2	OH^-	Pt or Ni	-20 − 250	64
Molten Carbonate	H_2/CO	CO_3^{2-}	Ni	620 − 660	50
Solid Oxide	H_2,CO	O^{2-}	Ni/YSZ	600 − 1000	65
Polymer Electrolyte	H_2	H^+	Pt	-40 − 100	58
Direct Methanol	CH_3OH, H_2O	H^+	Pt/Ru	-40 − 100	40
Phosphoric Acid	H_2	H^+	Pt	150 − 220	42

the hot source and the cold sink. In conventional steam plants and internal combustion engines, this efficiency is usually less than 30%, and modern combined cycle power plants can increase this value up to 60%.

There are different types of fuel cells depending on the materials used in the electrolytes, the substances that react in the anode and the cathode and the working temperature. Table 1.1 shows the different types of fuel cells, the fuel used, the temperature and their maximum efficiencies, among other features. More details can be found in reference [12].

The current work focuses on Polymer Electrolyte fuel cells (PEFC) because they deliver high-power density while providing low weight, cost and volume [10]. Although they are not the most efficient fuel cell type (Table 1.1), their wide range of applications and working temperature makes them attractive for commercialization. From the engineering point of view, their design and modeling are a challenge; phenomena occurring within a fuel cell involve fluid dynamics, heat transfer, diffusion, mass and ionic transport, electrochemistry and structural mechanics [10]. PEFCs can work between -40 and 100°C and use hydrogen as fuel, oxygen as reactant and Nafion® as the electrolyte (Fig. 1.1).

Working principle of a PEFC The working principle of the PEFCs is based on two electrochemical reactions. The process starts at the anode, where the hydrogen flows in the anode gas channel and diffuses through the pores in the Gas Diffusion Layer (GDL). Attached to the GDL is the Catalyst Layer (CL). The CL is made using a platinum-based ink which is painted on either the membrane or the GDL. The ink contains carbon, Pt and electrolyte. The resulting coating is a thin (about 10 μm) porous layer. The Pt catalyzes the first reaction: the hydrogen oxidation reaction,

$$H_2 \longrightarrow 2H^+ + 2e^- \tag{1.1}$$

The next layer is the membrane made of Nafion® [13]. The membrane allows the hydrogen protons to travel across its section but is impermeable for the electrons.The electrons have to travel in the opposite direction through the GDL and the current collector (that act as the walls of the anode gas flow channel) in order to meet the protons at the other side of the membrane, thus generating the desired electric current. In the cathode, the oxygen flows in the cathode gas channels, diffuses through the GDL and reacts in the catalyst layer with the protons from the anode,

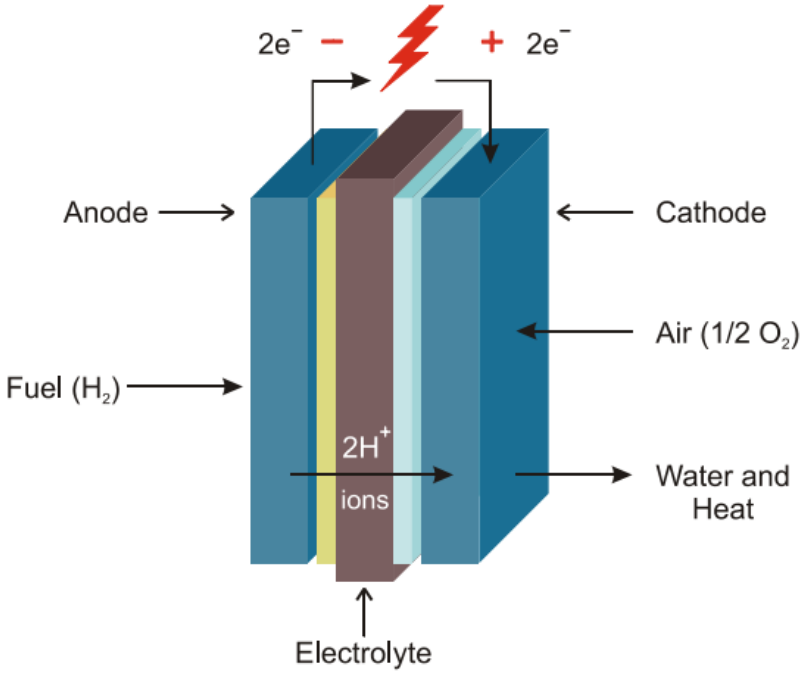

Figure 1.1: Schematic view of a Polymer Electrolyte fuel cell [1]

performing the second reaction (oxygen reduction reaction):

$$2H^+ + 2e^- + \frac{1}{2}O_2 \longrightarrow H_2O \tag{1.2}$$

The union of the anode GDL and CL, membrane and cathode CL and GDL is also known as membrane electrode assembly (MEA). When fueled with hydrogen, the fuel cell has zero emissions, since the only product of the electrochemical reaction is water and heat. The water generated in the reaction is one of the key factors influencing the fuel cell performance. The membrane requires humidification in order to maintain proton conductivity; if there is not enough water (less than 6% of volume fraction [14]), the membrane dries out and the fuel cell cannot operate[1]. Alternatively, if the amount of water is excessive (volume fraction greater than 80%), the pores in the CL and GDL fill with liquid water (flood) preventing the reactant gases from diffusing through it. The exceeding water has therefore to be evacuated through the cathode gas channels. The process of detecting and controlling water distribution within the fuel cell and designing it in order to improve its performance is often referred as *water management*.

Droplet dynamics and water management in gas channels Water management is one of the most critical issues in fuel cell design [11], [2], [15], [16], [17], [9], [18], [19], [20], [21]. During operation a fuel cell produces water. At moderate current densities the water can leave the cell in vapor form. At high current densities however, water vapor condenses in the GDL blocking the pores in the layer and

[1] At 30°C and 45% of water volume fraction, a membrane has a conductivity of 0.11 S cm^{-1} [14]

blocking the gas channels [9]. Blocking of the pores in the GDL leads to a lack of reactant at the reaction site (liquid water reduces gas diffusivity of the GDL) and a limited current density is reached. Similarly, excess of water in channels leads to non-uniform gas distribution and large pressure losses [22].

An exploded view of a PEFC is displayed in Fig. 1.2(a). The three main parts can be clearly identified: the anode and cathode sides, and the MEA. Gases (usually hydrogen in the anode side and air in the cathode side) enter the channels with variable velocity depending on the working conditions. For a PEFC producing 1 A cm^{-2}, the velocity is 0.15 m s^{-1} [11]. PEFC's gas channels are usually rectangular, with a cross section of 1×1 mm and 5 cm long. The exceeding water diffuses through the GDL and emerges as small droplets into the channel, as shown in Fig. 1.2(b). The liquid mass flow $\dot{Q}$ depends on the working conditions. If the current density produced is 1 A cm^{-2}, water is produced at a constant rate of 0.05 μl s^{-1} (see Section 2.4.3, Chapter 2).

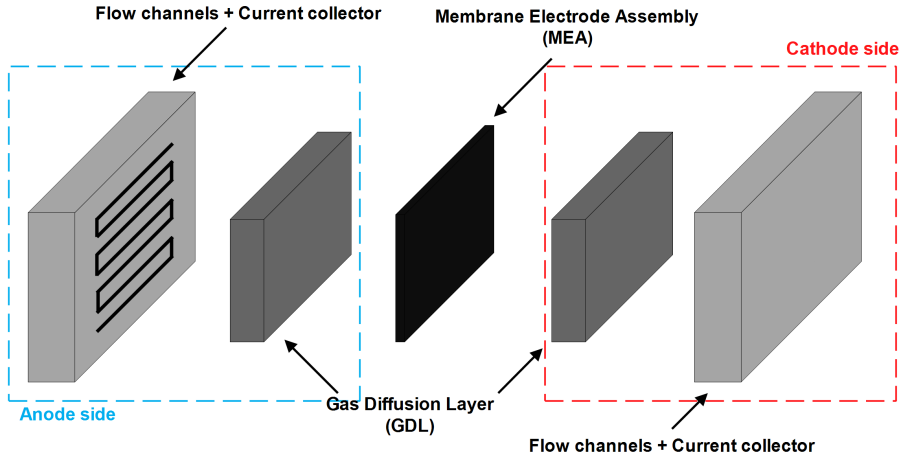

(a) Exploded view of a PEFC

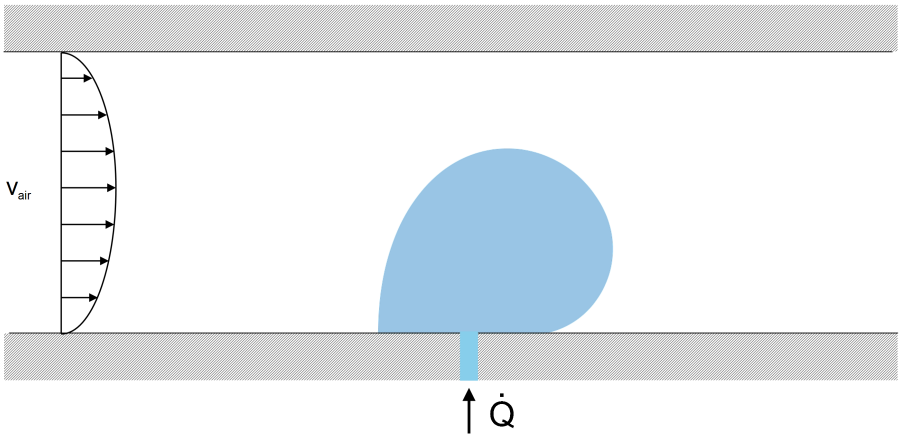

(b) Water droplet emerging into a fuel cell gas channel

Figure 1.2: Exploded view of a Polymer Electrolyte fuel cell (top) and detailed view of gas channel with an emerging droplet (bottom)

Three types of liquid flow can form in the gas channels depending on different

factors. These flows are usually known as droplet, film and slug flow [2], as shown on Fig. 1.3. Droplet flows can be observed in fuel cell channels where the current density is below 0.4 A cm^{-2}. Current density values between 0.4 and 1.5 A cm^{-2} lead to water film formation in channels, whereas slugs are found for currents greater than 2 A cm^{-2} [23].

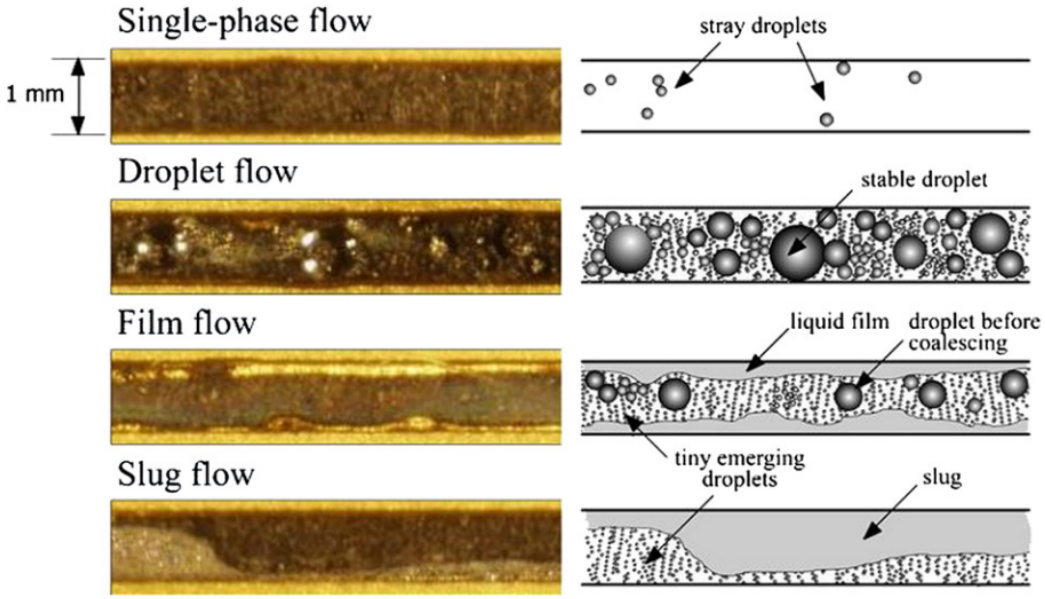

Figure 1.3: Flow types that can be found in a PEFC cathode channel. Reproduced from reference [2]

When a channel is completely flooded, a limiting current density is reached. This may lead not only to an extremely low efficiency, but even to the failure of the cell due to high pressure drops and oxygen starvation (leading to membrane degradation due to peroxyde formation). If water removal from the cell could be improved, higher current densities could be reached leading to fuel cells with higher power using the same materials. This would make fuel cells cheaper, lighter and smaller. Moreover, operation conditions leading to irreversible degradation of the cell would be avoided thus improving the fuel cell durability. A model capable of accurate water management predictions in gas channels must be developed. This requires understanding of the following points:

a) Evolution of the liquid phase (in particular, droplet) geometry exposed to the airflow in the channel. The forces acting on the droplet depend on the current geometry, so it is vital to have it fully characterized in order to obtain an accurate value of the forces.

b) Effect of flow rate on flow regime and droplet detachment. The detachment velocity is a key factor for the water removal from the gas channel.

c) Evolution of the area coverage of the water in the GDL surface of the channel. This variable is an indicator of the available area for the oxygen to diffuse through the GDL. If the area is fully covered, the fuel cell cannot operate.

d) Drag coefficient C_{D} characterization for the droplet under static and dynamic conditions. The drag force is responsible for the droplet deformation, and depends on flow conditions. Thus, it is important to have the values of this coefficient for the different flow regimes and droplet deformation states.

e) Consideration of two-way liquid-gas interactions in the channel. Droplets deform in airflow according to flow conditions. On the other hand, the presence of droplets alter the conditions of the airflow. A continuous interaction between both fluids has to be considered in order to predict detachment.

f) Contact angle condition on rough surfaces. GDL surface is rough and heterogeneous, which affects droplet adhesion. Effects of substrate must be considered in the numerical model in order to model not only ideal but also rough surfaces.

g) Multiple MEA models have been proposed in literature however they lack an appropriate description of the channel/GDL interface under two-phase flow conditions [14]. Accurate analytical and numerical two-phase channel models are needed.

In the next section, a review of existing approaches devoted to water management in gas channels is presented.

1.2 Literature Review

There is a vast literature devoted to the analysis of droplet dynamics in PEFC gas channels [15], [8], [16], [17], [9]. Finding the conditions that lead to droplet shedding is the main objective of these works. The physical system under consideration is a two-phase flow within a microchannel, with one phase dominated by surface tension effects. One can distinguish 3 main groups of approaches:

- analytical models
- numerical models
- experimental characterization

Analytical models Analytical models are based on a simple force balance equation. These models have a low computational cost and are relatively easy to implement. However, they oversimplify the phenomena by using predefined droplet shapes, neglect the continuum nature of droplets and are restricted to predicting pre-detachment behavior, not being able to model film or slug flow.

Chen et al. [19] proposed an analytical model of a water droplet in a PEFC cathode channel based on a macroscopic force balance. Other works of liquid droplets dynamics in solid surfaces are reported in the literature, but this study was the first one regarding a water droplet on a porous surface subjected to an airflow [19]. This work used a force balance equation considering equilibrium shape of a droplet, thus being able to find a relationship between the surface tension force and the external

forces acting on the droplet, i.e. pressure, shear and viscous forces. The force balance resulted in a single equation relating the flow conditions, i.e. mean velocity and air viscosity, and the droplet geometry, namely height, length and contact angle hysteresis[2]. The analytical study considered a steady-state.

Several important conclusions were made in [19] regarding optimal channel geometry. First, if the product of the channel length-to-height aspect ratio by the capillary number was greater than $\frac{\pi}{12}$, the droplets could be prevented from lodging in the channel. In addition, increasing the channel length while maintaining the other parameters fixed, such as GDL hydrophobicity or gas velocity, enlarged the instability window (the angle hysteresis that promotes droplet detachment). The same effect could be achieved if the mean gas flow velocity was increased, which meant that the pressure drop in the channel was higher. The last conclusion was that by increasing the static contact angle, or equivalently, making the GDL/gas channel interface more hydrophobic, water droplets could be prevented from lodging in the channel. The main drawback of that model was that it did not take into account the effect of pinning (i.e., the contact line between the droplet and the GDL surface was considered to be always circular). Droplet detachment depends on contact line deformation [24]. Additionally, area coverage of the water in the GDL surface was not included, and the two-way liquid-gas interaction was not taken into account (points *c* and *e* from section 1.1).

Kumbur et al. [18] developed a model of a water droplet in the gas channel of a PEFC in order to predict its detachment. By means of a macroscopic force balance they related the droplet geometry with channel height, GDL hydrophobicity and airflow velocity. The experimental data was used to find a relation between the content of Teflon in the GDL surface and the surface tension. Thus, they improved Chen's work by relating the contact angle hysteresis with the flow conditions, the Teflon content in the GDL and the roughness of the surface, in addition to several geometric variables. Nevertheless, this model could still not account for geometry of the deformed droplet, drag coefficient, area coverage and roughness effects of the GDL (points *a*, *d*, *c* and *f* from section 1.1). An important conclusion was that at low air velocities, the droplet instability was insensitive to the hydrophobicity of the surface. That fact could be used to minimize costs in the PEFC manufacture and avoid efficiency loss, since a highly hydrophobic GDL has more electrical resistance and is more expensive [18]. The analytical equations in this study were also based on the equilibrium of forces, i.e. it was a steady-state analysis.

An exhaustive analysis of the static and deformed shape of the water droplet was done by Esposito et al. [24]. While the study of Kumbur et al. gave an analytical expression for the hysteresis angle, it did not characterize the main geometric variables of the static and deformed droplet (point *a* from section 1.1). This study was an improvement compared with the two previous works since the analytical model was transient. Several geometric properties, such as advancing angle, droplet radius, height and perimeter, were expressed as a function of the center of mass x-coordinate (x_{CM}) for a fixed droplet volume. Although the wetting area over the GDL was approximated by a cylinder, results provided valuable information regard-

[2]Difference between the advancing and the receding angles, which are the contact angles when the droplet is in its deformed state

ing the studied phenomena. First, the drag force increased linearly with the increase of x_{CM}, whereas the force exerted by the surface tension and the inertial force had a linear decay. On the other hand, x_{CM} was found to decrease over time due to the deformation of the droplet. The transient model as a function of the droplet height proved to be valid for height over 0.5 mm, but the detachment height predictions did not agree with the results of the experiments carried out by the same group. One possible reason is that the drag coefficient used was that from a free spherical particle immersed in a fluid [24]. Therefore, an improvement on this coefficient would probably result in a more accurate model (points *d* and *e*). Furthermore, the models developed by Kumbur et al. and Esposito et al. do not take into account the gravity force since they impose a force balance exclusively in the x direction.

An extension of the study done by Chen et al. [19] was done by Cho et al. [6]. The study focused on droplets that were initially spherical and their deformed shape was close to a sphere, so the average curvature could be approximated by the initial radius. The authors took the results of Chen et al. [19] as a starting point but excluded the hypothesis of the droplet constant shape. Therefore, the study showed different plots regarding the force components acting on the droplet, the droplet shape change and the detachment velocity. At low gas velocities, the viscous force proved to be dominant on small droplets whereas on large droplets the normal force was dominant. On the other hand, the droplet deformation increased significantly when the droplet height was close to the channel height. The detachment velocity was analyzed using a generalized equation for the drag coefficient C_{D} obtained with fitted data for the conditions of the study. As expected, the detachment velocity decayed with an increasing droplet diameter, and the relationship between the Weber and the Reynolds numbers found in reference [19] was corrected. Despite the characterization of the droplet deformation, the authors did not characterize the deformed shape of the droplet, the evolution of the contact line with the GDL surface, and roughness effects of the GDL (points *a*, *d* and *f*).

Numerical models Numerical models use the continuum approach and are typically based on Navier-Stokes equations[3]. In principle, they allow to account for arbitrary geometries and thus are not limited to droplet type of flow. However, their implementation is more difficult and they are computationally expensive. Early numerical studies of water transport in gas channels include works of Quan et al. [25], Golpaygan and Ashgriz [26], and Theodorakakos et al. [15]. Zhu et al. [9] presented the first numerical analysis that considered water injection effects. The study included a two-dimensional numerical simulation considering a straight channel of 250μm of height and 1000μm of length, with a micropore of width 50μm. The interface between the water droplet and the air was simulated using the Volume of Fluid (VOF) method [27], and the velocity of the two-phase mixture was modeled using the Navier-Stokes equation. The surface tension was modeled using the Continuum Surface Force (CSF, reference [28]) as a volumetric force in the momentum equation. The main target of the study was to observe the effects of the static contact angle, pore size and air and water inlet velocities on the water droplet dynamics, and to predict a critical velocity for the water removal. As a result, it could be seen that

[3]Lattice-Boltzman approach has also been used, but it lies out of the scope of the present work

if the hydrophobicity of the GDL surface grew, the shear stress and the pressure forces dominated over the surface tension, thus promoting water removal and eventually detachment. Conversely, low hydrophobicity made the water droplet follow a film pattern due to surface tension. For hydrophobic surfaces, the advancing and receding angles evolved over time, whereas they remained constant if the surface was hydrophilic. Although that study took into account several variables that affected the behavior of the droplet, such as GDL hydrophobicity or water inlet velocity, it did not consider a change in the channel geometry (e.g. trapezoidal cross-section instead of squared). The contact angle on the GDL surface was considered constant, neglecting roughness effects (point *f* from section 1.1). Some analytical models predicted that certain length-to-height ratio of the channel promoted water removal [19] and that should have been taken into account. Moreover, the contact angle of the droplet with the channel surface was considered a boundary condition in these works, and contact angle hysteresis was not accounted for.

Considering the GDL surface completely hydrophobic, smaller pore size showed a slower rate of both droplet deformation and break-up processes. Forces responsible for droplet deformation and break-up (pressure and shear stress) were found to be proportional to the air inlet velocity. Results showed that for both low and high airflow velocities, water droplet formed a film flow. On the other hand, if the water injection velocity was lowered, the effects were found negligible. However, for high injection velocities (3 ms^{-1} in a 50 μl diameter pore) the water droplet blocked the channel almost instantly, and then it attached to the top wall (which was hydrophilic) forming a film pattern. Finally, the critical air velocity was found to be lower for higher hydrophobicity values and larger dimensions of the droplet. In addition, the predicted critical velocity was higher compared to the values obtained in previous studies [15].

A three-dimensional numerical study was performed by the same authors [16]. It provided more accurate results, since it included such important parameters as water coverage ratio, critical diameter, friction factor and water saturation. The numerical model was once again based on the VOF method. Results were similar to those from reference [9] regarding the static contact angle at the GDL surface: water removal was achieved with a hydrophobic GDL surface for a constant velocity value. The three-dimensional simulations also revealed that with higher hydrophobicity the contact line of the droplet was shorter and the droplet could achieve larger height prior to detachment. Moreover, it was stated that all the stages of water droplet evolution (i.e. emergence, growth, deformation, detachment and removal) were almost periodic, and the frequency of these processes increased with decreasing the wettability of the GDL [16]. It is important to remark that, despite the improvements from their previous work, they still considered a constant contact angle in the GDL surface (point *f*).

The effects of the air inlet velocity were similar to those of GDL hydrophobicity, adding the fact that the three-phase contact line deformed further downstream. Fast removal and smaller detachment diameters were obtained for high air velocities. Earlier detachment of droplets and larger detachment diameter were observed when the water injection velocity was increased. Nevertheless, the detachment diameter and flow resistance coefficient remained constant for low injection velocities. Be-

sides, for equivalent water volume, smaller pore size resulted in smaller detachment diameter. It is important to note that most of numerical simulations done until the present day are based on the VOF method [9] [16] [15] [2]. An extensive review on VOF-based models of droplet dynamics in fuel cell channels can be found in [29].

Some works found in literature use the Level-set (LS) method to model droplet dynamics in fuel cell channels [6], [30]. Choi and Son [31] showed the effects of number of pores in droplet dynamics in a PEFC channel. A similar model was used by Akhtar and Kerkhof [30] to study the effects of contact angle in channel walls on droplet detachment. LS method is able to handle complex topological changes in geometries and is simple to implement. However, this method suffers from bad mass conservation properties. VOF method is being widely used in two-phase flow analysis because it is mass conservative and it can be found in many commercial CFD software packages [29].

Experimental characterization Experimental characterization provides valuable data for water management studies. Experimental data is the key not only to validate analytical and numerical modes, but also to better understanding droplet dynamics in gas channels. One of the main problems related with fuel cell experiments is the limited accessibility of these devices. Two types of experiments can be identified: *in-situ* and *ex-situ*. In-situ experiments use sophisticated technologies such as neutron imaging [32], [33], IR-thermography [34], [35], MRI [36] and X-ray tomography [37]. These studies show valuable data of water distribution in channels, but they are difficult to perform and rely upon expensive equipment. On the other hand, most of ex-situ experiments are related with visualization using a transparent window [15], [38], [2], [39], [40], [21], [20]. Although ex-situ studies cannot reproduce an actual fuel cell channel, a good optical access to the channel is granted, enabling the caption of high resolution images. These studies can obtain important data to further understand wetting phenomena on porous substrates.

Zhang et al. [21] stated that for the experiments showed in their work, the airflow velocity threshold for water removal was 4 ms^{-1} for $0.5\times1\times100$ mm rectangular channels. Under those conditions, water tended to attach to the channel walls and flow in film form. Besides, Zhan et al. [20] took into account the channel turns, concluding that velocities higher than 7 ms^{-1} for the air were enough to move the water through the turns. Another solution to remove the water from the channels was to increase the operation temperature since it lowered the surface tension of the water, but it led to the dehydratation of the membrane, thus lowering the fuel cell performance and efficiency. The ex-situ study developed by Colosqui et al. [38] suggested that the effects of gravity were important depending on the orientation of the channels. On the other hand, high resolution images had proven the appearance of small residual droplets from previous films that acted as nucleating agents for the droplet-to-film transition [38].

An experimental study was carried out by Theodorakakos et al. [15] in order to study the water droplet dynamics inside the cathode microchannel. The set-up of the experiment showed the droplet behavior from a top-view, so it was easy to identify the shape and motion of the droplets. The results obtained suggested that with the considered conditions, the flow pattern corresponded to a single droplet and

no film flow was observed. On the other hand, the advancing and receding angles could not be directly measured, which was a drawback. Those angles were obtained in another experiment, where a water droplet was placed at the channel surface with an airflow circulating around it. The forces acting on the water droplet were not the same in the case of a droplet emerging from a pore than for a sessile droplet on a surface [15], [16]. The obtained angles were used in a numerical simulation based on the VOF method, and the results clearly showed the different dynamics for droplets laying on a surface and droplets emerging from a pore. The main drawback of this study was that the experiment was based on a droplet laying on a channel, and not emerging from it, hence its lack of accuracy regarding and actual fuel cell.

Carton et al. [2] performed an experiment in order to compare the observed phenomena with their numerical simulation. The experiment set-up was similar to that from [15], with a water droplet placed in a channel. Therefore, the effects of an emerging water droplet could not be recorded with enough accuracy. The results obtained were similar to previous studies, but the main difference was that the set-up of the experiment and the computational domain in the simulations was a double serpentine channel. If one of the channels was blocked due to slug flow formation, the other one had an increase in the velocity and pressure maximum values, which could damage the PEFC membrane [2]. Moreover, water flooding affected directly the fuel cell voltage, keeping it constant.

Recently, two studies of the cathode channel geometry have been performed [41], [42]. They aim at developing channel designs that lead to lower air pressure drops and promote water removal, which is an important contribution to predict optimal flow rate in channels and area coverage of water in the GDL surface (points *b* and *c*). Additionally, in [41] the authors identified the conditions that lead to water stagnation in the fuel channel turns, which is one of the critical factors in the fuel cell malfunction.

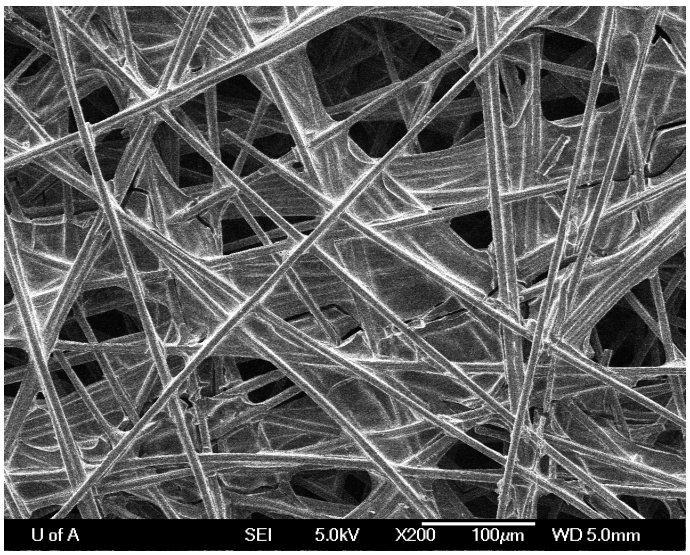

Figure 1.4: Microscale picture of the GDL surface covered with Teflon. Courtesy of Marc Secanell, ESDLab, University of Alberta

Literature shows that models for the analysis of liquid water in PEFC gas chan-

nels require further developments to provide accurate results. Although numerical simulations show accurate results regarding the shape evolution of the liquid phase inside the channel, the governing physics of the hysteresis angle remain without explanation. Based on the literature review, the presented analytical models have the following drawbacks:

- simplified expressions for adhesion force.
- differences between predicted and experimental results of drag force can be as high as 100%.
- results for droplet frequency of oscillation should be experimentally validated.

Moreover, analytical models are restricted to droplet type of flow (slugs and films cannot be considered) and cannot be used for post-detachment study. On the other hand, the main disadvantages found in numerical models are:

- an explicit treatment of the surface tension term results in an impractical limit for time step.
- a constant contact angle condition is typically used for the gas channel. GDLs used in fuel cells are characterized by rough surfaces with chemical heterogeneity (Fig. 1.4) and contact angle is not constant.
- Eulerian methods reconstruct air-water interface and require special techniques to improve mass conservation and represent material properties discontinuities across the interface.
- Multiple droplets and their interaction modeling has not been performed.

1.3 Objectives

It is clear from literature that there is a need for further improving models for the analysis of droplet dynamics in PEFC gas channels. The present thesis proposes two kinds of models. First, an improved semi-analytical model is developed. This model is capable of obtaining fast results for droplet detachment condition in gas channels for droplet flow regime at a reduced computational cost (e.g. 1 s simulation can be performed in 2 minutes). The new semi-analytical model should include the following features missing in the existing models of the kind:

- an expression for adhesion force that accounts for an arbitrary contact line geometry.
- an expression for drag force depending on droplet size, deformation state and droplet height-channel height ratio.

The intrinsic limitations of semi-analytical model, such as not being able to predict post-detachment behavior or to perform multiple droplets analysis, are overcome by a new numerical model. Although it is more computationally intensive (e.g. 1 s simulation can be performed in 3 hours), it is not restricted to droplet flow regime (it

can account for film and slug flow) and includes fully coupled gas-liquid interaction description. The numerical model should include the following features:

- an implicit form of the surface tension term.
- accurate description of sharp discontinuity in flow variables across the air-water interface.
- a dynamic contact angle condition to predict droplet shedding in rough surfaces.
- eliminate problems such as interface diffusion, mass conservation problems and allow for much larger time steps than VOF.

The new semi-analytical and numerical models will be applied to fuel cells and experimental validation.

1.4 Structure of the Thesis

The analysis of droplet dynamics in gas channels is the main research direction of this thesis. The structure of the present work is oriented towards an improved model to better understand the physical phenomena, first with a simple semi-analytical model and then with a numerical model.

Chapter 2 presents an improved semi-analytical model of droplet dynamics in a PEFC gas channel. The model is based on a simple equation that includes force balance applied to droplet's center of mass. A numerical study is carried out to find an expression for the drag force depending on droplet size, deformation state and ratio between droplet and channel height. Adhesion force is found by numerical integration and can be used for any contact angle shape. This model has a low computational cost but is limited to droplet flow. The model is validated with experimental data and compared to the detailed numerical models.

Subsequent Chapters 3 and 4 present the basic model developments for the numerical simulation of droplets in fuel cell gas channels. Chapter 3 presents a Lagrangian model of a droplet on a rough surface. The governing equations and boundary conditions described for the problem of interest are valid for two and three dimensions. Space and time discretization of the governing equations is also detailed. Special emphasis is given to the surface tension term and wetting modeling. Discretized equations are solved using two methods, the fractional step method and the monolithic approach. Numerical examples are used to compare between these two methods and to validate the model experimentally.

Chapter 4 is devoted to the description of a novel technique to study droplet dynamics within a microchannel: the embedded method. This method couples the Lagrangian formulation for droplets developed in Chapter 3 with an Eulerian model for the gas. Governing equations, boundary conditions and solution strategy for gas domain are described. The coupling technique to model gas-liquid interaction is detailed. Validation examples are solved.

In the last chapter the developed embedded model is applied to the simulation of droplet dynamics in PEFC gas channels, both in two and three dimensions. Results are compared to experimental data and previous results found in literature. Advantages of the proposed methodology in application to the problem of interest are highlighted. Analysis of droplet oscillation frequency, water injection rate and inlet air velocity are performed. Conclusions in Chapter 5 review the contributions presented in this thesis.

Chapter 2

A semi-analytical model for droplet dynamics on the GDL surface of a PEFC electrode

As discussed in Chapter 1, an analytical model of a droplet is a first approach of solving the actual problem. Although involving multiple simplification of the phenomena, it can provide useful results at a low computational cost when compared to numerical models. In this chapter, a semi-analytic model of droplet dynamics in gas channels is presented. It improves previous models used to understand the formation of droplets on the GDL surface [19], [15], [8], [16], [17], [9].

2.1 Physical phenomena

The physics involved in droplet growth, deformation and detachment are explained in the current section. One has to bear in mind that, although the subject of the study is a small droplet of a few microliters of volume, its behavior depends on multiple factors. The hydrophobicity of the surface where it is laying on is the main variable that determines its shape [43]. The surrounding fluid (air in our case) deforms the droplet via normal and viscous forces when set in motion [44], [45], [19], [9]. When the deformation process starts, the contact force of the droplet with the solid surface becomes unbalanced and starts increasing, deforming the gas-liquid interface in order to recover the force balance [43]. It is clear, then, that these phenomena have to be taken into account in the droplet model development.

2.1.1 Interfacial energies and contact angles

Interfacial energies Let us define the variables for characterizing liquids and surfaces in adhesive contact. Interfacial (or surface) energies quantify the variation of molecular bonds that occur when a surface is created. The first term that has to be defined is the work of adhesion. Let us consider the system displayed in Fig. 2.1, where two unit areas of different media are in contact. The work of adhesion is defined as the reversible work that needs to be done to separate these two unit areas from contact to the infinity in vacuum [46]. Depending on the separated media,

it is referred as work of adhesion (W_{12}) when the two media are different or work of cohesion (W_{11}) when a single material is considered. This magnitude is always positive since all media tend to attract each other in vacuum.

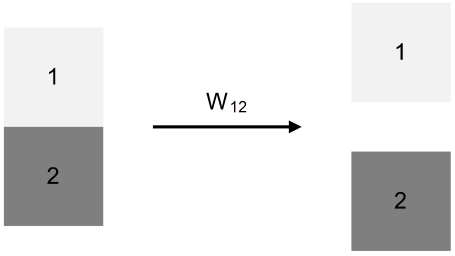

Figure 2.1: Work of adhesion

The next variables are the surface energy and the surface tension. Both of them are defined as the free energy change (γ) when the surface area of a medium is increased by a unit area, which is equivalent to separating two half-unit areas from contact:

$$\gamma_1 = \frac{1}{2} W_{11} \tag{2.1}$$

where γ_1 is expressed in N m^{-1} or, equivalently, in J m^{-2}.

The previous parameters have been defined in vacuum. If the process takes place in air, these values decrease since the media can absorb vapor [46]. The surface tension value for liquid water in air at room temperature is equal to 72 mN m^{-1} [46], [19], [24], [16].

The interfacial energy (γ_{12}) is identified as the free energy change when the interfacial area of two immiscible fluids changes by a unit area, as shown in 2.2:

$$\gamma_{12} = \frac{1}{2} W_{11} + \frac{1}{2} W_{22} - W_{12} = \gamma_1 + \gamma_2 - W_{12} > 0 \tag{2.2}$$

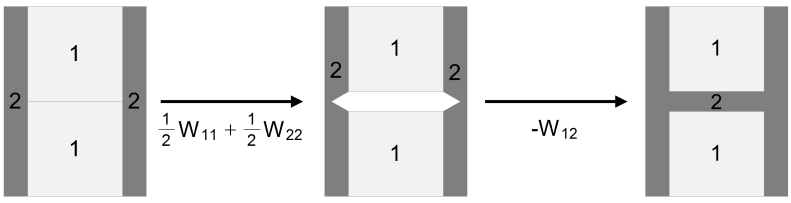

Figure 2.2: Interfacial energy

Note the positive condition, since if γ_{12} is negative it means that the area expands indefinitely or, in other words, both fluids are miscible and the interface dissolves, which is not the case of the present study. Eq. (2.2) is also known as the Dupré equation, and it can be written in an alternative form. The interfacial energy is, indeed, the same as the one expended on separating two media 1 in medium 2 (W_{121}) or in reverse (W_{212}):

$$\gamma_{12} = \frac{1}{2} W_{121} = \frac{1}{2} W_{212} \tag{2.3}$$

If one considers a liquid-solid interface, Eq. (2.2) can be rewritten as follows:

$$\gamma_{12} = \gamma_{\mathrm{SL}} = \gamma_{\mathrm{S}} + \gamma_{\mathrm{L}} - W_{\mathrm{SL}} \tag{2.4}$$

Since the problem of a water droplet in contact with a solid surface and surrounded by air involves three media, the third component must be added to the previous equations. The work of adhesion in a third medium is defined as the energy change due to separating two media 1 and 2 in medium 3 (Fig. 2.3) and is given by:

$$W_{132} = W_{12} + W_{33} - W_{13} - W_{23} = \gamma_{13} + \gamma_{23} - \gamma_{12} \tag{2.5}$$

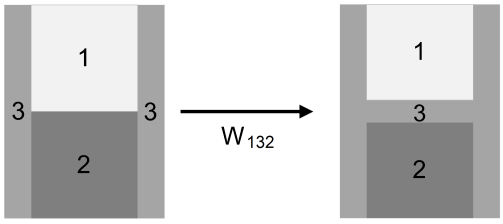

Figure 2.3: Work of adhesion considering a third medium

This magnitude can be either positive or negative. In the former case, the condition $\gamma_{13} + \gamma_{23} > \gamma_{12}$ is fulfilled and it means that medium 2 will spread over medium 1. If it is negative, then medium 3 will displace medium 2, which will totally wet the surface of medium 1.

One remark regarding adhesion energies and adhesion forces must be made. If one wants to separate two surfaces, the required adhesion force depends on the path and the duration of the process. Let us consider a simple example where two surfaces of the same material are separated from one another in two different ways: normal direction (the whole surface at a time) or peeling (Fig. 2.4). The energy needed in both cases is the same, but the required force is different: the peeling process needs a force 8 orders of magnitude less than the planar separation (see [46] for further details).

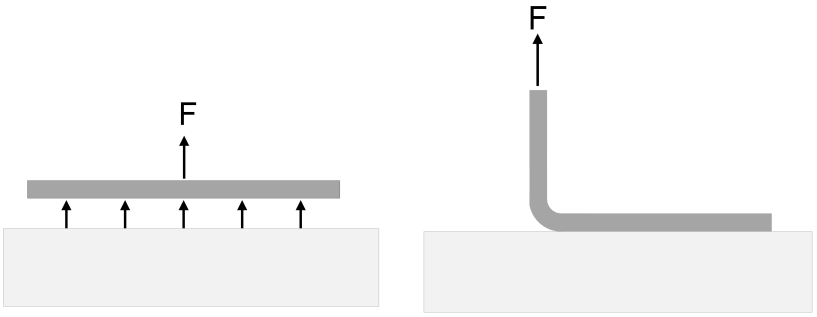

(a) Separation in the normal direction

(b) Separation by peeling

Figure 2.4: Different paths of surface separation

Contact angles Let us consider a spherical droplet in medium V that approaches and settles on the rigid flat surface S (Fig. 2.5).

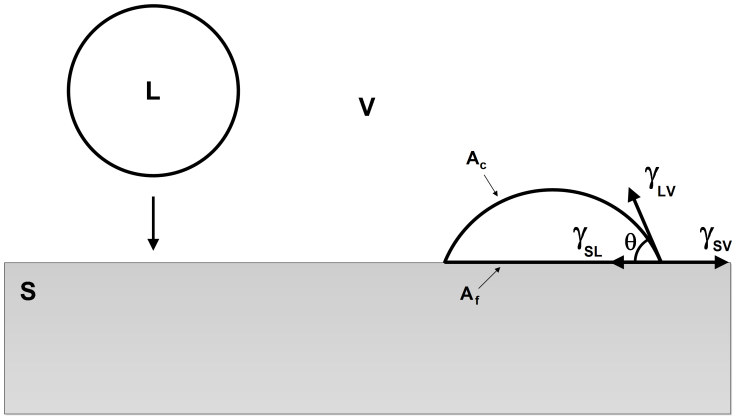

Figure 2.5: Settling of a liquid droplet on a solid surface

The interfacial energies between the three media can be related using the static contact angle as shown in Fig. 2.5:

$$\gamma_{SV} - \gamma_{LV}\cos\theta - \gamma_{SL} = 0 \tag{2.6}$$

The contact angle observed is therefore the macroscopic manifestation of equilibrium between the different surface free energies [46], [47]: γ_{SL} (solid-liquid), γ_{LG} (liquid-gas) and γ_{SG} (solid-gas). The deduction of Eq. (2.6) is done considering that the final total surface energy of the system is given by Eq. (2.7)

$$W_{\mathrm{TOT}} = \gamma_{LV}\left(A_{\mathrm{c}} + A_{\mathrm{f}}\right) - W_{\mathrm{SVL}}A_{\mathrm{f}} \tag{2.7}$$

where A_{f} is the flat area of the droplet and A_{c} is the curved area. At equilibrium, Eq. (2.7) becomes Eq. (2.8):

$$\gamma_{LV}\left(dA_{\mathrm{c}} + dA_{\mathrm{f}}\right) - W_{\mathrm{SVL}}dA_{\mathrm{f}} = 0 \tag{2.8}$$

The expression in Eq. (2.8) can be divided by dA_{f}, giving the following equation:

$$\gamma_{LV}\left(\frac{dA_{\mathrm{c}}}{dA_{\mathrm{f}}} + 1\right) - W_{\mathrm{SVL}} = 0 \tag{2.9}$$

The ratio $\frac{dA_{\mathrm{c}}}{dA_{\mathrm{f}}}$ equals $\cos\theta$ (see Appendix A) and if one does this substitution, Eq. (2.9) reads:

$$\gamma_{LV}\left(\cos\theta + 1\right) = W_{\mathrm{SVL}} = \gamma_{SV} + \gamma_{LV} - \gamma_{SL}$$

$$\gamma_{SL} + \gamma_{LV}\cos\theta = \gamma_{SV} \tag{2.10}$$

Further information regarding surface and interfacial forces can be found in Chapter 17 of [46]. The previous equations do not depend on the size of the droplet. However, when the curvature of the droplet is relatively high, the internal fluid

pressure starts to be significant and it is known as Laplace pressure. The pressure difference between the liquid and the gas surrounding the droplet are related with the surface tension and the radius of curvature according to the Young-Laplace equation:

$$p_{\text{liq}} - p_{\text{gas}} = \frac{2\gamma}{R} \tag{2.11}$$

where p_{liq} is the pressure inside the droplet, p_{gas} is the pressure of the surrounding gas, γ is the surface tension coefficient and R is the droplet radius.

The surface tension forces acting on the surface of the droplet have been described so far. However, the present problem involves a water droplet placed within an airflow, which generates two additional forces. The first one is the pressure force that appears due to the pressure gradient across the droplet's surface [19], [6]. The other one is the viscous force that the air produces when it flows around the droplet. Despite the fact that the mass of the droplet is extremely low, there is in fact an extra force, the gravitational force. Dominance of one force over the rest is explained in the following section.

2.1.2 Flow regime characterization

Several dimensionless numbers and flow pattern indicators are critical for describing the phenomena at hand.

Airflow in channels First is the Reynolds number, which relates the inertial and the viscous forces:

$$Re = \frac{\rho v L}{\mu} \tag{2.12}$$

where ρ and μ are the fluid density and viscosity, respectively, v is the mean velocity and L is a characteristic length (the droplet height in the present study). Typically, a PEFC gas channel has a cross section of 1×1 mm. Air enters the channel at 0.15 m s^{-1}, with a constant density of 1.2 kg m^{-3} and a dynamic viscosity of 1.83×10^{-6} Pa s (considering a constant temperature of 25°C). Considering these values, airflow in a PEFC gas channel has a Reynolds number equal to 98.5.

Droplets For droplets or a bubbles of a certain fluid, it is common to use several dimensionless parameters that relate the aforementioned forces with the surface tension force. First, there is the capillary number, which is the ratio between the viscous and the surface tension forces acting on the droplet:

$$Ca = \frac{\mu v}{\gamma} \tag{2.13}$$

where μ is the viscosity of water (1.98×10^{-5} Pa s for air at room temperature), v is the air velocity (0.15 m s^{-1} in gas channels, see section 2.4.3) and γ is the surface tension coefficient between the two phases (0.072 N m^{-1} for liquid water in air). Using these values in Eq. (2.13) it yields Ca = $4.13 \times 10^{-5} << 1$, which means that

surface tension force dominate over viscous effects in water, although the effects of the latter cannot be completely neglected.

The Bond number expresses the ratio between gravitational forces and the surface tension:

$$Bo = \frac{\rho g d^2}{\gamma} \tag{2.14}$$

where ρ is the fluid density (1000 kg m^{-3} for liquid water at room temperature), g is the gravity acceleration and d is the droplet diameter. In a 1×1 mm gas channel, the maximum value of the droplet diameter is 0.8 mm, and therefore the Bond number is 0.087, which means that surface tension forces are dominant over the gravitational forces. The Bond number is also known as the Eötvos number [6]. Finally, the ratio between the inertial forces and the surface tension is described by the Weber number:

$$We = \frac{\rho v^2 d}{\gamma} \tag{2.15}$$

For a typical fuel cell channel, and considering the same parameters as before, the values of the Capillary and Weber numbers are 4.13×10^{-5} and 3×10^{-4}, respectively. Thus, the surface tension effects are dominant over the rest of the forces in a fuel cell channel. The capillary and the Weber numbers are related by the Reynolds number:

$$We = Ca \cdot Re \tag{2.16}$$

Three types of flow patterns for water droplets can be distinguished: droplet, film and slug flow. A parameter that indicates whether the droplet is closer to a film or to a spherical droplet is the water coverage ratio (A_w), which is defined as the ratio between water coverage area and GDL area in the channel. It is expected that the higher the hydrophobicity of the GDL, the lower the water coverage ratio [16]. The same relationship is found with the critical diameter (D_p), which is the diameter of the detached sphere divided by the length of the microchannel.

The friction factor (f) is an indicator of the channel blockage, and it is defined by the following formula:

$$f = \frac{\Delta P}{\frac{1}{2}\rho u_a^2 \left(\frac{L}{D_H}\right)} \tag{2.17}$$

where ΔP is the pressure drop in the channel, u_a and ρ are the inlet velocity and density of the air, respectively, and L and D_H are the length and hydraulic diameter of the channel. As the droplet grows, f grows as well until the droplet detaches, which means a sudden drop of f. The water saturation (S_w) is another parameter that follows a similar pattern, and it has been defined as the ratio of water volume into the microchannel to the volume of the channel. In addition, the water saturation is lower for more hydrophobic surfaces [16].

2.1.3 Adhesion force modeling

When a droplet emerges from a pore in an airflow stream, the surface tension acts as the adhesion force since the air drag force tends to detach the droplet from the surface. One can distinguish between two types of adhesion models in literature: analytical expression and spring model. In 1995, Extrand and Kumagai [43] derived an analytical expression for the adhesion force:

$$F = \int_0^{2\pi} \gamma \cos\theta \cdot \cos\phi \zeta d\phi \tag{2.18}$$

where γ is the surface tension between both fluids, θ is the contact angle with the surface, ϕ is the azimuthal angle and ζ is the equivalent radius (Fig. 2.6).

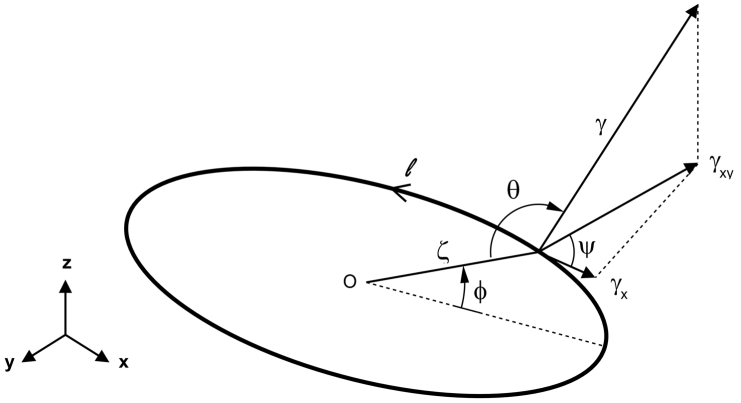

Figure 2.6: Variables used for the adhesion force computation

This expression is valid for droplets with circular contact lines. Note that the integration is done along the contact line and not the contact area. This force is considered to be a critical parameter for predicting the onset of the droplet detachment. Simplified expressions considering a predefined contact line shape (e.g. elliptic or parallel-sided) have been used in several studies [48], [49], [50], [5].

Celestini and Kofman [51] studied the fundamental vibration mode of a supported droplet, describing the surface tension force as a restoring force associated with the deformation:

$$F = -\gamma \frac{\Delta S}{dx} = -\frac{\gamma S_0 h\left(\theta\right)}{R^2} dx \tag{2.19}$$

where S_0 is the surface of the undeformed droplet, R is the radius of the truncated sphere, dx is the displacement of the center of mass and $h\left(\theta\right)$ is a quadratic function depending on the static contact angle. Note that Eq. (2.19) can be thought of as a spring model equation since the force is linear with the displacement. Esposito et al. [24] based their characterization of the surface tension force on the spring model from Celestini and Kofman [51], taking Eq. (2.19) as a partial derivative. Even though spring model of the surface tension is very intuitive, it is an approximation of the actual phenomena. Moreover, the spring model can be misunderstood since the spring force acts on the center of mass, whereas the adhesion force is applied at the contact line with the surface.

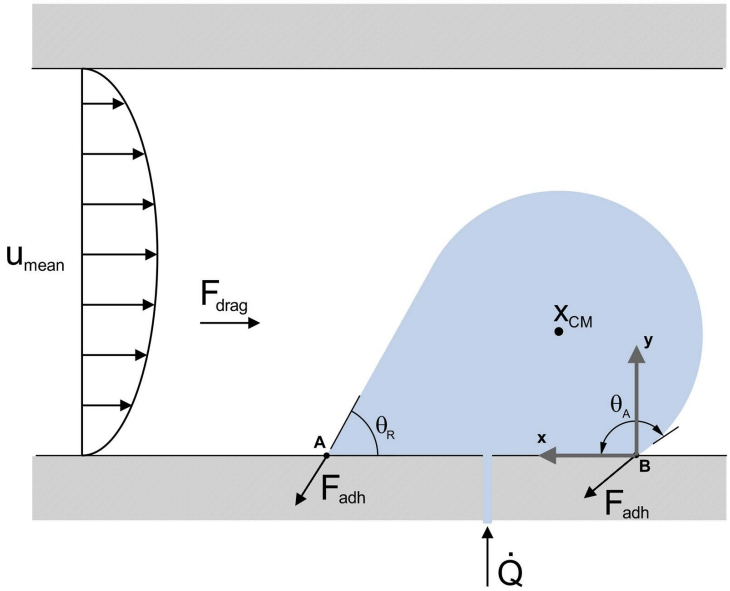

Figure 2.7: Droplet emerging on the GDL surface subjected to the drag and adhesion forces

2.2 Model description

The semi-analytical model presented in this chapter includes the following improved physical descriptions:

a) the adhesion force is obtained using the formula proposed by Extrand et al. [43], which can be used to obtain the adhesion force for any contact line geometry.

b) an expression for C_{D} based on CFD simulations considering several droplet geometries under study is used (thus, the model is entitled *semi-analytical*).

c) an improved characterization of the droplet deformed geometry is used.

The model assumes that gravity and viscous effects are negligible compared to the surface tension force. Fig. 2.7 shows a schematic view of the studied problem. A water droplet emerges from a pore into a channel with a constant volume flow $\dot{Q}$. The air flows with a fully developed velocity profile and an average velocity of u_{mean}. As the air flows around the droplet, it exerts a drag force, F_{drag}, on the droplet surface, which tends to deform it. Since this force breaks the droplet equilibrium, the adhesion force acts in the opposite direction, thus taking the droplet to a new equilibrium state. The difference between these two forces leads to droplet oscillations [11].

The equation that characterizes the balance of forces acting on the droplet is momentum conservation applied to the x-coordinate of the droplet center of mass:

$$m\frac{d^2x_{\mathrm{CM}}}{dt^2} = F_{\mathrm{adh}} - F_{\mathrm{drag}} \tag{2.20}$$

where m is the mass of the droplet and is a function of time, x_{CM} is the x-coordinate of the center of mass and F_{adh} and F_{drag} are the adhesion and drag forces, respectively. Forces are described by the following equations:

$$F_{\mathrm{drag}} = \frac{1}{2}\rho_{\mathrm{air}} u_{\mathrm{air}}^2 C_{\mathrm{D}} A \tag{2.21}$$

and

$$F_{\mathrm{adh}} = -\gamma \int_0^l \cos\left(\theta(l)\right) \cos\left(\psi(l)\right) dl \tag{2.22}$$

where ρ_{air} is the air density, C_{D} is the drag coefficient, A is the frontal projected area of the droplet and γ is the surface tension between the air and the water. Eq. (2.22) is the analytical expression for the adhesion force given by Extrand et al. [43].

2.3 Droplet geometry model

The droplet geometry and forces acting on the droplet are coupled, so it is vital to have the geometry of the droplet well characterized. In the model above, there are several parameters that define the geometry of the droplet such as the advancing and receding angles, the frontal area and the droplet thickness. In order to develop analytical expressions for the geometry of the droplet, the droplet is idealized as a semi-spherical cap together with a cone shape to model pinning [24], and these parameters can be obtained as a function of the droplet volume. Even though the idealized geometry cannot represent the complex geometries that might form, e.g. slugs, it contains mechanisms to account for pinning and contact angle hysteresis. This idealized geometry model is based on the one developed by Esposito et al. [24] with several corrections and improvements. Details on the geometry model development can be found in Appendix B.

The geometry model uses the water volume flow $\dot{Q}$ and an initial chord length c (distance AB in Figure 2.7) as input parameters to obtain the rest of the variables at every time step. Considering a constant chord and a constant area of the middle section for every deformation state, it is possible to find an expression of the chord length c of the droplet as a function of the contact angles:

$$c = \frac{R}{\sin\theta_{\mathrm{R}}} \left(1 + \sin\theta_{\mathrm{A}}\sin\theta_{\mathrm{R}} - \cos\theta_{\mathrm{A}}\cos\theta_{\mathrm{R}}\right) \tag{2.23}$$

and also an expression for the middle section area of the droplet,

$$A = \frac{R^2}{2\sin\theta_{\mathrm{R}}} \left(\left[\theta_{\mathrm{A}} + \theta_{\mathrm{R}} - \sin 2\theta_{\mathrm{A}} + \sin\Delta\right] \sin\theta_{\mathrm{R}} + 4\sin^3\left(\frac{\Delta}{2}\right) \sin\left(\frac{\theta_{\mathrm{A}}+\theta_{\mathrm{R}}}{2}\right)\right) \tag{2.24}$$

where $\Delta = \theta_{\mathrm{A}} - \theta_{\mathrm{R}}$ is the contact angle hysteresis. The equations of the droplet height and perimeter are shown below:

$$h = R\left(1 - \cos\theta_{\mathrm{A}}\right) \tag{2.25}$$

Table 2.1: Constants used in the fitting curve of the advancing and receding angles relationship

θ_A	a	b	c	d
[2.39, 2.43)	-0.5771	0.2414	-0.9432	0.2195
[2.43, π]	-1.5154	0.6500	-1.1679	0.3164

$$P = R\left(\theta_A + \theta_R\right) + \frac{2R\sin\frac{\beta}{2}}{\sin\theta_R}\sin\left(\theta_R + \frac{\beta}{2}\right) \tag{2.26}$$

More details about the formulation can be found in the ESDLab web page [52]. Using the model hypotheses together with equations (2.23) and (2.24), it is also possible to derive an implicit equation that relates both advancing and receding angles:

$$\frac{K_3}{4} = \frac{\sin\theta_R}{2K_2^2}\cdot K_1 \qquad \longrightarrow \qquad K_2^2\cdot K_3 - 2\sin\theta_R\cdot K_1 = 0 \tag{2.27}$$

where:

$$K_1 = \left(\left(\theta_A + \theta_R - \sin 2\theta_A + \sin\left(\Delta\right)\right)\sin\theta_R + 4\sin^3\left(\frac{\Delta}{2}\right)\sin\left(\frac{\theta_A+\theta_R}{2}\right)\right) \tag{2.28}$$

$$K_2 = 1 + \sin\theta_A\sin\theta_R - \cos\theta_A\cos\theta_R \tag{2.29}$$

$$K_3 = \frac{1}{\sin^2\theta_S}\left(\theta_S - \frac{\sin 2\theta_S}{2}\right) \tag{2.30}$$

Eq. (2.27) does not depend on the droplet size. Since it is not feasible to find an explicit equation for the receding angle, a fitting function needs to be found in order to have an expression for this magnitude. A single expression to fit all the values of the receding angle would introduce a high estimation error for values of the advancing angle close to θ_S because from $\theta_A = 2.39$ to 2.43 rad (values close to the static angle), the receding angle drops quickly, whereas from 2.43 to π, θ_R decreases almost linearly.

Using Eq. (2.27), a set of 200 values has been generated to estimate a fitting curve in each interval, giving θ_A values from 2.39 rad to π with an increment of 0.005 rad. Therefore, two different equations are proposed to estimate the receding angle based on the advancing angle. Both equations have been found using the commercial software CurveExpert Basic, which uses the Levenberg-Marquardt algorithm to perform nonlinear regression. Using this fitting curve software, the best curve for both cases is:

$$\theta_R = \frac{a + b\theta_A}{1 + c\theta_A + d\theta_A^2} \tag{2.31}$$

where the constants a, b, c and d have the values shown in Table 2.1.

In both cases, the coefficient of determination R^2 is higher than 0.999, which means that the proposed functions have an excellent fit with the numerical data.

2.4 Droplet dynamics model

As shown in Eq. (2.20), the deformation of the droplet depends on the surface tension and drag forces. Following sections provide with a detailed characterization of these forces.

2.4.1 Drag coefficient model

Drag coefficient C_{D} in Eq. (2.21) depends on the droplet geometry and the air velocity, amongst other factors. In reference [24], this parameter is computed using the formula proposed by White (see Chapter 4 [53]):

$$C_{\mathrm{D}} = 0.4 + \frac{24}{Re} + \frac{6}{1+\sqrt{Re}} \tag{2.32}$$

which is used to estimate the drag coefficient for a free sphere immersed in a gas flow and is based on the droplet diameter. Of course, the droplet shape is far away from a sphere, and this approximation has been identified as one of the factors that take the model predictions away from the experimental data [24]. Consequently, the best option is to implement the droplet geometry using a CFD software and compute the drag force numerically. Since there are a lot of factors involved in the value of F_{drag} and C_{D}, two of them have been chosen as the most important:

- The droplet height, which can be used as the characteristic length to compute the Reynolds number, i.e. Re_{h}
- The droplet deformation state, which can be described with the contact angle hysteresis.

The rest of the parameters, such as the channel geometry, the air density, viscosity and mean velocity or the water mass flow have been kept constant in the study of the drag coefficient. The effects of the droplet height and its contact angle hysteresis on the drag force have been studied by performing Computational Fluid Dynamics (CFD) simulations of a rectangular channel with different droplet geometries (i.e., modifying the size and the shape) and different flow conditions. The simulations were performed in 3D using Kratos[1], considering a cross-sectional area of the channel with the same value for both height and width. Two examples of the droplet geometries used in the numerical simulations are shown in Fig. 2.8.

In the simulations, the computational domain is a channel with a squared cross-sectional area of 1 mm per side and 50 mm long (Fig. 2.9). The simulations have been done considering a steady-state with a fully developed laminar profile for the velocity and an average value of u_{air} (Table 2.2 in Section 2.4.3) in the channel. The governing equations for the air's velocity and pressure are the stabilized mass and momentum conservation equations (see Chapter 4). The boundary conditions are the following:

- Dirichlet boundary condition for the velocity at the inlet; fully developed laminar profile with average velocity u_{air}.

[1]Kratos Multi-Physics System is a C++ object oriented FE framework [54]

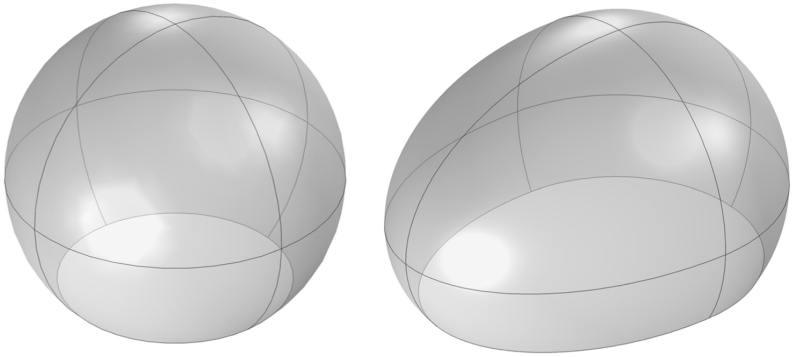

Figure 2.8: Static (left) and dynamic (right) droplet geometries used in the numerical analysis of the drag force

- Neumann boundary condition for the pressure at the outlet, i.e. no viscous stress (open boundary).
- No slip boundary condition to the rest of the walls and the droplet.

The droplet has been characterized as an obstacle laying on the channel floor. The channel has been meshed using 500000 elements (P1+P1 tetrahedrals) and solved using the iterative solver BICGSTAB. The nonlinearity in momentum equation is solved using the Newton-Raphson method. The drag force has been computed as the sum of the pressure drag and the viscous drag.

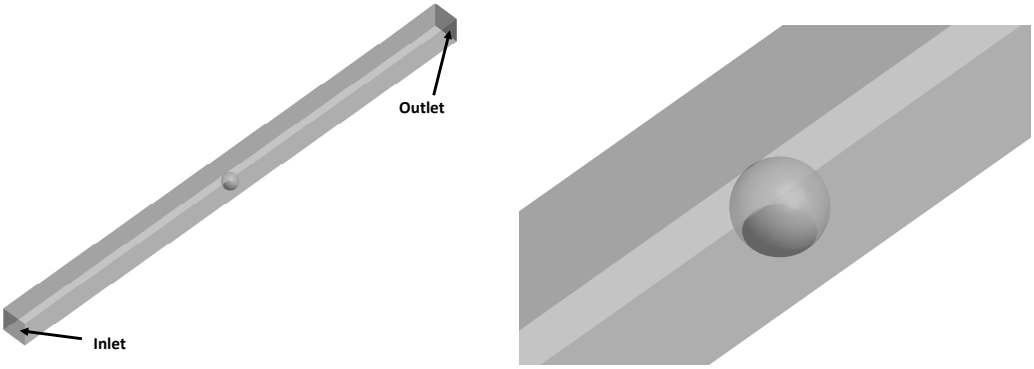

(a) Modeled channel (b) Detail of the droplet

Figure 2.9: Computational domain of the gas channel used in the drag coefficient calculation

Droplet height

The droplet height is clearly one of the main factors that influences the drag coefficient value. The two previous cases have included a change in the droplet height. Here the effect of this variable is studied alone. The computational domain is maintained at a constant geometry of 13 mm of height and width, and a length of 500

mm. Using the values in Section 2.4.3, the considered heights correspond to the values of the droplet from t = 0s to t = 1.5s, keeping the geometry in its static configuration. The obtained results are shown in Fig. 2.10(a).

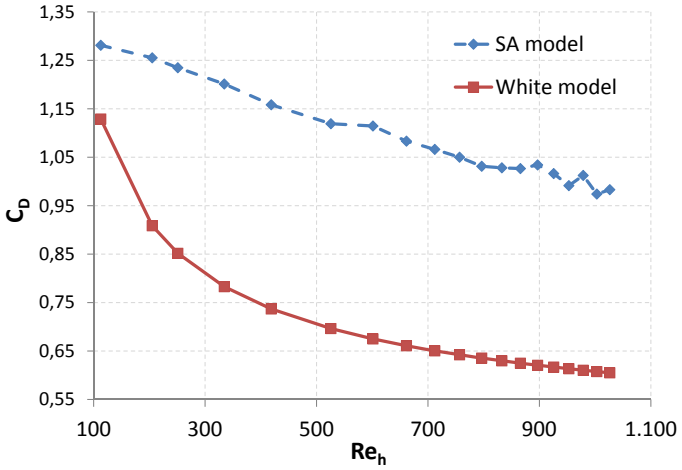

(a) Drag coefficient comparison

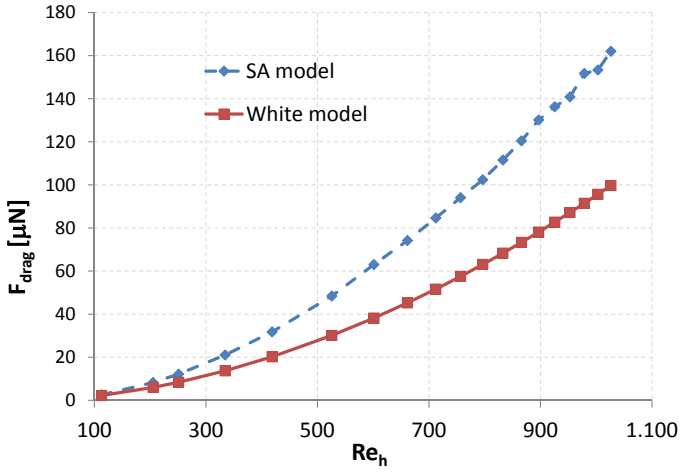

(b) Drag force comparison

Figure 2.10: Drag coefficient and drag force according to White (solid red line) and semi-analytical model (dashed blue line)

These two curves in the resulting plot correspond to the numerical result of the drag coefficient and the one obtained with Eq. (2.32) from White [53]. Note that the difference in some cases is almost 100% of the value. Since the water droplet is very small compared to the channel height, the hypothesis of the droplet under a free air stream is invalid. Thus, the drag force cannot be computed with the classic formula in Eq. (2.21). The new values of this parameter will be used. There is a significant difference between the computed and the theoretical drag force as well, as one can observe in Fig. 2.10(b)

In order to check that Eq. (2.21) is valid, two points have been chosen from the data used in Fig. 2.10(b). The first one is the point where $Re_h = 712$ and has half the area of the point located in $Re_h = 1003$. Since the force of the former ($8 \times$

10^{-4} N) is approximately half the drag force on the latter (1.57×10^{-3} N), it can be concluded that the equation for the drag force is valid in the scope of this work.

Droplet deformation

The other variable to be analyzed is the droplet deformation. The contact angle hysteresis is the indicator of this state: when the droplet is static, both advancing and receding angles are equal to the static contact angle, so the difference between them is 0. As the air flows around the droplet, the advancing angle grows and the receding angle diminishes as seen in Fig. B.3, thus increasing the difference between both angles. A more deformed shape of the droplet implies that it is more aerodynamic, which means that the drag coefficient is lower.

A three-dimensional deformed droplet has a complex geometry and is difficult to characterize. In the present study, it has been considered that the droplet tends to have the shape of a truncated ellipsoid, which coincides with previous studies that have analyzed droplet deformation [43], [18], [50]. Although the shape of the droplet has been approximated, geometry variables such as droplet chord length, height, radius and frontal area have been maintained constant. Fig. 2.8 shows the geometry of a static and deformed droplets. Numerical results obtained for three different deformation states are depicted in Fig. 2.11(a). Results show that the droplet deformation plays an important role in the value of both the drag coefficient and force (Fig. 2.11(b)).

Drag coefficient parametric equation

In the previous sections, the effects of the droplet height and its contact angle hysteresis on the drag coefficient have been studied. Multiple regression analysis is performed with the data obtained from the numerical simulations. The software Minitab v15 is used to run the statistical analysis, yielding the following output:

```
The regression equation is
Cd = 18.4 - 0.777 Re_h - 0.772 hyst

Predictor          Coef      SE Coef        T      P
Constant       18.40273      0,00731   182,33  0,000
Re_h         -0.776998   0,00000924   -39,58  0,000
hyst         -0,771978     0,003834   -19,04  0,000

S = 0,0182599   R-Sq = 97,7%   R-Sq(adj) = 97,6\%
```

The drag coefficient as a function of Reynolds number and hysteresis angle is shown in the second line of the analysis output. The previous table analysis each variable independently and also shows its significance in the model, represented by the p-value (rightmost column in the table). Given the chosen Confidence Interval (95%), a variable is considered statistically significant when the p-value is lower than 5% (i.e. $p < 0.05$). This percentage indicates the probability of accepting a linear relationship when it actually do not exist (Type I error). The resulting

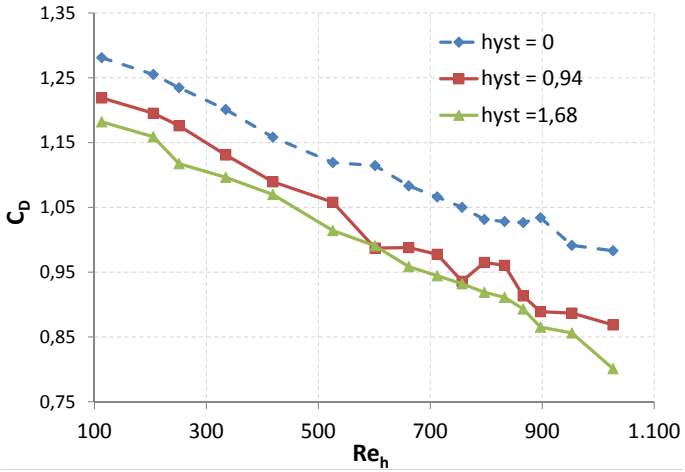

(a) Drag coefficient comparison

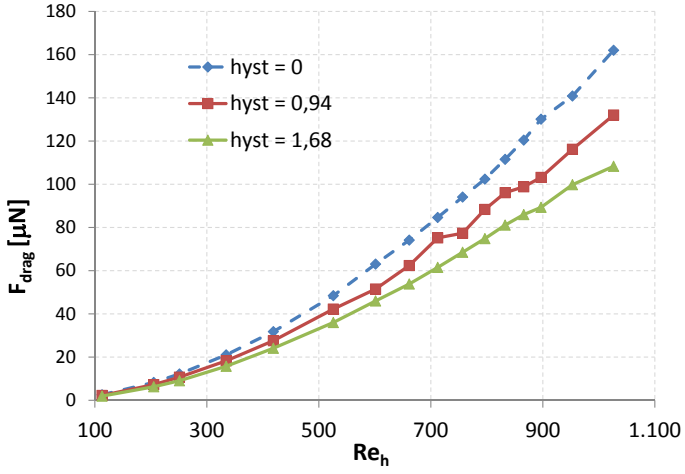

(b) Drag force comparison

Figure 2.11: Drag coefficient of the two deformed droplets compared to the static geometry

table indicates that the three variables included in the model have p-values lower than 0.001, and thus they are statistically significant in the model. The resulting equation is represented in a three-dimensional plot shown in Fig. 2.12.

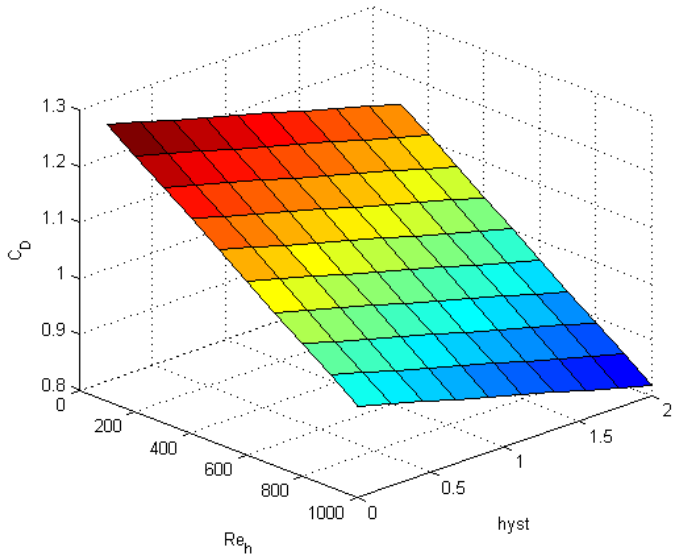

Figure 2.12: Drag coefficient representation as a function of the hysteresis angle and the Reynolds number for droplet heights less than 10% of channel height

The relationship between the drag coefficient and the considered variables can be considered linear since the $R-sq$ value of the resulting model is closer to 100%. For droplet height to channel height ratios below 10% the flow conditions inside the channel are not affected by the droplet and the drag force only depends on the droplet geometry. On the other hand, for droplet height to channel height ratios above 10%, the flow conditions in the channel are affected by the droplet. In this case, both droplet height and height of the channel influence the results. Furthermore, since the drag depends not only on the drop, Eq. (2.21) cannot be used. Several simulations were performed in this case and it was found that the drag force (expressed in μN) could be approximated by:

$$\begin{aligned} F_{\text{drag}} = 5.81 - 4.82Re_{\text{H-h}} + 1.67Re^2_{\text{H-h}} - 0.29Re^3_{\text{H-h}} + \\ +0.03Re^4_{\text{H-h}} - 8.66 \times 10^{-4} \cdot Re^5_{\text{H-h}} - 1.43\Delta \text{e}^{-0.959Re_{\text{H-h}}} \end{aligned} \tag{2.33}$$

The exponential term in Eq. (2.33) means that the difference between the static and deformed cases increases as $H-h$ decreases. The coefficients were obtained by running simulations with air fluid properties, droplet heights from 0.01 to 8 mm and channel geometries from 0.1 to 10 mm. In order to estimate the generality of the equation, different fluid properties were also studied. Results showed that the drag force obtained from the CFD simulation and the one predicted from the equation above differed by less than 1%.

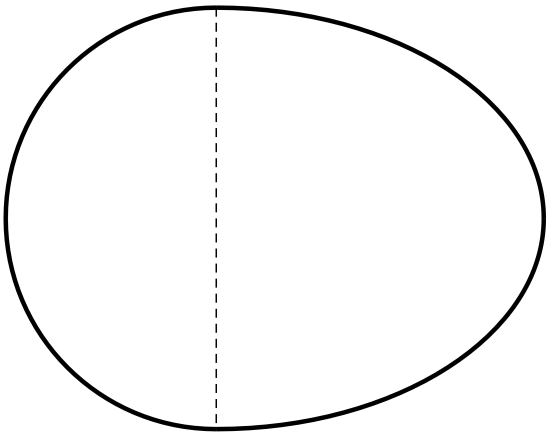

Figure 2.13: Contact line of a deformed droplet

2.4.2 Adhesion force model

The surface tension force acts on the droplet when the droplet is in a non-equilibrium configuration. The force is proportional to the droplet deformation. Celestini and Kofman (2006) stated that this restoring force can be expressed as [51]:

$$F_{\mathrm{ST}} = -\gamma \frac{\Delta S}{dx} \tag{2.34}$$

where γ is the water surface tension, ΔS is the surface variation due to the deformation and dx is the displacement of the center of mass from its original position. Even though this form of the surface tension is very intuitive, it is an approximation of the actual phenomena. Moreover, the spring model can be misunderstood since the spring force acts on the center of mass, whereas the adhesion force is applied at the contact line with the surface. Thus, in this work the adhesion force of the droplet is computed numerically using Eq. (2.22), where θ is the contact angle and ψ is the angle between the surface tension force in the xy plane and the x axis, as shown in Fig. 2.6.

This expression is integrated numerically to obtain the approximated value of the adhesion force at every deformation state [50]. As Antonini et al. showed in their work [50], for hydrophobic surfaces with static contact angle greater than 90° the contact line of a deformed droplet can be described as a double ellipse, as shown in Fig. 2.13. The proposed model considers that the y semi-radius remains constant for the two ellipses, and the sum of the two x semi-radii is equal to the droplet chord. Using this geometry and numerical integration, Eq. (2.22) is solved at every time step. In our model, the contact angle distribution in every semi-ellipse has been considered linear with respect to the x direction, going from the value of the static contact angle to the value of the advancing or receding angle in each case.

2.4.3 Boundary conditions

In order to solve the differential equation (2.20), initial conditions must be imposed for the x-coordinate of the center of mass. Since Eq. (2.20) is a second order

Table 2.2: Parameters used in the simulation

Variable	Symbol	Value	Units
Initial chord	c_0	0.07	mm
Water flow rate	Q	0.047	μl s^{-1}
Water surface tension	γ	0.072	N m^{-1}
Water density	ρ_{w}	1000	kg m^{-3}
Static contact angle	θ_{S}	135	deg
Air density	ρ_{air}	1.205	kg m^{-3}
Air viscosity	μ_{air}	1.98×10^{-5}	kg m^{-1} s^{-1}
Air velocity	u_{air}	0.1483	m s^{-1}
Channel height	H	1	mm

differential equation, the following two initial conditions are imposed,

$$x_{\mathrm{CM}}|_{t=0} = \frac{c_0}{2} \tag{2.35}$$

$$\left.\frac{dx_{\mathrm{CM}}}{dt}\right|_{t=0} = v_{\mathrm{CM}}|_{t=0} = 0 \tag{2.36}$$

In other words, at $t = 0$ the droplet is static. The term c_0 refers to the droplet chord at the beginning of the simulation. The rest of the parameters used in the simulation are described in Table 2.2.

The velocity of the air inside the channel is given by the geometry of the channel and the working conditions of the fuel cell. Typically, a fuel cell channel has a 1 mm $\times$ 1 mm cross-sectional area and 5 cm length. An usual value for the current density is 1 A cm^{-2}, and for this current the amount of oxygen needed in the cathode is given by:

$$\dot{m}_{\mathrm{O_2}} = \frac{I}{4F} = \frac{i \cdot A_{\mathrm{act}}}{4F} \tag{2.37}$$

where i is the current density, A_{act} is the active area of the channel and F is the Faraday's constant, which equals to 96485 C mol^{-1} or, equivalently, 96485 A s mol^{-1}. Given that the base of the channel is a rectangle of 1 by 50 mm, the oxygen needed is:

$$\dot{m}_{\mathrm{O_2}} = \frac{1\frac{\mathrm{A}}{\mathrm{cm}^2} \cdot 0.5\mathrm{cm}^2}{4 \cdot 96485\frac{\mathrm{C}}{\mathrm{mol}}} = 1.2955 \cdot 10^{-6}\frac{\mathrm{mol\ O_2}}{s} \tag{2.38}$$

Finally, the necessary mass flow of air needed to have the desired current density is:

$$\dot{m}_{\mathrm{air}} = 1.2955 \cdot 10^{-6}\frac{\mathrm{mol\ O_2}}{s} \times \frac{1\mathrm{mol\ air}}{0.21\mathrm{mol\ O_2}} \times 28.96\frac{\mathrm{g}}{\mathrm{mol\ air}} \times \frac{1m^3}{1205\mathrm{g}} = 1.4827 \cdot 10^{-7}\frac{m^3}{s} \tag{2.39}$$

For the considered geometry, this value of the mass flow gives an inlet air velocity of 0.1483 m s^{-1}. Eq. (2.20) and the aforementioned boundary conditions are implemented in MATLAB and solved using an in-house 4th order Runge-Kutta method.

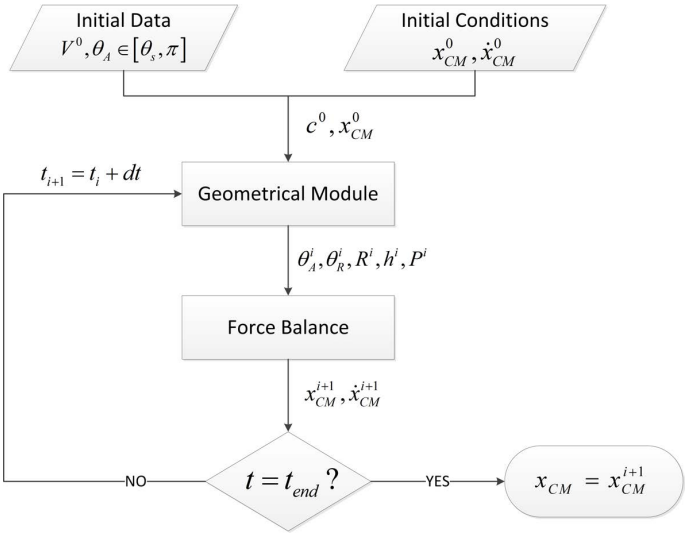

Figure 2.14: Flowchart of the algorithm to solve the dynamic problem

2.4.4 Geometry and dynamic model integration

Fig. 2.14 shows a flowchart of the algorithm implemented to solve the dynamic model. For a known value of the water mass flow $\dot{Q}$, the volume of the droplet is obtained. The volume is used with the initial conditions to find the initial value of the droplet chord and the x-coordinate of the center of mass. These values are used in the time integration of the dynamic model.

At every time step, the new droplet volume is used to calculate the new chord length and the x-coordinate of the center of mass. These parameters are used in the geometrical model to find the contact angles and the rest of geometrical variables. The forces at the current time step are computed using the known geometry of the droplet. Then, the force balance results in the x-coordinate of the center of mass and its velocity at the next time step. This process is repeated until the final time step is reached.

2.5 Results and discussion

In this section, the most important results regarding the droplet dynamics are discussed. The total time of the simulation is 1 s, considering a droplet that is injected at a constant flow rate. The inlet velocity of air is 0.1483 m s^{-1} (Table 2.2). The time step size chosen for this simulation is 10^{-4} s, and the total computational time is about 2 min.

The simulation shows the evolution of the droplet shape at every time step during its execution. Fig. 2.15 shows the simulation state at four different time steps.

2.5.1 Validation

The semi-analytical model is validated by reproducing several experiments. Milne et al. [5] measured the critical drag force needed to detach a sessile droplet from a hydrophobic surface. Different droplet volumes were considered in order to obtain a

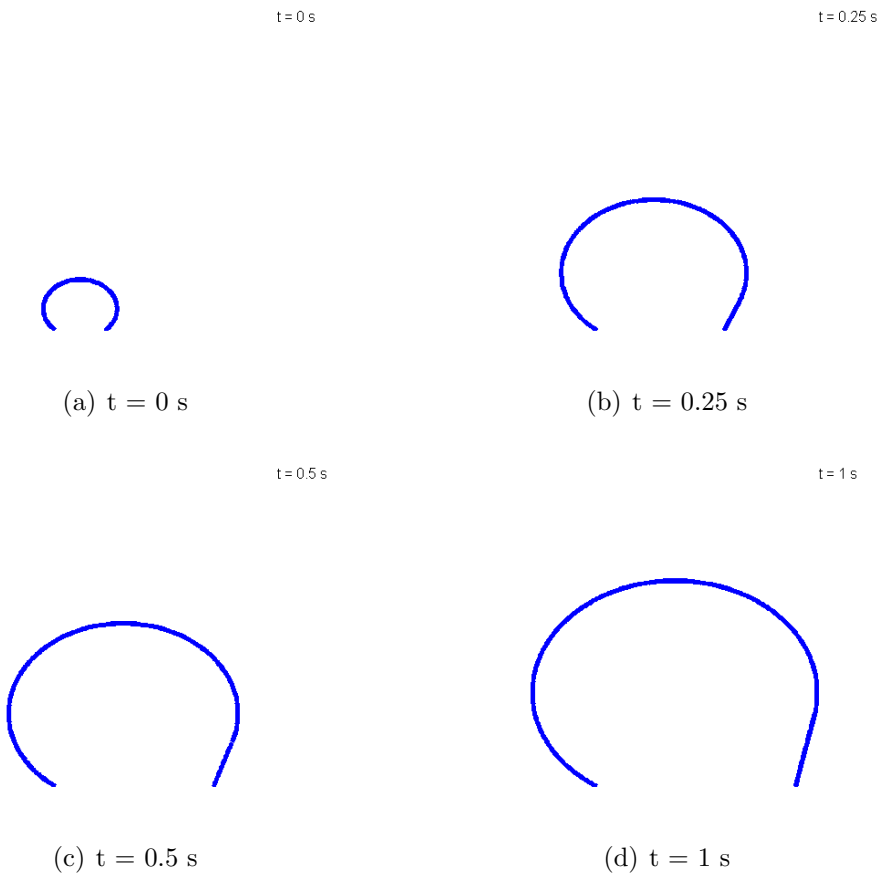

(a) t = 0 s

(b) t = 0.25 s

(c) t = 0.5 s

(d) t = 1 s

Figure 2.15: Droplet deformed shape representation at different time steps of the simulation

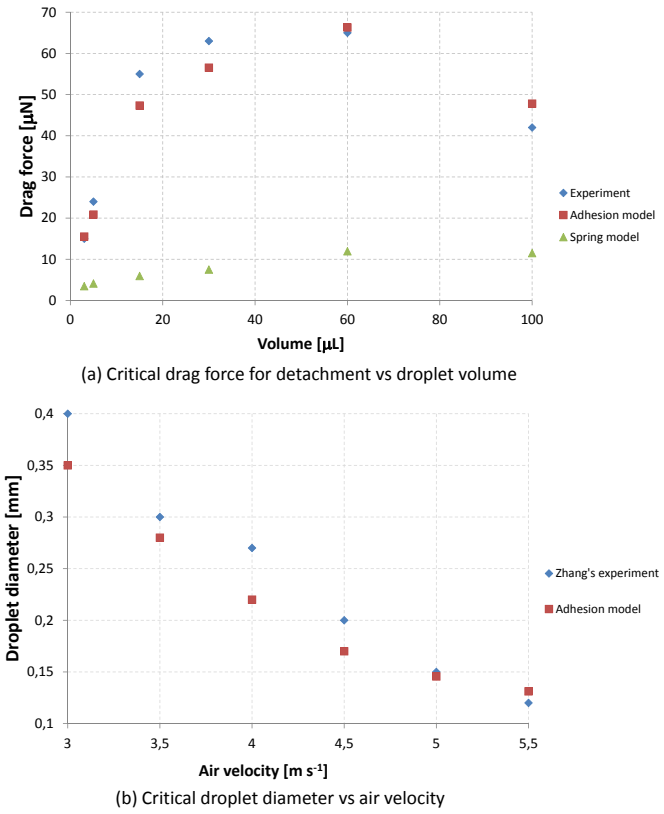

(a) Critical drag force for detachment vs droplet volume

(b) Critical droplet diameter vs air velocity

Figure 2.16: Validation results of the semi-analytical model

relationship between volume and critical drag force. The experiment is reproduced here by first computing the droplet geometry for every volume, setting a value of 0 for the water injection rate ($\dot{Q} = 0$) and increasing the velocity of the air until the detachment condition is fulfilled. According to Milne's work, the droplet detaches when the contact angle hysteresis is greater than 30 degrees [5] (results obtained for a GDL surface with Teflon). The drag force when the droplet detaches is easily obtained from either Eq. (2.21) or (2.33). Fig 2.16 (a) shows the comparison between the experimental results from Milne, the predicted values with the proposed model, and the values obtained with the spring model in reference [24].

The values predicted with the current semi-analytical model are in good agreement with the experimental data. The values obtained with a spring model largely underpredict the critical drag force. The difference between the experimental data and the predictions from the proposed model is larger at higher droplet volumes. As the droplet grows, gravity and viscous effects become more important. In the present model gravity effects are neglected, which can dominate for large droplet sizes. However, the proposed model predicts well the drag force necessary for droplet detachment for droplet volumes up to 100 μL.

In order to further validate the proposed model predictions, predicted droplet size before detachment is compared to the experimental results reported by Zhang et al. [21]. Zhang et al. [21] measured the droplet size before detachment for droplets at different air velocity. In the simulations, the air velocity is fixed and the droplet is allowed to grow until detachment takes place. Detachment occurs

when the transient hysteresis angle reaches 30 degrees. Fig. 2.16 (b) compares the experimental data in reference [21] and the predicted droplet size according to the proposed model, using Milne's conditions for the critical hysteresis angle. Results obtained are in good agreement with the experimental data in reference [5] Both results have the same tendency: the higher the air velocity, the lower the critical droplet diameter. Thus, the critical hysteresis angle can be taken as 30°.

2.5.2 Evolution of the center of mass, hysteresis angle and forces

Fig. 2.17(a) shows the effect of air velocity on the droplet center of mass for a droplet in a 1×1 mm rectangular channel typical of a fuel cell. For large flow rates, the center of mass position is well below the center of mass of the static droplet indicating that the center of mass approaches the advancing contact point (see point B in Fig. 2.7). When the velocity of the air is 0, the x-coordinate of the droplet center of mass evolves without almost any oscillation, as expected. It has been observed, e.g. references [24] [15], that the higher the air velocity, the bigger the amplitude of the droplet oscillations, i.e. the droplet is more unstable and is prone to detach from the GDL surface. The frequency of the oscillations however remains almost constant.

The green lines correspond to the spring model for the adhesion force proposed in reference [24]. The proposed model predicts higher adhesion forces, resulting in a stiffer droplet with less deformation. Therefore, the droplet is less prone to detach from the GDL surface. For both models, results show that for higher velocities the droplet is more deformed.

Since the two forces acting on the droplet have opposite directions, the center of mass oscillates during droplet growth. The advancing and receding angles have oscillations as well, as displayed on Fig. 2.17(b). In this simulation, as the droplet grows, the drag force deforms the droplet. As the drag increases, the difference between both angles also increases, which is represented as the hysteresis angle in Fig. 2.17(b).

The two forces acting on the droplet are responsible for its oscillation. Larger droplet sizes lead to increased values of the drag force. The surface tension force is modeled using Eq. (2.22). The evolution of both forces over time is shown in Figure 2.17(c). One can observe that the drag force oscillates with small amplitude compared to the surface tension force. The main reason is that, for a certain droplet size, the frontal area does not change much with the oscillation of the center of mass x-coordinate. The drag force has a quadratic growth due to its quadratic relationship with the droplet radius.

2.5.3 Detachment time and force

Using the proposed model, detachment times can be estimated based on the time it takes for a droplet to reach a critical hysteresis angle. Based on previous research, e.g. reference [5], it is estimated that a water droplet within airflow will detach from

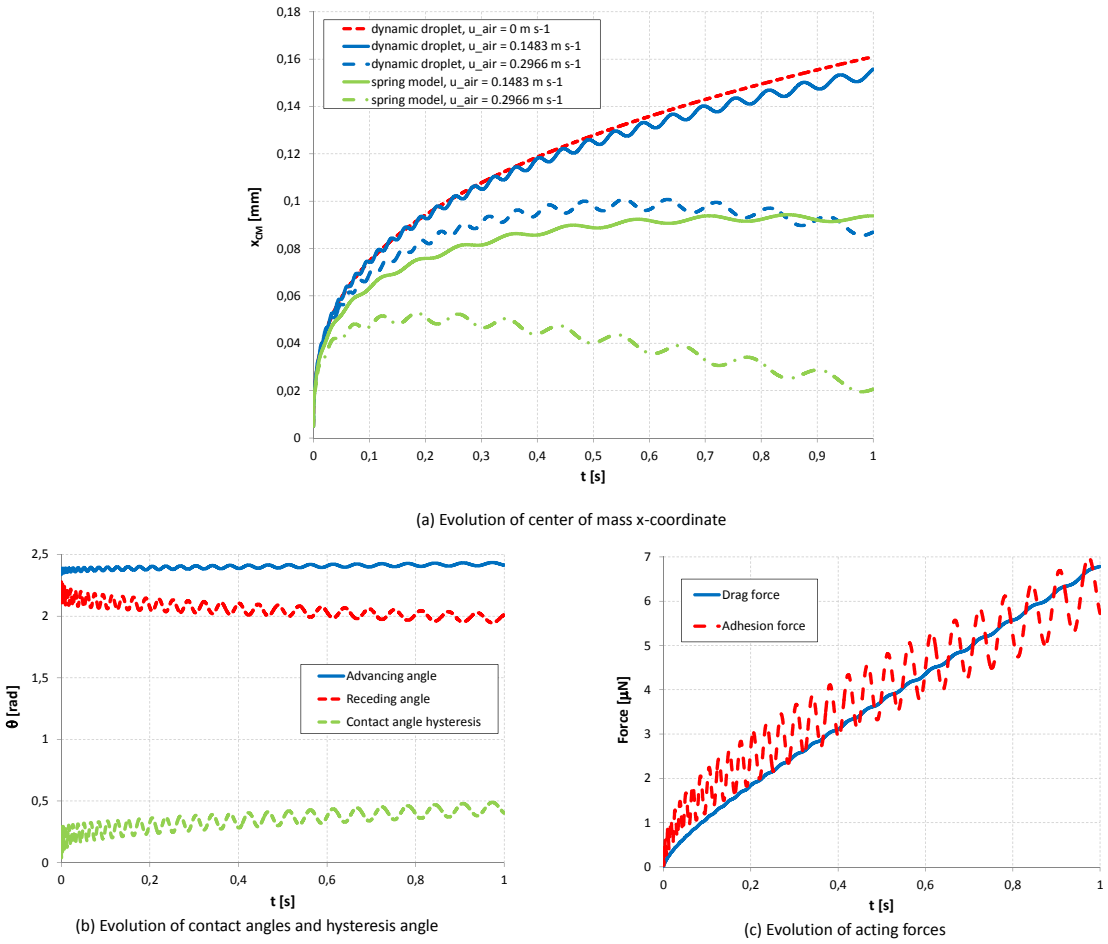

(a) Evolution of center of mass x-coordinate

(b) Evolution of contact angles and hysteresis angle

(c) Evolution of acting forces

Figure 2.17: Evolution of the center of mass x-coordinate, contact angles and forces acting on the droplet

Table 2.3: Detachment time, height, width, and area covered for different water injection rates ($\dot{Q}$) and air velocities (u_{air})

$\dot{Q}$ [μl s^{-1}]	t_{det} [s]		A_{cov} [mm^2]		h [mm]		w [mm]	
	u_1	u_2	u_1	u_2	u_1	u_2	u_1	u_2
0.01	49.32*	25.19	0.393	0.251	0.853	0.683	1.000	0.8
0.02	24.66*	12.58				0.681		0.799
0.04	11.52	6.31	0.376		0.834	0.683	0.978	0.8
0.08	5.31	4.60	0.356		0.812	0.682	0.952	0.8

the surface when the contact angle hysteresis is greater than 30 degrees[2].

For a droplet in a fuel cell channel, the values in Table 2.2 are used to predict detachment while the maximum hysteresis angle is set to 30°. The proposed model then predicts detachment after 9.83 s. When the droplet is subjected to airflow it oscillates and therefore is more prone to detachment. This result highlights the importance of a transient model for this problem. At high airflow rates, droplet geometry and droplet height will be independent of current density, and drops will not block the channel. However, at low air flow rates blockage is possible.

The detachment time is a function of the water injection rate [16], [9], [24], [18]. Several simulations have been done considering different values for the water inflow and two air velocities ($u_1 = 0.15$ ms^{-1}, $u_2 = 0.5$ ms^{-1}) and the results are shown in Table 2.3. These air velocities correspond to the air flow rate for a stoichiometric ratio of one at two different current densities, 1 A cm^{-2} and 3 A cm^{-2}, respectively.

The time values marked with an asterisk (*) correspond to those cases where the droplet blocks the channel before detachment. For the different water injection rates and the air flowing at $u_2 = 0.5$ ms^{-1}, the droplet detaches when it reaches a critical value of height, independently of liquid flow rate.

2.6 Conclusions

A semi-analytical model of a water droplet emerging from a GDL pore in a cathode gas channel has been developed. Several numerical simulations have been done to obtain the value of the drag coefficient for different droplet sizes. For a droplet height to channel height ratio below 10% the drag coefficient exhibited linear relationship with the Reynolds number and hysteresis angle. For a droplet height to channel height ratio above 10% the drag force shows a nonlinear relationship with the Reynolds number and the contact angle hysteresis.

From the analysis of the drag coefficient it can be concluded that using a spherical drop drag equation versus Reynolds number leads to underpredicted values of the drag coefficient and therefore the drag force. The results for the adhesion force show that the considered equation gives higher results than others obtained from a spring model [24], [51]. Previous approaches using a spring model might have

[2]This value corresponds to the problem at hand, i.e., 1 mm droplets on a surface with $\theta_s = 135$ deg

underestimated the adhesion force by as much as 50%. A lower value of the adhesion force means that the droplet oscillates with higher amplitude but with less frequency.

The value of the critical drag force corresponding to the droplet detachment is consistent with the experimental data in reference [5]. The detachment condition from reference [5] has been tested comparing the experimental data from reference [21]. Results show that the proposed model using a constant value of the critical hysteresis angle (Milne's condition) has good agreement with the experimental results.

The water injection rate study reveals that for low air velocities, the droplet blocks the channel before detaching the channel surface, whereas for high air velocities the droplet detaches when it reaches a critical height value. Applying this model to droplets in a fuel cell channel it has been found that at moderate flow rates and low airflow velocities droplets are likely to block the channels. Further, GDL coverage is at least 50% of the cross-sectional area, therefore it limits gas transport to the GDL.

The semi-analytical model has shown to be a fast tool to obtain preliminary results of droplet detachment in fuel cell gas channels. Simulations performed with this model have a computational cost of the order of several minutes. The computational cost of similar simulations using a numerical model is of the order of several hours.

Chapter 3

A Lagrangian finite element model for droplets

In this chapter, a numerical model in two and three dimensions for droplet dynamics using a Lagrangian finite element formulation is proposed. Although analytical models (such as [19] and the one proposed in the previous chapter) provide solutions at low computational cost, they oversimplify the phenomena by either using predefined droplet geometries or neglecting air-water interactions. For gravity-dominated flows, such as film or slug flows, analytical models cannot characterize the geometry and therefore they cannot be applied [11]. Moreover, a numerical model can be used to predict the dynamics of the droplet after detachment. Detached droplets can adhere to channel walls and modify flow conditions, or can reattach to the GDL surface and interact with other droplets. Even for droplet flow, the difference between experimental and analytical predictions can be as high as 30% for highly deformed droplets.

Numerical methods can be used to provide more accurate droplet dynamics predictions at the cost of explicitly including a continuum description of both phases (air and water) and their interaction in the model. Most of the studies in the literature analyze the phenomena using an Eulerian formulation equipped with the Volume of Fluid (VOF) method [55], [25], [16], [15]. This method is widely used since it is already implemented in most of commercial FEM codes. VOF method can represent complex interface geometries and has good mass conservation features. However, it suffers from interface diffusion and it is restricted to small time steps due to the explicit treatment of surface tension. Additionally, VOF method cannot be used to describe a single phase (i.e. a droplet) since it depends on a background fixed mesh (Fig. 3.1(a)). Hysing [56] used an Eulerian formulation, tracking the interface with the level set method. Although results were obtained using large time steps, the model could not be fully implicit since the interface could not be explicitly found using the Eulerian approach. Moreover, level set method is not mass conservative.

An alternative to Eulerian models are the Lagrangian models, such as the one proposed by Saksono and Perić [57]. Saksono and Perić [57] proposed an implicit variational formulation for the surface tension term. One of the advantages of Lagrangian models is that they can track exactly the water domain and its boundary (Fig. 3.1). This formulation could be used to describe quasistatic and dynamic

problems [58]. However, the model relied upon an axisymmetric formulation, not being able to solve complex geometries.

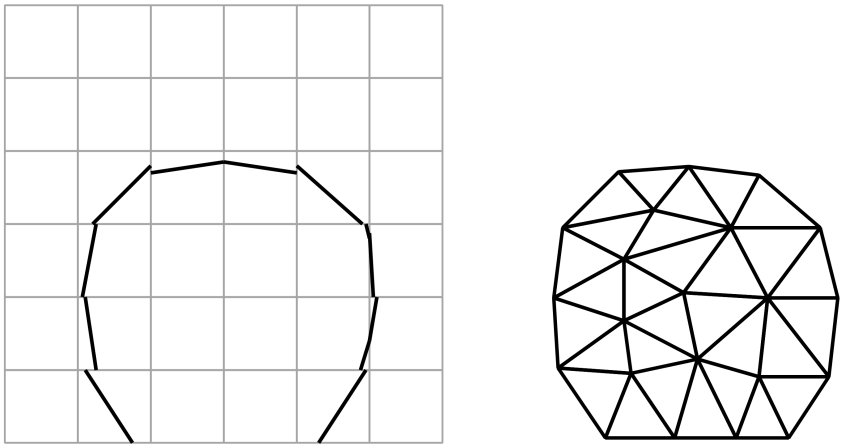

(a) Possible droplet representation in VOF method

(b) Possible droplet representation using a Lagrangian framework

Figure 3.1: Schematic representation of a water droplet using an Eulerian formulation with the VOF method (left) and a Lagrangian formulation (right)

Recent trends on water droplet dynamics research are reducing the working scale to the molecular size. In other words, researchers have realized that the best way to characterize the water droplet shape at any state is to model it as a subset of particles. Although these studies go beyond the scope of the present work, the results shown could give a different point of view for the studies in the macroscopic scale. As an example, two studies that should be considered are [59] and [60].

In PEFC context, numerical studies based on the VOF method typically rely upon an explicit treatment of the surface tension. This restricts the model to using extremely small time steps (governed by the time scale associated with the propagation of capillary waves) in order to achieve convergence [61]. This restriction is an important drawback for practical PEFC simulations. Additionally, VOF studies need very fine meshes to have an accurate description of the interface. This further increases the computational cost of the corresponding simulations.

This chapter presents a Lagrangian model for liquid drops since it allows for:

a) accurate definition and track of the boundary

b) implicit surface tension modeling and thus using large time steps

c) good mass conservation

d) mesh-based definition of contact angles and thus accurate modeling of wetting phenomena

e) symmetric resulting system

3.1 Governing equations

Let us consider a spatial domain $\Omega \subset \mathbb{R}^n$, where $n \in \{2, 3\}$ (see Fig. 3.2). The outer boundary of the fluid is designated as Γ_I. The part of the boundary in contact with the solid substrate is denoted by Γ_S.

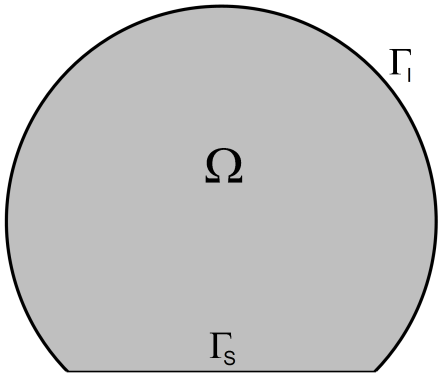

Figure 3.2: Schematic representation of the considered single-phase system

The governing equations for the fluid are the mass and momentum conservation equations [62], [53]:

$$\rho \frac{D\mathbf{v}}{Dt} - \nabla \cdot \boldsymbol{\sigma} = \rho \mathbf{g} \qquad \text{on } \Omega \tag{3.1}$$

$$\frac{D\rho}{Dt} + \rho \left(\nabla \cdot \mathbf{v}\right) = 0 \qquad \text{on } \Omega \tag{3.2}$$

where $\mathbf{v}$ is the velocity vector, $\boldsymbol{\sigma}$ is the Cauchy stress tensor, t is the time, $\mathbf{g}$ is the body force and ρ is the fluid density. The operator $\frac{D\phi}{Dt}$ stands for the total material derivative:

$$\frac{D\phi}{Dt} = \frac{\partial \phi}{\partial t} + \mathbf{v} \cdot \nabla \phi \tag{3.3}$$

For a Newtonian fluid, the Cauchy stress tensor is given by:

$$\boldsymbol{\sigma} = -\left(p + \frac{2}{3}\lambda \epsilon_{\mathrm{V}}\right)\mathbf{I} + 2\mu \mathbf{D} \tag{3.4}$$

where p is the pressure, μ is the dynamic viscosity, λ is the bulk viscosity, $\epsilon_{\mathrm{V}} = \nabla \cdot \mathbf{v}$ is the volumetric strain rate, $\mathbf{I}$ is the identity tensor and $\mathbf{D} = \frac{1}{2}\left(\nabla \mathbf{v} + \nabla^T \mathbf{v}\right)$ is the strain rate tensor.

If the density of the fluid is constant, first term in Eq. (3.2) is zero and the equation takes the following form:

$$\nabla \cdot \mathbf{v} = 0 \tag{3.5}$$

Eq. (3.5) is known as the mass conservation equation. If one uses this expression in Eq. (3.4), Cauchy stress tensor for an incompressible fluid yields:

$$\boldsymbol{\sigma} = -p\mathbf{I} + \mu\left(\nabla \mathbf{v} + \nabla^T \mathbf{v}\right) \tag{3.6}$$

Combining Eqs. (3.1), (3.5) and (3.6) gives Navier-Stokes equations for an incompressible fluid:

$$\rho\frac{\partial \mathbf{v}}{\partial t} - \nabla\cdot\mu\left(\nabla\mathbf{v} + \nabla^T\mathbf{v}\right) + \nabla p = \rho\mathbf{g} \qquad \text{on } \Omega \tag{3.7}$$

$$\nabla\cdot\mathbf{v} = 0 \qquad \text{on } \Omega \tag{3.8}$$

Note that, since the model uses the Lagrangian description, the convective term $\mathbf{v}\cdot\nabla\mathbf{v}$ is absent in the material derivative. Thermal effects are not taken into account in the model. Thus, viscosity remains constant as well.

Boundary conditions

In order to solve the problem at hand, governing equations (3.7) and (3.8) must be complemented with boundary conditions. In static conditions, the fluid has zero displacement on the x direction and therefore a no-slip Dirichlet boundary condition is imposed at Γ_S:

$$\mathbf{v} = 0 \qquad \text{at } \Gamma_S \tag{3.9}$$

The boundary condition applied in dynamic conditions is different for the contact line (i.e., $\partial\Gamma = \Gamma_S \cap \Gamma_I$). Further discussion can be found in Section 3.3.4. At boundary Γ_I, the following condition is prescribed:

$$\boldsymbol{\sigma}\cdot\mathbf{n} = \gamma\kappa\mathbf{n} \qquad \text{at } \Gamma_I \tag{3.10}$$

where $\mathbf{n}$ is the unit normal to Γ_I, γ is the surface tension coefficient and κ is the boundary curvature. Let us consider that the fluid is surrounded by an external fluid in static conditions with relative pressure $p_{\text{ext}} = 0$. Eq. (3.10) reads that the normal stress across Γ_I is balanced by surface tension. For an incompressible Newtonian fluid, the Cauchy stress tensor is given by Eq. (3.6). Projecting Eq. (3.10) onto normal and tangential directions leads to the following conditions:

$$\mathbf{n}\cdot(\boldsymbol{\sigma}\cdot\mathbf{n}) = \gamma\kappa \qquad \text{at } \Gamma_I \tag{3.11}$$

$$\mathbf{t}\cdot(\boldsymbol{\sigma}\cdot\mathbf{n}) = 0 \qquad \text{at } \Gamma_I \tag{3.12}$$

Using (3.6) in the previous equation yields[1]:

$$p - \mu\mathbf{n}\cdot\left(\left[\boldsymbol{\nabla}\mathbf{v} + \boldsymbol{\nabla}^T\mathbf{v}\right]\cdot\mathbf{n}\right) = \gamma\kappa \qquad \text{at } \Gamma_I \tag{3.13}$$

Considering that the projection of viscous stresses onto the normal direction can be neglected, Eq. (3.13) becomes Laplace-Young equation:

$$p = \gamma\kappa \tag{3.14}$$

[1] In systems where there are surfactants or temperature changes, the surface tension coefficient is variable. If surface tension varies, an additional term must be added in Eq. (3.13):

$$p - \mu\mathbf{n}\cdot\left(\left[\boldsymbol{\nabla}\mathbf{v} + \boldsymbol{\nabla}^T\mathbf{v}\right]\cdot\mathbf{n}\right) = -\gamma\kappa + \mathbf{n}\cdot\nabla\gamma \qquad \text{at } \Gamma_I$$

However, surface tension gradients are not considered in the present work.

3.2 FEM discretization

The first step towards the solution of Eqs. (3.7) and (3.8) is their discretization in space. The functional spaces where their discrete form is defined are described next.

Let us consider a domain $\Omega \subset \mathbb{R}^n$, with $n = 2, 3$, and its smooth boundary Γ. $\mathcal{L}^2(\Omega)$ denotes the Hilbert space of scalar functions that are square integrable over Ω, with inner product and norm defined by:

$$(u, v) = \int_\Omega uv \, \mathrm{d}\Omega \tag{3.15}$$

$$\|u\|_{\mathcal{L}^2} = (u, u)^{\frac{1}{2}} \tag{3.16}$$

For the discretization, not only the functions should be square integrable but also their derivatives. The Sobolev space $\mathcal{H}^k(\Omega)$ is the space where functions and their derivatives up to order k are square integrable. Space $\mathcal{L}^2(\Omega)$ is already a Sobolev space, since $\mathcal{H}^0(\Omega) = \mathcal{L}^2(\Omega)$. Space $\mathcal{H}^1(\Omega)$ is defined as follows:

$$\mathcal{H}^1(\Omega) = \left\{ u \in \mathcal{L}^2(\Omega) \quad \middle| \quad \frac{\partial u}{\partial x_i} \in \mathcal{L}^2(\Omega), i = 1, \ldots, n \right\} \tag{3.17}$$

The following subspace will also be used in the discretization of governing equations:

$$\mathcal{H}_0^1(\Omega) = \left\{ u \in \mathcal{H}^1(\Omega) \quad | \quad u = 0 \text{ on } \Gamma \right\} \tag{3.18}$$

For vector functions, such as velocity, this definition must be extended. We define $\boldsymbol{\mathcal{H}}^k(\Omega)$ the space of vector functions $\mathbf{v}$ where each i component belongs to $\mathcal{H}^k(\Omega)$, $u_i \in \mathcal{H}^k(\Omega)$. Further details on the function spaces can be found in [63].

To obtain the Galerkin variational form of Eqs. (3.7) and (3.8), we first multiply them by test functions and then integrate the product over the domain. Following the notation of [63], the set of test functions that satisfy homogeneous boundary conditions on Γ_D reads:

$$\boldsymbol{\mathcal{V}} = \left\{ \mathbf{v} \in \boldsymbol{\mathcal{H}}^1(\Omega) \quad | \quad \mathbf{v} = 0 \text{ on } \Gamma_D \right\} \tag{3.19}$$

Note that $\boldsymbol{\mathcal{V}} = \boldsymbol{\mathcal{H}}_0^1(\Omega)$. For non-homogeneous boundary conditions, we have:

$$\boldsymbol{\mathcal{S}} = \left\{ \mathbf{v} \in \boldsymbol{\mathcal{H}}^1(\Omega) \quad | \quad \mathbf{v} = \bar{\mathbf{v}} \text{ on } \Gamma_D \right\} \tag{3.20}$$

Following the notation presented in [64], the weak form of our boundary value problem is defined as follows: find $\mathbf{v} \in \boldsymbol{\mathcal{S}}$ such that $\forall \mathbf{w} \in \boldsymbol{\mathcal{V}}$, $\forall q \in \mathcal{L}^2(\Omega)$:

$$\int_\Omega \left(\rho \frac{\partial \mathbf{v}}{\partial t} \cdot \mathbf{w} - \mathbf{w} \cdot (\nabla \cdot \boldsymbol{\sigma}) \right) \mathrm{d}\Omega = \int_\Omega \rho \mathbf{g} \cdot \mathbf{w} \, \mathrm{d}\Omega \tag{3.21}$$

$$\int_\Omega q \nabla \cdot \mathbf{v} \, \mathrm{d}\Omega = 0 \tag{3.22}$$

where $\Omega = \Omega_W$. Integrating by parts and applying Stokes theorem, Eq. (3.21) reads:

$$\begin{aligned} \int_\Omega \left(\rho \frac{\partial \mathbf{v}}{\partial t} \cdot \mathbf{w} + \mu \left(\nabla \mathbf{v} + \nabla^T \mathbf{v} \right) : \nabla \mathbf{w} - p \nabla \cdot \mathbf{w} \right) \mathrm{d}\Omega = \\ = \int_\Omega \rho \mathbf{g} \cdot \mathbf{w} \, \mathrm{d}\Omega + \int_{\Gamma_N} \mathbf{w} \cdot \boldsymbol{\sigma} \mathbf{n} \, \mathrm{d}\Gamma \end{aligned} \tag{3.23}$$

Last term has been already defined in Eq. (3.10). Using this relationship, the weak form of the governing equations is obtained:

$$\int_\Omega \left(\rho \frac{\partial \mathbf{v}}{\partial t} \cdot \mathbf{w} + \mu \left(\nabla \mathbf{v} + \nabla^T \mathbf{v} \right) : \nabla \mathbf{w} - p \nabla \cdot \mathbf{w} \right) \, \mathrm{d}\Omega =$$

$$= \int_\Omega \rho \mathbf{g} \cdot \mathbf{w} \, \mathrm{d}\Omega + \int_{\Gamma_N} \gamma \kappa \mathbf{n} \cdot \mathbf{w} \, \mathrm{d}\Gamma \tag{3.24}$$

$$\int_\Omega q \nabla \cdot \mathbf{v} \, \mathrm{d}\Omega = 0 \tag{3.25}$$

The resulting weak form has derivatives in both $\mathbf{w}$ and $\mathbf{v}$, which means that functions with at least continuous first derivatives must be used. Let us consider the regular partition of Ω, $\boldsymbol{\mathcal{T}}^h(\Omega)$, into n_{elem} convex elements Ω_e such that:

$$\Omega \approx \Omega_h = \bigcup_{e=1}^{n_{\text{elem}}} \Omega_e \tag{3.26}$$

where n_{elem} is the number of elements. Increasing n_{elem} one obtains a better geometrical approximation of the computational domain. 3-noded triangles (in two dimensions) and 4-noded tetrahedra (in three dimensions) are chosen to discretize Ω for their simple implementation and their ability to represent complex domains [65]. Following the standard FEM procedure ([63], [64]), velocity and pressure are represented using interpolating functions as follows:

$$\mathrm{v}_i(\mathbf{x}, t) \approx \mathrm{v}_i^h(\mathbf{x}, t) = \sum_{J=1} N_J(\mathbf{x}) \mathrm{v}_i^J(t) = \mathbf{N}^T \mathbf{v}_i \tag{3.27}$$

$$p(\mathbf{x}, t) \approx p^h(\mathbf{x}, t) = \sum_{J=1} N_J(\mathbf{x}) p^J(t) = \mathbf{N}^T \mathbf{p} \tag{3.28}$$

where $\mathbf{N}_J(\mathbf{x})$ are vectors of interpolating functions, and $\mathbf{v}_i^J$ and p^J are the nodal values for the i-th component of velocity and pressure, respectively, at node J. In the present work, both velocity and pressure have been approximated by linear Lagrangian functions (i.e., P1P1 elements have been chosen). This leads to lower system sizes and therefore to solutions with lower computational cost. However, both velocity and pressure have the same degree of interpolation and pressure must be stabilized [64]. Using Eqs. (3.27) and (3.28) in Eqs. (3.24) and (3.25), and integrating over elements, governing equations yield:

$$\mathbf{M} \dot{\bar{\mathbf{v}}} + \mu \mathbf{L} \bar{\mathbf{v}} + \mathbf{G} \bar{p} = \bar{\mathbf{F}} + \bar{\mathbf{F}}_{\text{st}} \tag{3.29}$$

$$\mathbf{D} \bar{\mathbf{v}} = 0 \tag{3.30}$$

where $\mathbf{M}$ is the mass matrix, $\mathbf{L}$ is the Laplacian matrix, $\mathbf{G}$ is the gradient matrix, $\mathbf{D}$ is the divergence matrix, $\bar{\mathbf{v}}$ and $\bar{p}$ are the velocity and pressure respectively, $\bar{\mathbf{F}}$ is the body force vector and $\bar{\mathbf{F}}_{\text{st}}$ is the surface tension force vector. The matrices are

assembled from the elemental contributions defined as:

$$\mathbf{M} = m_{IJ} = \rho \int_{\Omega_e} \delta_{IJ} N_I N_J \, \mathrm{d}\Omega \tag{3.31}$$

$$\mathbf{L} = l_{IJ} = \int_{\Omega_e} \frac{\partial N_I}{\partial x_k} \frac{\partial N_J}{\partial x_k} \, \mathrm{d}\Omega \tag{3.32}$$

$$\mathbf{G} = g_{IJ} = -\int_{\Omega_e} \frac{\partial N_I}{\partial x_k} N_J \, \mathrm{d}\Omega \tag{3.33}$$

$$\bar{\mathbf{F}} = f_I = \rho \int_{\Omega_e} N_I g_k \, \mathrm{d}\Omega \tag{3.34}$$

$$\bar{\mathbf{F}}_{\mathrm{st}} = f_{\mathrm{st},I} = -\int_{\Gamma_I} \gamma \kappa n_k N_I \, \mathrm{d}\Omega \tag{3.35}$$

$$\mathbf{D} = -\mathbf{G}^T \tag{3.36}$$

where N_I stands for the standard linear FE shape function at node I, Ω_e is the element integration domain and k refers to spatial variables x, y and z. Note that due to using a Lagrangian framework for the domain, the elemental integration domains in Eqs. (3.31)-(3.36) must be updated according to changing mesh configuration. Governing equations have been discretized in space, but not in time. For sake of clarity, the derivation is shown using Backward Euler scheme as the integration scheme:

$$\frac{\mathbf{v}_{n+1} - \mathbf{v}_n}{\Delta t} = \dot{\mathbf{v}}_{n+1} \tag{3.37}$$

However, the Newmark-Bossak integration scheme has been actually implemented in our formulation (see Appendix C).

Finally, governing equations have been discretized in space and time and the problem can be stated as follows: Given $\bar{\mathbf{v}}_n$ and $\bar{p}_n$ at t_n, find $\bar{\mathbf{v}}_{n+1}$ and $\bar{p}_{n+1}$ at t_{n+1} as the solution of:

$$\mathbf{M}\frac{\bar{\mathbf{v}}_{n+1} - \bar{\mathbf{v}}_n}{\Delta t} + \mu \mathbf{L}\bar{\mathbf{v}}_{n+1} + \mathbf{G}\bar{p}_{n+1} = \bar{\mathbf{F}} + \bar{\mathbf{F}}_{\mathrm{st}} \tag{3.38}$$

$$\mathbf{D}\bar{\mathbf{v}}_{n+1} = 0 \tag{3.39}$$

The resulting system of equations can be solved using a monolithic scheme, i.e., pressure and velocity are solved simultaneously, or using a splitting method such as the fractional step method, where velocity and pressure are decoupled [65]. Solution strategy, advantages and disadvantages are discussed in the following sections. It will be also shown that the presence of surface tension force at the domain boundary precludes application of the classical splitting methods.

3.2.1 Monolithic approach

The monolithic (or coupled) approach is used to solve governing equations (3.38) and (3.39). The absence of pressure in Eq. (3.39) is the source of instabilities in the solution for velocity-pressure pairs that do not fulfill the inf-sup condition [63]. One option relies in relaxing the incompressible condition by an adding extra term that depends on pressure, as shown in [66]. Another option is to add some stabilization

terms depending on mesh size and time step. Different methods have been presented in literature, such as Galerkin/Least Squares (GLS) [67], Algebraic Sub-Grid Scales (ASGS) [68], Orthogonal Sub-Scales (OSS) [69] and Finite Increment Calculus (FIC) [70]. In our work, the ASGS stabilization technique is implemented because it is a symmetric stabilization. Thus the system of governing equations remains symmetric.

Let us consider again the discretized governing equations Eqs. (3.24) and (3.25). The stabilization of these equations is achieved by adding the following term to the left-hand side:

$$\sum_{e=1}^{n_e} \int_{\Omega_e} \tau \left[\mathbf{F} - \mathcal{L}(\mathbf{v}_h)\right]^T \mathcal{L}^*(\mathbf{w}_h) \, \mathrm{d}\Omega \tag{3.40}$$

where the time-dependent residual is:

$$\mathcal{L}(\mathbf{v}_h) = \begin{bmatrix} \rho \frac{\partial \mathbf{v}_h}{\partial t} - \mu \nabla \cdot (\nabla \mathbf{v}_h) + \nabla p_h \\ \nabla \cdot \mathbf{v}_h \end{bmatrix} = \begin{bmatrix} \rho \frac{\partial \mathbf{v}_h}{\partial t} + \nabla p_h \\ \nabla \cdot \mathbf{v}_h \end{bmatrix} \tag{3.41}$$

Note that the laplacian term in Eq. (3.41) is equal to 0 since linear interpolation functions are considered for the space discretization. Since the discretization in time has been performed applying Backward Euler scheme, the residual can be approximated as:

$$\mathcal{L}(\mathbf{v}_h) = \begin{bmatrix} \rho \frac{\mathbf{v}_{n+1} - \mathbf{v}_n}{\Delta t} + \nabla p_{n+1} \\ \nabla \cdot \mathbf{v}_{n+1} \end{bmatrix} \tag{3.42}$$

where discrete velocity and pressure correspond to the solution at the next time step $n+1$. The term $\mathcal{L}^*$ is the formal adjoint of $\mathcal{L}$ and it depends on the stabilization technique chosen. For ASGS (see [68] for further details):

$$\mathcal{L}^*(\mathbf{w}_h) = \begin{bmatrix} -\mu \Delta \mathbf{w}_h - \nabla q_h \\ -\nabla \cdot \mathbf{w}_h \end{bmatrix} = \begin{bmatrix} -\nabla q_h \\ -\nabla \cdot \mathbf{w}_h \end{bmatrix} \tag{3.43}$$

Using Eqs. (3.42) and (3.43) in Eq. (3.40), the stabilization term yields:

$$\int_{\Omega_e} \tau_1 \nabla q_h \left(\rho \frac{\mathbf{v}_{n+1} - \mathbf{v}_n}{\Delta t} + \nabla p_{n+1} - \mathbf{f} \right) \, \mathrm{d}\Omega + \int_{\Omega_e} \tau_2 \left(\nabla \cdot \mathbf{w}_h\right) \left(\nabla \cdot \mathbf{v}_{n+1}\right) \, \mathrm{d}\Omega \tag{3.44}$$

Terms multiplied by q_h are added to the continuity equation, whereas terms multiplied by $\mathbf{w}_h$ are added to the momentum equation. Expanding the first term and substituting by the interpolating functions, Eq. (3.44) yields:

$$\begin{aligned} \int_{\Omega_e} \frac{\rho}{\Delta t} \tau_1 \frac{\partial N_I}{\partial x_k} N_J \, \mathrm{d}\Omega + \int_{\Omega_e} \tau_1 \frac{\partial N_I}{\partial x_k} \frac{\partial N_J}{\partial x_k} \, \mathrm{d}\Omega - \int_{\Omega_e} \tau_1 \frac{\partial N_I}{\partial x_k} \left(\frac{\rho}{\Delta t} N_J + N_J \right) \, \mathrm{d}\Omega + \\ + \int_{\Omega_e} \tau_2 \frac{\partial N_I}{\partial x_k} \frac{\partial N_J}{\partial x_k} \, \mathrm{d}\Omega \end{aligned} \tag{3.45}$$

Parameters τ_1 and τ_2 are algorithmic stabilization parameters defined as:

$$\tau = \frac{1}{\frac{2 \left\| \bar{\mathbf{v}} \right\|}{h} + \frac{4\nu}{h^2}} \tag{3.46}$$

$$\tau_2 = \frac{h^2}{\tau_1} = 2h \left\| \bar{\mathbf{v}} \right\| + 4\nu \tag{3.47}$$

where h is the element size and ν is the kinematic viscosity of the fluid.

The stabilized governing equations read:

$$\left(\mathbf{M} \frac{1}{\Delta t} + \mu \mathbf{L} + \mathbf{S}_K \right) \bar{\mathbf{v}}_{n+1} + \mathbf{G} \bar{p}_{n+1} = \bar{\mathbf{F}} + \bar{\mathbf{F}}_{\text{st}} + \mathbf{M} \frac{\bar{\mathbf{v}}_n}{\Delta t} \tag{3.48}$$

$$\left(\mathbf{D} + \mathbf{S}_D \right) \bar{\mathbf{v}}_{n+1} + \mathbf{S}_L \bar{p}_{n+1} = \bar{\mathbf{F}}_q \tag{3.49}$$

where stabilization matrices are:

$$\mathbf{S}_K = s_{K,IJ} = \int_{\Omega_e} \tau_2 \frac{\partial N_I}{\partial x_k} \frac{\partial N_J}{\partial x_k} \, \mathrm{d}\Omega \tag{3.50}$$

$$\mathbf{S}_D = s_{D,IJ} = \int_{\Omega_e} \frac{\rho}{\Delta t} \tau_1 \frac{\partial N_I}{\partial x_k} N_J \, \mathrm{d}\Omega \tag{3.51}$$

$$\mathbf{S}_L = s_{L,IJ} = \int_{\Omega_e} \tau_1 \frac{\partial N_I}{\partial x_k} \frac{\partial N_J}{\partial x_k} \, \mathrm{d}\Omega \tag{3.52}$$

$$\bar{\mathbf{F}}_q = f_{q,I} = \int_{\Omega_e} \rho g_k \frac{\partial N_I}{\partial x_k} \left(\frac{\rho}{\Delta t} N_I + N_I \right) \, \mathrm{d}\Omega \tag{3.53}$$

Note that matrix $\mathbf{S}_L$ can be interpreted as a laplacian term. The presence of this term is particularly important for the computational efficiency of the method [71].

Although the nonlinear convective term is absent in Eq. (3.48), the system of governing equations is still nonlinear. This is caused by the definition of these equations in terms of the unknown configuration $\mathbf{X}_{n+1}$ and therefore dependence of the discrete operators defined by Eqs. (3.31)-(3.36) on the unknown nodal position. An option often encountered in numerical studies is to solve the linearized system of equations using a Newton-Raphson method since it provides second-order convergence of the non-linear iterative procedure. This is achieved by first expressing the governing equations in residual form:

$$\bar{\mathbf{r}}_m = \bar{\mathbf{F}} + \bar{\mathbf{F}}_{\text{st}} - \mathbf{M} \frac{\bar{\mathbf{v}}_{n+1} - \bar{\mathbf{v}}_n}{\Delta t} - \left(\mu \mathbf{L} + \mathbf{S}_K \right) \bar{\mathbf{v}}_{n+1} - \mathbf{G} \bar{p}_{n+1} = 0 \tag{3.54}$$

$$\bar{\mathbf{r}}_c = \bar{\mathbf{F}}_q - \left(\mathbf{D} + \mathbf{S}_D \right) \bar{\mathbf{v}}_{n+1} - \mathbf{S}_L \bar{p}_{n+1} = 0 \tag{3.55}$$

The Taylor series expansion of the residual is:

$$\mathbf{0} = \begin{pmatrix} \bar{\mathbf{r}}_m \\ \bar{\mathbf{r}}_c \end{pmatrix} + \begin{pmatrix} \frac{\partial \bar{\mathbf{r}}_m}{\partial \bar{\mathbf{v}}^i} & \frac{\partial \bar{\mathbf{r}}_m}{\partial \bar{p}^i} \\ \frac{\partial \bar{\mathbf{r}}_c}{\partial \bar{\mathbf{v}}^i} & \frac{\partial \bar{\mathbf{r}}_c}{\partial \bar{p}^i} \end{pmatrix} \begin{pmatrix} d\bar{\mathbf{v}} \\ d\bar{p} \end{pmatrix} + \mathcal{O}\left(d\bar{\mathbf{v}}, d\bar{p} \right)^2 \tag{3.56}$$

Neglecting terms of second order and higher, the Newton-Raphson equation to solve is:

$$- \begin{pmatrix} \frac{\partial \bar{\mathbf{r}}_m}{\partial \bar{\mathbf{v}}^i} & \frac{\partial \bar{\mathbf{r}}_m}{\partial \bar{p}^i} \\ \frac{\partial \bar{\mathbf{r}}_c}{\partial \bar{\mathbf{v}}^i} & \frac{\partial \bar{\mathbf{r}}_c}{\partial \bar{p}^i} \end{pmatrix} \begin{pmatrix} d\bar{\mathbf{v}} \\ d\bar{p} \end{pmatrix} = \begin{pmatrix} \bar{\mathbf{r}}_m \\ \bar{\mathbf{r}}_c \end{pmatrix} \tag{3.57}$$

where $d\bar{\mathbf{v}} = \bar{\mathbf{v}}_{n+1}^{i+1} - \bar{\mathbf{v}}_{n+1}^{i}$ and $d\bar{p} = \bar{p}_{n+1}^{i+1} - \bar{p}_{n+1}^{i}$. Index i denotes the nonlinear iteration of the Newton-Raphson solution. Derivatives of the residuals with respect to velocity and pressure are easily obtained, and the system to solve reads:

$$\begin{pmatrix} \mathbf{M} \frac{1}{\Delta t} + \mu \mathbf{L} + \mathbf{S}_K + \mathbf{H}_{ST} & \mathbf{G} \\ \mathbf{D} + \mathbf{S}_D & \mathbf{S}_L \end{pmatrix} \begin{pmatrix} d\bar{\mathbf{v}} \\ d\bar{p} \end{pmatrix} = \begin{pmatrix} \bar{\mathbf{r}}_m \left(\bar{\mathbf{v}}^i, \bar{p}^i \right) \\ \bar{\mathbf{r}}_c \left(\bar{\mathbf{v}}^i, \bar{p}^i \right) \end{pmatrix} \tag{3.58}$$

Matrix $\mathbf{H}_{ST}$ is the result of linearizing surface tension term with respect the velocity. Including this term is necessary to overcome time step restrictions that appear in problems where surface tension effects are present[2]. The derivation of this term is carried out in section 3.3.

Once the system (Eq. (3.58)) is solved, the velocity and the pressure are updated as $\bar{\mathbf{v}}_{n+1}^{i+1} = \bar{\mathbf{v}}_{n+1}^{i} + d\bar{\mathbf{v}}$ and $\bar{p}_{n+1}^{i+1} = \bar{p}_{n+1}^{i} + d\bar{p}$. The position of the nodes in Ω_L is updated as $\mathbf{X}_{n+1}^{i+1} = \mathbf{X}_n + \Delta t \cdot \bar{\mathbf{v}}_{n+1}^{i+1}$.

The integration domains necessary for the computation of the discrete operators (Eqs. (3.31)-(3.36)) are updated according to this new configuration $\mathbf{X}_{n+1}^{i+1}$. Once the convergence of the iterative loop is achieved and the end-of-step velocity ($\bar{\mathbf{v}}_{n+1}$) and pressure ($\bar{p}_{n+1}$) are obtained, the definitive mesh position is computed as:

$$\mathbf{X}_{n+1} = \mathbf{X}_n + \Delta t \cdot \bar{\mathbf{v}}_{n+1} \tag{3.59}$$

3.2.2 Fractional step approach

The resulting system of equations (3.38)-(3.39) is symmetric due to using the Lagrangian description (no skew-symmetric convective term). However, this system suffers from ill-conditioning due to different scales of velocity and pressure variables [71]. Pressure segregation methods have been developed in the past to overcome this difficulty. One such method is the fractional step method, presented by Chorin [72] and Temam [73]. This method has shown to be significantly more efficient in computational cost, but it suffers from mass conservation problems. Recently, Ryzhakov et al. [65] proposed a technique to alleviate this by improving the intermediate velocity solution.

Fractional step approach can be applied at the continuum level [3] or at a purely algebraic level [74]. For the sake of simplicity, we chose the latter option. First, an intermediate velocity $\tilde{\mathbf{v}}$ is introduced in Eq. (3.38):

$$\mathbf{M}\frac{(\bar{\mathbf{v}}_{n+1} - \tilde{\mathbf{v}}) + (\tilde{\mathbf{v}} - \bar{\mathbf{v}}_n)}{\Delta t} + (\mu\mathbf{L} + \mathbf{H}_{ST})\,\bar{\mathbf{v}}_{n+1} + \mathbf{G}\,(\bar{p}_{n+1} - \bar{p}_n + \bar{p}_n) = \bar{\mathbf{F}} + \bar{\mathbf{F}}_{\text{st}} \tag{3.60}$$

No approximation has been considered yet. Eq (3.60) can be split into two equations:

$$\mathbf{M}\frac{(\tilde{\mathbf{v}} - \bar{\mathbf{v}}_n)}{\Delta t} + (\mu\mathbf{L} + \mathbf{H}_{ST})\,\tilde{\mathbf{v}} + \mathbf{G}\bar{p}_n = \bar{\mathbf{F}} + \bar{\mathbf{F}}_{\text{st}} \tag{3.61}$$

$$\mathbf{M}\frac{(\bar{\mathbf{v}}_{n+1} - \tilde{\mathbf{v}})}{\Delta t} + \mathbf{G}\,(\bar{p}_{n+1} - \bar{p}_n) = 0 \tag{3.62}$$

Note that in Eq. (3.61) an approximation has been considered, assuming that the laplacian and surface tension matrices are multiplied by $\tilde{\mathbf{v}}$ instead of $\bar{\mathbf{v}}_{n+1}$. Eq.

[2]Considering $\mathbf{H}_{ST} = 0$ corresponds to methods where surface tension is treated explicitly.

(3.62) can be rearranged as follows:

$$\begin{aligned}
&\mathbf{M}\frac{(\bar{\mathbf{v}}_{n+1}-\tilde{\mathbf{v}})}{\Delta t}+\mathbf{G}\left(\bar{p}_{n+1}-\bar{p}_n\right)= \\
&=\mathbf{M}\frac{\bar{\mathbf{v}}_{n+1}}{\Delta t}-\mathbf{M}\frac{\tilde{\mathbf{v}}}{\Delta t}+\mathbf{G}\left(\bar{p}_{n+1}-\bar{p}_n\right)=0 \\
&\mathbf{M}\frac{\tilde{\mathbf{v}}}{\Delta t}=\mathbf{M}\frac{\bar{\mathbf{v}}_{n+1}}{\Delta t}+\mathbf{G}\left(\bar{p}_{n+1}-\bar{p}_n\right) \\
&\tilde{\mathbf{v}}=\bar{\mathbf{v}}_{n+1}+\Delta t\mathbf{M}^{-1}\mathbf{G}\left(\bar{p}_{n+1}-\bar{p}_n\right)
\end{aligned}$$

If last equation is multiplied by matrix $\mathbf{D}$ at both sides, it yields the pressure Poisson equation:

$$\mathbf{D}\tilde{\mathbf{v}}=\mathbf{D}\bar{\mathbf{v}}_{n+1}+\Delta t\mathbf{D}\mathbf{M}^{-1}\mathbf{G}\left(\bar{p}_{n+1}-\bar{p}_n\right)=\Delta t\mathbf{D}\mathbf{M}^{-1}\mathbf{G}\left(\bar{p}_{n+1}-\bar{p}_n\right) \tag{3.63}$$

Matrix $\mathbf{D}\mathbf{M}^{-1}\mathbf{G}$ can be approximated by $\mathbf{L}$, $\mathbf{D}\mathbf{M}^{-1}\mathbf{G}\approx\mathbf{L}$, as the former one requires performing global matrix-vector multiplications and is, thus, computationally more expensive [75]. However, the resulting matrix $\mathbf{L}$ is singular. Considering this approximation, Eq. (3.63) obtains the following form:

$$\mathbf{D}\tilde{\mathbf{v}}=\Delta t\mathbf{L}\left(\bar{p}_{n+1}-\bar{p}_n\right) \tag{3.64}$$

To sum up, the resulting equations in the fractional step method are:

$$\mathbf{M}\frac{(\tilde{\mathbf{v}}-\bar{\mathbf{v}}_n)}{\Delta t}+\left(\mu\mathbf{L}+\mathbf{H}_{ST}\right)\tilde{\mathbf{v}}+\mathbf{G}\bar{p}_n=\bar{\mathbf{F}}+\bar{\mathbf{F}}_{\mathrm{st}} \tag{3.65}$$

$$\mathbf{D}\tilde{\mathbf{v}}=\Delta t\mathbf{D}\mathbf{M}^{-1}\mathbf{G}\left(\bar{p}_{n+1}-\bar{p}_n\right) \tag{3.66}$$

$$\mathbf{M}\frac{(\bar{\mathbf{v}}_{n+1}-\tilde{\mathbf{v}})}{\Delta t}+\mathbf{G}\left(\bar{p}_{n+1}-\bar{p}_n\right)=0 \tag{3.67}$$

where Eq. (3.65) is the *fractional momentum* equation, Eq. (3.66) is the pressure Poisson equation and Eq. (3.67) is referred as the *end-of-step* momentum equation. Once Eq. (3.65) is solved for $\tilde{\mathbf{v}}$, pressure $\bar{p}_{n+1}$ is obtained by solving Eq. (3.66) and finally the end-of-step velocity $\bar{\mathbf{v}}_{n+1}$ is obtained using Eq. (3.67). Velocity and pressure have been decoupled, but $\bar{\mathbf{v}}_{n+1}$ has been approximated by $\tilde{\mathbf{v}}$ in Eq. (3.65), introducing a numerical error of order Δt^2.

The monolithic approach for solving Eqs. (3.48)-(3.49) is more computationally intensive than fractional step method, since it involves solving both velocity and pressure simultaneously. On the other hand, fractional step method needs a boundary condition for pressure in Γ_N in order to overcome the singularity of the Laplacian matrix $\mathbf{L}$ in pressure Poisson's equation (Eq. (3.66)). The essential boundary condition $p=0$ is valid for free surface problems where surface tension effects are negligible. This boundary condition is not valid however in problems involving surface tension effects, such as water droplet dynamics. Using the fractional step method in droplets may lead to instabilities in the solution, specially for low viscosity values. Section 3.4 includes an example where the performance of the monolithic approach and the fractional step method is compared.

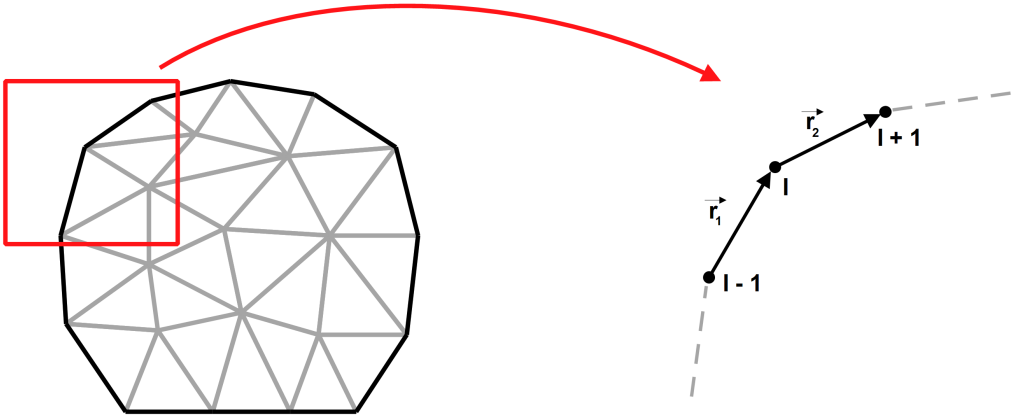

Figure 3.3: Discrete boundary

3.3 Surface tension

The force term $\bar{\mathbf{F}}_{\text{st}}$ in Eq. (3.38) is the surface tension force, corresponding to the projection of the Cauchy stress tensor onto the normal direction at the interface:

$$\bar{\mathbf{F}}_{\text{st}} = -\int_{\Gamma} \gamma\kappa\mathbf{n}\cdot\mathbf{w}\ \mathrm{d}\Gamma \tag{3.68}$$

Negative sign in Eq. (3.68) means that the surface tension force is a vector pointing inwards Ω when Γ_I is convex, and it points outwards Ω when the boundary is concave. Since surface tension term depends on the curvature, a model for curvature in two and three dimensions must be developed first.

3.3.1 Curvature in two dimensions

The curvature in two dimensions is defined as follows [16], [15]:

$$\kappa = \nabla_s \cdot \mathbf{n} = \left\| \frac{\mathrm{d}\mathbf{n}}{\mathrm{d}s} \right\| \tag{3.69}$$

where ∇_s is the surface gradient operator (i.e., the conventional gradient without the component normal to the surface) and $\frac{\mathrm{d}\phi}{\mathrm{d}s}$ is the rate of change of variable ϕ along a given curve. Eq. (3.69) can be interpreted as the change in direction of the normal vector along the interface. This equation can be approximated using subsets of three nodes at the interface on a Lagrangian mesh. Let us consider a segment of the Lagrangian boundary defined by node I and its nearest neighbors. At every node I, the curvature is computed using its nearest neighbors at the interface. Let us denote the vector pointing from node $I-1$ to node I as $\mathbf{r_1}$, and the vector pointing from node I to node $I+1$ as $\mathbf{r_2}$ (Figure 3.3). To find the change in direction of the contact line at node I, one must normalize the vector $\mathbf{r_1} - \mathbf{r_2}$. The normalized vectors $\mathbf{r_1}$ and $\mathbf{r_2}$ will be denoted as $\hat{\mathbf{r}}_\mathbf{1}$ and $\hat{\mathbf{r}}_\mathbf{2}$:

$$\hat{\mathbf{r}}_\mathbf{k} = \frac{\mathbf{r_k}}{||\mathbf{r_k}||} \tag{3.70}$$

The curvature is the norm of the vector $\hat{\mathbf{r}}_\mathbf{1} - \hat{\mathbf{r}}_\mathbf{2}$ divided by the length of the polyline pointing from node $I-1$ to $I+1$:

$$\kappa = \frac{||\hat{\mathbf{r}}_\mathbf{1} - \hat{\mathbf{r}}_\mathbf{2}||}{||\mathbf{r}_\mathbf{1}|| + ||\mathbf{r}_\mathbf{2}||} \tag{3.71}$$

Eq. (3.71) is a direct measure of the change in direction of the tangent vector along the interface. Since tangent and normal vectors at the surface are orthogonal, the curvature value remains unaltered. In addition to the curvature, one must compute its sign at node I: if the midpoint of the line connecting the neighbors of node I is inside the water domain, then the sign is positive (convex interface). On the contrary, if the midpoint lies outside the water domain, the sign is negative and the surface tension force at node I points outwards the interface.

In order to determine whether the midpoint is inside the water domain, the following process is performed. For node I, the neighbor elements are identified (i.e., elements that contain node I). For every neighbor element, the shape functions of every node are evaluated at coordinates of the midpoint. If the three shape functions are positive in one or more elements, the midpoint is inside water domain and curvature of node I is positive. Curvature is negative if there are no elements that fulfill the previous condition.

3.3.2 Curvature in three dimensions

For many computer graphics applications (optimal triangulation, surface modeling and denoising, to name a few), it is important to have an accurate approximation of the simple geometry attributes, such as normal vector and surface curvature. Usually, surfaces are represented by triangular meshes. The notion of continuous normal vectors and curvatures is not trivial for discrete surfaces.

Curvature in three dimensions is usually computed using differential geometry. Tasso et al. [76] compared several studies and Meyer's method [77] provided the most accurate results. The three-dimensional model for the curvature computation adopted here has been therefore based on Meyer's method. The method is summarized next.

Let S be a surface in $\mathbb{R}^3$ described by a parametrization of two variables. For each point in S, the surface can be approximated by its tangent plane. This plane is defined by the normal vector $\mathbf{n}$ at that point, and the point itself. For every direction, normal curvature $\kappa^N(\theta)$ at point P is defined as the curvature of the curve contained in the surface and in the plane defined by $\mathbf{n}$ and $\mathbf{e}_\theta$ (vector pointing in the considered direction, as shown in Fig. 3.4(a)). Mean curvature is defined as the average of the normal curvatures:

$$\kappa_H = \frac{1}{2\pi} \int_0^{2\pi} \kappa^N(\theta) d\theta \tag{3.72}$$

Equation $\kappa_H = 0$ is the Euler-Lagrange equation for surface minimization. Surface area minimization and mean curvature flow can be related using the following equation:

$$2\kappa_H \mathbf{n} = \lim_{d(A)\to 0} \frac{\nabla A}{A} \tag{3.73}$$

where A is the infinitesimal area around point P, $d(A)$ its diameter, and ∇A is the gradient with respect to (x, y, z) coordinates of P. Fig. 3.4(b) shows a schematic of the infinitesimal area around a point, its normal vector $\mathbf{n}$ and the principal directions $\mathbf{e}_1$ and $\mathbf{e}_2$.

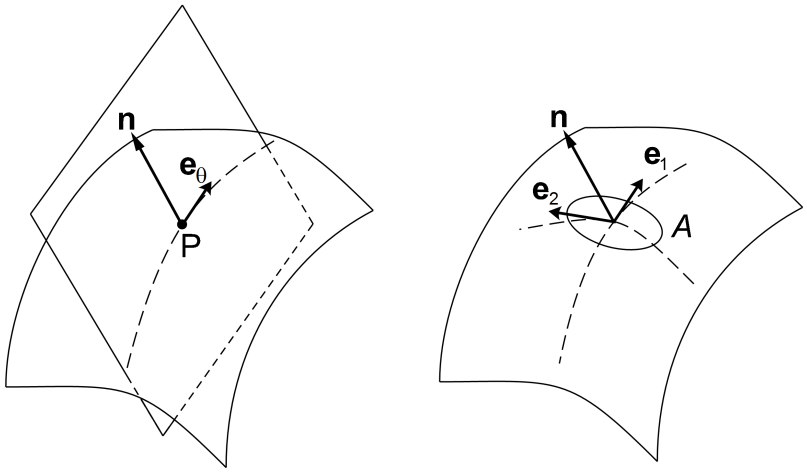

(a) Normal curvature (b) Principal directions

Figure 3.4: (a) Plane defined by normal vector to surface and tangent vector to the considered curve and (b) Infinitessimal area around a considered point, with normal vector $\mathbf{n}$ and principal directions $\mathbf{e}_1$ and $\mathbf{e}_2$

Left-hand side term in Eq. (3.73) is the Laplace-Beltrami operator of surface S: $\mathbf{K}(P) = 2\kappa_H(P)\mathbf{n}(P)$. For $\mathscr{C}^0$ surfaces the above definition (Eq. (3.73)) must be reformulated. Properties will be obtained using the immediately neighboring triangles, also known as *1-ring neighborhood*. The first step is to find the discrete area around each vertex $\mathbf{x}_i$ of the mesh. For each triangle, the local area is generated connecting an interior point with the midpoints of the edges of adjacent triangles. Usually this interior point is taken as the circumcenter, and the area becomes the local Voronoi cell (A_{Voronoi}). Fig. 3.5(a) shows the 1-ring neighborhood of node $\mathbf{x}_i$ and its Voronoi region (shaded area).

Note that all triangles in Fig. 3.5(a) are non-obtuse. When a triangle is obtuse, part of the associated Voronoi cell lays outside the triangle. Two cases arise if the triangle is obtuse: the angle formed in node $\mathbf{x}_i$ is obtuse (Fig. 3.5(c)), or one of the other two angles is obtuse (Fig. 3.5(d)). In the former case, A_{Voronoi} is computed as half the area of the triangle ($A_{\text{T}}/2$), and as a quarter of the triangle area in the latter case ($A_{\text{T}}/4$). In either case, the cell is referred as A_M instead of A_{Voronoi}.

Once area A_M has been computed for every node $\mathbf{x}_i$, the mean curvature normal $\mathbf{K}(\mathbf{x}_i)$ has to be integrated over the area A_M. From [77] it is shown that expressing $\mathbf{K}(\mathbf{x}_i)$ as the Laplacian with respect the conformal space parameters and using Gauss' theorem, the mean curvature normal operator yields [77]:

$$\mathbf{K}(\mathbf{x}_i) = \frac{1}{2A_M} \sum_{j \in N_1(i)} (\cot \alpha_{ij} + \cot \beta_{ij}) (\mathbf{x}_i - \mathbf{x}_j) \tag{3.74}$$

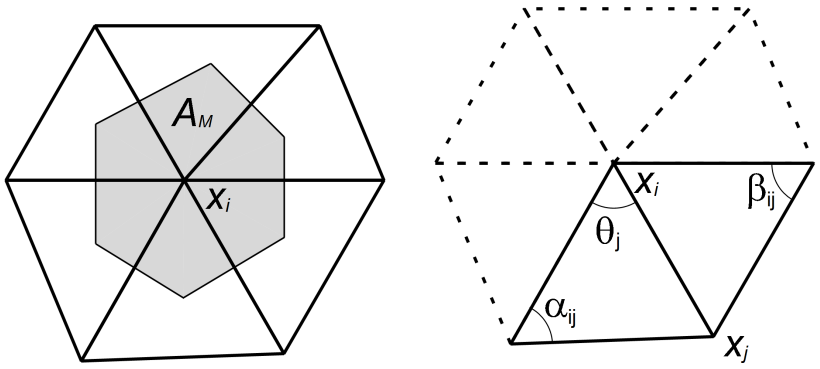

(a) Voronoi area

(b) Angles opposite to an edge

(c) Obtuse angle at node $\mathbf{x}_i$

(d) Obtuse triangle, non-obtuse angle at node $\mathbf{x}_i$

Figure 3.5: (a)-(b) 1-ring neighborhood of node $\mathbf{x}_i$ with its Voronoi region (shaded area) and angles opposite to an edge, (c)-(d) Voronoi region for obtuse triangles

where α_{ij} and β_{ij} are the two angles opposite to edge $\overline{\mathbf{x}_i\mathbf{x}_j}$ (Fig. 3.5(b)), and $N_1(i)$ denotes the 1-ring neighborhood of node $\mathbf{x}_i$. The value of A_M has been given for obtuse triangles. For non-obtuse triangles, it can be shown that [77]:

$$A_{\text{Voronoi}} = \frac{1}{8} \sum_{j \in N_1(i)} \left(\cot \alpha_{ij} + \cot \beta_{ij}\right) \|\mathbf{x}_i - \mathbf{x}_j\|^2 \tag{3.75}$$

From Eq. (3.74), two important attributes can be obtained: the normal vector $\mathbf{n}$ (Eq. (3.76)) and the mean curvature κ_H (Eq. (3.77)).

$$\mathbf{n} = \frac{\mathbf{K}(\mathbf{x}_i)}{\|\mathbf{K}(\mathbf{x}_i)\|} \tag{3.76}$$

$$\kappa_H = \frac{1}{2} \|\mathbf{K}(\mathbf{x}_i)\| \tag{3.77}$$

Using Eqs. (3.76) and (3.77), the surface tension force term in three dimensions yields:

$$\begin{aligned} \bar{\mathbf{F}}_{\text{st}} &= -\int_\Gamma \gamma \kappa \mathbf{n} \cdot \mathbf{w} \, \mathrm{d}\Gamma \\ &= -\int_\Gamma \gamma \frac{1}{2} \|\mathbf{K}(\mathbf{x}_i)\| \frac{\mathbf{K}(\mathbf{x}_i)}{\|\mathbf{K}(\mathbf{x}_i)\|} \cdot \mathbf{w} \, \mathrm{d}\Gamma \\ &= -\frac{\gamma}{2} \int_\Gamma \left(\frac{1}{2A_M} \sum_{j \in N_1(i)} \left(\cot \alpha_{ij} + \cot \beta_{ij}\right) (\mathbf{x}_i - \mathbf{x}_j) \right) \cdot \mathbf{w} \, \mathrm{d}\Gamma \end{aligned} \tag{3.78}$$

3.3.3 Implicit treatment of the surface tension term

The explicit treatment of the surface tension term leads to severe restrictions upon the critical time step size in the simulation of dynamic problems [61],[78]. It is governed by the time scale associated to the propagation of capillary waves [28], [56], [61].

Let us consider a liquid-gas system with an interface Γ separating the domains. Let us also consider the coordinate system (x, y), where x represents the direction tangent to the interface and y is the orthogonal direction. Let us assume that any perturbation in the interface (i.e., capillary wave) is governed by the mean curvature flow and that it propagates as a harmonic plane wave [79]. Its amplitude of oscillation can be expressed as [61]:

$$y(x,t) = A_0 e^{i(kx - \omega t)} = f(t) e^{ikx} \tag{3.79}$$

where A_0 is the peak magnitude of oscillation, i is the unit complex number, k is the wave number and ω is the angular frequency. The wave number k is equal to:

$$k = \frac{2\pi}{h} \tag{3.80}$$

where h is the element size. From Eq. (3.79), $f(t)$ reads:

$$f(t) = A_0 e^{-i\omega t} \tag{3.81}$$

Its time derivative has the following expression:

$$\frac{\mathrm{d}f(t)}{\mathrm{d}t} = f'(t) = A_0 e^{-i\omega t}\,(-i\omega) = -i\omega A_0 e^{-i\omega t} = -i\omega f(t) \tag{3.82}$$

For a capillary wave, the angular frequency and the wave number are related by the dispersion equation [80]:

$$\omega^2 = \frac{\gamma}{\rho_L + \rho_G} k^3 \tag{3.83}$$

where γ is the surface tension coefficient and ρ_L and ρ_G are the liquid and the gas densities, respectively. Taking into account Eq. (3.83), the following expression arises for $f'(t)$:

$$f'(t) = \pm i \sqrt{\frac{\gamma}{\rho_L + \rho_G}} k^{\frac{3}{2}} f(t) \tag{3.84}$$

If Eq. (3.84) is solved using an explicit time integration scheme, such as forward Euler, the region of absolute stability requires that:

$$\left| \Delta t \sqrt{\frac{\gamma}{\rho_L + \rho_G}} k^{\frac{3}{2}} \right| < 1 \tag{3.85}$$

This equation leads to the following time step constraint:

$$\Delta t < \sqrt{\frac{\rho_L + \rho_G}{\gamma}} k^{-\frac{3}{2}} = \sqrt{\frac{\rho_L + \rho_G}{\gamma}} \left(\frac{2\pi}{h} \right)^{-\frac{3}{2}} = \sqrt{\frac{\rho_L + \rho_G}{\gamma (2\pi)^3} h^3} \tag{3.86}$$

For PEFC channels (1×1 mm cross-section), a typical droplet is $\sim 10^{-4}$ m in height. Considering a mesh based on elements of 10^{-6} m, the critical time step would be of the order of 10^{-8} s. Such small time step would be impractical for PEFC simulations since usually they require to consider from several seconds to several minutes of real time in order to study the desired phenomena.

Explicit treatment of the surface tension term implies that:

$$\bar{\mathbf{F}}_{\mathrm{st}} = \bar{\mathbf{F}}^n_{\mathrm{st}} = -\int_{\Gamma_n} \gamma \kappa_n \mathbf{n} \cdot \mathbf{w} \, \mathrm{d}\Gamma \tag{3.87}$$

Term κ_n denotes that curvature is being obtained using the known last step domain configuration $\mathbf{x}_n$. To avoid severe time restriction (Eq. (3.86)), one has to treat the surface tension implicitly[3]. This can be achieved by transforming the curvature term in the integral form (Eq. (3.68)) applying the surface divergence theorem [78]. Let us define the tangential gradient of a function f, considering that it is differentiable in a neighborhood $\mathcal{N}$ of a surface Γ:

[3]Although surface tension is treated explicitly in the majority of Eulerian models using VOF, the overall method is semi-implicit (a fully explicit method would introduce even smaller time step restrictions due to acoustic wave propagation)

$$\nabla_s f(x) = \nabla f(x) - \mathbf{n} \otimes \mathbf{n} \cdot \nabla f(x) \qquad x \in \Gamma_I \tag{3.88}$$

where $\mathbf{n}$ is the normal vector of surface Γ. Note that this operator has been already used in Eq. (3.69). If f is twice differentiable in a neighborhood $\mathcal{N}$ of Γ, then the Laplace-Beltrami operator of f can be defined as [81], [56]:

$$\Delta_s f(x) = \nabla_s \cdot (\nabla_s f(x)) \qquad x \in \Gamma_I \tag{3.89}$$

In differential geometry, the identity map on a surface Γ is defined as $\mathrm{id}_\Gamma(\mathbf{x}) = \mathbf{x}$ for all $\mathbf{x} \in \Gamma$. The surface gradient of the identity map yields:

$$\nabla_s \mathrm{id}_\Gamma = \nabla \mathrm{id}_\Gamma - \mathbf{n} \otimes \mathbf{n} \cdot \nabla \mathrm{id}_\Gamma = \mathbf{I} - \mathbf{n} \otimes \mathbf{n} \tag{3.90}$$

The Laplace-Beltrami operator applied to the identity mapping on a surface Γ leads to the following expression:

$$\Delta_s \mathrm{id}_\Gamma = \nabla_s \cdot (\nabla_s \mathrm{id}_\Gamma) = \nabla_s \cdot (\mathbf{I} - \mathbf{n} \otimes \mathbf{n}) = -\nabla_s \cdot \mathbf{n} \otimes \mathbf{n} = -\kappa \mathbf{n} \tag{3.91}$$

where κ is the mean curvature of the surface. Note that Eq. (3.69) has been used in the last step of Eq. (3.91). Using Eq. (3.91) in (3.68), yields:

$$\bar{\mathbf{F}}_{\mathrm{st}} = \int_\Gamma \gamma \kappa \mathbf{n} \cdot \mathbf{w} \, \mathrm{d}\Gamma = -\int_\Gamma \gamma \Delta_s \mathrm{id}_\Gamma \cdot \mathbf{w} \, \mathrm{d}\Gamma \tag{3.92}$$

Integrating by parts and applying the surface divergence theorem ([78], [56], [82]), Eq. (3.92) reads:

$$\begin{aligned} -\int_\Gamma \gamma \Delta_s \mathrm{id}_\Gamma \cdot \mathbf{w} \, \mathrm{d}\Gamma &= -\int_\Gamma \gamma \nabla_s (\nabla_s \mathrm{id}_\Gamma \cdot \mathbf{w}) \, \mathrm{d}\Gamma + \int_\Gamma \gamma \nabla_s \mathrm{id}_\Gamma \cdot \nabla_s \mathbf{w} \, \mathrm{d}\Gamma = \\ &= -\int_{\partial\Gamma} \gamma (\mathbf{m} \cdot \nabla_s \mathrm{id}_\Gamma) \cdot \mathbf{w} \, \mathrm{d}(\partial\Gamma) + \int_\Gamma \gamma \nabla_s \mathrm{id}_\Gamma \cdot \nabla_s \mathbf{w} \, \mathrm{d}\Gamma = \\ &= -\int_{\partial\Gamma} \gamma \mathbf{m} \cdot \mathbf{w} \, \mathrm{d}(\partial\Gamma) + \int_\Gamma \gamma \nabla_s \mathrm{id}_\Gamma \cdot \nabla_s \mathbf{w} \, \mathrm{d}\Gamma \end{aligned} \tag{3.93}$$

where $\partial\Gamma$ is the boundary of Γ, and $\mathbf{m}$[4] is the normal of the boundary $\partial\Gamma$, perpendicular to $\mathbf{n}$ and $\mathbf{ds}$ (unit vector tangent to $\partial\Gamma$), as shown on Figure 3.6. Note that the second term in Eq. (3.93) has the form of a Laplacian term integrated by parts.

Terms $\nabla_s \mathrm{id}_\Gamma$ and $\mathbf{m}$ depend on the domain configuration in Eq. (3.93). If this equation is expressed using the unknown (current) configuration $\mathbf{x}_{n+1}$, an implicit equation for the surface tension term is obtained:

$$\left(\bar{\mathbf{F}}_{\mathrm{st}}\right)_{n+1} = -\int_{\partial\Gamma_{n+1}} \gamma \mathbf{m}_{n+1} \cdot \mathbf{w} \, \mathrm{d}(\partial\Gamma) + \int_{\Gamma_{n+1}} \gamma \left(\nabla_s \mathrm{id}_\Gamma\right)_{n+1} \cdot \nabla_s \mathbf{w} \, \mathrm{d}\Gamma \tag{3.94}$$

[4]Note that in Eq. (3.93), $\mathbf{m} \cdot \nabla_s \mathrm{id}_\Gamma = \mathbf{m}(\mathbf{I} - \mathbf{n} \otimes \mathbf{n}) = \mathbf{m} - \mathbf{m} \cdot \mathbf{n} \otimes \mathbf{n} = \mathbf{m}$, since vectors $\mathbf{m}$ and $\mathbf{n}$ and orthogonal (i.e., $\mathbf{m} \cdot \mathbf{n} = 0$)

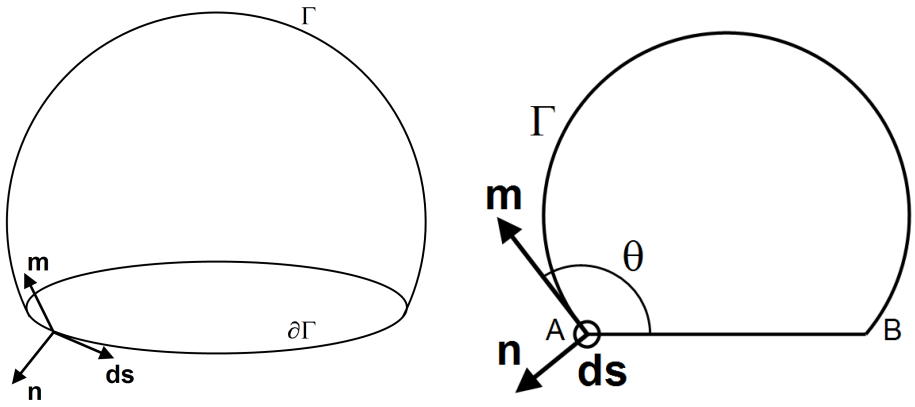

(a) 3D case (b) 2D case

Figure 3.6: Interface domain, boundary and normal vector to the boundary

Note that Eq. (3.94) is evaluated over boundary Γ. A major drawback in Eulerian formulations is that boundary Γ has to be explicitly found. This task can be rather complex for high order schemes, specially in three dimensions, leading to significant errors [56]. However, the Lagrangian formulation does not have this drawback since the position of the boundary is defined by the deforming mesh.

Recall that governing equations (Eqs. (3.24) and (3.25)) are solved via the Newton-Raphson iterative method for non-linear equations. Considering that the identity map is equal to the unknown configuration $\mathbf{x}^i_{n+1}$, it can be updated in every non-linear iteration (Eq. (3.58)) as follows:

$$(\mathrm{id}_\Gamma)^{i+1}_{n+1} = (\mathrm{id}_\Gamma)^{i}_{n+1} + \Delta t \ \mathrm{d}\bar{\mathbf{v}} \tag{3.95}$$

This term depends on the variable of interest and can be therefore substituted in Eq. (3.94):

$$\begin{aligned}\int_{\Gamma_{n+1}} \gamma \left(\nabla_s \mathrm{id}_\Gamma\right)^{i+1}_{n+1} \cdot \nabla_s \mathbf{w} \ \mathrm{d}\Gamma = \int_{\Gamma_{n+1}} \gamma \left(\nabla_s \mathrm{id}_\Gamma\right)^{i}_{n+1} \cdot \nabla_s \mathbf{w} \ \mathrm{d}\Gamma + \\ + \Delta t \int_{\Gamma_{n+1}} \gamma \nabla_s \ \mathrm{d}\bar{\mathbf{v}} \cdot \nabla_s \mathbf{w} \ \mathrm{d}\Gamma\end{aligned} \tag{3.96}$$

The right-hand side term in Eq. (3.96) is a Laplacian term, acting as a diffusive term that can possibly be interpreted as a diffusion added to the interface nodes in the tangential direction, responsible for stabilizing the surface tension effects for relatively large time steps. Note also that this term is multiplied by the time step, and therefore it will become more important for larger time steps.

Thus, the surface tension contributions that must be added to the right and left-hand side of the momentum equation (Eq. (3.58)) are:

$$\mathbf{F}_{\mathrm{st}} = -\int_{\partial\Gamma_{n+1}} \gamma \mathbf{m}_{n+1} \cdot \mathbf{w} \ \mathrm{d}\left(\partial\Gamma\right) + \int_{\Gamma_{n+1}} \gamma \left(\nabla_s \mathrm{id}_\Gamma\right)_{n+1} \cdot \nabla_s \mathbf{w} \ \mathrm{d}\Gamma \tag{3.97}$$

$$\mathbf{H}_{ST} = -\Delta t \int_{\partial\Gamma_{n+1}} \gamma d\bar{\mathbf{v}} \cdot \mathbf{w} \, \mathrm{d}\left(\partial\Gamma\right) + \Delta t \int_{\Gamma_{n+1}} \gamma \nabla_s \, \mathrm{d}\bar{\mathbf{v}} \cdot \nabla_s \mathbf{w} \, \mathrm{d}\Gamma \tag{3.98}$$

or in index notation:

$$F_I k = -\int_{\partial\Gamma_{n+1}} \gamma N m_k \, \mathrm{d}\left(\partial\Gamma\right) + \int_{\Gamma_{n+1}} \gamma \left(\delta_{ij} - n_i n_j\right) \frac{\partial N_I}{\partial x_k} \left(\delta_{kj} - n_k n_j\right) \, \mathrm{d}\Gamma \tag{3.99}$$

$$\begin{aligned} \mathbf{H}_{IJij} = &- \gamma \Delta t \int_{\partial\Gamma_{n+1}} N_I N_J \, \mathrm{d}\left(\partial\Gamma\right) + \\ &+ \gamma \Delta t \int_{\Gamma_{n+1}} \frac{\partial N_I}{\partial x_j} \frac{\partial N_J}{\partial x_l} \left(\delta_{ji} - n_j n_i\right) \left(\delta_{lk} - n_l n_k\right) \, \mathrm{d}\Gamma \end{aligned} \tag{3.100}$$

Since vector $\mathbf{m}_{n+1}$ also depends on the unknown configuration, the same procedure is applied to first term in Eq. 3.94 for its linearization, given that:

$$\mathbf{m}_{n+1}^{i+1} = \mathbf{m}_{n+1}^{i} + \Delta t \, \mathrm{d}\bar{\mathbf{v}} \tag{3.101}$$

The integral involving vector $\mathbf{m}$ is only added in case that the domain Ω is open (recall that if Ω is closed, $\partial\Gamma = \emptyset$). This term will be added only on the contact line nodes and they must be properly marked, as shown in Fig. 3.7.

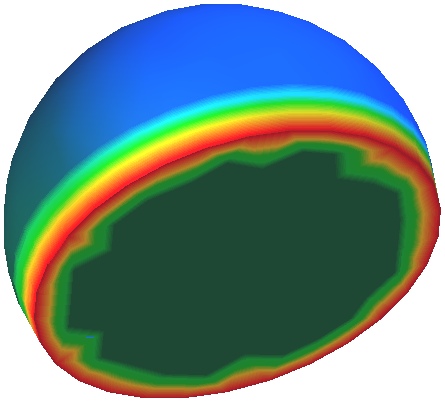

Figure 3.7: TRIPLE_POINT flag used to identify the contact points

3.3.4 Dynamic contact angle condition and adhesion force

Dynamic contact angle condition

The surface tension term along the contact line $\partial\Gamma$ (Fig. 3.6(a)) requires special treatment. At Γ_S (Fig. 3.2), since curvature is zero surface tension is also zero. At the contact line, Eq. (3.68) is solved using the normal vector corresponding to

the static equilibrium configuration $\mathbf{n}_{eq}$ instead of the actual normal vector $\mathbf{n}$ [29]. Fig. 3.8 shows the difference between the two normal vectors. The normal vector at equilibrium is constant and forms an angle θ_S with the vertical axis (Fig. 3.8(b)), whereas the actual normal vector depends on the configuration of the droplet and forms an angle θ (Fig. 3.8(a)). The curvature at the nodes that represent the contact line is computed using the normal vector at the contact line ($\mathbf{n}_1$ in Fig. 3.8(c)) and the normal vector at its nearest neighbor node from Γ_I (node 2 in Fig. 3.8(c)). Using the definition of curvature from Eq. (3.69), the curvature at the contact line is:

$$\kappa_1 = \left\| \frac{\mathrm{d}\mathbf{n}}{\mathrm{d}s} \right\| = \frac{\|\mathbf{n}_1 - \mathbf{n}_2\|}{\mathrm{d}s} \tag{3.102}$$

where $\mathrm{d}s$ is the distance between nodes 1 and 2.

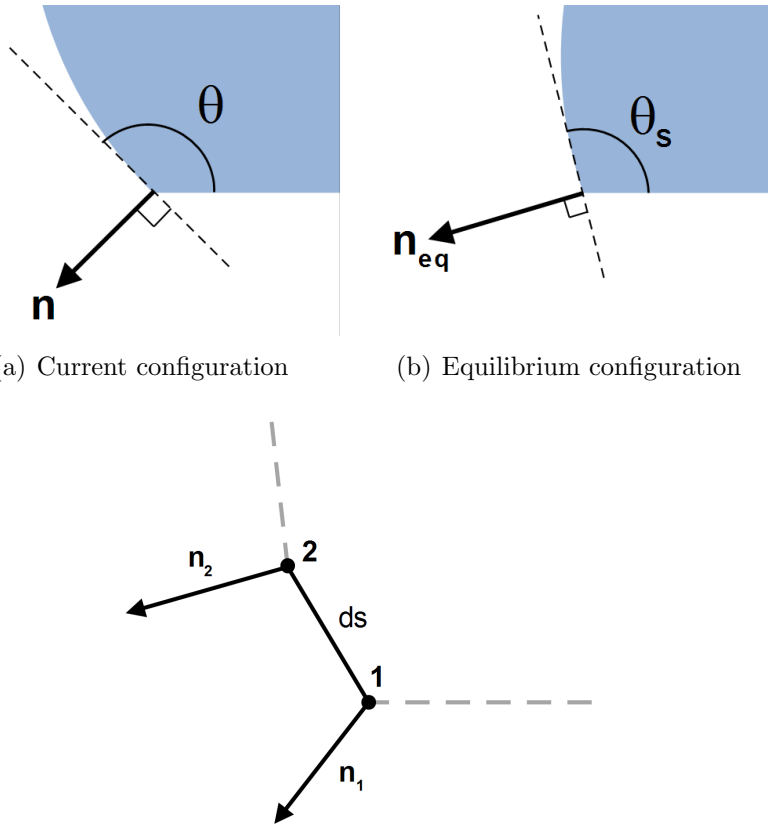

(a) Current configuration

(b) Equilibrium configuration

(c) Normal vector at contact line node and its nearest neighbor

Figure 3.8: (a)-(b) Normal vector and contact angle at current and equilibrium configurations and (c) Normal vector at contact line node and its nearest neighbor to obtain the curvature at contact line

An alternative to the above approach can be found in [57], [78].

When a droplet lays on a rough surface, such as those used in PEFC gas channels, the concept of *static contact angle* cannot be used. In rough surfaces, the contact

line pins and the contact angle changes from one equilibrium configuration to another. The present work uses two threshold values, $\theta_{\min}$ and $\theta_{\max}$, as contact angle conditions. The contact line is fixed only within the range $\theta \in [\theta_{\min}, \theta_{\max}]$. These maximum and minimum values represent the measured contact angles for incipient motion when the droplet is placed on a tilted plane of a given material. Further details of the method are discussed in section 3.4.4. Note also the contact angle might not correspond to that of the material due to surface roughness as described by Wenzel and Cassie-Baxter models [83].

When the dynamic contact angle is not fulfilled (i.e., $\theta < \theta_{\min}$ or $\theta > \theta_{\max}$), the contact line is allowed to move. Instead of the no-slip boundary condition (Eq. (3.9)), a slip boundary condition is applied at those nodes representing the contact line:

$$\mathbf{v} \cdot \mathbf{n} = 0 \tag{3.103}$$

where $\mathbf{n}$ is the unit normal vector of the substrate.

Adhesion force

When an external force acts on a droplet, such as gravity, surface tension acts as an opposing adhesion force in order to maintain equilibrium. Adhesion force acts on the contact line, where the three phases (air, water and the substrate) meet [84]. Thus, the summation of surface tension force along the contact line is equal to the adhesion force [43]:

$$F_{\text{adh}} = -\gamma \int_0^l \cos\left(\theta(l)\right) \cos\left(\psi(l)\right) dl \tag{3.104}$$

This expression has been already introduced in Chapter 2. Angles $\theta(l)$ and $\psi(l)$ are displayed in Fig. 2.6. For the three-dimensional problem, Eq. (3.104) is evaluated on the nodes representing the contact line. However, in two dimensions, the contact line is represented by two nodes. Thus, a lumped force is applied at each node I [84]:

$$F^{2D}_{\text{adh,I}} = \gamma \frac{\pi}{2} R \cos\theta \tag{3.105}$$

where R is the radius of the contact line, assuming that it is circular. The total adhesion force is therefore:

$$F^{2D}_{\text{adh}} = \gamma \frac{\pi}{2} R \left(\cos\theta_{\min} - \cos\theta_{\max}\right) \tag{3.106}$$

3.4 Results and discussion

The numerical model has been implemented within *Kratos Multi-Physics*, a C++ object oriented FE framework [54]. The resulting system of equations is solved using the Bi-conjugate gradient stabilized method (BICGSTAB). The additional term S_D in Eq. (3.49) precludes using solvers for symmetric systems of equations, such as Conjugate Gradient (CG).

Table 3.1: Input parameters used in the solver for monolithic scheme

Parameter	Value
Linear solver iterative tolerance	10^{-6}
Linear solver max number of iterations	5000

Table 3.2: Input parameters used in the velocity and pressure solvers for fractional step scheme

Parameter	Value
Velocity iterative tolerance	10^{-6}
Pressure iterative tolerance	10^{-3}
Velocity solver max number of iterations	5000
Pressure solver max number of iterations	1000
Velocity relative tolerance	10^{-3}
Velocity absolute tolerance	10^{-5}
Pressure relative tolerance	10^{-2}
Pressure absolute tolerance	10^{-4}

Table 3.1 shows the input parameters used in the model when monolithic scheme is used. Table 3.2 contains parameters used in velocity and pressure solvers when the problem is solved using the fractional step scheme. These parameters are used only in example 3.4.1, section *Different solution schemes*. The rest of examples are solved using a monolithic scheme with parameters from Table 3.1.

Results were obtained using a Linux 12.04 box with an Intel® Core™ i5 CPU M450 @ 2.40Ghz with 4 processors. Time to perform simulations is different on each example. Sessile drop examples only involved the solution of the Lagrangian domain, and the cost was remarkably low. Depending on the droplet size, simulations in these examples took between 20 and 300 seconds.

3.4.1 Static drop

The first example models a circular liquid droplet. The surface tension force is the only acting force and gravity is neglected ($g = 0$). Fluid's density, viscosity and surface tension coefficient are set to 1 ($\rho = 1$ kg m^{-3}, $\mu = 1$ kg m^{-1} s^{-1}, $\gamma = 1$ N m^{-1}). The fluid domain is a circular droplet with radius $R = 0.25$ m. Initial pressure in the liquid is set to $p_0 = 0$ Pa. The domain is meshed using triangular elements of size $h = 1/25$ m, as shown in Fig. 3.9(a).

According to Laplace-Young equation, the pressure in the interior of the droplet must be equal to $p = \gamma/R = 4$ Pa at steady state. The result of the simulation of 1 s with a time step of 0.01 s is shown in Figs. 3.9. Pressure distribution within the droplet is depicted in Fig. 3.9(b). Fig. 3.9(c) shows how pressure varies at the center of the droplet during the simulation. It can be observed that the steady state pressure is obtained in the second solution step. This value remains constant during the rest of the simulation. No overshoot values or oscillations are observed in the

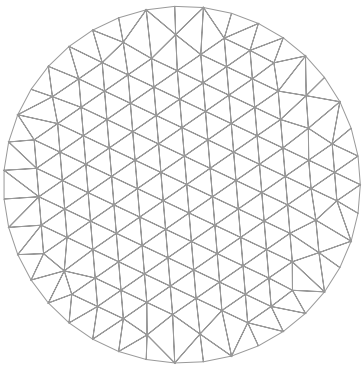

(a) Circular domain meshed with triangular elements

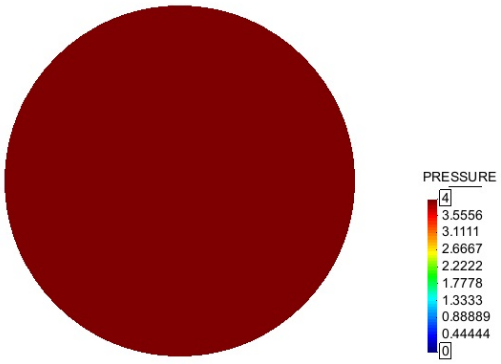

(b) Pressure field at $t = 1$ s

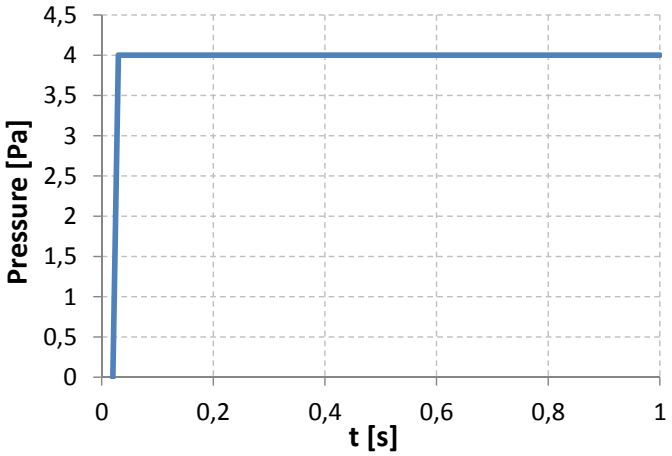

(c) Pressure evolution at the center of the droplet

Figure 3.9: (a) Mesh used to discretize the domain, (b) pressure distribution inside the droplet and (c) pressure evolution at the central node

pressure solution.

Mesh sensitivity analysis

In order to check that the solution obtained by the current model does not depend on the size of the mesh, the relative error as a function of the mesh size is plotted. For different droplet sizes ranging from $h = 0.1$ to $h = 0.005$ m, a simulation of 1 s using a time step of 10^{-2} s has been performed. Pressure at the center of the droplet has been compared to the exact value, which in this case is $p = 4$ Pa. The relative error has been obtained as:

$$error = \frac{p_{\text{sim}} - p_{\text{exact}}}{p_{\text{exact}}} \cdot 100 \tag{3.107}$$

Fig. 3.10 shows that for a coarse mesh with 27 nodes (Fig. 3.10(b)), the error is of the order of 1%. As the mesh is refined, the error decreases. Thus, the solution of the model does not depend on the mesh size.

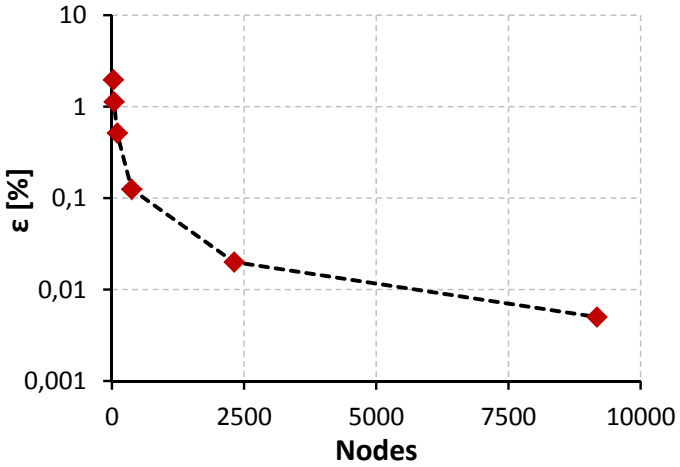

(a) Relative error as a function of grid size

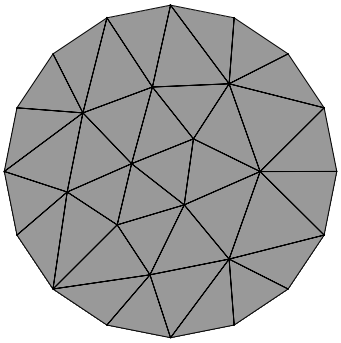

(b) Coarser mesh used with 27 nodes

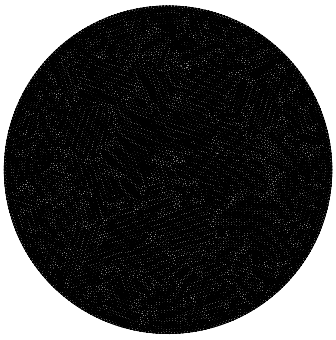

(c) Finest mesh used with 9174 nodes

Figure 3.10: (a) Relative error vs number of nodes, (b) mesh with $h = 0.1$ m and (c) mesh with $h = 0.05$ m

Different solution schemes

Two different solution schemes have been presented in Section 3.2: the fractional step method and the monolithic approach. The solution obtained with each method are compared in Fig. 3.11. The example is solved for lower viscosity values (μ =0.001 kg m^{-1} s^{-1} and μ =0.00001 kg m^{-1} s^{-1} were considered) in order to reduce the damping. The velocity at the boundary and the pressure at the first layer of nodes in the vicinity of the boundary are analyzed (the coordinates of the nodes are (0.25, 0.5) and (0.29, 0.5), respectively). The pressure of the external fluid is neglected ($p_{\text{ext}} = 0$) and the only acting force is the surface tension.

The solutions obtained using the coupled velocity-pressure (monolithic) solver and the one of the fractional step solver are compared in Fig. 3.11(a). In the fractional step method, the pressure at the liquid surface is fixed. This "strong" way of imposing pressure violates the incompressibility condition, leading to the motion of the boundary. Thus, the curvature and therefore the surface tension force also deviate from the exact value. As a consequence, oscillations appear in the solution. For low viscosity values the oscillations become more pronounced.

In the case of the coupled velocity-pressure (monolithic) solver no "artificial" pressure boundary condition is necessary. One can see an exact stable solution. Next, the surface tension (γ=0) term is neglected, however external pressure ($p_{\text{ext}} = 4Pa$) is applied. In this case both schemes show stable results (see Fig. 3.11(b)). Evolution of the velocity at a boundary node for different schemes is depicted in Fig. 3.11(c).

Different initial shapes

The same example is considered now using different initial configurations. Since the initial shape considered first is the expected one at steady state (i.e., a circle), the domain almost remains without deformation. Two initial configurations are considered here in order to make the effects of surface tension more evident. A three-dimensional cube domain of 0.5 m per side is considered first, where the boundary has either zero or positive values for the curvature. Second configuration is a two-dimensional *step* based on a square domain, where a quarter of it has been removed. The second domain includes a corner where the curvature is negative. The evolution of the two domains is shown in Fig. 3.12. In both configurations, steady state solution exhibits circular and spherical shapes, respectively.

3.4.2 Dynamic drop

The free oscillations of a droplet are examined in this example. When its initial shape is different from the equilibrium one (i.e., spherical if gravity is neglected) the droplet exhibits several oscillations prior to reaching the equilibrium state. Lamb (see p. 475 in [79]) performed an analytical study and found the expression for droplets' eigenfrequencies:

$$f_n = \frac{1}{2\pi}\sqrt{\frac{n(n-1)(n+2)\gamma}{\rho R^3}} \tag{3.108}$$

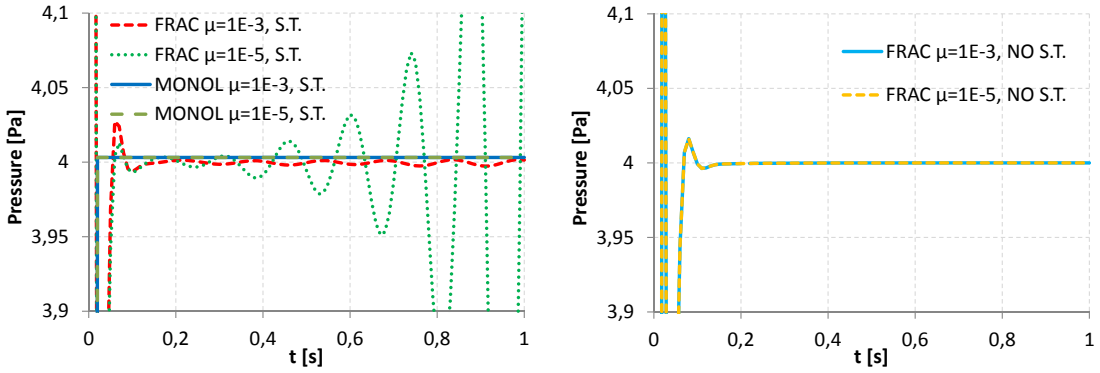

(a) $p_{\text{ext}} = 0$ Pa, $\gamma = 1$ N m^{-1} (b) $p_{\text{ext}} = 4$ Pa, $\gamma = 0$ N m^{-1}

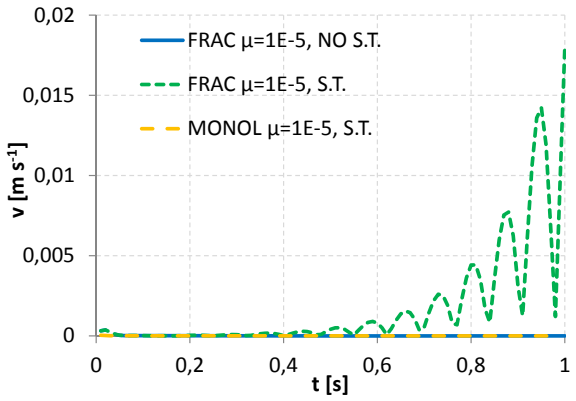

(c) Velocity at a boundary node

Figure 3.11: Comparison among the solutions obtained using the coupled (monolithic) and the fractional step scheme in the liquid phase.

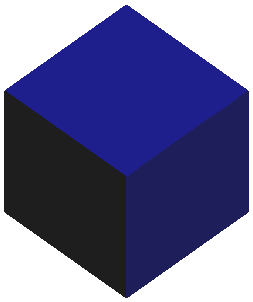

(a) Cube at $t = 0$ s

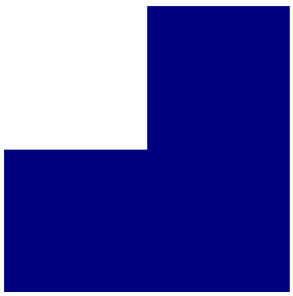

(b) Step at $t = 0$ s

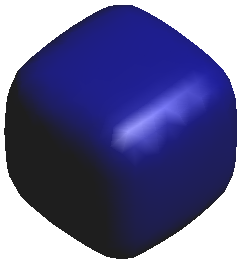

(c) Cube at $t = 0.25$ s

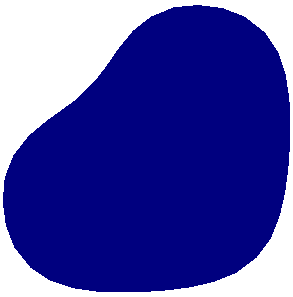

(d) Step at $t = 0.25$ s

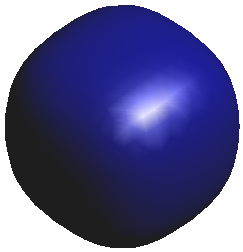

(e) Cube at $t = 0.5$ s

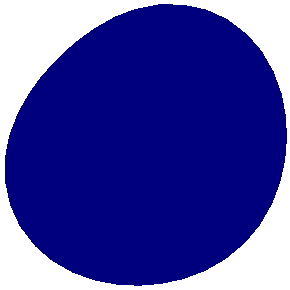

(f) Step at $t = 0.5$ s

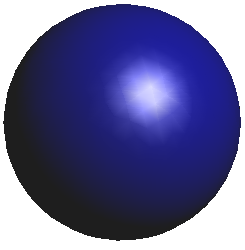

(g) Cube at $t = 1$ s

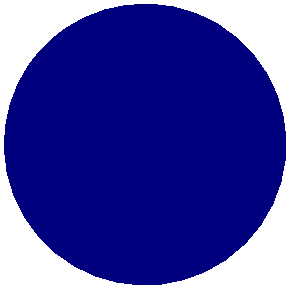

(h) Step at $t = 1$ s

Figure 3.12: Domain evolution for two different initial configurations

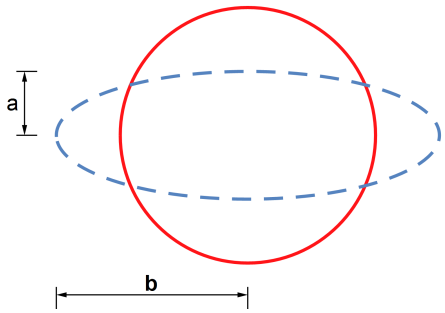

(a) Initial and final droplet shapes

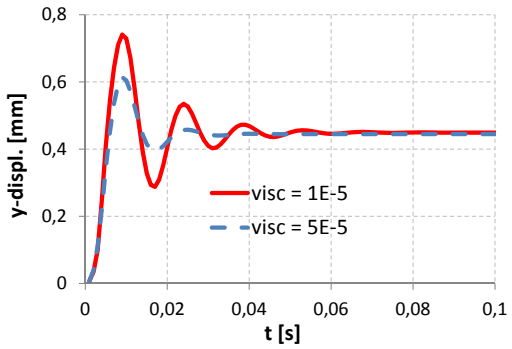

(b) y-displacement of an interface node, 2D case

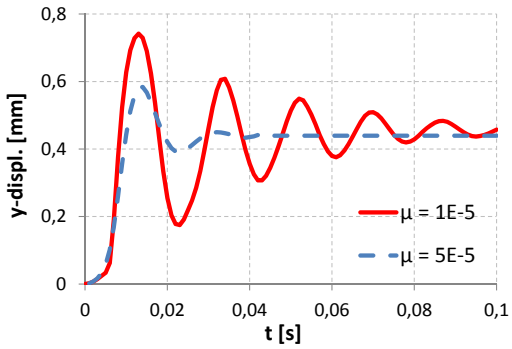

(c) y-displacement of an interface node, 2D case

Figure 3.13: Shape and y-displacement evolution of an elliptic droplet with different viscosities, in two and three dimensions

where n is the oscillation mode, ρ is the liquid's density and R is the droplet radius.

The considered setup is similar to the one shown in the previous example. However, the initial shape of the droplet is elliptical instead of circular (Fig. 3.13(a)), with $a = 1$ and $b = 3$ mm, as proposed in [85]. In the three-dimensional model, the initial shape is an ellipsoid with $a = c = 1$ and $b = 3$ mm. The actual physical density of water ($\rho = 1000$ kg m^{-3}) is used in this example. The gravity force is neglected. Two different values of viscosity are used in order to check its effect on the resulting oscillations, and the time step is set to 10^{-5} s.

According to Eq. (3.108) and considering the first non-zero oscillation mode (n=2), the frequency should be $\sim$ 43 Hz. The values obtained using the present model ($f = 46$ Hz in 2D, $f = 42$ Hz in 3D) show a very good agreement with the analytical value. The predicted value shows good agreement with the numerical simulation results from [85] as well ($\sim$ 50 Hz). Figs. 3.13(b) and 3.13(c) show the y-displacement of an interface node P, with initial coordinates (0,1,0) mm. Resulting displacement in the 3D example shows more oscillations than the 2D case. Since z displacements are not taken into account in the 2D case, inertial effects in this direction are neglected as well. Fig. 3.14 shows the evolution of the liquid domain over the simulation.

It is important to note that both the viscosity and the time step used in the numerical simulations have to be sufficiently low in order to observe oscillations in

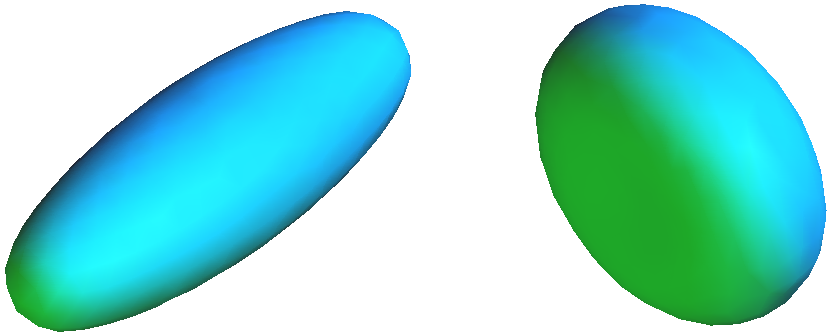

(a) $t = 0$ s

(b) $t = 0.01$ s

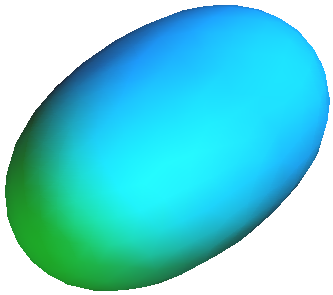

(c) $t = 0.025$ s

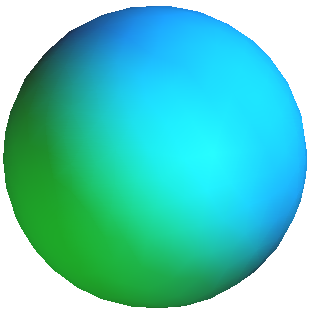

(d) $t = 0.1$ s

Figure 3.14: Domain evolution for an elliptic drop with $\mu = 10^{-5}$ Pa s

Table 3.3: Prescribed (θ_s) and obtained (θ_{obs}) contact angles, and relative error (ϵ_θ) between these variables

	$\theta_s = 70$ deg	$\theta_s = 90$ deg	$\theta_s = 135$ deg
θ_{obs} [deg]	70.15	89.91	135.08
ϵ_θ [%]	0.21	-0.10	0.06

the droplet boundary [85]. No oscillations may be detected for large viscosity values, confirming the observation of Bouwhuis.

3.4.3 Sessile drop

Sessile drop in different substrates

The contact angle condition is validated first in this example. A square of 1×1 mm is set as the initial configuration. Triangular elements of $h = 0.1$ mm have been used to discretize the domain. Three different contact angles are taken into account: θ_s = 70, 90 and 135 deg. For the considered droplet size, gravitational effects can be neglected as given by the Bond number:

$$Bo = \frac{\rho g d^2}{\gamma} = \frac{1000 \cdot 9.81 \cdot (10^{-3})^2}{0.072} \approx 0.14 < 1 \tag{3.109}$$

Results for the three different conditions are depicted in Fig. 3.15. Table 3.3 shows the difference between the prescribed and the modeled contact angle. Obtained results show good agreement with the prescribed contact angle, giving a maximum relative error of 0.21% with a relatively coarse mesh.

Sessile drop on a GDL surface This example aims to validate experimentally the numerical model by characterizing a sessile drop. The experiments were carried out as follows. A water droplet of a given volume was injected on top of a gas diffusion layer (SIGRALET 24BC, GDL side). The experiment was performed with droplets of volumes ranging from 3 to 30 μl. More details on the injection process can be found in [86]. In order to find the static contact angle of the droplet with the surface, the smallest droplet (3 μl volume) was generated at the tip of the needle. The droplet of given volume was brought near to the membrane and allowed to spread. After attaining the equilibrium contact angle, the needle was retracted and the contact angle measurements were preformed.

After the injection process was finished, a snapshot of the resulting droplet was taken at different time instances (Fig. 3.16 (a)-(c)). Using ImageJ software [87] together with DropShape [88], the static contact angle was estimated (Fig. 3.16(d)). The value of $\theta_s = 135$ deg was used as a reference for the rest of the examples for the contact angle condition.

Fig. 3.17(a) shows a direct comparison of numerical and numerical results. In order to provide a more detailed comparison, the x and y scales have been normalized to compare other droplet volumes. In Fig. 3.17(b) and 3.17(c) the x scale goes

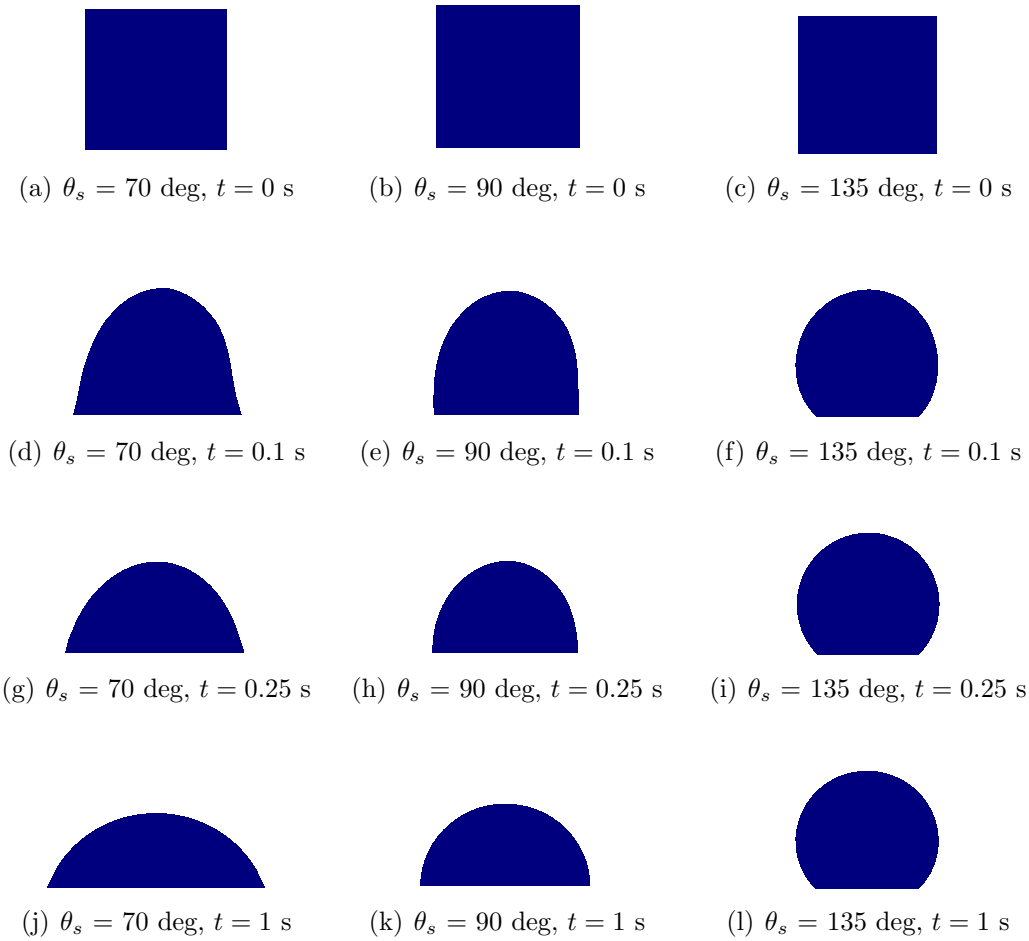

(a) $\theta_s = 70$ deg, $t = 0$ s (b) $\theta_s = 90$ deg, $t = 0$ s (c) $\theta_s = 135$ deg, $t = 0$ s

(d) $\theta_s = 70$ deg, $t = 0.1$ s (e) $\theta_s = 90$ deg, $t = 0.1$ s (f) $\theta_s = 135$ deg, $t = 0.1$ s

(g) $\theta_s = 70$ deg, $t = 0.25$ s (h) $\theta_s = 90$ deg, $t = 0.25$ s (i) $\theta_s = 135$ deg, $t = 0.25$ s

(j) $\theta_s = 70$ deg, $t = 1$ s (k) $\theta_s = 90$ deg, $t = 1$ s (l) $\theta_s = 135$ deg, $t = 1$ s

Figure 3.15: Droplet evolution for three different contact angles

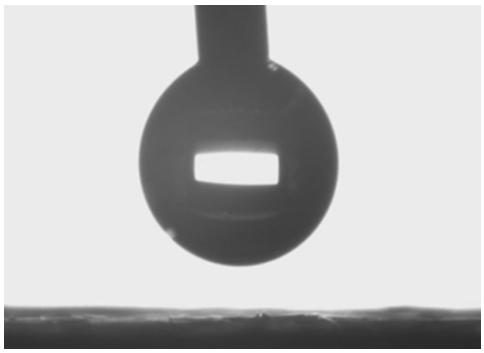

(a) Droplet injection at $t = 0$ s

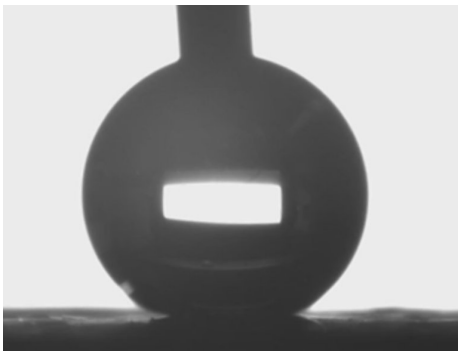

(b) Droplet injection at $t = 5$ s

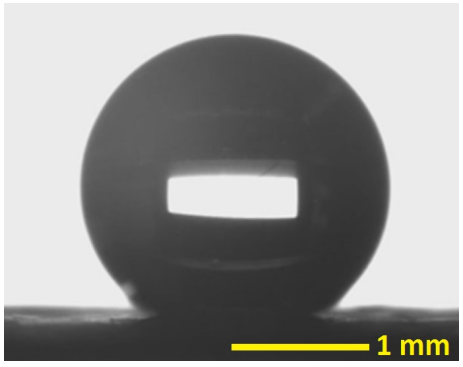

(c) Sessile drop formed at $t = 25$ s

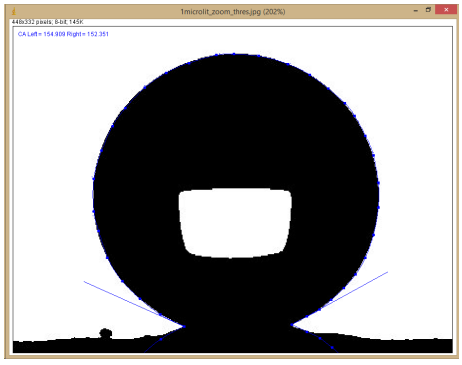

(d) Image processing of experimental result

Figure 3.16: Injection process of a droplet on a hydrophobic surface. All images have the same scale.

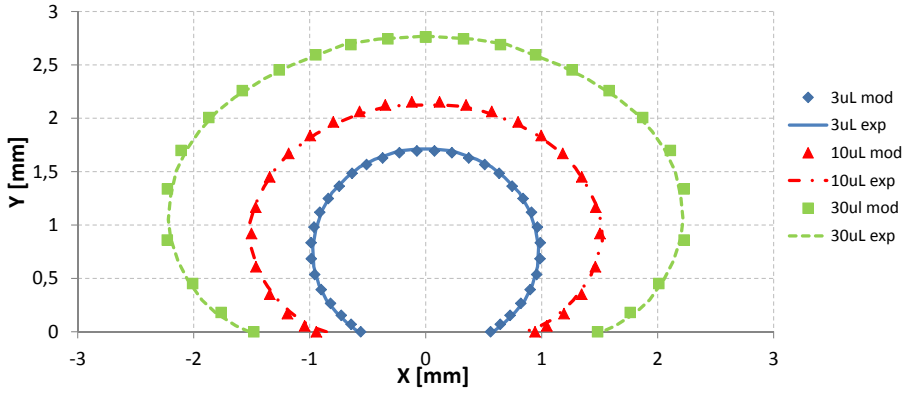

(a) 3, 10 and 30 μl-volume droplets

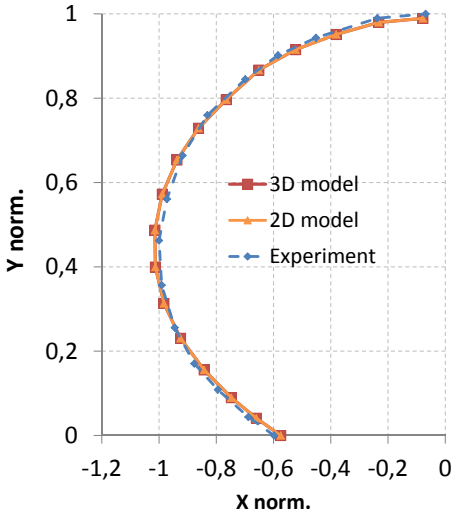

(b) 3 μl droplet

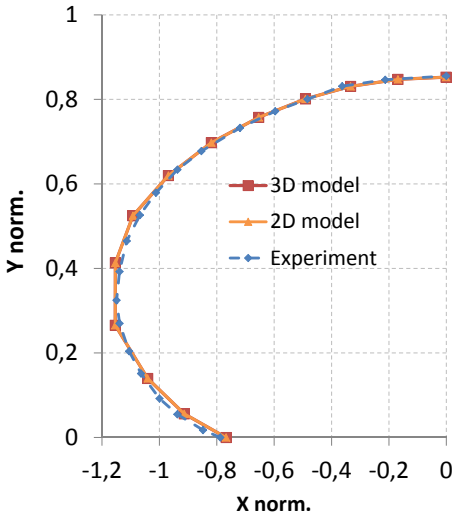

(c) 30 μl droplet

Figure 3.17: Comparison between modeled (in 2D and 3D) and experimental droplets with volumes from 3 to 30 μl using a scale in mm (top) and normalized (bottom), using pinning with variable contact angle

Table 3.4: Relative error between numerical and experimental results with respect to contact angle (ϵ_θ), height (ϵ_h) and chord (ϵ_h) for different droplet volumes (V), considering fixed (fix) and dynamic (dyn) contact angles

V [μl]	ϵ_θ [%]		ϵ_h [%]		ϵ_c [%]	
	fix	dyn	fix	dyn	fix	dyn
3	-1.40	-1.40	-2.42	-2.42	13.14	13.14
5	-7.56	-3.22	0.07	-0.27	25.00	2.84
10	-6.35	-2.49	-5.64	-4.18	23.93	7.73
20	-8.48	-3.45	-1.13	-6.28	27.67	7.89
30	-4.77	-2.50	-3.43	-2.60	9.66	3.11

from 0 to -1, being 0 the center of the droplet and -1 the minimum x coordinate. The coordinates are taken from a spherical cap, meaning that a curve that passes through the points $x_{\text{norm}} = -1$ and $y_{\text{norm}} = 1$ is a perfect spherical cap. Fig. 3.17(b) shows that the 3 μl drop obtained experimentally is a perfect spherical cap, which means that for this droplet size surface tension dominates over gravity. The numerical simulation using the method proposed here predicts a slightly more deformed droplet.

Other droplet volumes ranging from 5 to 30 μl have been compared with experimental data. As the droplet volume increases, gravity effects become more evident. Fig. 3.17(c) shows the comparison between numerical and experimental results obtained with a 30 μl-volume droplet. Overall, the obtained numerical profiles show good agreement with experimental data. Results using the two-dimensional model coincide with the model implemented in three dimensions, as shown in Figs. 3.17(b) and 3.17(c)

Table 3.4 shows the relative errors of contact angle (ϵ_θ), drop height (ϵ_h) and chord (ϵ_c) of numerical results compared to experimental data. Two numerical models have been used. The former is based on a fixed value of the equilibrium contact angle ("fix" columns), which corresponds to the aforementioned value of 135 deg. In the latter, a variable value of the contact angle is taken. The contact line undergoes pinning as long as the contact angle is lower than 162 deg. In other words, this threshold value is considered as the advancing contact angle.

Results in table 3.4 show that if the phenomenon is modeled considering a dynamic contact angle, the error is considerably reduced. This is not the case for the 3 μl example, however, because in this case gravity effects are negligible and therefore the contact angle remains constant. Differences between the two and the three-dimensional model are again negligible. It can be concluded that for sessile drop examples, a two-dimensional model is able to reproduce experimental results with the same accuracy as the 3D model.

3.4.4 Sessile drop on an inclined plane

This example aims to show the effects of contact angle hysteresis and pinning observed when an external force (such as gravity or air flowing) acts on a droplet. The

sessile drop example is repeated but introducing a slight difference: the droplet is laying on an inclined plane. A video camera is attached to the plane, and the plane is tilted at a constant rate of 0.4 deg s^{-1}. A schematic view of the experimental set-up is depicted in Fig. 3.18.

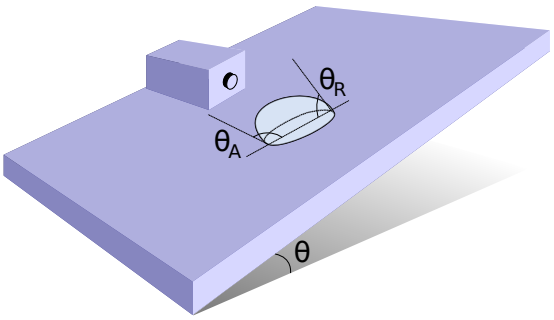

Figure 3.18: Experimental set-up to measure gravity effects on a sessile droplet

Fig. 3.20 shows the comparison between the measured contact angles (red square and blue diamond markers) and the modeled values (red solid and blue dashed lines). In these plots, *REC* and *ADV* stand for receding and advancing contact angles, respectively. Results show that numerical values agree well with experimental data. For each droplet volume, detachment can be read directly from its corresponding plot, and it occurs when the tilt angle reaches its maximum value. For instance, the 10 μl droplet detaches when the plane is tilted 36 deg, and the advancing and receding angles are 150 and 115 deg, respectively.

Contact angle distribution along the contact line The contact line of a deformed droplet with contact angle $\theta_s > 90$ deg can be modeled as two semi-ellipses, as shown in Chapter 2 and in reference [50]. Equations for both semi-ellipses are:

$$\frac{x^2}{a_1^2} + \frac{y^2}{b_1^2} = 1 \qquad \text{for } x < 0 \tag{3.110}$$

$$\frac{x^2}{a_2^2} + \frac{y^2}{b_2^2} = 1 \qquad \text{for } x > 0 \tag{3.111}$$

where:

$$b_1 = b_2 = R \tag{3.112}$$

$$a_1 + a_2 = c = 2R \tag{3.113}$$

where R is the radius of the circle (considering a circular contact line when it is undeformed). The deformation parameter λ can be defined as the ratio between both semi-radii a_1 and a_2 (i.e., $\lambda = 1$ for an undeformed droplet). One of the hypothesis used in the semi-analytical model presented in Chapter 2 is that the contact angle along the contact line is linear with respect the x coordinate for a deformed droplet. The three-dimensional model can be used to check whether this

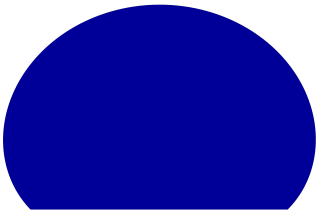

(a) t = 0 s, $\theta = 0$ deg

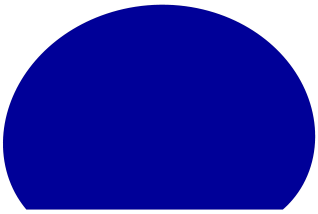

(b) t = 20 s, $\theta = 8$ deg

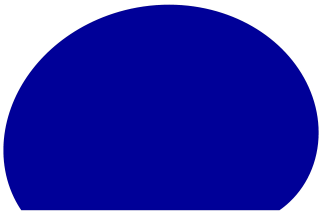

(c) t = 42.5 s, $\theta = 17$ deg

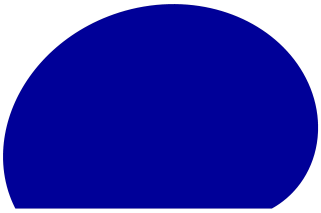

(d) t = 62.5 s, $\theta = 25$ deg

Figure 3.19: Resulting animation of the modeled droplet during deformation process

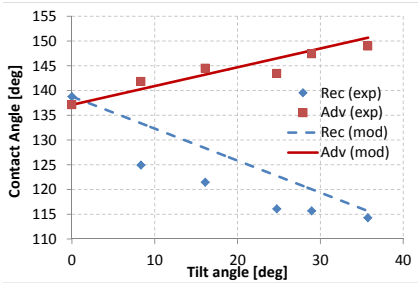

(a) V = 10 μl

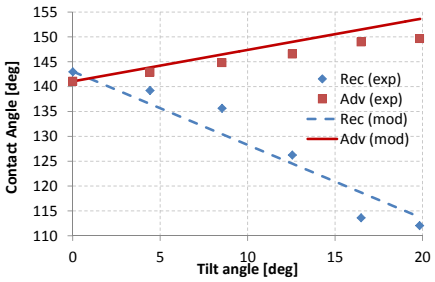

(b) V = 20 μl

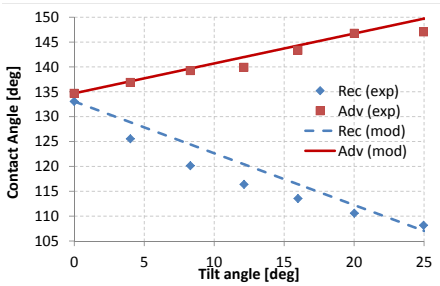

(c) V = 30 μl

Figure 3.20: Comparison between the measured contact angle (square and diamond markers) and the modeled contact angle (solid and dashed lines)

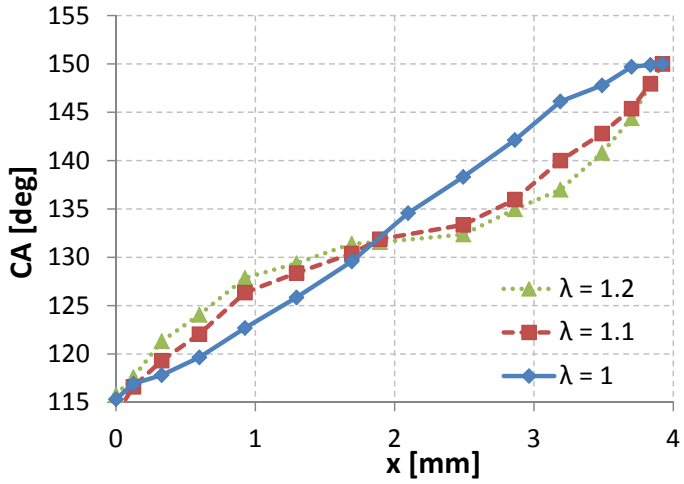

Figure 3.21: Contact angle along the contact line as a function of coordinate x and the deformation parameter λ

assumption is valid or not. Fig. 3.21 shows the contact angle modeled along the contact line for the 10uL-volume droplet.

Results show that this assumption is only valid if the contact line is circular ($\lambda = 1$). For this case, results can be considered linear with respect coordinate x since the obtained coefficient of determination is $R^2 = 0.996$. The contact line distribution for a deformed droplet ($\lambda > 1$) is a third-degree polynomial with respect to x. The coefficient of determination for $\lambda = 1.1$ and $\lambda = 1.2$ is 0.995 and 0.997, respectively, when results are fitted by a third-degree curve. These results can be used to improve semi-analytical models like the one presented in Chapter 2.

3.5 Conclusions

A Lagrangian finite element model for droplets has been developed and validated experimentally. The model proposed can represent the droplet surface exactly via the Lagrangian boundary mesh, and it does not depend on a background fixed mesh. An implicit surface tension model has been proposed. Results show that this formulation is advantageous from the computational point of view; it alleviates the severe time restrictions characteristic of the commonly used explicit surface tension models.

For surface tension dominated problems, such as droplet analysis, solution obtained with a monolithic scheme is stable. Surface tension acting on the droplet's surface precludes the use of pressure segregation method, such as fractional step. For fluids with low viscosity, solution for problems with surface tension exhibit non-stable behavior. A stable solution with fractional step method is obtained only if surface tension effects are substituted by an artificial external pressure. However, for droplet dynamics in gas channels the external pressure is variable and therefore it is difficult to use these kinds of methods. On the other hand, monolithic scheme is more computationally expensive than fractional step method.

Present model can be used to analyze the dynamics of a droplet with a given

arbitrary shape. Results show that the obtained frequency of oscillation is consistent with the analytical solution. However, results obtained with two and three-dimensional models can be significantly different for highly distorted initial shapes. Since inertial effects in z direction are neglected in the 2D model, results obtained by the 3D model exhibit more oscillations.

Sessile droplets in smooth and rough surfaces with a given contact angle can be studied with the proposed model. Results show that given an arbitrary shape of the domain, the steady state of the sessile droplet is reached. Contact angles obtained in the simulation differ less than 1% from the prescribed value.

From the analysis of a sessile droplet laying on a rough surface it can be concluded that numerical error is considerably lower when the proposed dynamic contact angle condition is used. For rough surfaces, such as the ones encountered in PEFC electrode channels, a static contact angle condition leads to significant numerical errors. Whereas the error of the droplet's chord length obtained with a dynamic contact angle condition can be equal to 3%, the error obtained using a static contact condition can be as high as 25%. Two and three-dimensional models obtain the same results for sessile droplet examples.

Results from the tilted plane example show a linear relationship between tilting angle and contact angles. Both advancing and receding angle numerical results are in reasonable agreement with experimental data. However, values of the receding contact angle observed experimentally have a non-linear relationship with tilted plane angle. This difference may be caused by the absence of roughness effects in the present model.

Distribution of the contact angle along the contact line has been studied. Results show that for circular (undeformed) contact lines, contact angle has a linear relationship with x coordinate. Deformed contact lines show that this relationship becomes a third-degree polynomial. This result is in contradiction with the assumption made in Chapter 2 that the relationship remains linear. Future semi-analytical models could be improved using this result. However, contact angle results obtained using a linear and a third-order relationship differ less than 5%. Thus, if a linear relationship is assumed, error obtained in contact angle along the line and adhesion force is acceptable.

Chapter 4

An embedded multiphase model

This chapter presents an embedded model to study air-water systems, such as droplets in PEFC gas channels. A Lagrangian finite element model has been proposed in the previous chapter. However, this model is limited to the study of a single domain. In order to study droplet dynamics in PEFC channels, a model that takes into account both air and water and their continuous interaction should be developed. There exist several approaches in literature to study systems involving two or more interacting phases.

4.1 Multiphase flow modeling

Multiphase flow problems are an active area of research and their applications include chemistry [89], biology [90], and engineering [91]. These problems usually take into account multiple phenomena such as fluid transport, heat transfer, phase change and chemical reactions. There exists a vast number of books ([62], [92], [93]) and reviews ([29], [91]) on multiphase flow problems. In accordance with the topic of the present work, we shall restrict our review to two-phase flow in microchannels and consider exclusively the mechanical problem. Microchannels are gas channels where at least one of the dimensions is below a few millimeters [91]. Such devices are used in microreactors, micro heat exchangers or in low-temperature fuel cells. When two or more fluids are present, it is vital to characterize their dynamics, as well as the interface between them and their interaction. Dominant effects depend on the considered scale. As explained in section 2.1.2, surface tension and viscous effects become more important than gravitational or inertial effects within microchannels. These latter effects however cannot be neglected. At the considered length scale (i.e., droplets with less than 1 mm height), even if they are not dominant, they have a significant impact on droplet dynamics.

Most multiphase flow models consider gas-liquid systems and, possibly, their contact with the solid. The challenges of multiphase flow modeling consist in:

- detecting the interface between the phases
- accounting for changes in the material properties (i.e., density and viscosity)
- accurately representing the discontinuities in the flow variables (typically, pressure) across the interface

- accounting for surface tension and wetting of the solid phase

The way these challenges are tackled is strongly related to the kinematic frameworks chosen for describing the continuum. One can distinguish between two kinds of approaches: Eulerian and Lagrangian methods. Eulerian methods solve the fluid dynamics problem using a fixed mesh and therefore they need additional techniques to represent the interface between phases and describe its motion. Two alternatives arise at this point: front-capturing and front-tracking methods. In the front-capturing methods, the interface is described using a scalar function. The Volume of Fluid (VOF) and the Level Set (LS) methods are the most known front-capturing methods. The first published work on VOF was released in 1981 by Hirt and Nichols [27]. Together with mass and momentum equations, the method is based on an additional convection equation for the interface volume fraction variable C_k:

$$\frac{\partial}{\partial t}\left(C_\mathrm{k}\rho_\mathrm{k}\right) + \nabla \cdot \left(C_\mathrm{k}\rho_\mathrm{k}\mathbf{v}_\mathrm{k}\right) = 0 \tag{4.1}$$

where ρ_k and $\mathbf{v}_\mathrm{k}$ are the density and the velocity of the fluid k, respectively. The volume fraction variable, C_k, takes the value 0 for the nodes outside the fluid k, 1 inside the fluid, and between 0 and 1 when the considered element contains the interface between two fluids. Consequently, the interface between fluids can be determined by applying that surface-tracking technique to a fixed Eulerian mesh, thus enabling the user to know the location and shape of it [9], [16]. The interface is represented using piecewise constant functions. Piecewise linear interface calculation (PLIC) techniques ([94], [95]) are the most used nowadays and have been included in commercial codes. VOF method, however, has some drawbacks. For example, the advective term of equation (4.1) is very difficult to discretize due to the jump of the volume fraction function in the interface [55]. Moreover, artificial diffusion of the interface is observed in the solution in case of coarse meshes in the vicinity of the interface. However, Eulerian formulations can handle theoretically arbitrary large deformations since the mesh is fixed and elements do no deteriorate.

Alternatively, LS method was presented by Osher and Sethian in 1988 [96] as a general technique to capture a moving interface. It was then applied to two-phase flows and other applications [91]. The basic idea of the level set method is to represent the interface by the zero level set of a smooth scalar function $\phi(\mathbf{x})$ [97], [98]:

$$\phi(\mathbf{x}) : \mathbb{R}^n \longrightarrow \mathbb{R} \qquad \mathbf{\Gamma} = \{x : \phi(\mathbf{x}) = 0\} \tag{4.2}$$

The position of the interface is known implicitly by the nodal values of ϕ: nodes with positive values are inside the fluid, whereas negative values mark nodes outside the fluid domain. The position of the interface is then obtained by interpolation of nodal values of function ϕ. LS method has the advantage of being capable of handling topological changes and complex shapes of the interface. It may however give inaccurate results for normal vector and interface curvature, and it also fails at mass conservation. Additional techniques to alleviate these drawbacks have been reported in literature [4], [91], [99], [100], [101], [102].

Front-tracking methods on the other hand represent explicitly the interface using Lagrangian markers. Several examples of this method can be found in references

[4], [103] and [104]. The velocity of the interface is interpolated from the velocity field given by the Eulerian mesh. This method requires remeshing of the boundary interconnecting the interface markers.

An alternative to the Eulerian models are the Lagrangian models. These models use moving meshes to represent the computational domains and thus the interface is identified by the moving boundary mesh. In addition, boundary conditions such as surface tension force are easier to be applied as the boundary is explicitly represented by the mesh. Moreover, the discretized equations system matrix becomes symmetric due to the absence of the convective term. Multi-fluid models using a pure Lagrangian finite element-based formulation for both air and water have been presented in [3] and [105]. These models do not require any additional technique for detecting the moving interface, and it remains sharp with time (interface smearing is often observed in Eulerian approaches). However, steady-state solutions using Lagrangian methods usually exhibit spurious velocities at the interface due to the steep pressure gradient on the interface. Certain remedies based upon degree of freedom duplication have been proposed in [106]. An additional disadvantage is that the domain has to be remeshed after each time step in order to avoid mesh degradation, and connectivity preserving techniques must be applied to maintain the interface and avoid edge-swapping [3]. In the context of PEFC gas channels, a model treating both the gas and the liquid droplets in a Lagrangian framework would have a large computational cost due to remeshing.

Different kind of Lagrangian methods are the meshless methods, such as lattice Boltzmann method (LBM). LBM is used for CFD simulations at the continuum level. The basic idea of this method is to apply simplified kinetic models considering essential physics at the mesoscopic level so that average macroscopic properties follow the continuum equations [107]. This explicit algorithm is associated with a square in two dimensions or with a cubic lattice in three-dimensional studies. The particles evolve within this region synchronously from one point to its neighbors, according to the lattice Boltzmann equation [107]. This equation describes the particle dynamics and includes external forces and collisions between the different particles. When the model describes two immiscible fluids, this method must be equipped with a coloring function in order to avoid artificial diffusion. An advantage of the Lattice Boltzmann method is the ease of implementation compared with Navier-Stokes, since the governing equation of the former is semi-linear. However, this method cannot prescribe macroscopic properties of the fluid (such as density, viscosity or surface tension coefficient) because these properties are consequences of mesoscopic dynamics, and is not mass conservative.

Smoothed Particle Hydrodynamics (SPH) method uses a set of discrete points (or particles) to represent a whole physical system [108]. It was first developed for astrophysics by Gingold and Monaghan [109], but recently it has been used in fluid dynamics simulations. In this method, an interpolation kernel $W(r)$ is used to interpolate any function or material property at a given point using its neighbor particles. Contrary to CFD-based method, smoothed particle hydrodynamics uses these particles and a certain radius around them instead of cells. Although this method can represent complex geometries and has good mass conservation properties, generally the number of particles needed to solve a problem is larger than the

number of elements in a CFD simulation. Moreover, SPH and LB methods share common drawbacks: the treatment of the boundaries is rather ambiguous [110], and pressure solution tends to show a noisy behavior.

The Particle Finite Element Method (PFEM) is a combination of the particle method and the Finite Element Method. It was presented by Oñate et al. [111] and Idelsohn et al. [112]. In PFEM, the domain is represented by a set of particles that move in a Lagrangian manner according to the velocity field [3]. Forces are obtained using a background mesh, and the nodes of this mesh coincide with the particles. Since all the information is stored in the particles, PFEM does not show numerical diffusion due to remeshing. Mesh is obtained using Delaunay triangulation [113]. Conclusively, PFEM combines the advantages of both particle and FE methods. An exhaustive review on Lagrangian methods can be found in Chapter 2 of reference [3].

A numerical method that combines the advantages of both Eulerian and Lagrangian formulation would be beneficial for droplet dynamics simulation in gas channels. This chapter presents a Lagrangian-Eulerian numerical approach, the embedded method, to study air-water systems. Our particular problem of interest is droplet dynamics in fuel cell gas channels, but the method can be used in any gas-liquid or immiscible liquid-liquid system. The embedded concept, also known as *immersed boundary* or *fictitious domain* approach, has been widely used for fluid-structure interaction (FSI) modeling [114],[115], [116]. In FSI, this approach naturally represents the structure from the Lagrangian point of view, whereas the Eulerian framework is used for the fluid.

For multi-fluid problems, this approach is much less studied and has been introduced only recently. Conceptually, the embedded framework for multiphase analysis was proposed in [117] (Chapter 5) and [118]. In both works it has been applied to a particular class of problems dealing with the interaction of polymer melts with air. Moreover, [118] proposes a model so as to account for complex thermal interaction between the phases faced in fire situations. However, only a weak one-way mechanical coupling was introduced since the stresses exerted by the air upon the liquid (melted polymer) were negligible.

In the present work the formulation is further developed so as to account for the two-way coupled nature of the problem. In airflow-droplet interaction problems the forces exerted by air upon the liquid are dominant and thus cannot be neglected. Moreover, the surface tension effects (neglected in previous works) are included in the model. However, one must keep in mind that the overall "architecture" of the method is inherited from [117] and [118].

In the embedded method, both fluids are solved in a partitioned manner. The basic idea of this method is that the Lagrangian domain (representing the water) moves on top of a fixed Eulerian mesh (air domain). Note that this formulation is particularly advantageous in fuel cell gas channel applications, where water represents a small part of the whole domain. Additionally, the Lagrangian formulation can naturally track the air-water interface.

4.2 Numerical model

4.2.1 Governing equations

Let us consider Lagrangian domain Ω_L (representing liquid) embedded into the Eulerian domain Ω_E (gas) with an external boundary Γ_E (see Fig. 4.1). In the embedded setting the interface Γ_I between the two fluids is defined by the position of the boundary of the Lagrangian domain Γ_L. The interface Γ_I splits the Eulerian domain into two parts: the real one Ω_E^r (representing the gas) and the fictitious one Ω_E^f that does not have physical meaning. Note that at the continuous level the fictitious Eulerian domain exactly coincides with the Lagrangian domain and $\Gamma_I = \Gamma_L$. Next we present the governing equations for the gas and the liquid domains.

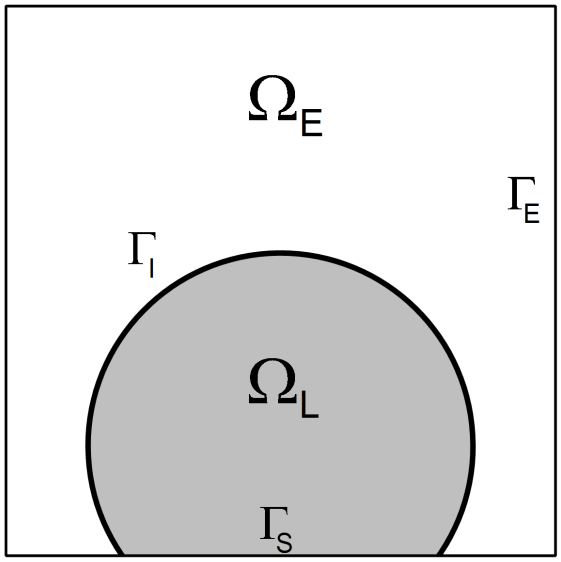

Figure 4.1: Embedded setting

Liquid domain represents water, whereas air is considered for the gas domain. The governing system of equations in either domain is therefore the Navier-Stokes equations equipped with the incompressibility condition:

$$\rho\frac{D\mathbf{v}}{Dt} - \mu\nabla\cdot(\nabla\mathbf{v} + \nabla^T(\mathbf{v})) + \nabla p = \rho\mathbf{g} \qquad \text{in } \Omega_E^r \text{ and } \Omega_L \qquad (4.3)$$

$$\nabla\cdot\mathbf{v} = 0 \qquad \text{in } \Omega_E^r \text{ and } \Omega_L \qquad (4.4)$$

where $\frac{D\mathbf{v}}{Dt}$ is the material time derivative of the velocity, p is the pressure, t is the time, $\mathbf{g}$ is the body force, ρ is the fluid density and μ is the fluid dynamic viscosity. The physical properties are defined as $\rho = \rho_E$ and $\mu = \mu_E$ in Ω_E, and $\rho = \rho_L$ and $\mu = \mu_L$ in Ω_L.

Boundary and interface conditions

In order to ensure the well-posedness of the Navier-Stokes problem defined by Eqs. (4.3) and (4.4), suitable boundary conditions must be specified. On the external

boundary $\Gamma_E = \Gamma_D \cup \Gamma_N$, such that $\Gamma_D \cap \Gamma_N = \emptyset$, the following conditions are prescribed:

$$\mathbf{v} = \mathbf{v}^{pr} \qquad \text{at } \Gamma_D \tag{4.5}$$

$$\boldsymbol{\sigma} \cdot \mathbf{n} = \boldsymbol{\sigma}_n^{pr} \qquad \text{at } \Gamma_N \tag{4.6}$$

where $\mathbf{v}^{pr}$ is the prescribed velocity, $\mathbf{n}$ is the outer unit normal to Γ_N, and $\boldsymbol{\sigma}_n^{pr}$ is the prescribed traction vector.

On the internal interface Γ_I the coupling conditions are:

$$[\![\mathbf{v}]\!] = 0 \qquad \text{at } \Gamma_I \tag{4.7}$$

$$[\![\boldsymbol{\sigma}]\!] \cdot \mathbf{n} = \gamma\kappa\mathbf{n} \qquad \text{at } \Gamma_I \tag{4.8}$$

where $\mathbf{n}$ now is the unit normal to the interface Γ_I, γ and κ are the surface tension coefficient and the interface curvature, respectively. The $[\![x]\!]$ symbol represents the jump of the quantity x across the interface.

Eq. (4.7) expresses the continuity of all velocity components ($[\![\mathbf{v}]\!] = \mathbf{v}_E - \mathbf{v}_L$, where indexes E and L distinguish the quantities corresponding to the air and water, respectively). The equality of the normal components of velocity ensures no mass flow across the interface. The tangential components' equality is similar to a no-slip condition and is necessary when fluids with non-zero viscosity are considered. Eq. (4.8) expresses that the difference in the normal stress across the interface is balanced by the surface tension force.

Projecting Eq. (4.8) onto the normal and tangential directions leads to the following scalar interface conditions:

$$\mathbf{n} \cdot ([\![\boldsymbol{\sigma}]\!] \cdot \mathbf{n}) = \gamma\kappa \qquad \text{at } \Gamma_I \tag{4.9}$$

$$\mathbf{t} \cdot ([\![\boldsymbol{\sigma}]\!] \cdot \mathbf{n}) = 0 \qquad \text{at } \Gamma_I \tag{4.10}$$

Noting that the jump in the stress across the interface is equal to the difference between the stresses of the two fluids $[\![\boldsymbol{\sigma}]\!] = \boldsymbol{\sigma}_E - \boldsymbol{\sigma}_L$ and splitting the stress tensor into volumetric and deviatoric part (Eq. (3.6))results in:

$$(p_L - p_E) + \left[\mu_E \mathbf{n} \cdot \left(\left[\nabla\mathbf{v} + \nabla^T\mathbf{v}\right]_E \cdot \mathbf{n}\right) - \mu_L \cdot \mathbf{n} \cdot \left(\left[\nabla\mathbf{v} + \nabla^T\mathbf{v}\right]_L \cdot \mathbf{n}\right)\right] = \gamma\kappa \tag{4.11}$$

$$\mu_E \mathbf{t} \cdot \left(\left[\nabla\mathbf{v} + \nabla^T\mathbf{v}\right]_E \cdot \mathbf{n}\right) - \mu_L \cdot \mathbf{t} \cdot \left(\left[\nabla\mathbf{v} + \nabla^T\mathbf{v}\right]_L \cdot \mathbf{n}\right) = 0 \tag{4.12}$$

4.2.2 Finite Element formulation for the gas

Governing equations (4.3) and (4.4) are discretized in space following the procedure from Section 3.2. Linear velocity and pressure interpolations over 3-noded triangles (2D) or 4-noded tetrahedra (3D) are used. For sake of simplicity, Backward Euler time discretization scheme is chosen, although governing equations are discretized using Newmark-Bossak scheme (see Appendix C). Newmark-Bossak scheme is an unconditionally stable implicit time integration scheme with second-order accuracy. Bossak modification improves stability for highly geometrically non-linear problems, which is particularly advantageous for the problem at hand.

Given $\bar{\mathbf{v}}_n$ and $\bar{p}_n$ at t_n, the time discrete problem consists in finding $\bar{\mathbf{v}}_{n+1}$ and $\bar{p}_{n+1}$ at t_{n+1} as the solution of:

$$\mathbf{M}\frac{\bar{\mathbf{v}}_{n+1}-\bar{\mathbf{v}}_n}{\Delta t}+\left[\bar{\mathbf{K}}\left(\bar{\mathbf{v}}_{n+1}\right)+\mu\mathbf{L}\right]\bar{\mathbf{v}}_{n+1}+\mathbf{G}\bar{p}_{n+1}=\bar{\mathbf{F}} \tag{4.13}$$

$$\mathbf{D}\bar{\mathbf{v}}_{n+1}=0 \tag{4.14}$$

where $\bar{\mathbf{K}}(\bar{\mathbf{v}}_{n+1})$ is the non-linear convection operator, and the rest of terms have been already defined in Section 3.2. The convection operator is assembled from the elemental contribution defined as:

$$\bar{\mathbf{K}}=k_{IJ}=\rho\int_{\Omega_e}N_I\bar{\mathrm{v}}_k\frac{\partial N_J}{\partial x_k}\,\mathrm{d}\Omega \tag{4.15}$$

The conditions at the external boundary are:

$$\bar{\mathbf{v}}=0 \qquad \text{at } \Gamma_D \tag{4.16}$$

$$\boldsymbol{\sigma}\cdot\mathbf{n}=0 \qquad \text{at } \Gamma_N \tag{4.17}$$

Algebraic Sub-Grid Scales (ASGS) stabilization [68] is chosen as the technique to stabilize governing system defined by Eqs. (4.13) and (4.14). These equations are stabilized as discussed in Section 3.2.1, where the following term is added to the left-hand side:

$$\sum_{e=1}^{n_e}\int_{\Omega_e}\tau\left[\mathbf{F}-\mathcal{L}(\mathbf{v}_h)\right]^T\mathcal{L}^*(\mathbf{w}_h)\,\mathrm{d}\Omega \tag{4.18}$$

where the time-dependent residual is:

$$\begin{aligned}\mathcal{L}(\mathbf{v}_h)&=\begin{bmatrix}\rho\frac{\partial\mathbf{v}_h}{\partial t}+\rho\mathbf{v}_h\cdot\nabla\mathbf{v}_h-\mu\nabla\cdot(\nabla\mathbf{v}_h)+\nabla p_h\\ \nabla\cdot\mathbf{v}_h\end{bmatrix}=\\&=\begin{bmatrix}\rho\frac{\mathbf{v}_{n+1}-\mathbf{v}_n}{\Delta t}+\rho\mathbf{v}_{n+1}\cdot\nabla\mathbf{v}_{n+1}+\nabla p_{n+1}\\ \nabla\cdot\mathbf{v}_{n+1}\end{bmatrix}\end{aligned} \tag{4.19}$$

where the convective term has been linearized considering a constant convective velocity equal to $\mathbf{v}_{n+1}$ [68]. Note that the Backward Euler time integration scheme has been applied, as discussed in Chapter (3). The term $\mathcal{L}^*$ for ASGS for linear interpolation functions is equal to:

$$\mathcal{L}^*(\mathbf{w}_h)=\begin{bmatrix}-\mathbf{v}_{n+1}\cdot\nabla\mathbf{w}_h-\nabla q_h\\ -\nabla\cdot\mathbf{w}_h\end{bmatrix} \tag{4.20}$$

Using Eqs. (4.19) and (4.20) in Eq. (4.18), the stabilization term yields:

$$\begin{aligned}&\int_{\Omega_e}\tau_1\left(\mathbf{v}_{n+1}\cdot\nabla\mathbf{w}_h+\nabla q_h\right)\left(\rho\frac{\mathbf{v}_{n+1}-\mathbf{v}_n}{\Delta t}+\rho\mathbf{v}_{n+1}\cdot\nabla\mathbf{v}_{n+1}+\nabla p_{n+1}-\mathbf{f}\right)\,\mathrm{d}\Omega+\\&+\int_{\Omega_e}\tau_2\left(\nabla\cdot\mathbf{w}_h\right)\left(\nabla\cdot\mathbf{v}_{n+1}\right)\,\mathrm{d}\Omega\end{aligned} \tag{4.21}$$

Terms multiplied by q_h are added to the continuity equation, whereas terms multiplied by $\mathbf{w}_h$ are added to the momentum equation. The following terms are added to Eq. (4.13):

$$\begin{aligned}
&\int_{\Omega_e} \tau_1 \left(\mathbf{v}_{n+1} \cdot \nabla \mathbf{w}_h\right) \left(\rho \frac{\mathbf{v}_{n+1}}{\Delta t} + \rho \mathbf{v}_{n+1} \cdot \nabla \mathbf{v}_{n+1}\right) \, \mathrm{d}\Omega + \\
&+ \int_{\Omega_e} \tau_2 \left(\nabla \cdot \mathbf{w}_h\right) \left(\nabla \cdot \mathbf{v}_{n+1}\right) \, \mathrm{d}\Omega + \\
&+ \int_{\Omega_e} \tau_1 \left(\mathbf{v}_{n+1} \cdot \nabla \mathbf{w}_h\right) \nabla p_{n+1} \, \mathrm{d}\Omega - \\
&- \int_{\Omega_e} \tau_1 \left(\mathbf{v}_{n+1} \cdot \nabla \mathbf{w}_h\right) \left(\rho \frac{\mathbf{v}_n}{\Delta t} + \mathbf{f}\right) \, \mathrm{d}\Omega
\end{aligned} \tag{4.22}$$

On the other hand, the following terms are added to Eq. (4.14):

$$\begin{aligned}
&\int_{\Omega_e} \tau_1 \nabla q_h \left(\rho \frac{\mathbf{v}_{n+1}}{\Delta t} + \rho \mathbf{v}_{n+1} \cdot \nabla \mathbf{v}_{n+1}\right) \, \mathrm{d}\Omega + \\
&+ \int_{\Omega_e} \tau_1 \nabla p_{n+1} \nabla q_h \, \mathrm{d}\Omega - \\
&- \int_{\Omega_e} \tau_1 \nabla q_h \cdot \left(\rho \frac{\mathbf{v}_n}{\Delta t} + \mathbf{f}\right) \, \mathrm{d}\Omega
\end{aligned} \tag{4.23}$$

The stabilized governing equations read:

$$\mathbf{M} \frac{\bar{\mathbf{v}}_{n+1} - \bar{\mathbf{v}}_n}{\Delta t} + \left[\bar{\mathbf{K}}\left(\bar{\mathbf{v}}_{n+1}\right) + \mu \mathbf{L} + \mathbf{S}_K\right] \bar{\mathbf{v}}_{n+1} + \left[\mathbf{G} + \mathbf{S}_G\right] \bar{p}_{n+1} = \bar{\mathbf{F}} + \bar{\mathbf{F}}_m \tag{4.24}$$

$$\left[\mathbf{D} + \mathbf{S}_D\right] \bar{\mathbf{v}}_{n+1} + \mathbf{S}_L \bar{p}_{n+1} = \bar{\mathbf{F}}_q \tag{4.25}$$

where the stabilization matrices read:

$$\mathbf{S}_K = s_{K,IJ} = \int_{\Omega_e} \left[\tau_1 \left(\bar{\mathrm{v}}_k \frac{\partial N_I}{\partial x_k}\right) \left(\rho \frac{N_J}{\Delta t} + \rho \bar{\mathrm{v}}_k \frac{\partial N_J}{\partial x_k}\right) + \tau_2 \frac{\partial N_I}{\partial x_k} \frac{\partial N_J}{\partial x_k}\right] \, \mathrm{d}\Omega \tag{4.26}$$

$$\mathbf{S}_G = s_{G,IJ} = \int_{\Omega_e} \tau_1 \left(\bar{\mathrm{v}}_k \frac{\partial N_I}{\partial x_k}\right) \frac{\partial N_J}{\partial x_k} \, \mathrm{d}\Omega \tag{4.27}$$

$$\mathbf{S}_D = s_{D,IJ} = \int_{\Omega_e} \tau_1 \frac{\partial N_I}{\partial x_k} \left(\frac{\rho}{\Delta t} N_J + \bar{\mathrm{v}}_k \frac{\partial N_J}{\partial x_k}\right) \, \mathrm{d}\Omega \tag{4.28}$$

$$\mathbf{S}_L = s_{L,IJ} = \int_{\Omega_e} \tau_1 \frac{\partial N_I}{\partial x_k} \frac{\partial N_J}{\partial x_k} \, \mathrm{d}\Omega \tag{4.29}$$

$$\bar{\mathbf{F}}_m = f_{m,I} = \int_{\Omega_e} \rho g_k \left(\bar{\mathrm{v}}_k \frac{\partial N_I}{\partial x_k}\right) \left(\frac{\rho}{\Delta t} N_I + N_I\right) \, \mathrm{d}\Omega \tag{4.30}$$

$$\bar{\mathbf{F}}_q = f_{q,I} = \int_{\Omega_e} \rho g_k \frac{\partial N_I}{\partial x_k} \left(\frac{\rho}{\Delta t} N_I + N_I\right) \, \mathrm{d}\Omega \tag{4.31}$$

where parameters τ_1 and τ_2 are algorithmic stabilization parameters defined as:

$$\tau = \frac{1}{\dfrac{2 \left\|\bar{\mathbf{v}}\right\|}{h} + \dfrac{4\nu}{h^2}} \tag{4.32}$$

$$\tau_2 = \frac{h^2}{\tau_1} = 2h \left\| \bar{\mathbf{v}} \right\| + 4\nu \tag{4.33}$$

where h is the element size and ν is the kinematic viscosity of the fluid.

Fractional step approach

For reducing the computational cost associated to the solution of the governing system, the fractional splitting is applied. Fractional step or pressure projection approach (see [72], [73] or [119]) uncouples the velocity and the pressure. Instead of one large and poorly conditioned system of equations two smaller and better conditioned systems are solved. Fractional step approach is applied here at a purely algebraic level (according to [74]), splitting the momentum equation Eqs. (4.24) into two parts by introducing the intermediate velocity $\tilde{\mathbf{v}}$.

Following the steps detailed in Section 3.2.2, the original monolithic system given by Eqs. (4.24) and (4.25) is replaced by:

$$\mathbf{M}\frac{\tilde{\mathbf{v}} - \bar{\mathbf{v}}_n}{\Delta t} + \left[\bar{\mathbf{K}}\left(\tilde{\mathbf{v}}\right) + \mu\mathbf{L} + \mathbf{S}_K\right]\tilde{\mathbf{v}} + \left[\mathbf{G} + \mathbf{S}_G\right]\bar{p}_n = \bar{\mathbf{F}} \tag{4.34}$$

$$\mathbf{M}\frac{\bar{\mathbf{v}}_{n+1} - \tilde{\mathbf{v}}}{\Delta t} + \left[\mathbf{G} + \mathbf{S}_G\right]\left(\bar{p}_{n+1} - \bar{p}_n\right) = 0 \tag{4.35}$$

$$\mathbf{D}\tilde{\mathbf{v}} = \left[\Delta t\mathbf{L} - \mathbf{S}_D\right]\left(\bar{p}_{n+1} - \bar{p}_n\right) \tag{4.36}$$

In order to overcome the singularity of the Laplacian matrix $\mathbf{L}$, an essential boundary condition for the pressure ($p = 0$) at Γ_N is specified. Eqs. (4.34), (4.35) and (4.36) define the set of discrete governing equations in the Eulerian domain. The fractional momentum equation is non-linear due to the dependence of the convective term (and the corresponding stabilization terms) upon the unknown velocity. The fixed point iteration method is applied for their solution. Once Eq. (4.34) is solved for the fractional velocity $\tilde{\mathbf{v}}$, pressure $\bar{p}_{n+1}$ is obtained by solving Eq. (4.36) and finally the end-of-step velocity $\bar{\mathbf{v}}_{n+1}$ is obtained using Eq. (4.35).

4.2.3 Finite Element formulation for the liquid

The Lagrangian finite element model for the liquid has been already described in Section 3.2.1. The governing equations are reproduced here for the sake of clarity:

$$\left(\mathbf{M}\frac{1}{\Delta t} + \mu\mathbf{L} + \mathbf{S}_K\right)\bar{\mathbf{v}}_{n+1} + \mathbf{G}\bar{p}_{n+1} = \bar{\mathbf{F}} + \bar{\mathbf{F}}_{\text{int}} + \mathbf{M}\frac{\bar{\mathbf{v}}_n}{\Delta t} \tag{4.37}$$

$$\left(\mathbf{D} + \mathbf{S}_D\right)\bar{\mathbf{v}}_{n+1} + \mathbf{S}_L\bar{p}_{n+1} = \bar{\mathbf{F}}_q \tag{4.38}$$

The force $\bar{\mathbf{F}}_{int}$ in Eq. (4.37) includes the Neumann term due to the interaction with gas (normal and shear stresses as well as surface tension). They are described in detail in Section 4.2.4.

4.2.4 Coupling strategy

Lets us consider the Eulerian and the Lagrangian domains discretized with a finite element mesh. Fig. 4.2(a) shows the overlapping meshes. One can distinguish the boundary of the Lagrangian domain Γ_L and its representation on the Eulerian mesh Γ_I. Note that as the element size $h \to 0$ in both domains, the two boundaries tend to coincide (i.e., $\Gamma_I \approx \Gamma_L$). The embedded interface Γ_I (see black polyline in Fig. 4.2(b)) splits the Eulerian domain into real and fictitious parts Ω_E^r and Ω_E^f, as already mentioned. Nodes and elements contained in Ω_E^r will be denoted *real*, whereas *fictitious* nodes and elements are those contained in Ω_E^f (see Fig. 4.2(b)). Elements cut by Γ_I that contain both the real and the fictitious nodes will be referred as *interface elements*. This is shown in Fig. 4.2(c), where the interface elements are shown in gray, fictitious and real nodes are indicated by black and gray dots, respectively.

To model the interaction of the two sub-domains, a coupling technique must be implemented. A Dirichlet-Neumann coupling is proposed in this work. Effects of water (Lagrangian fluid) onto air (Eulerian fluid) are represented via the Dirichlet boundary condition at Γ_I. The boundary condition ensures the interface condition defined by Eq. (4.7). Effects of air onto water are represented by a Neumann boundary condition applied at the water boundary Γ_L. This boundary condition represents the interface condition defined by Eqs. (4.11) and (4.12).

Dirichlet boundary condition

Fig. 4.2 shows that the interface Γ_I intersects the Eulerian mesh at arbitrary positions. The Dirichlet boundary condition at the interface (i.e., $\mathbf{v}_E = \mathbf{v}_L$ at Γ_I) can be applied in two different manners. First option relies upon dividing the cut Eulerian elements into two new elements. Therefore, the intersection between Γ_L and Eulerian mesh coincide with the introduced nodes. Velocity can be therefore prescribed in these new nodes and the boundary condition is applied in a *strong way*. However, adding new nodes in the Eulerian mesh leads to resizing the global system matrices at every solution step, increasing the computational cost.

An alternative to this option is to apply the Dirichlet boundary condition of the interface in a *weak* sense by minimizing the difference between the velocity of the Lagrangian and Eulerian domain at Γ_L. The Dirichlet boundary condition is therefore applied at the existing fictitious nodes of the interface elements (black dots in Fig. 4.2(c)) according to the approach proposed originally in [120]. The advantage of this option with respect to the previous one is that no degrees of freedom are added and the global matrix structure remains unaltered.

Given the velocity $\mathbf{v}_L$ of water at its boundary, the difference to be minimized is given by (see e.g. [117] or [120] for details):

$$\int_{\Gamma_I} (\mathrm{v}_k^{n+1} - \mathrm{v}_k^{\mathrm{L}}) N_I \, \mathrm{d}\Gamma_I = 0 \tag{4.39}$$

where v_k^{n+1} is the k-th velocity component of the Eulerian domain and $\mathrm{v}_k^{\mathrm{L}}$ represents the velocity of the Lagrangian domain at the interface. Discretizing the velocity (see

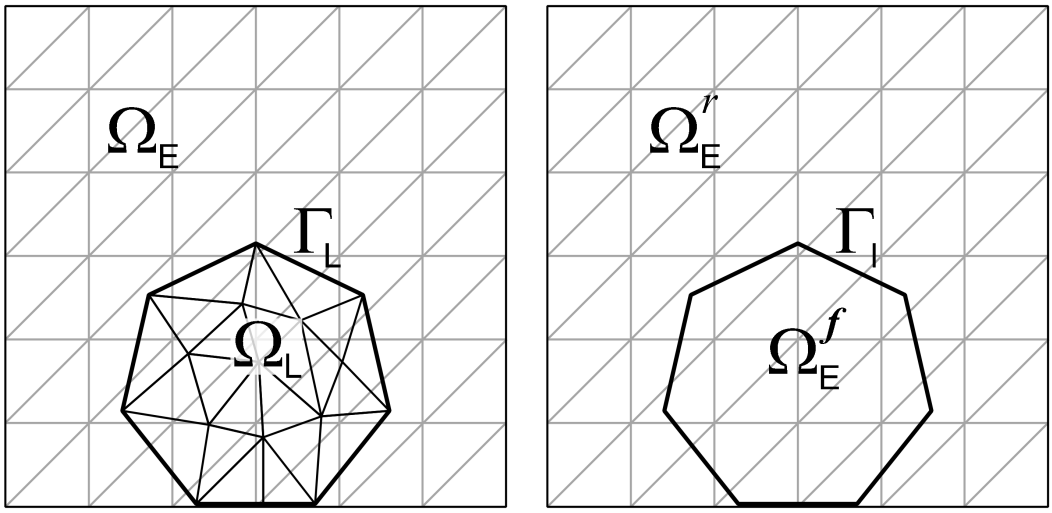

(a) Superimposed discretized domains

(b) Interface on the Eulerian mesh

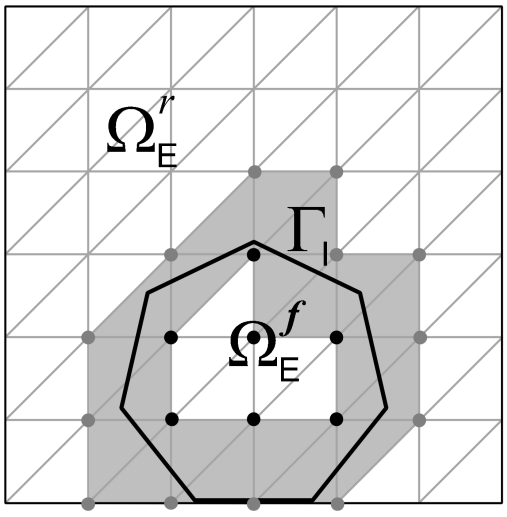

(c) Interface elements

Figure 4.2: Embedded setting: real, fictitious and interface parts of the Eulerian domain

Section 3.2), Eq. (4.39) reads:

$$\mathbf{M}_{\Gamma_I}\bar{\mathbf{v}}_{n+1} = \mathbf{f}_{\Gamma_I} \tag{4.40}$$

where $\bar{\mathbf{v}}_{n+1}$ is the velocity of the nodes of the interface elements and:

$$\mathbf{M}_{\Gamma_I} = m_{\Gamma_I,IJ} = \int_{\Gamma_I} N_I N_J \, \mathrm{d}\Gamma_I \tag{4.41}$$

$$\mathbf{f}_{\Gamma_I} = f_{\Gamma_I,I} = \int_{\Gamma_I} N_I^f \mathrm{v}_k^{\mathrm{L}} \, \mathrm{d}\Gamma_I \tag{4.42}$$

where N_I^f is the shape function of fictitious node I. Considering that the interface elements contain both *real* and *fictitious* nodes (with a certain abuse of notation $\bar{\mathbf{v}}_{n+1} = \bar{\mathbf{v}}^r_{n+1} + \bar{\mathbf{v}}^f_{n+1}$, assuming that the entries in the vectors of the *real* nodal velocities corresponding to the *fictitious* nodes are zero and vice versa[1]), one can rewrite Eq. (4.40) as

$$\mathbf{M}_{\Gamma_I}\bar{\mathbf{v}}^r_{n+1} + \mathbf{M}_{\Gamma_I}\bar{\mathbf{v}}^f_{n+1} = \mathbf{f}_{\Gamma_I} \tag{4.43}$$

which is a constraint that complements Eqs. (4.34), (4.35)) and (4.36) accounting for the motion of the Lagrangian fluid. Eqs. (4.34), (4.35), (4.36) and Eq. (4.43) can be solved in a staggered fashion according to [117] and [118], which is equivalent to treating the constraint explicitly. Velocity at *real* nodes of interface elements (gray dots in Fig. 4.3) is assumed to be equal to the velocity obtained at the previous time step.

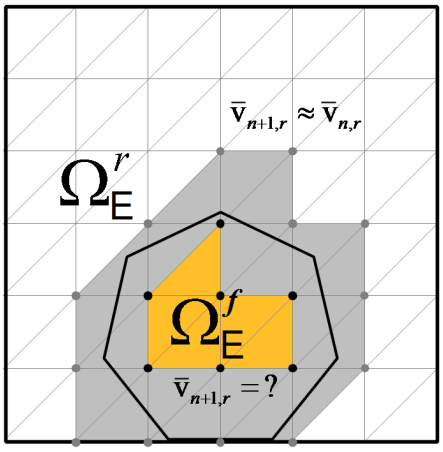

Figure 4.3: Explicit treatment of interface boundary condition for velocity.

This can be expressed as:

$$\mathbf{M}_{\Gamma_I}\bar{\mathbf{v}}^f_{n+1} = \mathbf{f}_{\Gamma_I} - \mathbf{M}_{\Gamma_I}\bar{\mathbf{v}}^r_{n+1} \tag{4.44}$$

$$\bar{\mathbf{v}}^r_{n+1} \approx \bar{\mathbf{v}}^r_n \tag{4.45}$$

[1]for example, let us consider a triangular interface element, whose nodes 1 and 3 are *real* and 2 is *fictitious*. Then $\bar{\mathbf{v}}_r = [\bar{\mathbf{v}}_1, 0, \bar{\mathbf{v}}_3]^T$ and $\bar{\mathbf{v}}_f = [0, \bar{\mathbf{v}}_2, 0]^T$

where n corresponds to the time step index. Solving Eq. (4.44) the velocity at the fictitious nodes (black dots in Fig. 4.3) is obtained. The velocity is applied as the interface Dirichlet boundary condition at the next time step. This boundary condition can be interpreted as the effect of water onto air. Elements with all nodes in Ω_E^f are excluded from the system.

Neumann boundary condition

Interface Neumann boundary condition represents the normal and shear stress components exerted by the gas upon the liquid as well as the surface tension. It corresponds to the interface condition defined by Eqs. (4.9) and (4.10). It is accounted for by the term $\bar{\mathbf{F}}_{int}$ (Eq. (4.46)) in the momentum equation of the liquid (Eq. (4.37)). This term is computed as a sum of the following contributions:

$$\bar{\mathbf{F}}_{int} = \bar{\mathbf{F}}_N + \bar{\mathbf{F}}_{st} + \bar{\mathbf{F}}_{sh} \qquad \text{on } \Gamma_L \tag{4.46}$$

where individual terms have the following expressions:

$$\bar{\mathbf{F}}_N = f_{N,I} = -\int_{\Gamma_L} N_I n_k \, \mathrm{d}\Gamma + \mu_E \int_{\Gamma_L} \left(\frac{\partial N_I}{\partial x_k} + \frac{\partial N_I}{\partial x_l} \right)_E n_k \, \mathrm{d}\Gamma \qquad \text{on } \Gamma_L \tag{4.47}$$

$$\bar{\mathbf{F}}_{st} = f_{ST,I} = -\int_{\Gamma_L} \gamma \kappa N_I n_k \, \mathrm{d}\Gamma \qquad \text{on } \Gamma_L \tag{4.48}$$

$$\bar{\mathbf{F}}_{sh} = f_{sh,I} = \mu_E \int_{\Gamma_L} \left(\frac{\partial N_I}{\partial x_k} + \frac{\partial N_I}{\partial x_l} \right)_E m_k \, \mathrm{d}\Gamma_L \tag{4.49}$$

where vector m is the vector tangent to Γ_L, as shown in Fig. 3.6(a) in Chapter 3. The integrands in the terms $\mathbf{F}_N$ and $\mathbf{F}_{sh}$ are computed in the interface elements of the Eulerian mesh and then are projected onto Γ_L, where the integrals are computed. The surface tension force is computed directly on the Lagrangian mesh. Implementation of the viscous stresses is detailed in the next section.

Viscous stress implementation

Two-dimensional model The viscous stress tensor in two dimensions reads:

$$\boldsymbol{\tau} = \begin{pmatrix} \tau_{xx} & \tau_{xy} \\ \tau_{yx} & \tau_{yy} \end{pmatrix} \tag{4.50}$$

where its components are:

$$\tau_{xx} = 2\mu \frac{\partial u}{\partial x} \tag{4.51}$$

$$\tau_{xy} = \tau_{yx} = \mu \left(\frac{\partial u}{\partial y} + \frac{\partial v}{\partial x} \right) \tag{4.52}$$

$$\tau_{yy} = 2\mu \frac{\partial v}{\partial y} \tag{4.53}$$

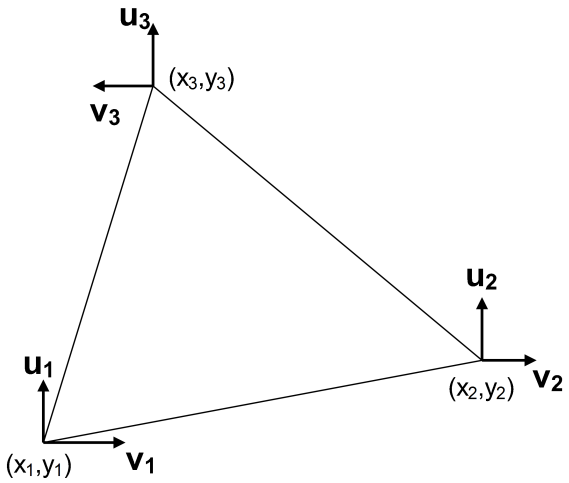

Figure 4.4: Triangular element with linear velocity interpolation

where u and v are the x and y velocity components. One has to find an expression for the velocity derivatives within an element.

Let us consider the linear triangular element shown in Fig. 4.4. Velocity derivatives can be found applying the chain rule:

$$\frac{\partial \mathbf{v}}{\partial \mathbf{x}} = \frac{\partial \mathbf{v}}{\partial \boldsymbol{\xi}} \frac{\partial \boldsymbol{\xi}}{\partial \mathbf{x}} = \frac{\partial \mathbf{v}}{\partial \boldsymbol{\xi}} \mathbf{J}^{-1} \tag{4.54}$$

where $\boldsymbol{\xi}$ represents the isoparametric coordinates (ξ, η), and $\mathbf{J}$ is the Jacobian matrix of first derivatives. The shape functions using this system of coordinates is the following:

$$N_1 = \xi \tag{4.55}$$

$$N_2 = \eta \tag{4.56}$$

$$N_3 = 1 - \xi - \eta \tag{4.57}$$

The Cartesian coordinates (x, y) can be expressed using the isoparametric coordinates as follows:

$$\begin{aligned} x = N_1 x_1 + N_2 x_2 + N_3 x_3 = \xi x_1 + \eta x_2 + (1 - \xi - \eta)\, x_3 = \\ = (x_1 - x_3)\, \xi + (x_2 - x_3)\, \eta + x_3 \end{aligned} \tag{4.58}$$

$$\begin{aligned} y = N_1 y_1 + N_2 y_2 + N_3 y_3 = \xi y_1 + \eta y_2 + (1 - \xi - \eta)\, y_3 = \\ = (y_1 - y_3)\, \xi + (y_2 - y_3)\, \eta + y_3 \end{aligned} \tag{4.59}$$

Considering these expressions, the Jacobian matrix reads:

$$\mathbf{J} = \begin{bmatrix} \frac{\partial x}{\partial \xi} & \frac{\partial y}{\partial \xi} \\ \frac{\partial x}{\partial \eta} & \frac{\partial y}{\partial \eta} \end{bmatrix} = \begin{bmatrix} x_{13} & y_{13} \\ x_{23} & y_{23} \end{bmatrix} \tag{4.60}$$

where $x_{ij} = x_i - x_j$. The inverse of the Jacobian takes the following form:

$$\mathbf{J}^{-1} = \frac{1}{2A} \begin{bmatrix} y_{23} & -y_{13} \\ -x_{23} & x_{13} \end{bmatrix} \tag{4.61}$$

where $A = \frac{1}{2}\det\mathbf{J}$ is the area of the element. The velocity at any point of the element can be obtained as follows:

$$\begin{aligned} u = N_1 u_1 + N_2 u_2 + N_3 u_3 &= \xi u_1 + \eta u_2 + (1 - \xi - \eta)\, u_3 = \\ &= (u_1 - u_3)\, \xi + (u_2 - u_3)\, \eta + u_3 \end{aligned} \tag{4.62}$$

$$\begin{aligned} v = N_1 v_1 + N_2 v_2 + N_3 v_3 &= \xi v_1 + \eta v_2 + (1 - \xi - \eta)\, v_3 = \\ &= (v_1 - v_3)\, \xi + (v_2 - v_3)\, \eta + v_3 \end{aligned} \tag{4.63}$$

Using Eqs. (4.54) and (4.61), the derivatives of the velocity in Cartesian coordinates yields:

$$\begin{pmatrix} \frac{\partial u}{\partial x} \\ \frac{\partial u}{\partial y} \end{pmatrix} = \mathbf{J}^{-1} \begin{pmatrix} \frac{\partial u}{\partial \xi} \\ \frac{\partial u}{\partial \eta} \end{pmatrix} = \frac{1}{2A} \begin{pmatrix} y_{23} u_{13} - y_{13} u_{23} \\ -x_{23} u_{13} + x_{13} u_{23} \end{pmatrix} \tag{4.64}$$

$$\begin{pmatrix} \frac{\partial v}{\partial x} \\ \frac{\partial v}{\partial y} \end{pmatrix} = \mathbf{J}^{-1} \begin{pmatrix} \frac{\partial v}{\partial \xi} \\ \frac{\partial v}{\partial \eta} \end{pmatrix} = \frac{1}{2A} \begin{pmatrix} y_{23} v_{13} - y_{13} v_{23} \\ -x_{23} v_{13} + x_{13} v_{23} \end{pmatrix} \tag{4.65}$$

Finally, the discrete expression for the viscous stress can be obtained by substituting Eqs. (4.64) and (4.65) in Eqs. (4.51)-(4.53).

Three-dimensional model The viscous stress tensor in three dimensions reads:

$$\boldsymbol{\tau} = \begin{pmatrix} \tau_{xx} & \tau_{xy} & \tau_{xz} \\ \tau_{yx} & \tau_{yy} & \tau_{yz} \\ \tau_{zx} & \tau_{zy} & \tau_{zz} \end{pmatrix} \tag{4.66}$$

where its components are:

$$\tau_{xx} = 2\mu \frac{\partial u}{\partial x} \tag{4.67}$$

$$\tau_{xy} = \tau_{yx} = \mu \left(\frac{\partial u}{\partial y} + \frac{\partial v}{\partial x} \right) \tag{4.68}$$

$$\tau_{xz} = \tau_{zx} = \mu \left(\frac{\partial u}{\partial z} + \frac{\partial w}{\partial x} \right) \tag{4.69}$$

$$\tau_{yy} = 2\mu \frac{\partial v}{\partial y} \tag{4.70}$$

$$\tau_{yz} = \tau_{zz} = \mu \left(\frac{\partial v}{\partial z} + \frac{\partial w}{\partial z} \right) \tag{4.71}$$

$$\tau_{zz} = 2\mu \frac{\partial w}{\partial z} \tag{4.72}$$

where u, v and w are the Cartesian components of the velocity. One has to find an expression for the velocity derivatives within an element.

Let us consider the linear tetrahedron element shown in Fig. 4.5. Velocity derivatives can be found applying the chain rule:

$$\frac{\partial \mathbf{v}}{\partial \mathbf{x}} = \frac{\partial \mathbf{v}}{\partial \boldsymbol{\xi}} \frac{\partial \boldsymbol{\xi}}{\partial \mathbf{x}} = \frac{\partial \mathbf{v}}{\partial \boldsymbol{\xi}} \mathbf{J}^{-1} \tag{4.73}$$

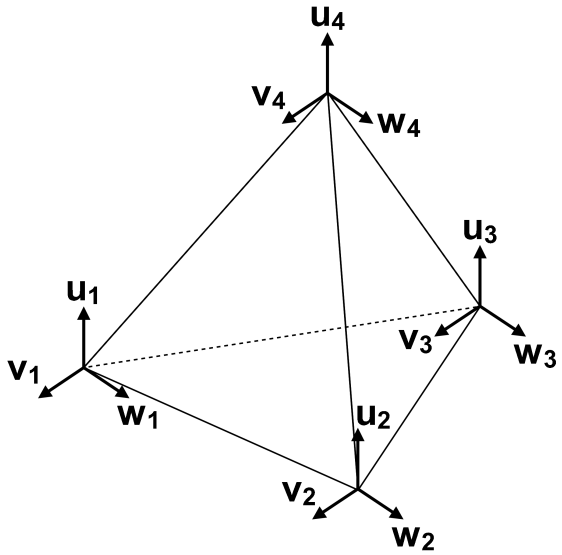

Figure 4.5: Tetrahedron element with linear velocity interpolation

where $\boldsymbol{\xi}$ represents the isoparametric coordinates (ξ, η, ζ). The shape functions using this system of coordinates is the following:

$$N_1 = \xi \tag{4.74}$$
$$N_2 = \eta \tag{4.75}$$
$$N_3 = \zeta \tag{4.76}$$
$$N_4 = 1 - \xi - \eta - \zeta \tag{4.77}$$

Following the same procedure than the two-dimensional model, the derivatives of the velocity in Cartesian coordinates yield:

$$\begin{pmatrix} \frac{\partial u}{\partial x} \\ \frac{\partial u}{\partial y} \\ \frac{\partial u}{\partial z} \end{pmatrix} = \mathbf{J}^{-1} \begin{pmatrix} \frac{\partial u}{\partial \xi} \\ \frac{\partial u}{\partial \eta} \\ \frac{\partial u}{\partial \zeta} \end{pmatrix} = \frac{1}{6V} \begin{pmatrix} J_{11}^{inv} u_{14} + J_{12}^{inv} u_{24} + J_{13}^{inv} u_{34} \\ J_{21}^{inv} u_{14} + J_{22}^{inv} u_{24} + J_{23}^{inv} u_{34} \\ J_{31}^{inv} u_{14} + J_{32}^{inv} u_{24} + J_{33}^{inv} u_{34} \end{pmatrix} \tag{4.78}$$

where $V = \frac{1}{6}\text{det}\mathbf{J}$ is the volume of the element and terms J_{ij}^{inv} correspond to the $i-j$ component of the inverse Jacobian:

$$\mathbf{J}^{-1} = \frac{1}{6V} \begin{bmatrix} y_{24}z_{34} - y_{34}z_{24} & -x_{24}z_{34} + x_{34}z_{24} & x_{24}y_{34} - x_{34}y_{24} \\ -y_{14}z_{34} + y_{34}z_{14} & x_{14}z_{34} - x_{34}z_{14} & -x_{14}y_{34} - x_{34}y_{14} \\ y_{14}z_{24} - y_{24}z_{14} & -x_{14}z_{24} + x_{24}z_{14} & x_{14}y_{34} - x_{24}y_{14} \end{bmatrix} \tag{4.79}$$

Derivatives for components v and w are equivalent to Eq. (4.78).

4.2.5 Solution algorithm

All the necessary elements of the embedded method have been defined so far. The overall algorithm of the air-water problem is presented in this section. Let us consider that at the time step t_n the solution (velocity $\bar{\mathbf{v}}_n$ and pressure $\bar{p}_n$) is known in

both the domains Ω_E and Ω_L. To find the velocity and pressure fields at t_{n+1} the following algorithm is implemented:

1. Solve the water problem using Eq. (3.58) and update the mesh position (Eq. (3.59)).
   Output: new position of the Lagrangian mesh, $\bar{\mathbf{v}}_{n+1}$ $\bar{p}_{n+1}$ in Ω_L^{n+1}

2. Identify the position of Lagrangian domain within the Eulerian one. Identify the interface elements, the *real* and the *fictitious* elements and nodes.
   Output: Γ_I

3. In Ω_E: fix the velocity at the *real* nodes of the interface elements to the known gas velocity: $\bar{\mathbf{v}}_{r,\,n+1} = \bar{\mathbf{v}}_n$.

4. Solve the minimization problem (Eq. (4.44)) obtaining the velocity at the *fictitious* nodes of the interface elements $\bar{\mathbf{v}}_{f,\,n+1}$.
   Fix the velocity at the fictitious nodes (interface Dirichlet b.c.).

5. "Switch off" the fictitious Eulerian elements (Ω_{E_f}).

6. Solve the gas problem (using real part of the Eulerian domain Ω_{E_r}) (Eqs. (4.34), (4.35) and (4.36)) equipped with the interface Dirichlet boundary condition applied to the fictitious nodes.
   Output: velocity and pressure $\bar{\mathbf{v}}_{n+1}$ and $\bar{p}_{n+1}$ in Ω_E^{n+1}.

7. Project the air stresses onto the liquid boundary Γ_L surface and compute the corresponding force term $\bar{\mathbf{F}}_{int}$ (Eq. (4.46)) for the momentum equation of the liquid (Eq. (4.37)).

8. Go to next time step

An iterative version of the coupled scheme is obtained by repeating steps 1-7 until convergence in terms of the velocity of the Lagrangian boundary nodes of Γ_L is achieved to the required precision ϵ:

$$\frac{\|\delta\bar{\mathbf{v}}\|}{\|\bar{\mathbf{v}}_{n+1}\|} < \epsilon \tag{4.80}$$

4.3 Examples

4.3.1 Static droplet

The first example models a circular liquid droplet (Lagrangian fluid L) immersed into gas (Eulerian fluid E) at rest. The surface tension force is the only acting force and gravity is neglected ($g = 0$). Both fluids have equal densities ($\rho_E = \rho_L = 1$ kg m^{-3}), viscosities ($\mu_E = \mu_L = 1$ kg m^{-1} s^{-1}) and the corresponding surface tension coefficient is $\gamma = 1$ N m^{-1}. The domain is defined by a square of 1×1 m filled with gas E, and a circular droplet of liquid L with radius $R = 0.25$ m at the center of the domain. The whole domain is meshed using triangular elements of size $h = 1/25$ m. According to the Laplace-Young equation, the pressure jump across the interface

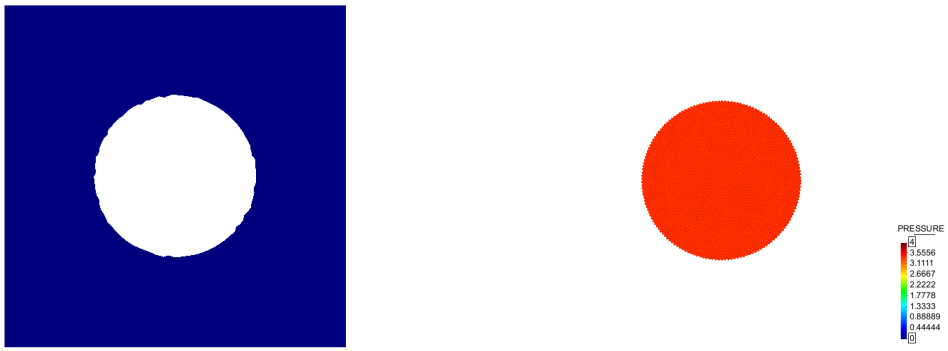

(a) Eulerian domain (b) Lagrangian domain

Figure 4.6: Pressure field at the final time step

between the liquid and the surrounding gas is $\Delta p = \gamma/R = 4$ Pa at the steady state. The result of the simulation of 1 s with a time step of 0.01 s is shown in Fig. 4.6.

Fig. 4.7(a) shows the pressure profile across the middle section of the domain. The purely Lagrangian multi-fluid formulation proposed in [3] has been implemented to compare results with the analytical solution and the present embedded method.

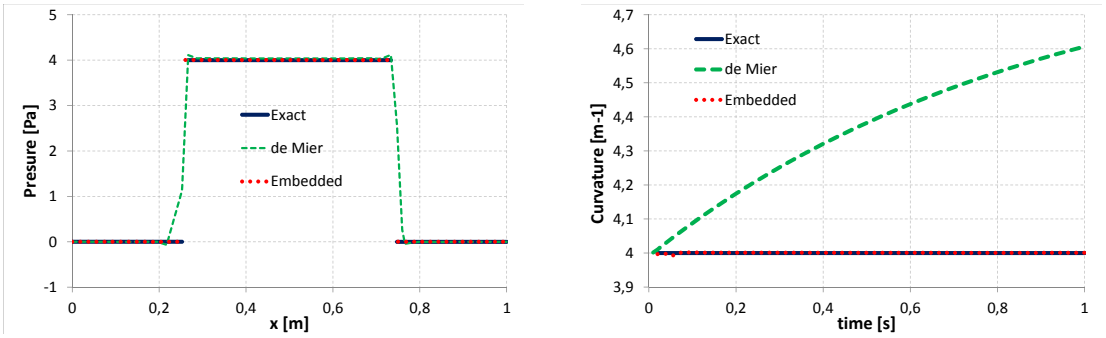

(a) Pressure profiles across the middle section (b) Evolution of curvature over time

Figure 4.7: Comparison between the fully Lagrangian formulation ([3]), the embedded method and the analytical solution. $p_E^{init} = 0$ Pa

Results show that the pressure profile obtained with the presented method has better agreement with the exact solution than the one obtained with the fully Lagrangian formulation. The pressure discontinuity at the interface is represented exactly when using the present method.

De Mier [3] shows that if the pressure discontinuity is modeled by a continuous approximation with steep gradient, the steady state solution exhibits spurious velocities at the interface because the pressure gradient term dominates in the governing equation. This effect can be seen in 4.7(a), where the pressure discontinuity is approximated by a continuous steep change across the interface elements. One can also observe slight under and over-shoots of pressure in the results corresponding the fully Lagrangian method [3]. The corresponding spurious velocities, in turn, lead to temporal evolution of curvature (which, according to the analytical solution must be constant). Thus the solution deviates from the exact one (constant). Fig. 4.7(b) shows the evolution of the curvature at an interface node with coordinates

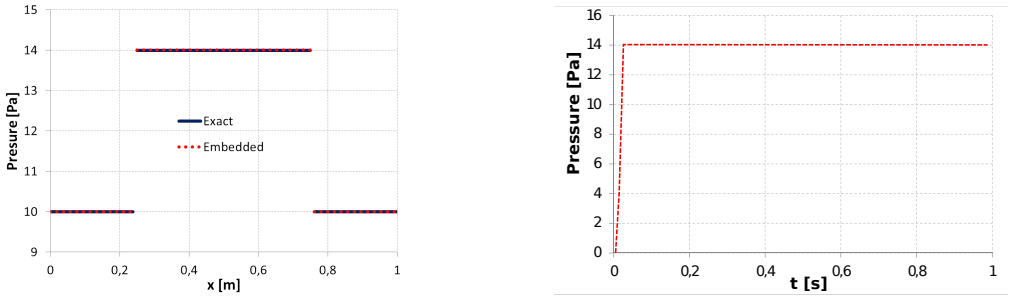

(a) Pressure profiles across the middle section (b) Evolution of pressure at an inner node

Figure 4.8: Results for the non-zero initial pressure in the gas phase ($p_E^{init} = 10$ Pa)

$(0.5, 0.75)$ according to both models. The result obtained with the embedded formulation shows perfect agreement with the exact solution. In the fully Lagrangian formulation, degrees of freedom should be duplicated at interface nodes in order to alleviate steep pressure gradient effects, as proposed in [106].

Different initial conditions

Next, the example is examined under different initial conditions. A non-zero initial pressure (10 Pa) is applied in gas E. Zero initial pressure in liquid L is maintained. According to Laplace-Young equation, the pressure jump must remain $\Delta p = p_L - p_E = \gamma/R = 4$ Pa at the steady state. To achieve this value the pressure in liquid L must increase up to 14 Pa. Fig. 4.8(a) shows that the simulation results coincide with the analytical solution.

4.3.2 Oscillation of a droplet levitated by an airflow

In this section the behavior of a droplet exposed to an airflow is studied. This example was studied by Bouwhuis et al. [85]. A liquid droplet is immersed in a rectangular channel of 10 mm width. The initial shape of the droplet is a circle of 2 mm radius. A constant air flux is generated at the bottom of the channel. A schematic representation of the test case is shown in Fig. 4.9. The data is taken from [85].

For a given set of parameters the droplet levitates on top of the air cushion. At the beginning, the droplet tends to approach the channel bottom. As the droplet descends, the air velocity and pressure increase (the cushion is created) producing the desired effect of levitation.

The parameters describing the behavior of the droplet can be combined into 3 dimensionless numbers: the Bond number Bo (accounting for gravity against surface tension effects), the capillary number Ca (gas viscosity against surface tension) and

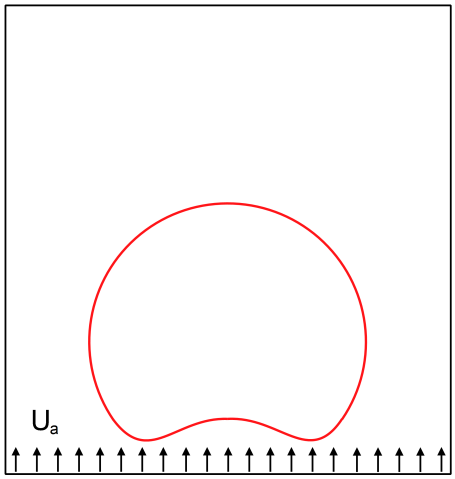

Figure 4.9: Drop levitated by an airflow entering the domain with uniform velocity U_a

the ratio between the dynamic viscosity of the gas and the liquid, Λ:

$$Bo = \sqrt{\frac{\rho_L R^2 g}{\gamma}} \tag{4.81}$$

$$Ca = \frac{\mu_E u_E}{\gamma} \tag{4.82}$$

$$\Lambda = \frac{\mu_L}{\mu_E} \tag{4.83}$$

where R is the unperturbed droplet radius and μ_L and μ_E are the liquid and gas viscosities, respectively. The simulation was performed for $Bo = 1$, $Ca = 2.5 \times 10^{-4}$, $\Lambda = 11 \times 10^3$. The time step used in the simulations was 10^{-5} s.

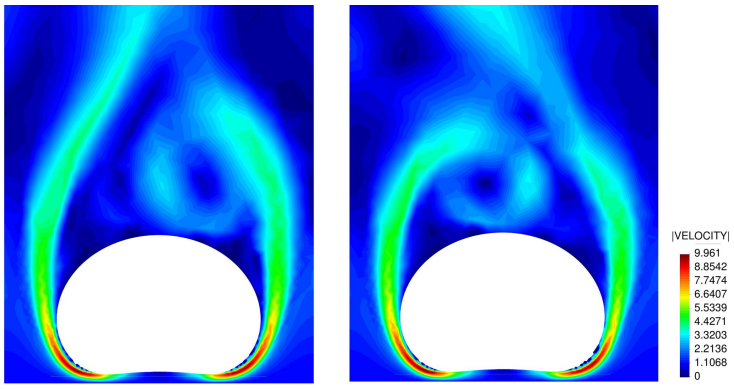

(a) t = 65 ms (b) t = 75 ms

Figure 4.10: Velocity field in the air domain

Fig. 4.10 shows the velocity pattern in the air domain. One can see the non-steady oscillatory nature of the airflow. In the present work the dynamic simulation

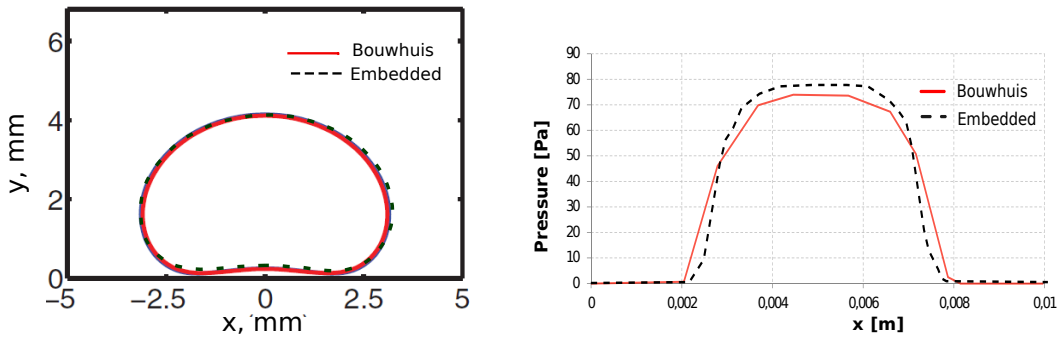

(a) Droplet shape

(b) Pressure profile in the air

Figure 4.11: Drop exposed to airflow

Table 4.1: Summary of the frequencies and "chimney" heights obtained in scenarios 1-3.

Set	f_x [Hz]	h_c [mm]
1	135	0.0985
2	120	0.2376
3	-	-

was performed for both the gas and the liquid, while in [85] the inertial effects in the gas were neglected.

The mean droplet shape after the onset of the periodic oscillations and the corresponding air pressure across the "cushion" are shown in Fig. 4.11. Results are compared against the ones of [85].

The "chimney" effect is observed as expected (an air bubble develops below the drop and pierces the center of the droplet). The maximum pressure gradient coincides with the neck position. The obtained pressure distribution and the droplet shape closely resembles the results in [85].

In order to provide several reference results for the dynamic simulation, the test was carried out for 3 other sets of data:

- Set 1: $Bo = 0.8$, $Ca = 1.25 \times 10^{-5}$, $\Lambda = 5.5 \times 10^3$
- Set 2: $Bo = 0.8$, $Ca = 2.5 \times 10^{-5}$, $\Lambda = 5.5 \times 10^3$
- Set 3: $Bo = 0.8$, $Ca = 5 \times 10^{-4}$, $\Lambda = 5.5 \times 10^3$

For each case, the oscillations in x and y directions and the evolution of droplet's deformed shape are examined. The maximum displacements' evolution of the droplet surface is displayed in Fig. 4.12. The corresponding oscillation frequencies and the "chimney" heights are summarized in Table 4.1.

Fig. 4.12 shows that the droplet reaches the stable periodic oscillatory state for Sets 1 and 2. For Set 3, the droplet exhibits oscillation instability leading to a non-convergent solution. This confirms the result of [85], where the continuous growth of the oscillation amplitude and subsequent instability were reported.

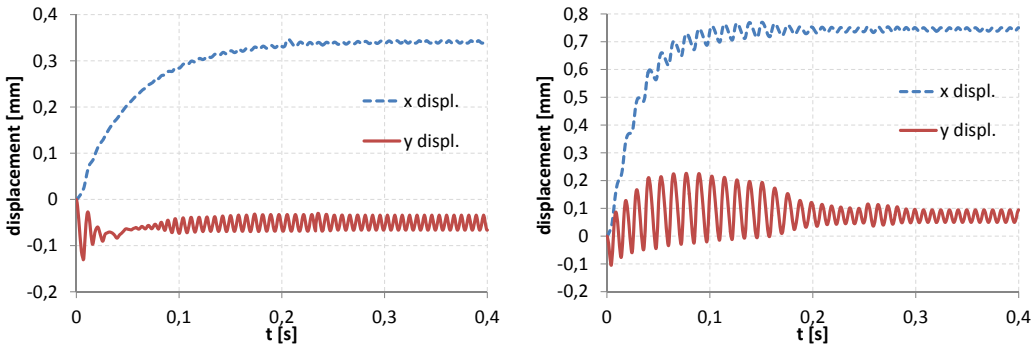

(a) Set 1

(b) Set 2

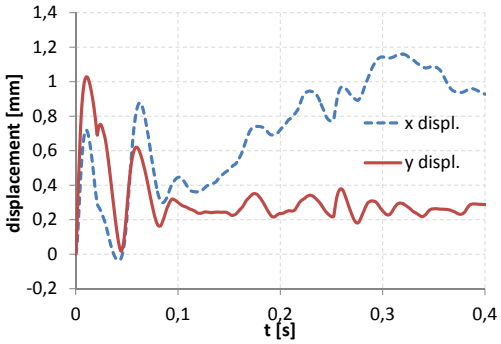

(c) Set 3

Figure 4.12: Vertical and horizontal displacements of the droplet's surface

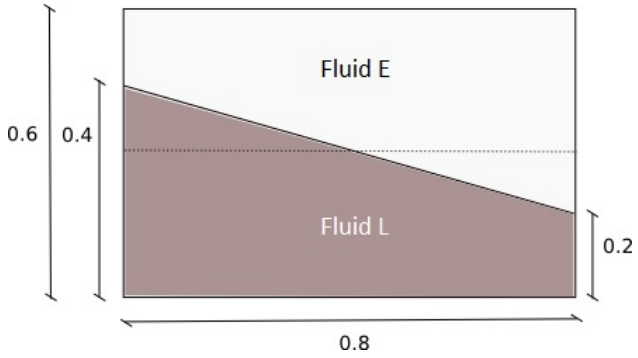

Figure 4.13: Two-fluid sloshing model (in meters)

4.3.3 Two-fluid sloshing

Two previous examples dealt with the problems where the effect of surface tension was dominating and the liquid domain was not undergoing severe deformations. Next, the embedded method is tested in application to the case where gravitational effects are dominating, the domain undergoes severe deformations and the surface tension effects are negligible.

This numerical test for two-fluid problems was proposed originally by Tezduyar et al. in [121], studied in detail by Cruchaga et al. [4], [122] and recently by de Mier [3]. The computational domain consists of a closed container with the dimensions 0.8×0.6 m. The container is filled with two immiscible fluids, the lighter one being on top of the heavier one. The initial, inclined interface is linear with an average height of 0.3 m. The fluid properties used in [121] are taken here as the reference parameters. The top fluid has density $\rho_L = 1$ kg m^{-3}, the dynamic viscosity is constant $\mu_E = \mu_L = 10^{-3}$ Pa s in both fluids, and the gravity acceleration is set to $g = -0.294$ m s^{-2} in the vertical direction. The density value of the bottom fluid is varied. A no-slip condition is set at the horizontal walls, while at the vertical walls a slip condition is prescribed. Following the proposal of de Mier [3] the slip condition in the Lagrangian domain is modeled by considering viscosity $\mu_L = 0$ at the elements encountered in contact with the wall.

Partitioning validation Prior to considering fluids with different densities, we test the capability of the proposed partitioned approach in representing the hydrostatic case ($\rho_E = \rho_L = 1$ kg m^{-3}). The corresponding exact solution is zero velocity in the entire domain and the hydrostatic pressure distribution.

Before the coupling is applied, a non-zero velocity arises at the interface and the pressure distribution is different from the hydrostatic one. However, the exact hydrostatic solution is recovered already in the first time step (see Fig. 4.14). The time step size used in the simulation is set to 0.01 s.

Time accuracy The convergence rate is assessed by measuring the absolute error in the velocity as a function of time step size for the hydrostatic case. Four time step sizes have been considered: dt=0.1 s, dt=0.01 s, dt=0.003 s, dt=0.001 s. Convergence of the time approximation is displayed in Fig. 4.15. The diminishing of

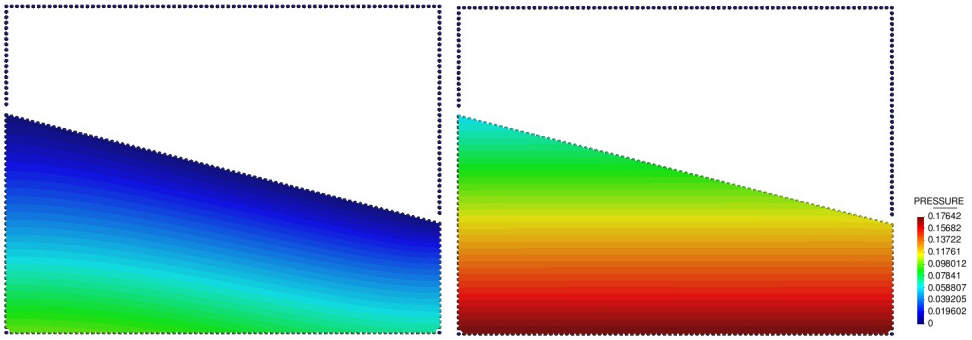

Figure 4.14: Pressure field in the Lagrangian domain for the density ratio 1:1. Prior to the application of the coupling (left) and after applying the coupling (right).

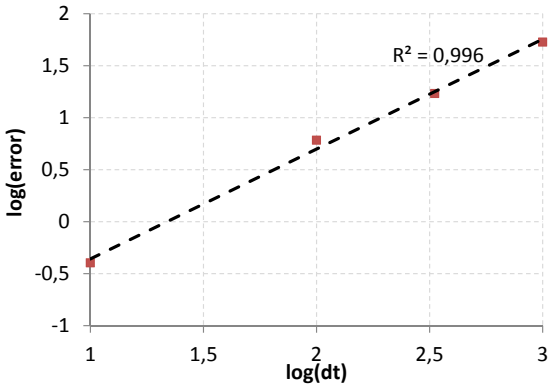

Figure 4.15: Error at $t = 0.5$ s against time step

the error with decreasing the time step is plotted. The error has been computed as the sum of the nodal errors at time $t = 0.5$ s:

$$\text{error} = \sum_n \left\| \mathbf{v}_y - \mathbf{v}_y^{exact} \right\|$$

where n is the number of nodes. Since the exact solution of the problem is the zero velocity in the entire domain, the error is simply the sum of nodal velocities.

One can see that the proposed method exhibits linear convergence rate.

Fluids with different densities Next, two fluids with different densities are considered. The densities of the bottom and the top fluids are $\rho_L = 2$ kg m^{-3} and $\rho_E = 1$ kg m^{-3}, respectively. The unstructured uniform triangular FE meshes with approximately 20000 elements and the time step size of $dt = 0.005$ s have been used if not mentioned otherwise. Fig. 4.16 displays the pressure fields at different time instances for each domain. The Eulerian and the Lagrangian domains are juxtaposed.

Pressure distribution along the vertical cut made at the end of the simulation ($t = 100$ s) is shown on Fig. 4.17. One can see the continuous pressure and the discontinuous pressure gradient at the interface due to density change. The pressure distribution is hydrostatic at the steady state.

Fig. 4.19(a) shows the evolution of the relative height of the interface ($h_{rel} =$

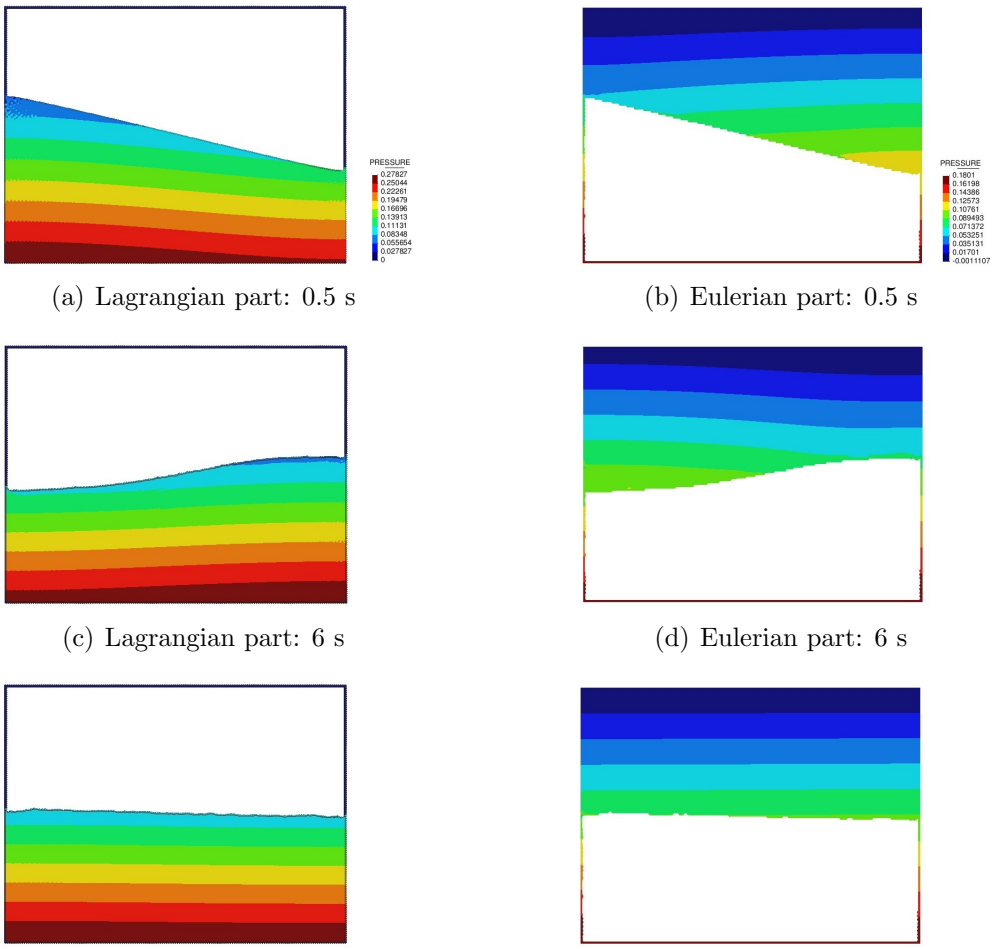

(a) Lagrangian part: 0.5 s

(b) Eulerian part: 0.5 s

(c) Lagrangian part: 6 s

(d) Eulerian part: 6 s

(e) Lagrangian part: 21 s

(f) Eulerian part: 21 s

Figure 4.16: Pressure contours for two-fluid sloshing with density ratio 2:1

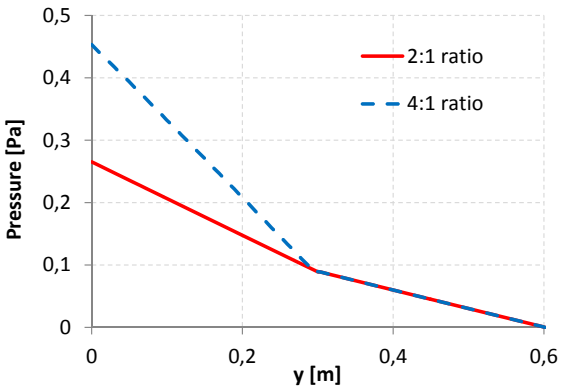

Figure 4.17: Pressure along the height (x=0.4 m) at time=0.5 s

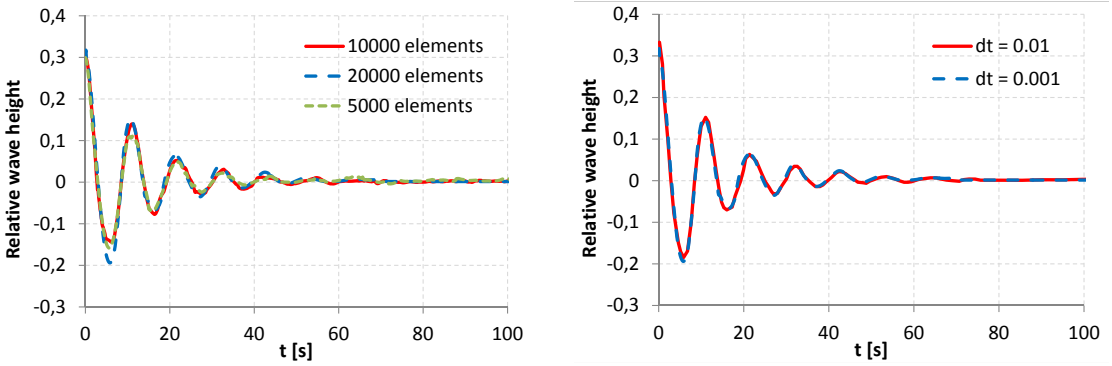

(a) Different mesh resolutions (b) Explicit vs. iterative

Figure 4.18: Liquid wave height at the left wall using different mesh sizes and time steps. Density ratio 2:1

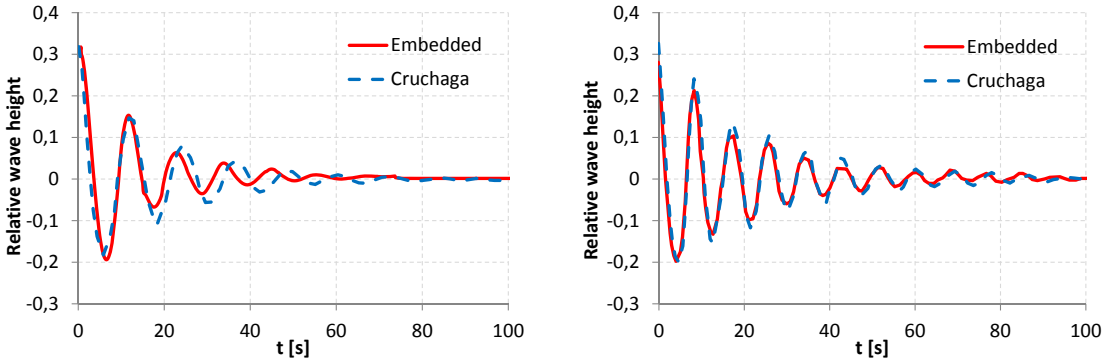

(a) Density ratio 2:1 (b) Density ratio 4:1

Figure 4.19: Liquid wave height at the left wall compared to reference [4]

$\frac{h-0.3}{0.3}$. where h_{rel} and h are the relative and absolute interface heights, respectively) at the left vertical wall, comparing the results obtained using the present formulations with the ones found in literature [4]. One can see a good agreement both in the amplitude evolution and the frequency. However, slight difference (around 10 %) in the period of oscillation is observed for this case. It is worth mentioning that Cruchaga et al. observed a slightly lower period of oscillation when their method was applied without the mass correction technique (see e.g. p. 8 in [4]). No mass correction was applied in the present work.

Fig. 4.18(a) displays the comparison of the solutions obtained using three different meshes (5000, 10000 and 20000 elements). One can observe convergent solution. The solution obtained with the iterative version of the coupling (convergence tolerance was set to $\epsilon = 10^{-6}$) is compared with the staggered one. Comparison of the solutions obtained using time steps is shown in Fig. 4.18(b).

The same example is examined next, increasing the liquid density to $\rho_L = 4$ kg m^{-3} and maintaining the gas density as $\rho_E = 1$ kg m^{-3}. Fig. 4.19(b) shows the evolution of the relative height of the interface at the left vertical wall (comparison with the results reported in [4]). In this case, oscillation amplitude, frequency, and the time it takes to reach the equilibrium position have increased with respect to

the 2:1 density ratio exmaple. One can see a very good agreement with the results found in [4].

In application to this example, the embedded approach allowed to avoid:

- interface distortions faced in the purely Lagrangian multi-fluid formulations (see e.g. p. 71 in [3])
- necessity of using discontinuous pressure shape functions or enrichment for representing the pressure gradient discontinuity

It is worth mentioning that the interface height at the steady state is coinciding with the theoretical one (0.3), giving an insight of a good overall mass conservation of the method. The volume change encountered at $t = 100$ s for the meshes containing 5000 and 20000 elements is of order of around 2% and 0.5%, respectively.

4.4 Conclusions

An embedded formulation for gas-liquid systems based upon a combination of the Eulerian and the Lagrangian formulations has been presented in this chapter. Gas is modeled by the Eulerian formulation, while the Lagrangian one is adopted for the liquid. The fluids are coupled using a Dirichlet-Neumann coupling. The interface Dirichlet boundary condition is satisfied in an integral sense minimizing the velocity difference of the two fluids across the interface. This condition is applied at the fictitious nodes of the interface elements of the Eulerian mesh. Normal and shear stresses in the gas phase projected onto Lagrangian boundary mesh as well as the surface tension provide Neumann boundary condition for the liquid surface. Staggered approach for the solution of the coupled problem has been adopted. An important advantage of the proposed embedded approach is that the interface position is exactly defined by the Lagrangian mesh. The interface maintains itself sharp without diffusion along time. The weak/strong pressure discontinuity along the interface due density change/surface tension is naturally accounted for by the method. Moreover, no interface breakups typical for the fully Lagrangian approaches occur.

The formulation is particularly advantageous for the problems where the gas phase constitutes the major part of the overall computational domain (such as air-water systems encountered in PEFC gas channels). This allows to take the maximum advantage of the Lagrangian description for the liquid with changing boundaries while not increasing considerably the overall computational cost due to re-meshing or the use of the coupled velocity-pressure scheme.

Several test computations have been carried out to evaluate the performance of the method. The formulation leads to stable solutions for a wide range of the density ratios of the fluids involved. It has been found that for the staggered version of the formulation is first order accurate in time. Viscous stress in the coupling is essential in the problems dealing with droplets exposed to the air flux.

The main advantages of the formulation are

- Modular approach
- Natural representation of the pressure discontinuity across the interface

- Application of Dirichlet boundary condition in an integral way using the fictitious nodes of the interface elements
- Additional techniques (typical for fully Eulerian formulations) for interface tracking are not necessary
- Absence of problems with interface preservation (typical for the purely Lagrangian multi-fluid formulations)
- Good mass conservation

Keeping in mind all the advantages of the formulation, it is important to note that it also has some limitations. For optimal functionality of the method the mesh sizes of the involved domains should be similar. This precludes the use of highly heterogeneous meshes. Time step size is generally restricted due to the danger of the element inversion faced in the method used for the liquid in the present work. Modeling the liquid domain using a novel Lagrangian explicit stream-line temporal integration [123] is a promising alternative that must be studied in the future for alleviating zero-Jacobian restriction. While keeping the overall *architecture* of the approach proposed here, this alternative Lagrangian formulation may lead to considerable advantages in computational efficiency.

Chapter 5

Analysis of droplet-gas interactions in a PEFC channel using an embedded formulation

This chapter is devoted to the study of droplet dynamics in a PEFC gas channel using the models proposed in Chapters 3 and 4. As previously mentioned, the semi-analytical model presented in Chapter 2 is restricted to droplet flow regime. The embedded method can be used to perform simulations of water injection into a PEFC gas channel under any condition. Thus, simulations of droplet, film and slug flow, often encountered in an operating PEFC, can be performed.

The aim of this study is to model and validate the conditions that lead to droplet detachment in gas channels, as well as slug or film formation. Critical variables that affect fuel cell performance, such as critical air velocity leading to detachment, droplet size and area coverage of water are calculated. These variables provide with valuable information that can be used to predict fuel cell performance and durability.

5.1 Introduction

This thesis focuses on Polymer Electrolyte fuel cells (PEFC), highly promising efficient energy conversion devices suitable for a wide range of applications. From the engineering point of view, their design and modeling are a challenge. In the present work the emphasis is given to the two-phase transport responsible for non-uniform gas distribution and large pressure losses [22]. As explained in Chapter 1, the exceeding water produced in the cathode side of the membrane has to be evacuated through the GDL (Fig. 5.1(a)) and the cathode gas channels (Fig. 5.1(b)).

Three types of liquid flow can form in the gas channels depending on different factors. These flows are usually known as droplet, film and slug flow [2], as shown on Fig. 1.3. This chapter is devoted to study droplet emergence, deformation and conditions that lead to detachment in a PEFC gas channel using the formulations presented in Chapters 3 and 4. Droplet detachment depends on several factors, such as air velocity, GDL hydrophobicity and water injection rate [15], [16]. Effects of these variables on droplet deformation and detachment are studied.

Moreover, it is also important to identify the conditions that lead to slug or film

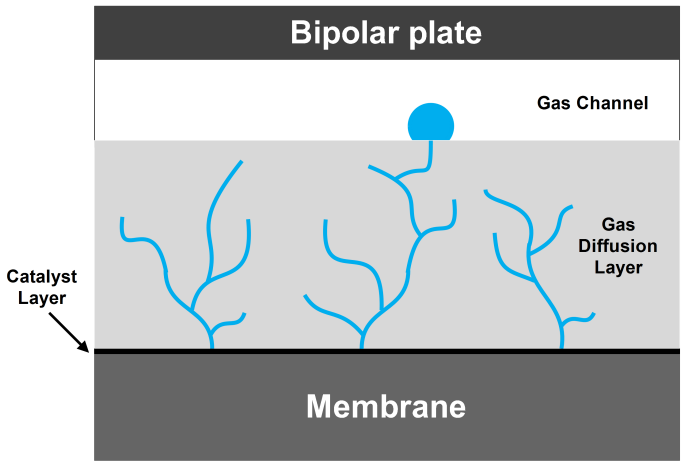

(a) Exceeding water produced in the membrane diffuses through the GDL

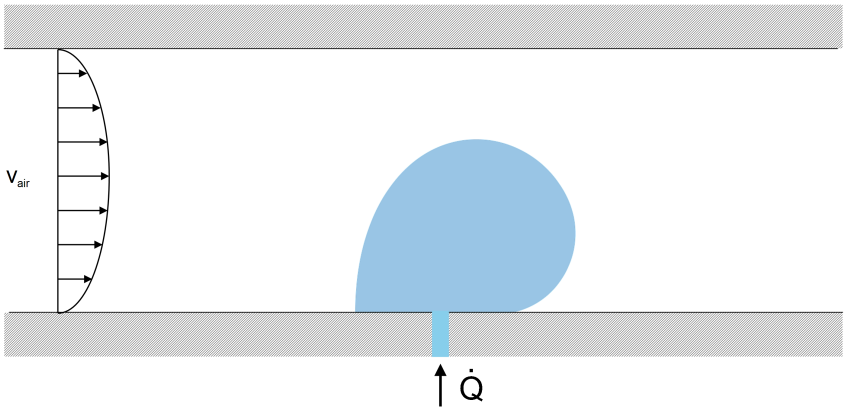

(b) Water droplet emerging into a fuel cell gas channel

Figure 5.1: (a) Exceeding water produced within the membrane diffuses through the GDL and emerges into the gas channel and (b) detailed view of gas channel with an emerging droplet and air flowing from left to right

formation in gas channels. The presence of slugs in gas flow channels leads to large pressure losses. On the other hand, films covering the GDL surface prevent air from diffusing through the pores, leading to non-uniform gas distributions. These factors can reduce both fuel cell efficiency and durability. Thus, it is vital to characterize the effects of process parameters, such as air velocity or water volume flow rate, on droplet, slug and film formation.

5.2 Results and discussion

In order to study water transport in PEFC gas channels and obtain results on droplet deformation, detachment and GDL area coverage, which represent important factors for fuel cell performance and durability, three cases are studied:

- Sessile droplet in free space: when droplet height to channel height ratio is less than 10%, effects of channel height are negligible and the gas channel can be modeled as an open channel with infinite height [11]. This flow type can appear under low current density conditions (i ¡ 0.1 A cm^{-2}).

- Sessile droplet in a channel: when the height ratio is greater than 10%, droplet deformation and detachment depends on this ratio and inlet air velocity. When the current density values are between 0.1 and 0.4 A cm^{-2}, these larger droplets may form in fuel cell channels.

- Droplet injection in a channel: for a given air velocity, slug or film flow can be observed depending on the injection rate of water. Slugs or films are observed when i ¿ 0.4 A cm^{-2}.

The previous cases represent the different kinds of flow types found in operating fuel cells. The governing equations for air and water are the Navier-Stokes equations. Droplet is modeled using a Lagrangian method while air is modeled with the Eulerian formulation. These are coupled using an embedded strategy presented in Chapter 4. The computational domain for the three cases of study is similar, with different boundary conditions and channel sizes in each example. Let us consider a rectangular channel of $H \times L$ in two dimensions (Fig. 5.2(a)) and $H \times W \times L$ in three dimensions (Fig. 5.2(b)). Air enters into the channel through the inlet, Γ_E^{in}, and flows in the positive x-direction. A no-slip boundary condition for air velocity is applied on the GDL surface, Γ_E^{GDL}, and zero viscous stress in the normal direction is imposed at the outlet Γ_E^{out} (i.e., the outlet of the channel is considered an open boundary). The channel has the sufficient length to ensure that results do not depend on this parameter.

On the other hand, a water droplet is considered to occupy the central position of the channel. The air-water interface is represented by Γ_I (Fig. 5.2), whereas Γ_S denotes the wet area of the GDL (i.e., GDL surface covered by water). The center of Γ_S contains the region Γ_S^{in}, representing a circular pore with diameter D. The distance between the pore and channel inlet is sufficiently big to avoid entrance effects [6] and air velocity profile is fully developed before the droplet's position. A slip boundary condition for water velocity is applied at Γ_S. Fluids' properties that

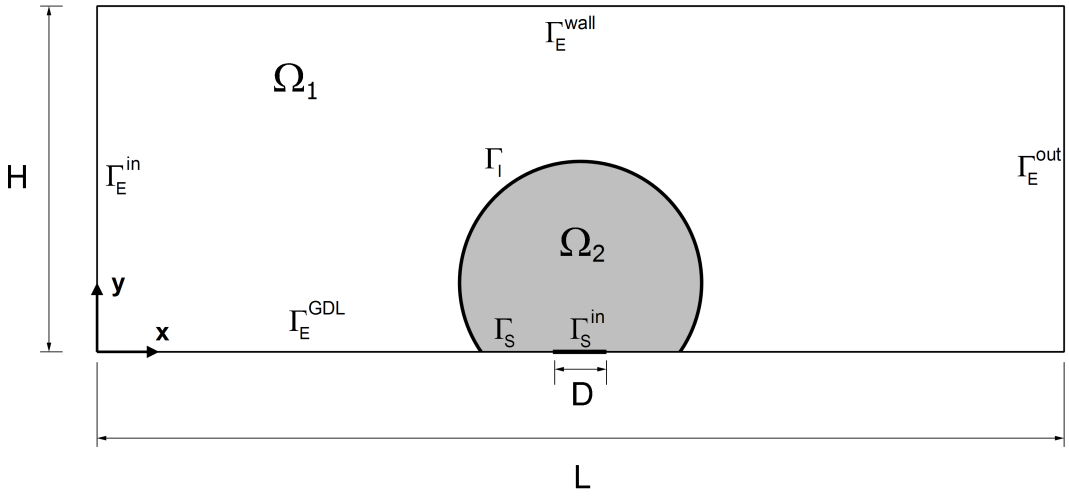

(a) 2D view of the channel

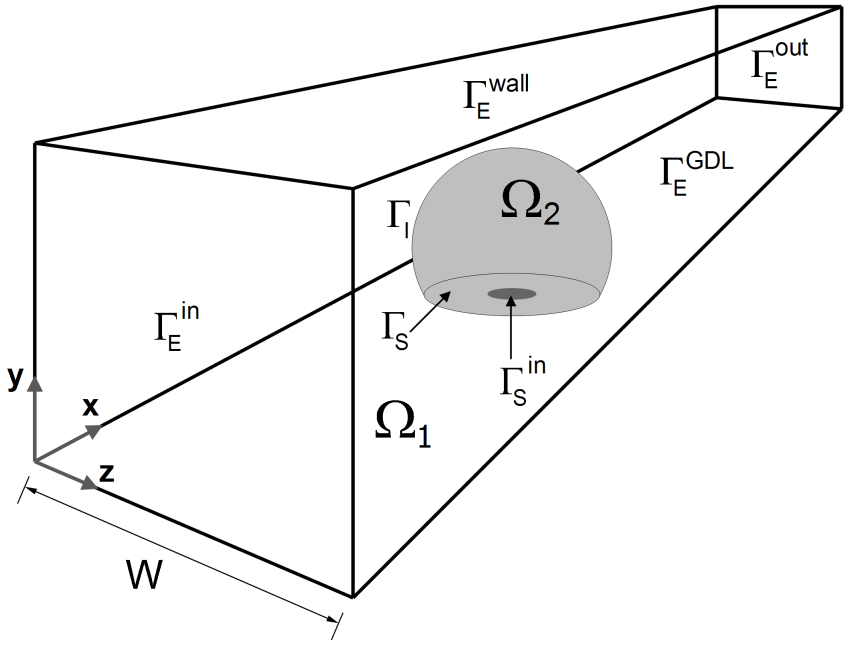

(b) 3D view of the channel

Figure 5.2: Schematic representation of a water droplet in a PEFC gas channel in two (top) and three dimensions (bottom)

Table 5.1: Water and air properties used in the simulations, considering $T = 298$ K and $p = 1$ atm

Variable	Symbol	Value	Units
Surface tension coefficient	γ	0.072	N m^{-1}
Water density	ρ_{w}	1000	kg m^{-3}
Water viscosity	μ_{w}	10^{-3}	kg m^{-1} s^{-1}
Air density	ρ_{air}	1.205	kg m^{-3}
Air viscosity	μ_{air}	1.98×10^{-5}	kg m^{-1} s^{-1}

have been used in the examples are displayed in Table 5.1. These values correspond to a constant temperature of 298 K and a pressure of 1 atm.

5.2.1 Sessile droplet in a free space

Droplet oscillation has been studied since the mid-1800s. Early works of Lord Rayleigh and Lamb [79] on free drop oscillation revealed that surface tension and inertial forces produced a balancing-unbalancing process, yielding drop oscillations. Recent studies on droplet dynamics in PEFC show that oscillations are responsible for droplet detachment [5], [11], [16], [24].

A review on droplet oscillation can be found in Chapter 5 of Milne's work [5]. This review is focused on constrained droplet oscillation (i.e., sessile droplets on surfaces). When a constrained droplet oscillates, surface oscillation is coupled to oscillation of the center of mass [5]. Thus, in the following examples droplet oscillations will be measured by the displacements of the center of mass in x and y directions.

In this example, the frequency of oscillation of a sessile droplet subjected to an airflow is studied. Milne [5] developed an experimental work to observe these oscillations. In the experimental setup a droplet was placed on a Teflon surface, and this setup was placed in a wind tunnel of 470×927×216 mm (height × length × width). Droplet oscillations were obtained with airflow a velocity that was increased from 0 to 30 m s^{-1}. For different droplet volumes, the frequency of oscillation was observed. This example reproduces the experimental results obtained by Milne.

Drag force exerted by air on a sessile droplet does not depend on channel dimensions if the droplet height is below 10% of the channel height [11]. Droplet volumes ranging from 13 to 100 μl are considered. The maximum droplet height, corresponding to a volume of 100 μl, is 4.7 mm. Thus, channel height is set to 50 mm in order to fulfill the aforementioned condition. The droplet is considered to have a constant volume with zero volume flow rate ($\dot{Q} = 0$). Boundary conditions for the air are the following:

- Dirichlet boundary condition at Γ_E^{in} with $\mathbf{v}_{\mathrm{air}}^0 = \mathbf{v}_{\mathrm{air}}(0)$ and $\mathbf{v}_{\mathrm{air}}^{st} = \mathbf{v}_{\mathrm{air}}(t_{st})$
- No-slip boundary condition at Γ_E^{GDL}, $\mathbf{v}_{\mathrm{air}} = 0$
- Slip boundary condition at Γ_E^{wall}, $\mathbf{v}_{\mathrm{air}} \cdot \mathbf{n} = 0$

Table 5.2: Parameters used in the sessile droplet in a free space example

Variable	Symbol	Value	Units
Static contact angle	θ_S	135	deg
Initial air velocity	$\mathbf{v}_{air}^0$	1	m s^{-1}
Steady-state air velocity	$\mathbf{v}_{air}^{st}$	6	m s^{-1}
Channel height	H	50	mm
Channel width	W	50	mm
Channel length	L	500	mm

Slip boundary condition on the upper wall of the channel is imposed in order to recreate the wind tunnel flow conditions. Channel size as well as flow parameters are detailed in Table 5.2. Channel geometry has been discretized using an unstructured mesh of 20000 triangular elements (Fig. 5.3(a)). The mesh has been refined in the region of the channel where the droplet is placed, as shown in Fig. 5.3(b). Element sizes range from $h = 10^{-2}$ m to $h = 10^{-4}$ m. Droplet mesh is unstructured with 1000 triangular elements. Element size is constant, ranging from $h = 10^{-4}$ (13 μl-volume droplet) to $h = 3 \times 10^{-4}$ m (100 μl-volume droplet). Fig. 5.3(c) shows the mesh used for the 13 μl-volume droplet. Simulations have been performed with a time step $\delta t = 10^{-3}$ s, and the simulation time is 1 s.

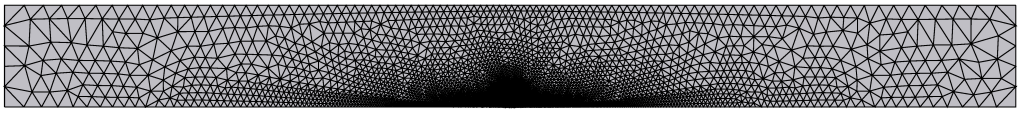

(a) Mesh used for channel domain

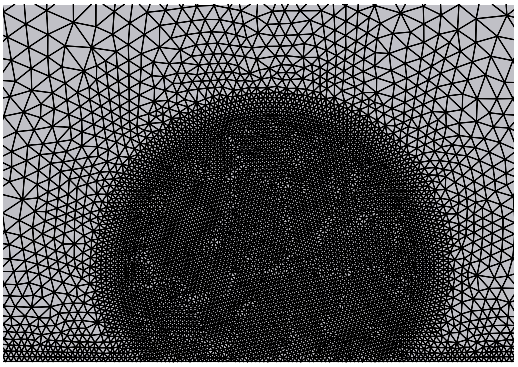

(b) Detail of the channel mesh around the droplet

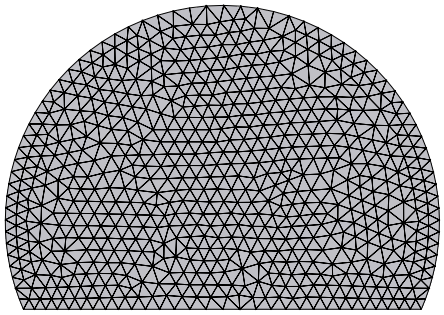

(c) Mesh used for droplet domain

Figure 5.3: (a) Mesh used to represent the PEFC gas channel, (b) detail of the finer mesh around the droplet and (c) mesh used to represent the 13 μl-volume droplet

Validation

Experimental results from Milne's study on droplet oscillation are used to validate the model presented in Chapters 3 and 4. Several air velocity values were used in

the experiments, and the measured frequencies did not depend on the air velocity. No data was provided to support this observation. For a droplet of 13 μl volume, simulations have been performed varying air velocities and the droplet oscillation frequency has been obtained. Fig. 5.4 shows that droplet frequency of oscillation remains relatively constant for all simulations. In every case, oscillation is measured as the x and y displacement of the node corresponding to the droplet's centroid. This result agrees with the aforementioned experimental observation.

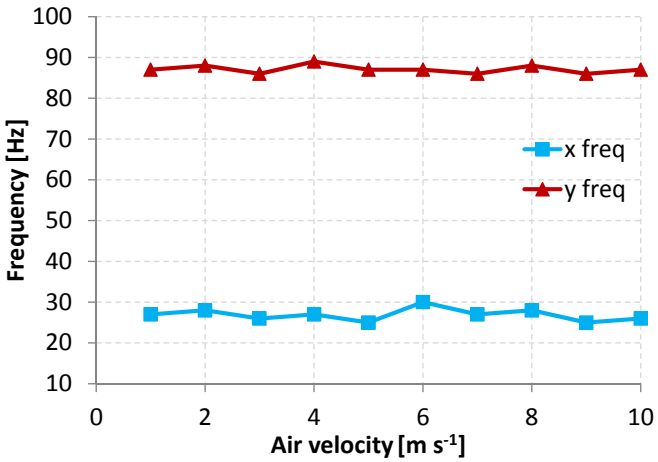

Figure 5.4: Frequency of oscillation in x and y directions for several air velocities

Effects of droplet volume on frequency of oscillation

Effects of the droplet volume on the frequency of oscillation are studied next. Simulations have been performed considering droplet volumes between 13 and 100 μl. Initially, air enters the channel at $v_{air} = 1$ m s^{-1}. Afterwards, air velocity is increased during 0.5 s up to 6 m s^{-1} and then is maintained constant. The evolution of shape, pressure profile and velocity distribution for the case of a 13 μl-volume droplet are depicted in Fig. 5.5.

One can observe a nearly hydrostatic pressure profile within the droplet, with mild oscillations due to the drag exerted by air. After a certain time, the droplet reaches a periodic state. At that moment, the drag exerted by the air is deforming the droplet, whereas the adhesion force is opposing this force and trying to take the droplet to a new equilibrium state. A recirculation pattern can be observed in Fig. 5.5(d). This phenomenon has been observed experimentally in reference [124].

Evolution of pressure and velocity distributions in the channel are displayed in Fig. 5.6 and 5.7, respectively. Transient solution shows the vortex formation when air flows past the droplet. These vortices can be observed in Figs. 5.6(b) and 5.6(c) as circular regions with low pressure. At steady state, pressure is higher on the upstream side of the droplet, and low pressure and velocity values are observed on the wake side. A recirculation pattern for velocity is observed in this region, as depicted in Fig. 5.8. It can be observed that viscous stress and pressure difference across the droplet deform the droplet in the downstream direction. Surface tension force act as a restoring force, acting on the opposite direction of external forces. Consequently, the droplet oscillates due to this unbalancing and balancing process.

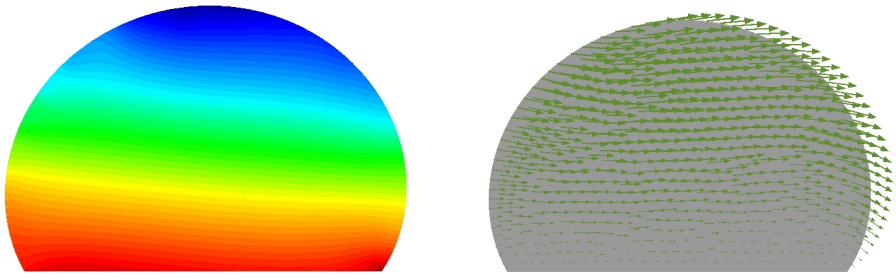

(a) Pressure profile at $t = 0$ s

(b) Velocity field at $t = 0$ s

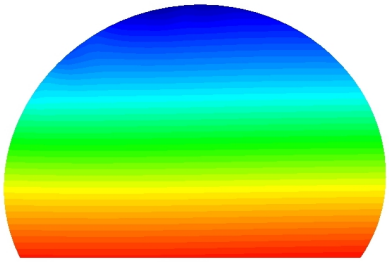

(c) Pressure profile at $t = 0.25$ s

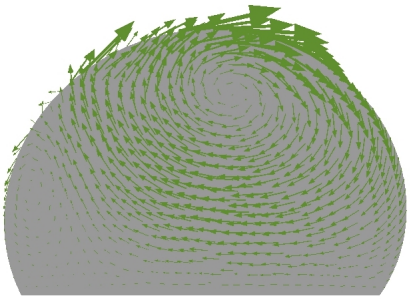

(d) Velocity field at $t = 0.25$ s

Figure 5.5: Evolution of the droplet deformation, pressure profile and velocity field within a PEFC channel

Fig. 5.9 shows the frequency of oscillation in x and y directions observed at the droplet's center of mass for several droplet volumes. Numerical results (square and triangle markers) are compared to experimental data (represented by solid and dashed lines) from reference [5]. They show good agreement, with a maximum difference of 7%. It is important to note that the relationship between frequency of oscillation and droplet volume is exponential. Transforming x axis in Fig 5.9 into the inverse of the square root of volume, this relationship becomes linear.

Larger droplets have lower values of oscillation frequency, as already reported in [24] and [5]. Results also show that in the limit case, a zero value of frequency is achieved by an infinitely large drop [5]. Fig. 5.9 also shows numerical results obtained with the semi-analytical model presented in Chapter 2. The semi-analytical model estimates frequencies that are in reasonable agreement with computational and experimental observations thereby further validating the model compared to the results of Esposito et al. [24] which reported much higher frequencies. Even though the predictions are in relatively good agreement, the semi-analytical model is not able to provide the degree of accuracy obtained by the numerical model, especially as the volume of the droplet increases. The semi-analytical model assumes a predefined shape and does not consider gravitational effects. The former might be responsible for the discrepancies for small droplet volumes while the latter may be the cause of the differences for larger droplets.

(a) Air pressure, $t = 0.001$ s

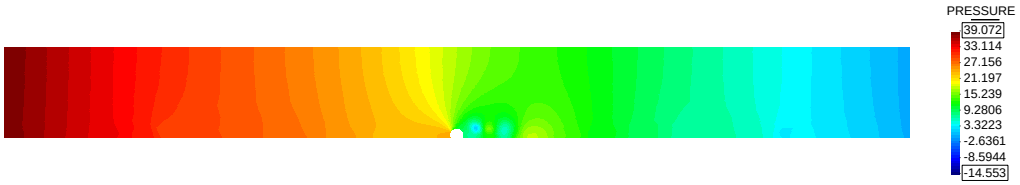

(b) Air pressure, $t = 0.25$ s

(c) Air pressure, $t = 0.5$ s

(d) Air pressure, $t = 1.0$ s

Figure 5.6: Pressure profiles in air for the wind tunnel simulation

(a) Air velocity, $t = 0.001$ s

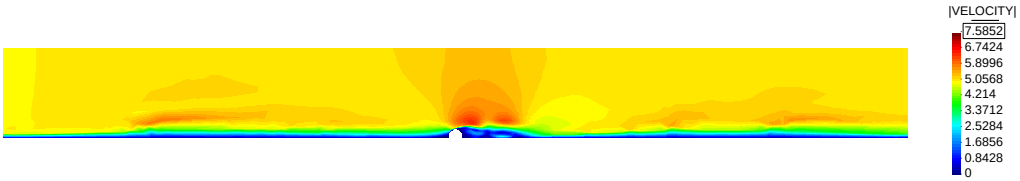

(b) Air velocity, $t = 0.25$ s

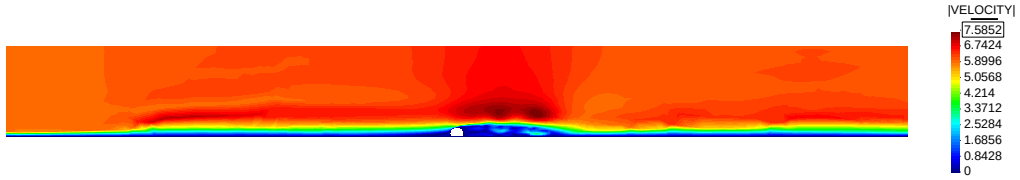

(c) Air velocity, $t = 0.5$ s

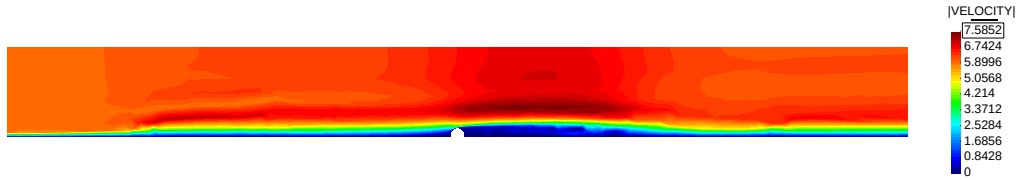

(d) Air velocity, $t = 1.0$ s

Figure 5.7: Magnitude of the velocity profiles in air for the wind tunnel simulation

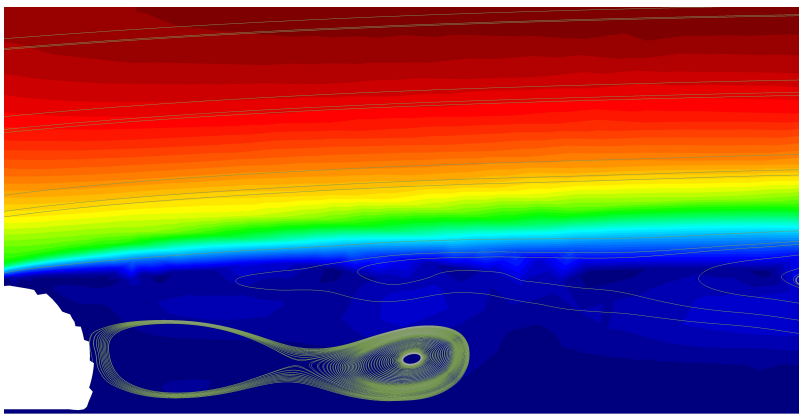

Figure 5.8: Velocity profile and streamlines on the wake side of the droplet

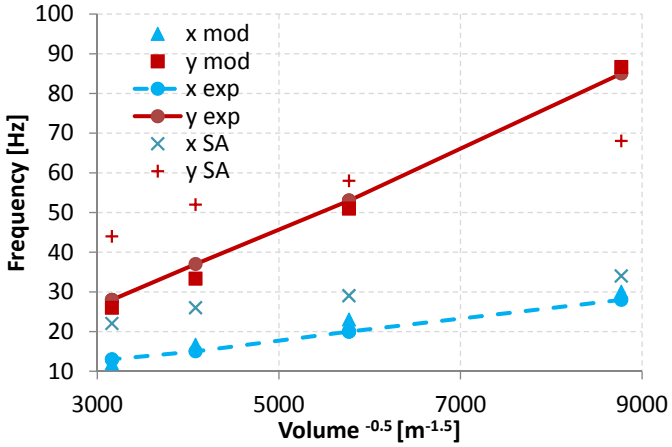

Figure 5.9: Oscillation frequency versus the inverse of the square root of droplet volume, according to experiments (exp), numerical model (mod) and semi-analytical model (SA). Droplet volumes of 13, 30, 58 and 100 μl have been used to reproduce the results from reference [5]

5.2.2 Sessile droplet in a channel

The previous example studied the oscillation of a sessile droplet immersed in an airflow. In an operating PEFC channel, water emerges from the GDL. At high current densities, water may not be evacuated fast enough. Under these conditions, droplets may form with heights greater than 25% of the channel height, or even slugs that block the channel. Thus, channel height plays an important role on droplet oscillation and posterior detachment.

Cho et al. [7] performed an experimental study of droplet dynamics in a PEFC gas channel. The experimental setup was a $1 \times 1.6 \times 40$ mm channel where water was injected in a GDL. The GDL material was carbon paper with 30% PTFE loading. Static contact angle of the surface was 128°. Their work analyzed the effects of several parameters, such as air velocity, on droplet detachment size and time. Experimental results from [7] are reproduced numerically in order to validate the present model. An analytical model based on a force balance was presented by the same authors in reference [6]. Results obtained with this model are also used for validation.

Boundary conditions for the air velocity are the following:

- Dirichlet boundary condition at Γ_E^{in} with $\mathbf{v}_{\text{air}} = \mathbf{v}_{\text{air}}^0$
- No-slip boundary condition at Γ_E^{GDL} and Γ_E^{wall}, $\mathbf{v}_{\text{air}} = 0$

Channel size as well as flow parameters are detailed in Table 5.3. Channel geometry has been discretized using an unstructured mesh of 22000 triangular elements. Similarly to the previous case, the mesh has been refined in the region of the channel where the droplet is placed, as shown in Fig. 5.3(b). Element sizes range from $h = 2 \times 10^{-4}$ m to $h = 10^{-5}$ m. Droplet mesh is unstructured with 1000 triangular elements. Element size is constant, ranging from $h = 10^{-5}$ (0.17 mm-height droplet) to $h = 4 \times 10^{-5}$ m (0.7 mm-height droplet). Simulations have been performed with a time step $\delta t = 10^{-4}$ s

Table 5.3: Parameters used in the sessile droplet in a channel example

Variable	Symbol	Value	Units
Static contact angle	θ_S	128	deg
Channel height	H	1	mm
Channel width	W	1.6	mm
Channel length	L	40	mm

One of the factors affecting droplet detachment is the velocity of the airflow. Cho et al. [7] performed an experiment where the critical air velocity for different droplet sizes was obtained. Experimental results are used to validate the numerical model. For droplet diameters ranging from 0.6 to 1 mm, simulations have been performed at varying air velocities and the critical value for detachment has been obtained. For a sessile droplet in a GDL treated with Teflon, Cho et al. observed that detachment occurs when contact angle hysteresis is greater than 40 deg [7]. Therefore, this value is taken as a threshold condition for droplet detachment. All simulations have been performed with a time step $\delta t = 10^{-4}$ s.

Detachment velocity

Fig. 5.10 shows experimental results from reference [7] (blue circle markers) and numerical results (green diamond markers). For the given channel geometry and droplet diameters, the critical air velocity needed for detachment ranges from 5 to 13 m s^{-1}. Taking the channel height as the characteristic length, Reynolds numbers range from 300 to 600, approximately.

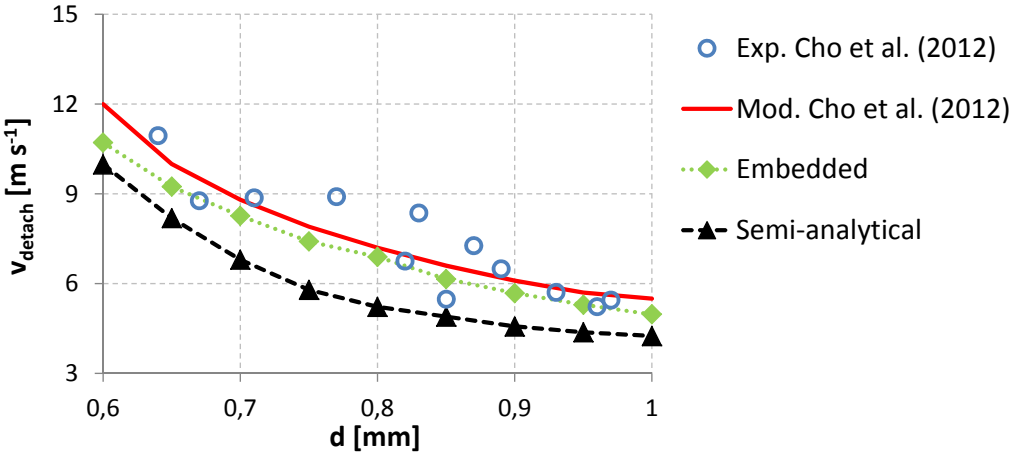

Figure 5.10: Critical air velocity for detachment as a function of droplet diameter obtained with analytical model from [6] (red line), experimental data from [7] (blue circle markers), the embedded model (green diamond markers) and the semi-analytical model (black triangle markers)

Results show that higher values of critical air velocity are obtained for smaller droplet sizes. This result is consistent with previous works [11], [15], [9], [26]. Obtained numerical results show good agreement with experimental data from Cho et al. [7]. Results are also compared to an analytical model developed by the same

authors [6] (red line in Fig. 5.10), and with the semi-analytical model presented in Chapter 2. The same trend is observed in all predicted values. The analytical model in reference [6] predicts similar results to the embedded model for droplets with diameters greater than 0.7 mm. Cho's analytical model however overpredicts critical air velocities for droplet detachment. Results obtained with the semi-analytical model show reasonable agreement with experimental data, although values for critical air velocity are underpredicted for smaller droplet diameters.

Fig. 5.11 depicts droplet profile (blue solid line) and velocity distribution (red dashed line) prior to detachment. Primary horizontal axis (bottom) represents x coordinate ($x = 0$ mm corresponds to the center of droplet chord), whereas air velocity is represented by secondary horizontal axis (top).

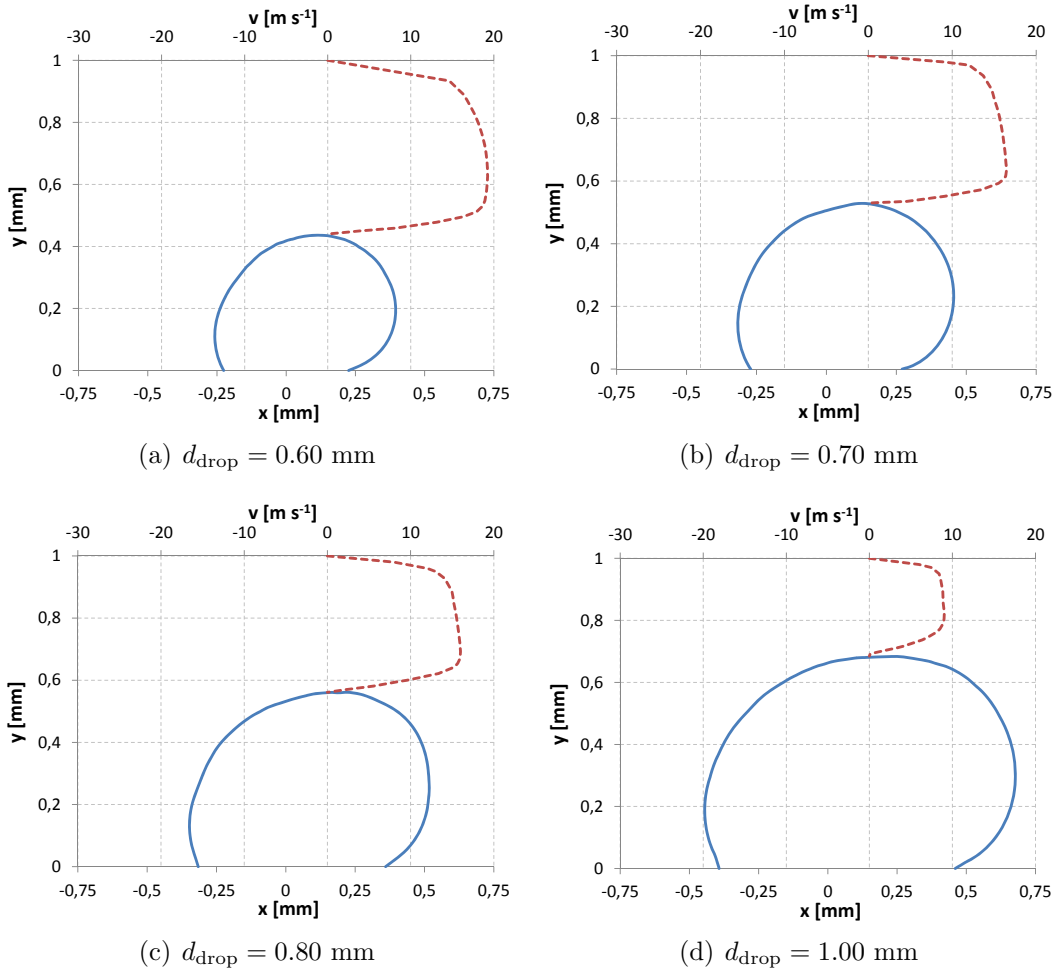

(a) $d_{\text{drop}} = 0.60$ mm

(b) $d_{\text{drop}} = 0.70$ mm

(c) $d_{\text{drop}} = 0.80$ mm

(d) $d_{\text{drop}} = 1.00$ mm

Figure 5.11: Drop (blue solid line) and air velocity (red dashed line) profiles at detachment in a PEFC channel

Detachment time

The time of detachment for a sessile droplet in a PEFC gas channel can be computed using the simulations in the previous section. The experimental study of Cho et al.

Table 5.4: Detachment time (t_{det}) and area covered (A_{cov}) for different droplet heights (h) according to current model and semi-analytical model presented in [11]

d [mm]	Embedded		Semi-analytical		Cho et al.	
	t_{det} [s]	A_{cov} [mm^2]	t_{det} [s]	A_{cov} [mm^2]	t_{det} [s]	A_{cov} [mm^2]
0.6	1.02	0.107	1.24	0.122	0.88	0.097
0.7	1.62	0.146	1.92	0.163	1.24	0.122
0.8	2.42	0.190	2.71	0.205	1.56	0.142
0.9	3.45	0.241	4.69	0.296	2.0	0.168
1.0	4.73	0.298	6.3	0.360	2.42	0.190

[7] did not include details about detachment time. Let us consider the results shown in Fig. 5.10. Assuming that the PEFC is generating 1 A cm^{-2} of current density, a constant water volume rate $\dot{Q} = 0.1$ μl s^{-1} emerges into the gas channel. Given the volume rate and the droplet size at detachment, the time needed for the droplet to detach the GDL surface is obtained. A comparison between the analytical model presented in [7] and the embedded and semi-analytical models is included in Table 5.4.

Time and area coverage values corresponding to the embedded model have been obtained using detachment velocities from Fig. 5.10. Detachment time and area for analytical and semi-analytical models have been obtained as follows. First, a detachment diameter used in the previous example is considered. For this droplet size, the detachment velocity predicted by the embedded model is extracted from Fig. 5.10. Considering this velocity value as a reference, the critical droplet diameter according to the other models is obtained. For instance, the critical velocity for a 0.8 mm-diameter droplet is 6.89 m s^{-1}. Predicted sizes of the detached droplet for this velocity are 0.69 and 0.83 mm according to Cho et al. [7] and the semi-analytical model, respectively.

Detachment times are in agreement between the models, specially for droplets with diameters below 0.8 mm. The semi-analytical model predicts sooner detachment values. On the other hand, for droplets sizes above 1 mm, Cho et al. predict channel blockage for velocities below 4.5 m s^{-1}.

Deformation and contact angle evolution

The evolution of advancing and receding angles for the 0.7 mm-diameter droplet in the simulation is shown in Fig. 5.12. The rate of change of contact angles is not constant. Three regions can be distinguished in Fig. 5.12 during the deformation process.

Initially, the droplet is in equilibrium (Fig. 5.13(a)) with no airflow. As air starts flowing around the droplet, pressure and viscous forces deform the droplet in the vertical direction (Fig. 5.13(b)). Both advancing and receding angles increase at the same rate. This region is identified as *I* in Fig. 5.12. A transition area is observed, where the receding angle remains constant (denoted as *II* in Fig. 5.12). Increasing airflow velocity leads to higher pressure drop across the droplet, and

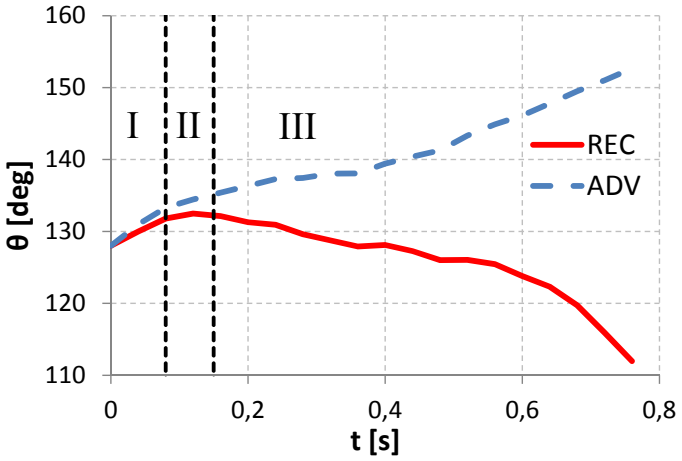

Figure 5.12: Advancing (blue dashed line) and receding (red solid line) angle evolution for the 0.7 mm-diameter droplet

receding angle diminishes (Fig. 5.13(c)) until the droplet detaches from the GDL surface (Fig. 5.13(d)). Rate of change of advancing contact angle is constant during the deformation process, as shown in Fig. 5.12 (marked as *III*). Same trends in contact angle evolution were observed experimentally by Wu and Djilali [8]. Further discussion of this result is included in section 5.2.3.

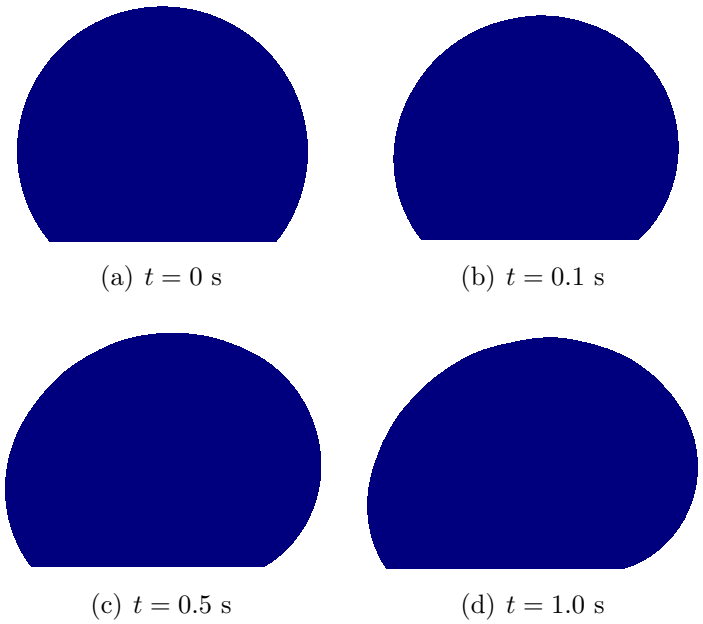

(a) $t = 0$ s (b) $t = 0.1$ s

(c) $t = 0.5$ s (d) $t = 1.0$ s

Figure 5.13: Deformation process of a 0.7 mm-diameter droplet subjected to airflow

Evolution of pressure and velocity distributions in the channel are depicted in Fig. 5.14 and 5.15, respectively. Similarly to the wind tunnel simulation, transient solution shows vortex formation when air flows past the droplet (Figs. 5.14(b) and 5.14(c)). Effect of the channel wall can be observed in Fig. 5.14(d). After air flows around the droplet, it recovers the velocity profile in a relatively small distance.

However, when air flows around a droplet in a free space, the low pressure zone at the wake of the droplet is significantly longer.

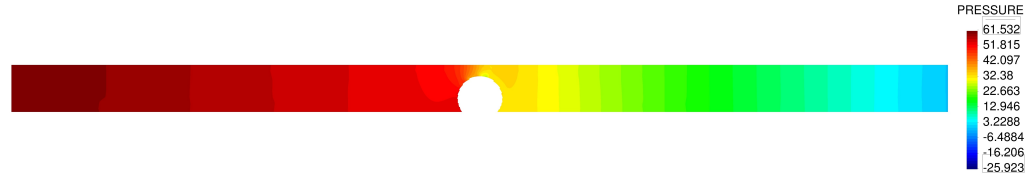

(a) Air pressure, $t = 0.001$ s

(b) Air pressure, $t = 0.010$ s

(c) Air pressure, $t = 0.015$ s

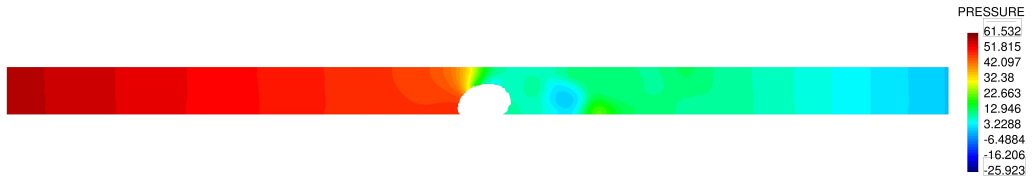

(d) Air pressure, $t = 0.025$ s

Figure 5.14: Pressure profiles in air for a 1 mm-diameter droplet

5.2.3 Droplet injection in a channel

Droplet emergence, deformation and detachment are studied in this case. Wu and Djilali [8] performed an experiment to investigate the dynamics of water droplets emerging from a squared 50×50 μm pore into a 250×250 μm air channel. Although dimensions of the channel were different than from a channel typically encountered in PEFCs, results provided with valuable data on droplet deformation and detachment.

Channel was build using a transparent elastomer (polydimethylsiloxane, PDMS) with a static contact angle of 110 deg. This value is similar to that of carbon paper without PTFE coating [8]. Different flow regimes were considered, with Reynolds numbers ranging from 50 to 1200. Droplet flow was obtained for an air velocity of 10 m s^{-1} and water volume flow of 0.1 μl s^{-1}. Inlet velocity of water was 0.04 m s^{-1}.

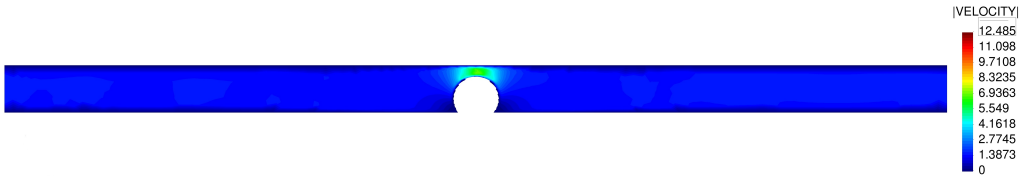

(a) Air velocity, $t = 0.001$ s

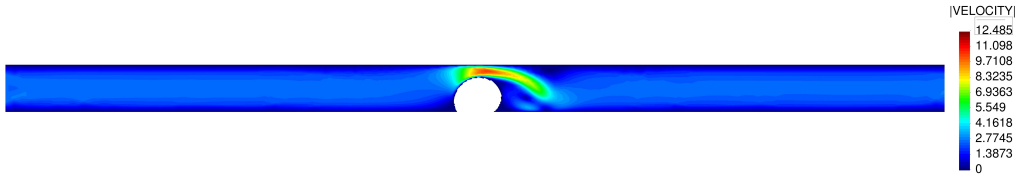

(b) Air velocity, $t = 0.010$ s

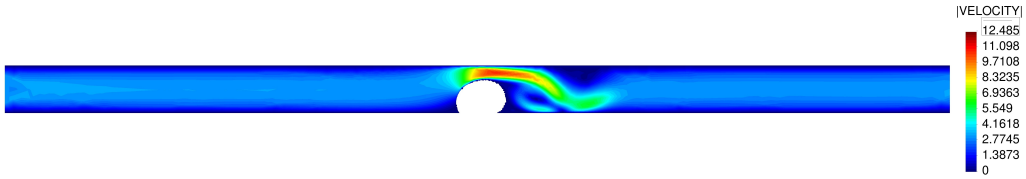

(c) Air velocity, $t = 0.015$ s

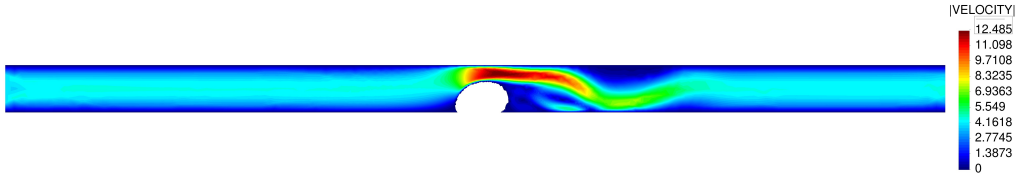

(d) Air velocity, $t = 0.025$ s

Figure 5.15: Magnitude of the velocity profiles in air for a 1 mm-diameter droplet

Table 5.5: Parameters used in the droplet injection in a channel example

Variable	Symbol	Value	Units
Initial chord	c	100	μm
Water flow rate	Q	0.1	μl s^{-1}
Water inlet velocity	$\mathbf{v}_{\mathrm{w}}^{0}$	0.04	m s^{-1}
Static contact angle	θ_{S}	110	deg
Air velocity	$\mathbf{v}_{\mathrm{air}}^{0}$	10	m s^{-1}
Channel height	H	250	μm
Channel width	W	250	μm
Channel length	L	3	mm
Pore diameter	D	50	μm

This examples reproduces the experimental results from reference [8] to validate the numerical model. Boundary conditions for the air and water are the following:

- Dirichlet boundary condition at Γ_E^{in} with $\mathbf{v}_{\mathrm{air}} = \mathbf{v}_{\mathrm{air}}^{0}$
- No-slip boundary condition at Γ_E^{GDL} and Γ_E^{wall}, $\mathbf{v}_{\mathrm{air}} = 0$
- Dirichlet boundary condition at Γ_S^{in} with $\mathbf{v}_{\mathrm{w}} = \mathbf{v}_{\mathrm{w}}^{0}$

Channel size as well as flow parameters are detailed in Table 5.5. Channel geometry has been discretized using an unstructured mesh of 25000 triangular elements. The mesh has been refined in the region of the channel where the pore and the emerging droplet are placed (Fig. 5.3(b)). Element sizes range from $h = 5 \times 10^{-5}$ m to $h = 5 \times 10^{-6}$ m. Droplet mesh is unstructured with 200 triangular elements. Element size is constant with $h = 5 \times 10^{-6}$. Simulations have been performed with a time step $\delta t = 10^{-6}$ s

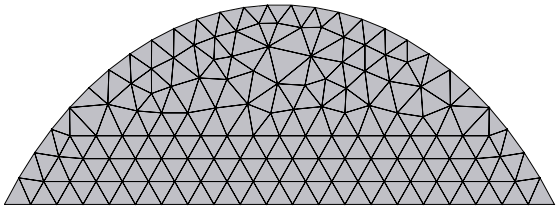

Figure 5.16: Mesh used for the droplet injection example

Lagrangian inlet In order to simulate water injection into the droplet, water must be injected in the Lagrangian domain. Inlet conditions, such as air entering the channel, are represented via Dirichlet boundary conditions in fixed Eulerian meshes. However, an inlet condition applied to a moving Lagrangian mesh is not trivial. In this work, the water injection process is done by creating new nodes in a specific region of the boundary, as shown in Fig. 5.17.

Initially, the inlet region is represented by a set of nodes with a given initial velocity (colored in red in Fig. 5.17(a)). These nodes start to move according to the given velocity, leaving an empty space in the domain (Fig. 5.17(b)). The area

occupied by this *empty* space is the same than the increase of area of the whole domain. After a certain time, when the distance from the nodes to the injection boundary is bigger than a prescribed value, a new set of nodes is created (Fig. 5.17(c)). Since the Lagrangian domain is discretized using the PFEM methodology, the re-meshing process introduces the new nodes in the updated mesh. This *Lagrangian inlet* method is advantageous for the problem at hand, since water can be considered an infinite reservoir. However, the system size increases each time a new node has been added, and the computational cost increases accordingly.

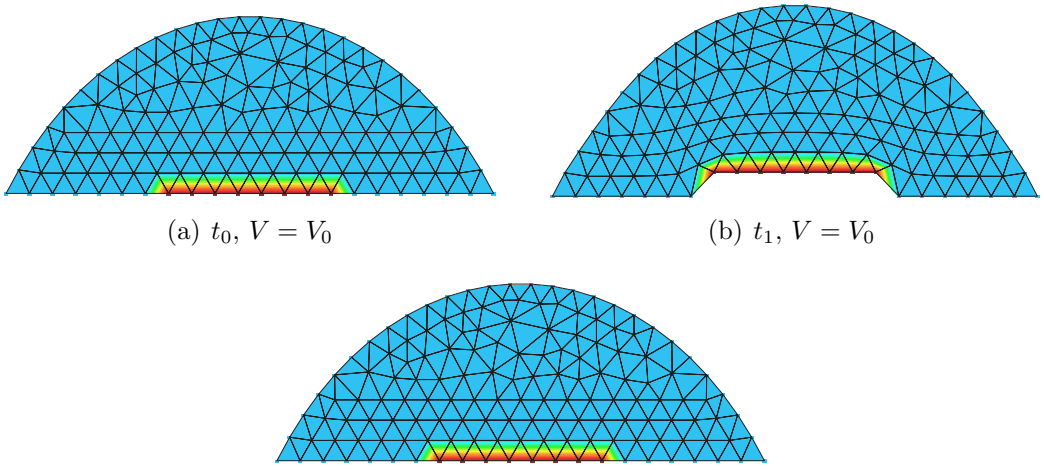

(a) t_0, $V = V_0$ (b) t_1, $V = V_0$

(c) t_2, $V = V_0 + \Delta V$

Figure 5.17: Lagrangian inlet process in a channel

In this section, the dynamics of an emerging droplet in a PEFC gas channel are studied. Water produced within the fuel cell emerges into the channel from the GDL pores. Depending on the operating conditions, water may evolve as a droplet, a slug or a film. The following examples recreate these flow types.

Droplet flow

Experimental validation Wu performed an experimental study to observe effects of air and water inflow velocities on droplet dynamics [8]. The experimental setup was a rectangular channel of 250×250 μm cross-section and 3 mm length. Air entered the channel at a constant velocity of 10 m s^{-1}. Water was injected via a 50×50 μm pore with an inlet velocity of 0.04 m s^{-1}. Wu observed that emergence and posterior detachment process was repeated every 0.075 ms approximately, giving a frequency $f = 13.2$ Hz (i.e., approximately 13 droplets per second emerged and detached from the pore). Experimental results are used to validate the numerical model.

Fig. 5.18 depicts the process of water injection into a gas channel. Experimental results obtained in [8] are displayed in left-hand side column. Right-hand side column shows the predicted droplet profile according to the embedded method. Channel walls are represented by black lines, whereas the blue line is the droplet

profile. The gap in the channel surface is the pore where water is injected. Predicted profiles are similar to those observed in [8], specially at the beginning of the injection process.

Evolution of contact advancing and receding angles according to Wu is shown in Fig. 5.19. The same contact angle evolution has been obtained numerically in Section 5.2.2 (Fig. 5.12). Three regions can be distinguished; (I) both advancing and receding angles increase at the same rate, (II) receding angle remains constant and (III) receding angle decreases at a constant rate.

Numerical results show good agreement with experimental data from reference [8]. At early stages of droplet emergence (regions I and II), both predicted and measured contact angles have an excellent fit. After time $t = 0.02$ s, results obtained with the present numerical method are overpredicted. This difference between results is probably due to significant effects on the z direction, which is not considered in the 2D model. Additionally, the droplet starts to break up from water stream injected through the pore. Droplet breakup has not been included in the present model.

Comparison with VOF Zhu et al. [9] performed a numerical investigation of droplet emergence in a channel using VOF method in two dimensions. The numerical simulation is reproduced here. The computational domain of the simulation was the same than the experimental setup in [8]. The position of the pore was different in the numerical study. Instead of being in the center of the channel, the pore location was at 250 μm from the inlet. The length of the channel was set to 1 mm, although effects of the channel length on results were negligible [9]. Air entered the channel at 10 m s^{-1}. Water was injected via a 50 μm-diameter circular pore with an inlet velocity of 0.1 m s^{-1}. The time step used in the simulations has been set to $\delta t = 10^{-6}$ s, whereas results reported in [9] used a time step between 1 an 2 orders of magnitude smaller. Results obtained in reference [9] are depicted in Fig. 5.20.

Results obtained by Zhu et al. [9] predict that a droplet is formed (Figs. 5.20(a)-5.20(e)). The droplet reaches a critical height (Fig. 5.20(g)) and then it deforms on the x-direction (Fig. 5.20(i)). Results according to the embedded formulation show a droplet more deformed in x-direction are more prone to form a film pattern.

Let us consider the previous example. In the experimental setup from Wu [8] injection pore is located at 1.5 mm from the channel entrance, and velocity of injection is 0.04 m s^{-1}. On the other hand, the computational domain from Zhu [9] considers a pore located at 0.25 mm from the channel entrance and that water is injected at 0.1 m s^{-1}. Although the velocity of injection is higher in this second example, pressure effects on the droplet are more important, as shown in Fig. 5.21. Thus, water may form a film as it emerges from the pore. Both VOF and embedded formulations however predict a film formation under these conditions.

Slug flow

The previous examples have performed analysis on droplet flow. However, slugs and films may form in operating fuel cell gas channels [2]. Analytical models, such as the semi-analytical model presented in Chapter 2 are restricted to droplet flow. The

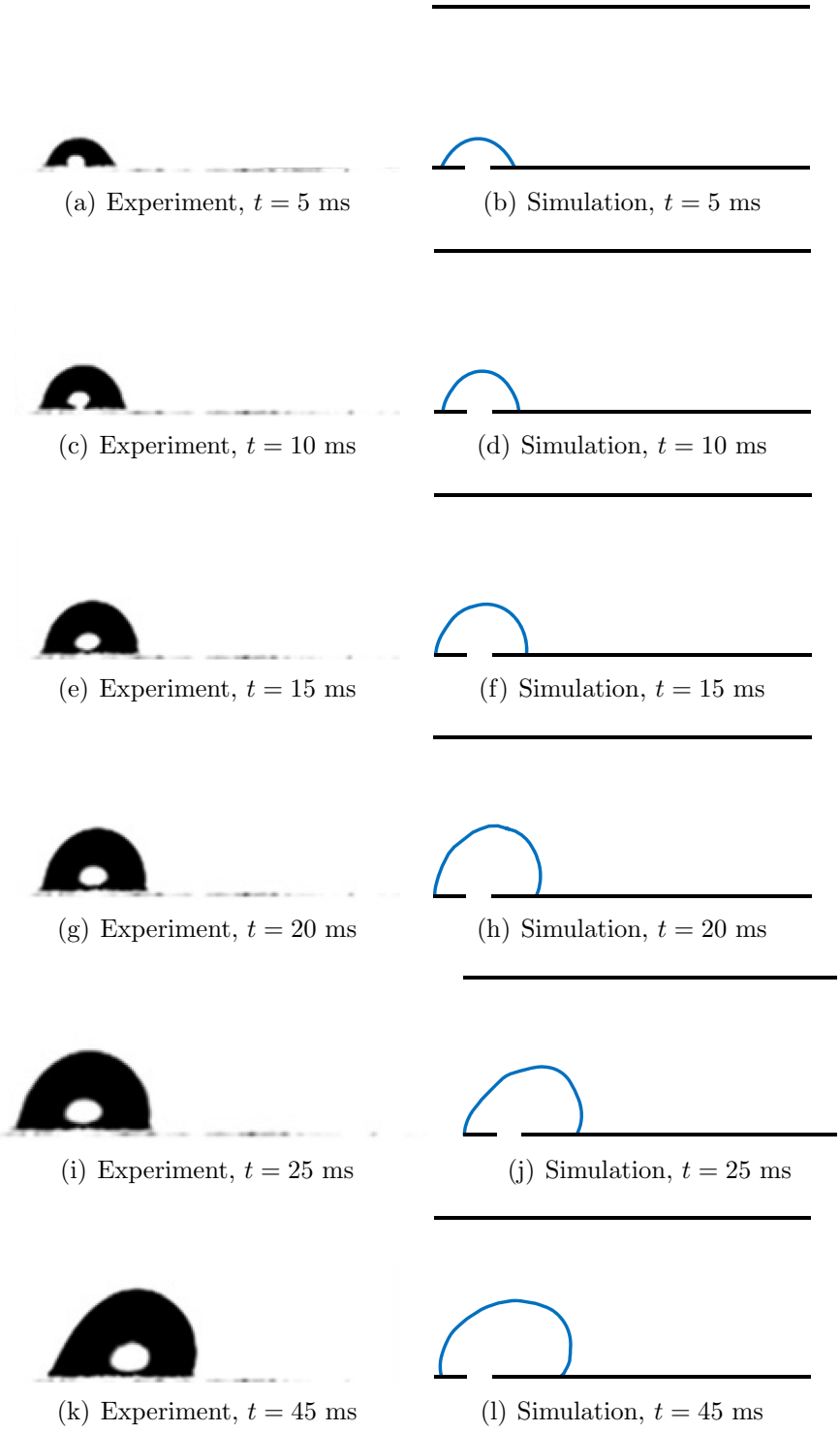

(a) Experiment, $t = 5$ ms (b) Simulation, $t = 5$ ms

(c) Experiment, $t = 10$ ms (d) Simulation, $t = 10$ ms

(e) Experiment, $t = 15$ ms (f) Simulation, $t = 15$ ms

(g) Experiment, $t = 20$ ms (h) Simulation, $t = 20$ ms

(i) Experiment, $t = 25$ ms (j) Simulation, $t = 25$ ms

(k) Experiment, $t = 45$ ms (l) Simulation, $t = 45$ ms

Figure 5.18: Experimental (left column) and simulated (right column) deformation process of an emerging droplet into a gas channel. Experimental results extracted from [8]

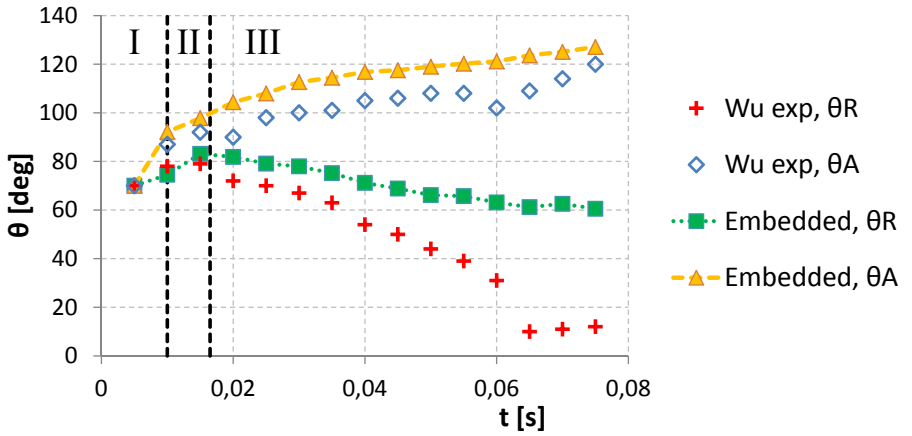

Figure 5.19: Advancing (blue diamond markers) and receding angles observed in [8]

present numerical method can overcome this drawback and can be used to reproduce slug or film flow conditions.

At high current densities (i.e., $i \geq 2$ A cm^{-2}), water is produced at a faster rate and may form slugs and block the channel when it emerges from the GDL pores. In order to observe slug formation in the channel, air inlet velocity is set to 1.0 m s^{-1}. Water is injected through a 50 μm pore at a constant velocity v = 0.1 m s^{-1}.

For the considered conditions, a slug is formed after 4 ms. Pressure drop across the droplet and air velocity are not significantly altered for droplet height to channel height ratio of 0.5 (Figs. 5.23(a) and 5.23(b)). For ratios between 0.5 and 0.8, the channel cross-section at the droplet position diminishes (Fig. 5.23(c)) and air velocity increases. Droplet height to channel height ratios above 0.8 are characterized by a sudden increase of the pressure drop (Fig. 5.22(a)) as well as the velocity magnitude (Fig. 5.23(d)). Pressure losses in PEFC channels reduce the fuel cell efficiency due to non-uniform gas distribution [22].

Film flow

When a PEFC is producing a current density between 0.5 and 1.5 A cm^{-2}, water is prone to form films in the gas channels. In this example, the same computational domain from Section 5.2.2 is considered. Air enters the channel at v = 5 m s^{-1}, and water is injected at a constant velocity of 0.01 m s^{-1}. Pressure and velocity distribution in air and water domains are depicted in Figs. 5.24-5.27.

Film flow formation in a PEFC gas channel can be therefore modeled using the embedded approach. As shown in Fig. 5.25, as water covers the GDL surface, air velocity is increased. Additionally, the area covered by water prevents air from diffusing through the GDL pores, reducing the fuel cell efficiency.

5.3 Conclusions

A numerical study of droplet dynamics using an embedded formulation has been carried out and validated experimentally. Oscillatory behavior of a sessile droplet subjected to an airflow in a free space has been analyzed. Observed oscillations are

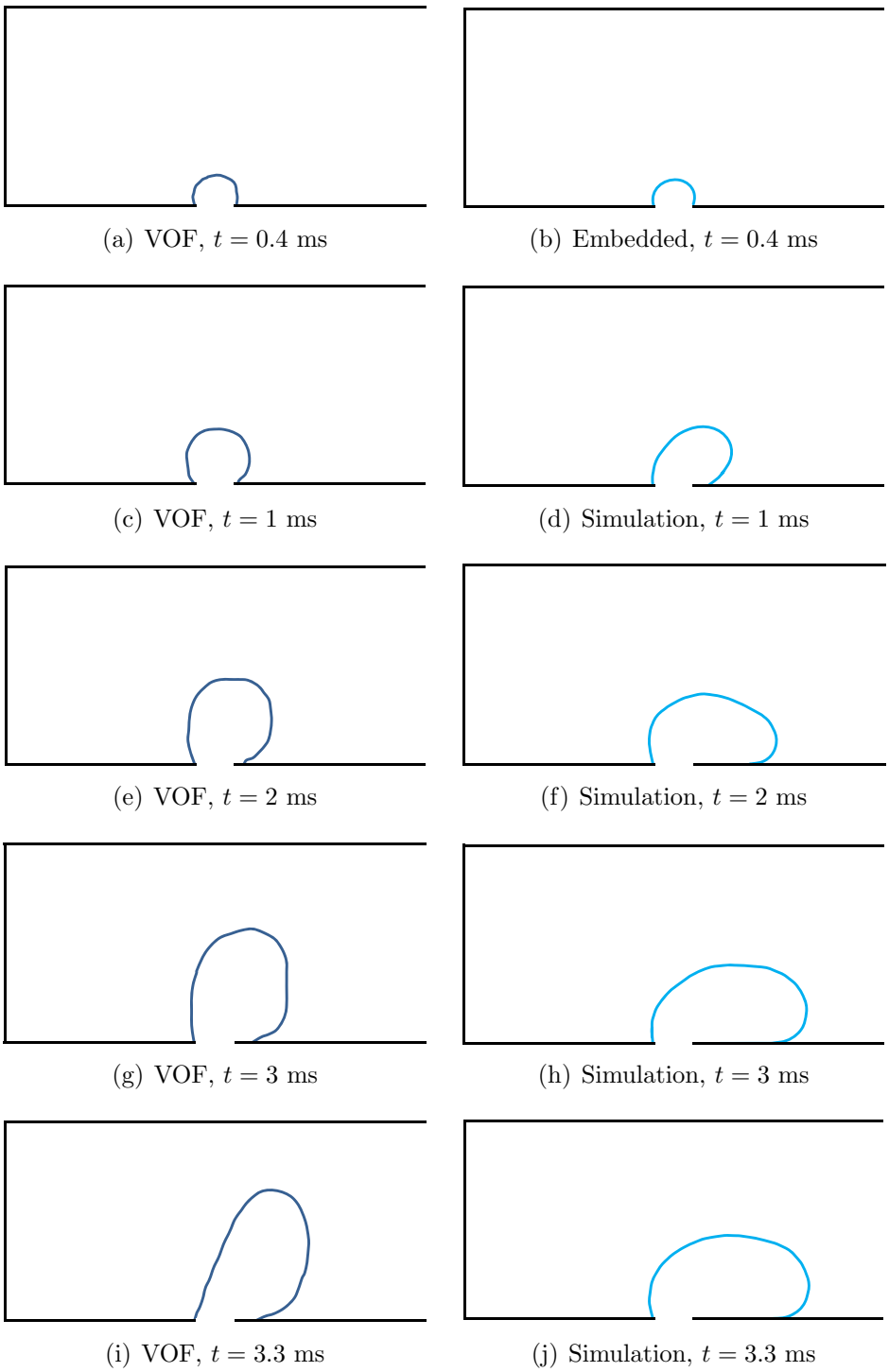

(a) VOF, $t = 0.4$ ms (b) Embedded, $t = 0.4$ ms

(c) VOF, $t = 1$ ms (d) Simulation, $t = 1$ ms

(e) VOF, $t = 2$ ms (f) Simulation, $t = 2$ ms

(g) VOF, $t = 3$ ms (h) Simulation, $t = 3$ ms

(i) VOF, $t = 3.3$ ms (j) Simulation, $t = 3.3$ ms

Figure 5.20: Numerical results according to VOF model from [9] (left column) and embedded model (right column) of the deformation process of an emerging droplet into a gas channel.

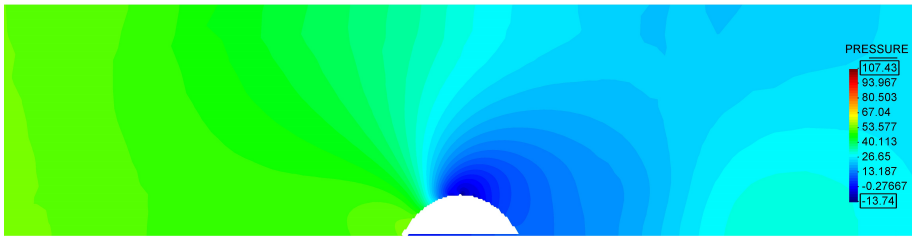

(a) Air pressure profile at $t = 0.4$ ms. Pore located at 1.5 mm from entrance

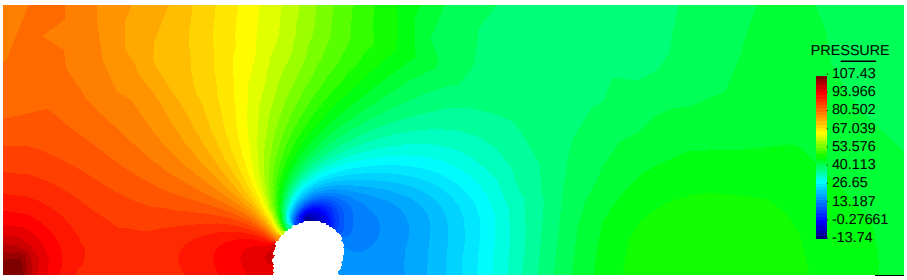

(b) Air pressure profile at $t = 0.4$ ms. Pore located at 0.25 mm from entrance

Figure 5.21: Air pressure profile at $t = 0.4$ ms for a channel with a pore located at (a) 1.5 mm and (b) 0.25 mm from entrance.

consistent with previous works [24], [11], [5]. A simulation of 1 s has been performed considering several droplet volumes, and the obtained numerical results agree well with experimental observations from reference [5]. This result is particularly important since droplet oscillation is responsible for droplet detachment [24], [11], [5], [16]. A recirculation pattern is observed within the droplet when it reaches steady-state, as observed by Minor's experiments [124]. Results obtained with the semi-analytical model presented in Chapter 2 show the same trend.

The effect of airflow velocity on droplet detachment is also studied. Larger droplets exhibit lower values of critical air velocity for detachment, but the time that takes to reach this condition is longer. Results have been validated experimentally using available data from Cho et al. [7]. Contact angle evolution observed in the numerical simulations is similar to that from reference [8].

Results for water injection in a gas channel have been validated experimentally. Predicted droplet profiles and experimental observations show good agreement at early stages of droplet formation. Advancing contact angle increases approximately at a constant rate, whereas receding contact angle shows three regions of different behavior. Comparison between VOF and embedded models has studied as well. Current model predicts film formation, whereas VOF results show that a droplet is formed first. Large discrepancies with VOF results were observed, specially with predicted flow type and contact angles on the advancing and receding points.

For low air velocities (i.e., less than 1 m s^{-1}) water can block the channel, specially at high injection rates (i.e., 0.05 μl s^{-1}). Alternatively, water films are formed in fuel cell channels for air velocities greater than 10 m s^{-1}. Critical air velocities are lower for emerging droplets than for already formed droplets. Therefore, droplets formed in the channel are more difficult to detach from the GDL surface

(a) Air pressure, $t = 0.001$ s

(b) Air pressure, $t = 0.002$ s

(c) Air pressure, $t = 0.003$ s

(d) Air pressure, $t = 0.004$ s

Figure 5.22: Slug formation in a gas channel. Pressure profiles in air

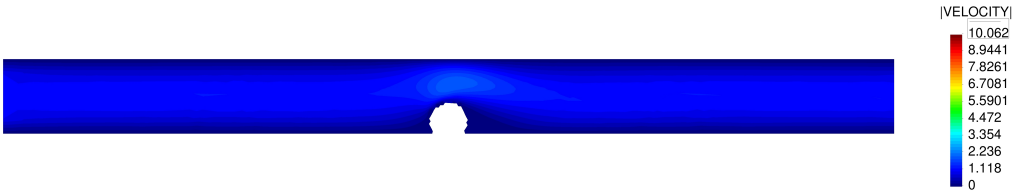

(a) Air velocity, $t = 0.001$ s

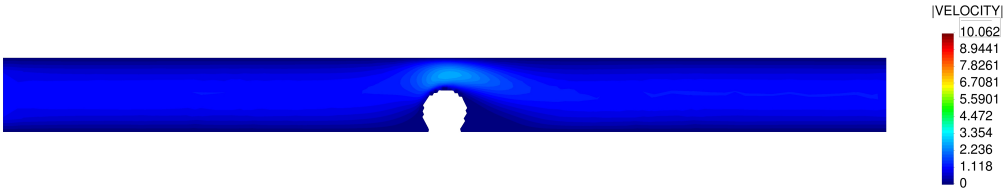

(b) Air velocity, $t = 0.002$ s

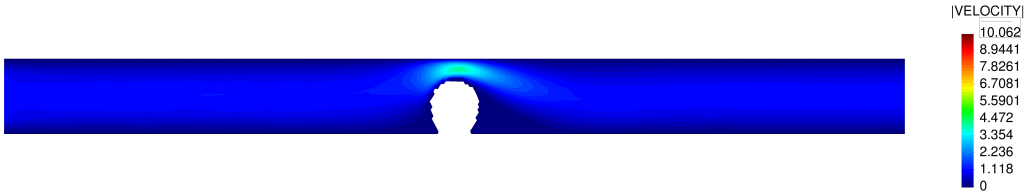

(c) Air velocity, $t = 0.003$ s

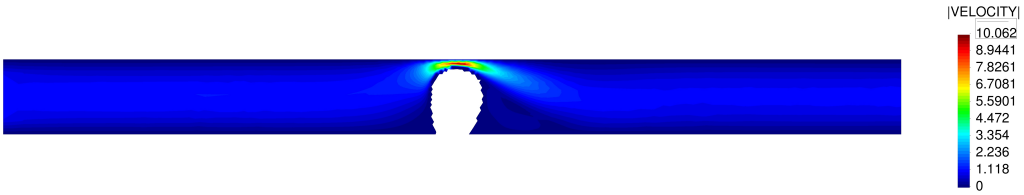

(d) Air velocity, $t = 0.004$ s

Figure 5.23: Slug formation in a gas channel. Magnitude of velocity profiles in air

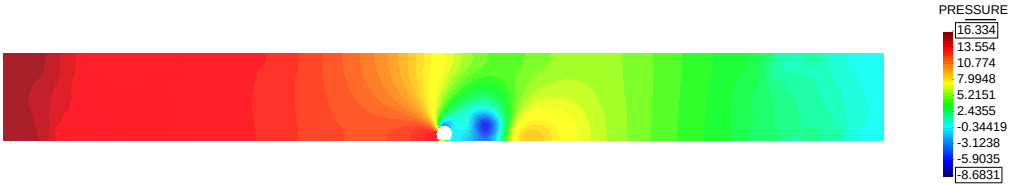

(a) Air pressure, $t = 0.001$ s

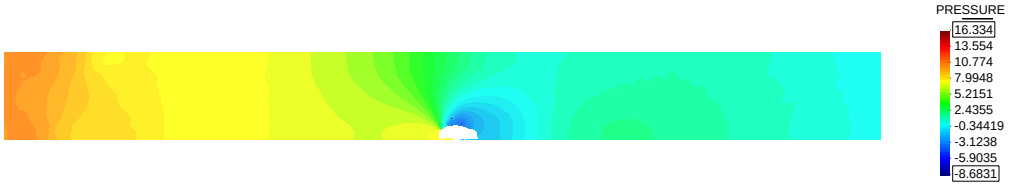

(b) Air pressure, $t = 0.05$ s

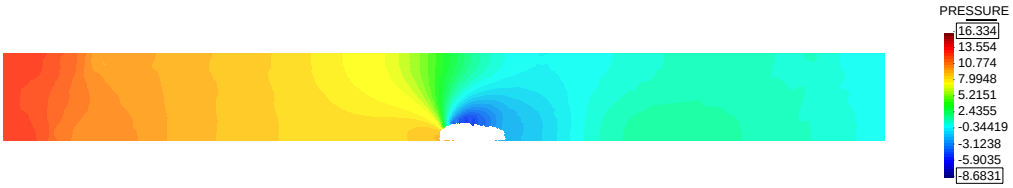

(c) Air pressure, $t = 0.15$ s

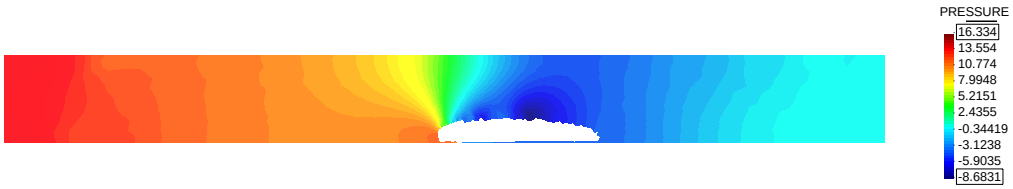

(d) Air pressure, $t = 0.5$ s

Figure 5.24: Pressure profiles in air

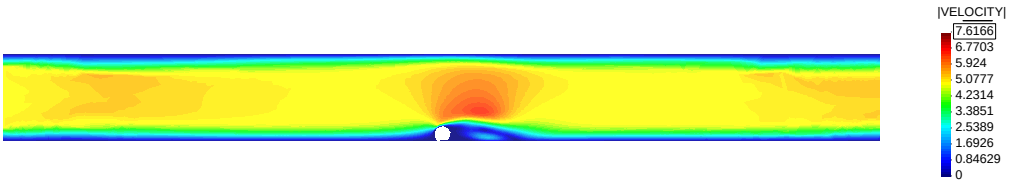

(a) Air velocity, $t = 0.001$ s

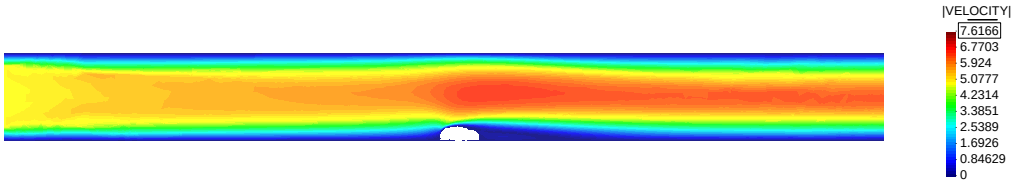

(b) Air velocity, $t = 0.05$ s

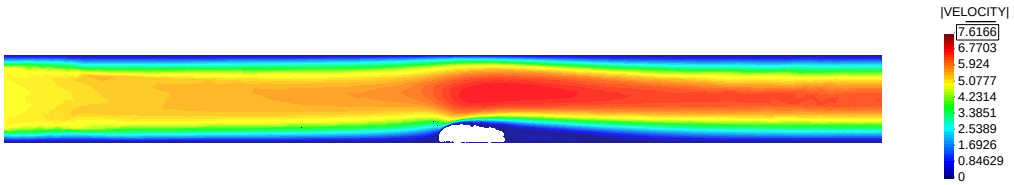

(c) Air velocity, $t = 0.15$ s

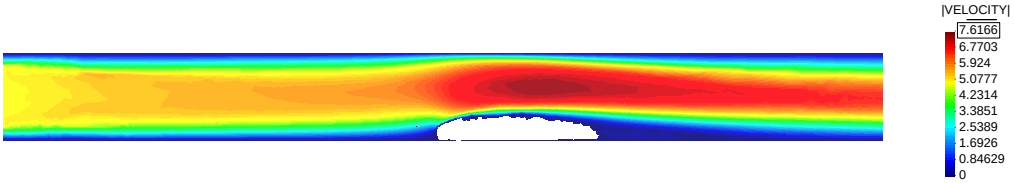

(d) Air velocity, $t = 0.5$ s

Figure 5.25: Velocity profiles in air

(a) Drop pressure, $t = 0.001$ s

(b) Drop pressure, $t = 0.05$ s

(c) Drop pressure, $t = 0.15$ s

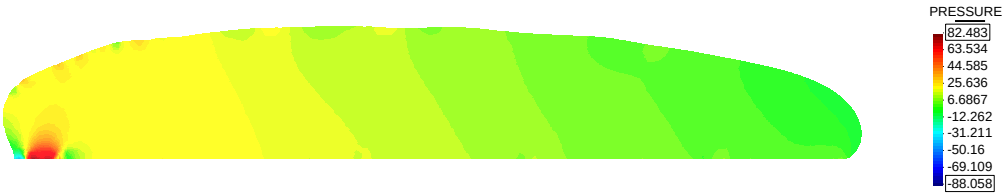

(d) Drop pressure, $t = 0.5$ s

Figure 5.26: Pressure profiles in water

(a) Drop velocity, $t = 0.001$ s

(b) Drop velocity, $t = 0.05$ s

(c) Drop velocity, $t = 0.15$ s

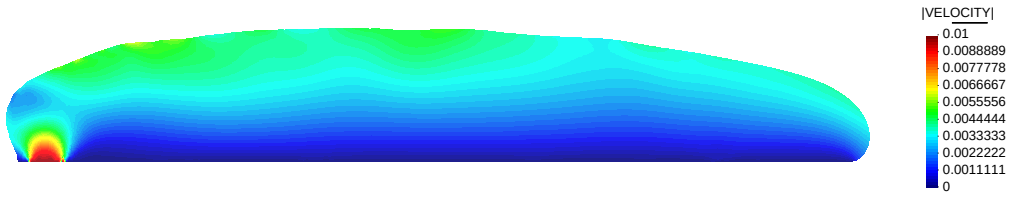

(d) Drop velocity, $t = 0.5$ s

Figure 5.27: Velocity profiles in water

than emerging ones. It is worth mentioning that for water droplets in gas channels, the one-way Neumann coupling and a "homogeneous" negligible (zero-velocity) interface Dirichlet coupling are sufficient as the droplet velocity in the pre-detachment stage is negligible.

Chapter 6

Conclusions and future work

This chapter includes a summary of this thesis, where the main results and conclusions are highlighted. Further improvements are identified as future work.

6.1 Summary and conclusions

The objective of this work has been the development and implementation of novel techniques to study droplet dynamics in PEFC gas channels. Two models have been presented and validated experimentally:

- Semi-analytical model: a numerical tool capable of obtaining fast results for droplet detachment condition in gas channels for droplet flow regime at a reduced computational cost.

- Embedded model: a novel numerical method to include the fully coupled air-water interaction and overcome the intrinsic limitations of semi-analytical model.

The first model, extending the idea of Esposito et al. [24], was based on a force balance applied to an emerging droplet in a PEFC channel. Forces acting on the droplet are drag force exerted by airflow and adhesion force. The latter has been modeled in the present work using an analytical expression and integrated numerically at every time step. For the drag force, several numerical simulations have been done to obtain the value of the drag coefficient for different droplet sizes. Results show the drag force dependency on droplet height to channel height ratio. The model has been validated, obtaining good agreement with available experimental data. However, differences between semi-analytical model and experimental results become more evident for higher droplet volumes. The semi-analytical model tends to underpredict detachment velocities in such cases. This is probably caused by the absence of gravity effects and the assumed geometry used in the semi-analytical model. For small droplets, where gravity effects are negligible, like the ones appearing in fuel cell channels, the semi-analytical model shows good predictive capabilities.

Analytical models are not able to deal with strongly deforming droplets, predict post-detachment behavior or to perform multiple droplets analysis. In order to overcome these drawbacks, a monolithic Lagrangian finite element model for droplets

has been developed and validated experimentally. The model proposed can represent the droplet surface exactly via the Lagrangian boundary mesh, and it does not depend on a background fixed mesh (contrary to Eulerian formulations, such as Volume of Fluid). A monolithic (coupled velocity-pressure) scheme has been adopted for the numerical solution of the governing equations. It has been discovered that the presence of surface tension precludes using fractional step schemes. An implicit surface tension model has been proposed. Results show that this formulation is advantageous from the computational point of view; it alleviates the severe time restrictions characteristic of the commonly used explicit surface tension models.

In order to model droplet dynamics in a PEFC gas channel, the developed Lagrangian model was coupled to an Eulerian model for the air. The coupling has been done in an embedded fashion extending the idea proposed in [117] and [118]. The fluids were coupled using a Dirichlet-Neumann coupling. An important advantage of the proposed embedded approach is that the interface position is exactly defined by the Lagrangian mesh. Thus, no additional techniques (typically used in fully Eulerian formulations) for interface tracking were necessary. The strong discontinuity of pressure across the air-water interface due to surface tension effects was accounted for naturally in the proposed model. The embedded formulation has been further extended by including viscous effects on the interface as a boundary condition for the water domain. Additionally, a two-way coupling technique has been included to account for the continuous air-water interaction. The convergence of the method has been studied, showing first order accuracy in time for the staggered version of the method.

The embedded multi-phase formulation presented in this work has been used to model the dynamics of a droplet in a PEFC channel. Oscillations of a sessile droplet in a free space have been obtained using both semi-analytical and embedded methods. Results were consistent with previous works, and excellent agreement was obtained with experimental data available. Effects of droplet size on detachment velocity and time have been also studied. Smaller droplets exhibit higher values of air velocity needed for detachment. Reasonable agreement between results and experimental data found in literature was obtained. Water injection in a gas channel has been studied and results have been compared to previous numerical and experimental results. Excellent agreement between experimental observation and numerical results has been obtained for early stages of droplet deformation. Results for water injection in a gas channel have been validated experimentally. Predicted droplet profiles and experimental observations show good agreement at early stages of droplet formation. Advancing contact angle increases approximately at a constant rate. On the other hand, receding angle increases during a short period of time, followed by a transition zone where receding angle remains constant. As the droplet volume increases, pressure and viscous effects deform the droplet in x-direction, and receding constant angle decreases until detachment was observed. Numerical results predict a lower rate of decrease than experimental results. This discrepancy may be due to effects in z-direction, not included in the present model for droplets in gas channels. Comparison between VOF and embedded models has studied as well. Current model predicts film formation, whereas VOF results show that a droplet was formed first. The present work manifests the first attempt of modeling droplet

dynamics in PEFC channels using an embedded Eulerian-Lagrangian approach.

It is worth mentioning that in the last decade there has been a general trend for most of numerical studies of water transport in fuel cell channels to use Volume of Fluid method. This method can be found in most commercial software, which makes it an attractive option to perform numerical modeling. The present work focuses on the development of novel techniques to study air-water (or gas-liquid) interactions in gas channels, instead of being limited to use an existing methodology. Results show that the embedded approach is a viable alternative to most used models in the fuel cell community and it can be used in future numerical studies.

6.2 Outcome

The following publications have been created as a result of the work presented in this thesis:

- A. Jarauta, M. Secanell, J. Pons-Prats, P. B. Ryzhakov, S. R. Idelsohn, and E. Oñate. A semi-analytical model for droplet dynamics on the GDL surface of a PEFC electrode. *International Journal of Hydrogen Energy*, 40:5375-5383,2015.

- P. B. Ryzhakov and A. Jarauta. An embedded approach for immiscible multi-fluid problems. *International Journal of Numerical Methods in Fluids*, 2015 (published online).

- A. Jarauta, P.B. Ryzhakov, M. Secanell and J. Pons-Prats. Numerical study of droplet dynamics in a Proton Exchange Fuel Cell gas channel using an embedded formulation. *Journal of Power Sources*, 2015 (under review, submitted on 2015/10/19).

6.3 Future work

a) **Substrate roughness.** Water droplets in gas channels emerge from GDL pores. Although a dynamic contact angle condition has been included in the model in order to account for the nature of GDL surface, roughness effects should be studied in more detail.

b) **Droplet breakup and coalescence.** Water droplets in gas channels may break into smaller droplets or may coalesce with other droplets in the channel. Droplet breakup and coalescence should be included in the model.

c) **Thermal effects.** Polymer Electrolyte fuel cells can operate at temperatures ranging from -40 to 100°C. For low temperatures, ice formation in the GDL pores drops the efficiency of the device, specially at start-up. On the other hand, for temperatures above 70°C part of the exceeding water evaporates. Thermal effects should be included to model phase change in water.

d) **Alternative solution schemes**. A Lagrangian monolithic scheme has been proposed for water. Monolithic schemes have a higher computational cost than other numerical schemes, such as pressure-correction scheme. The computational cost can increase drastically when slug or film flow modeling, specially in 3D studies. Alternative solution schemes for the water domain should be studied.

e) **Improved time accuracy**. The time accuracy of the embedded formulation is limited by the first time order accuracy of the coupling technique. Novel coupling techniques should be implemented to improve the time accuracy of the overall method.

f) **Computational optimization.** Droplet dynamics in PEFC channels often rely in fine meshes and small time steps. In order to perform numerical simulations of a fuel cell in working conditions, the C++ code implemented in this work should be further improved to reduce the computational cost.

References

[1] USA College of the Desert. *Hydrogen Fuel Cell Engines and Related Technologies*. College of the Desert, 1st edition, 2001.

[2] J.G. Carton, V. Lawlor, A.G. Olabi, C. Hochenauer, and G. Zauner. Water droplet accumulation and motion in PEM (Proton Exchange Membrane) fuel cell mini-channels. *Energy*, 39:63–73, 2012.

[3] M. Mier-Torrecilla. *Numerical simulation of multi-fluid flows with the Particle Finite Element Method*. PhD thesis, Universitat Politècnica de Catalunya, 2010.

[4] M. Cruchaga, D. Celentano, and T. Tezduyar. A moving Lagrangian interface technique for flow computations over fixed meshes. *Computer Methods in Applied Mechanics and Engineering*, 191(6):525–543, 2001.

[5] A.J.B. Milne and A. Amirfazli. Drop shedding by shear flow or hydrophilic to superhydrophobic surfaces. *Langmuir*, 25(24):14155–14164, 2009.

[6] S. C. Cho, Y. Wang, and K.S. Chen. Droplet dynamics in a polymer electrolyte fuel cell gas flow channel: Forces, deformation, and detachment. I: Theoretical and numerical analyses. *Journal of Power Sources*, 206:119–128, 2012.

[7] S. C. Cho, Y. Wang, and K.S. Chen. Droplet dynamics in a polymer electrolyte fuel cell gas flow channel: Forces, deformation and detachment. II: Comparisons of analytical solution with numerical and experimental results. *Journal of Power Sources*, 210:191–197, 2012.

[8] T.C. Wu and N. Djilali. Experimental investigation of water droplet emergence in a model polymer electrolyte membrane fuel cell microchannel. *Journal of Power Sources*, 208:248–256, 2012.

[9] X. Zhu, P.C. Sui, and N. Djilali. Numerical simulation of emergence of a water droplet from a pore into a microchannel gas stream. *Microfluid Nanofluid*, 4:543–555, 2008.

[10] C. Spiegel. *Designing and building fuel cells*. Mcgraw-hill New York, 2007.

[11] A. Jarauta, M. Secanell, J. Pons-Prats, P. B. Ryzhakov, S. R. Idelsohn, and E. Oñate. A semi-analytical model for droplet dynamics on the GDL surface of a PEFC electrode. *International Journal of Hydrogen Energy*, 40:5375–5383, 2015.

[12] A. Jarauta and J. Pons-Prats. Fuel cells: State of the art. *CIMNE technical report*, 2009.

[13] Nafion Store. `http://www.nafionstore.com/`. Accessed: 2015-12-10.

[14] A. Z. Weber, R. L. Borup, R. M. Darling, P. K. Das, T. J. Dursch, W. Gu, D. Harvey, A. Kusoglu, S. Litster, M. M. Mench, R. Mukundan, J. P. Owejan, J. G Pharoah, M. Secanell, and I. V. Zenyuk. A critical review of modeling transport phenomena in Polymer-Electrolyte fuel cells. *Journal of the Electrochemical Society*, 161(12):F1254–F1299, 2014.

[15] A. Theodorakakos, T. Ous, M. Gavaises, J.M. Nouri, N. Nikolopoulos, and H. Yanagihara. Dynamics of water droplets detached from porous surfaces of relevance to PEM fuel cells. *Journal of Colloid and Interface Science*, 300:673–687, 2006.

[16] X. Zhu, P.C. Sui, and N. Djilali. Three-dimensional numerical simulations of water droplet dynamics in a PEMFC gas channel. *Journal of Power Sources*, 181:101–115, 2008.

[17] X. Zhu, Q. Liao, P.C. Sui, and N. Djilali. Numerical investigation of water droplet dynamics in a low-temperature fuel cell microchannel: Effect of channel geometry. *Journal of Power Sources*, 195:801–812, 2010.

[18] E.C. Kumbur, K.V. Sharp, and M.M. Mench. Liquid droplet behavior and instability in a polymer electrolyte fuel cell flow channel. *Journal of Power Sources*, 161:333–345, 2006.

[19] K.S. Chen, M.A. Hickner, and D.R. Noble. Simplified models for predicting the onset of liquid water droplet instability at the gas diffusion layer/gas flow channel interface. *International Journal of Energy Research*, 29(12):1113–1132, 2005.

[20] Z. Zhan, C. Wang, W. Fu, and M. Pan. Visualization of water transport in a transparent PEMFC. *International Journal of Hydrogen Energy*, 37:1094–1105, 2012.

[21] F. Y. Zhang, X. G. Yang, and C. Y. Wang. Liquid water removal from a polymer electrolyte fuel cell. *Journal of The Electrochemical Society*, 153(2):A225–A232, 2006.

[22] M. Secanell, J. Wishart, and P. Dobson. Computational design and optimization of fuel cells and fuel cell systems: A review. *Journal of Power Sources*, 196:3690–3704, 2011.

[23] Z. Lu, S. G. Kandlikar, C. Rath, M. Grimm, W Domigan, A. D. White, M Hardbarger, J. P. Owejan, and T. A. Trabold. Water management studies in PEM fuel cells, Part II: Ex situ investigation of flow maldistribution, pressure drop and two-phase flow pattern in gas channels. *International Journal of Hydrogen Energy*, 34(8):3445–3456, 2009.

[24] A. Esposito, P. Polverino, C. Pianese, and Y.G. Guezennec. A lumped model of single droplet deformation, oscillation and detachment on the GDL surface of a PEM fuel cell. *ASME 2010 8th International Fuel Cell Science, Engineering and Technology Conference*, 2010.

[25] P. Quan and M.C. Lai. Numerical study of water management in the air flow channel of a PEM fuel cell cathode. *Journal of Power Sources*, 164:222–237, 2007.

[26] A. Golpaygan and N. Ashgriz. Effects of oxidant fluid properties on the mobility of water droplets in the channels of PEM fuel cell. *International journal of energy research*, 29(12):1027–1040, 2005.

[27] C.W. Hirt and B.D. Nichols. Volume of Fluid (VOF) method for the dynamics of free boundaries. *Journal of Computational Physics*, 39:201–225, 1981.

[28] J.U. Brackbill, D.B. Kothe, and C. Zemach. A continuum method for modeling surface tension. *Journal of Computational Physics*, 100:335–354, 1992.

[29] R. B. Ferreira, D. S. Falcão, V. B. Oliveira, and A. M. F. R. Pinto. Numerical simulations of two-phase flow in proton exchange membrane fuel cells using the volume of fluid method - A review. *Journal of Power Sources*, 277:329–342, 2015.

[30] N. Akhtar and P. J. A. M. Kerkhof. Dynamic behavior of liquid water transport in a tapered channel of a proton exchange membrane fuel cell cathode. *International Journal of Hydrogen Energy*, 36(4):3076–3086, 2011.

[31] J. Choi and G. Son. Numerical study of droplet dynamics in a PEMFC gas channel with multiple pores. *Journal of Mechanical Science and Technology*, 23(7):1765–1772, 2009.

[32] M. A. Hickner, N. P. Siegel, K. S. Chen, D. N. McBrayer, D. S. Hussey, D. L. Jacobson, and M. Arif. Real-time imaging of liquid water in an operating proton exchange membrane fuel cell. *Langmuir*, 22(14):6234–6237, 2006.

[33] R. Satija, D.L. Jacobson, M. Arif, and S.A. Werner. In situ neutron imaging technique for evaluation of water management systems in operating PEM fuel cells. *Journal of Power Sources*, 129:238–245, 2004.

[34] A. Hakenjos, H. Muenter, U. Wittstadt, and C. Hebling. A PEM fuel cell for combined measurement of current and temperature distribution, and flow field flooding. *Journal of Power Sources*, 131:213–216, 2004.

[35] M. M. Daino, Z. Lu, J. M. LaManna, J. P. Owejan, T. A. Trabold, and S. G. Kandlikar. Through-plane water transport visualization in a PEMFC by visible and infrared imaging. *Electrochemical and Solid-State Letters*, 14(6):B51–B54, 2011.

[36] M. Wang, K. W. Feindel, S. H. Bergens, and R. E. Wasylishen. In situ quantification of the in-plane water content in the nafion membrane of an operating polymer-electrolyte membrane fuel cell using 1h micro-magnetic resonance imaging experiments. *Journal of Power Sources*, 195:7316–7322, 2010.

[37] J. Eller and F. N. Büchi. Polymer electrolyte fuel cell performance degradation at different synchrotron beam intensities. *Journal of Synchrotron Radiation*, 21(1):82–88, 2014.

[38] C. E. Colosqui, M. J. Cheah, I. G. Kevrekidis, and J. B. Benziger. Droplet and slug formation in polymer electrolyte membrane fuel cell flow channels: The role of interfacial forces. *Journal of Power Sources*, 196:10057–10068, 2011.

[39] K. Tuber, D. Pócza, and C. Hebling. Visualization of water buildup in the cathode of a transparent PEM fuel cell. *Journal of Power Sources*, 124:403–414, 2003.

[40] X. G. Yang, F. Y. Zhang, A. L. Lubawy, and C. Y. Wang. Visualization of liquid water transport in a PEFC. *Electrochemical and Solid-State Letters*, 7(11):A408–A411, 2004.

[41] S.G. Kandlikar, Z. Lu, W.E. Domigan, A.D. White, and M.W. Benedict. Measurement of flow maldistribution in parallel channels and its application to ex-situ and in-situ experiments in PEMFC water management studies. *International Journal of Heat and Mass Transfer*, 52:1741–1752, 2009.

[42] N. Akhtar, A. Qureshi, J. Scholta, C. Hartnig, M. Messerschmidt, and W. Lehnert. Investigation of water droplet kinetics and optimization of channel geometry for PEM fuel cell cathodes. *International Journal of Hydrogen Energy*, 34:3104–3111, 2009.

[43] C.W. Extrand and Y. Kumagai. Liquid drops on an inclined plane: the relation between contact angles, drop shape, and retentive force. *Journal of Colloid and Interface Science*, 170:515–521, 1995.

[44] P. Dimitrakopoulos and J.J.L. Higdon. Displacement of fluid droplets from solid surfaces in low-Reynolds-number shear flows. *Journal of Fluid Mechanichs*, 336:351–378, 1997.

[45] P. Dimitrakopoulos. Deformation of a droplet adhering to a soplid interface in shear flow: onset of interfacial sliding. *Journal of Fluid Mechanichs*, 580:451–466, 2007.

[46] J.N. Israelachvili. *Intermolecular and Surface Forces*. Elsevier, 3rd edition, 2011.

[47] M. Bellet. Implementation of surface tension with wall adhesion effects in a three-dimensional finite element model for fluid flow. *Communications in Numerical Methods in Engineering*, 17:563–579, 2001.

[48] C.W. Extrand and A.N. Gent. Retention of liquid drops by solid surfaces. *Journal of Colloid and Interface Science*, 138(2):431–442, 1990.

[49] E.B. Dussan and R.T. Chow. On the ability of drops or bubbles to stick to non-horizontal surfaces of solids. *Journal of Fluid Mechanichs*, 137:1–29, 1983.

[50] C. Antonini, F.J. Carmona, E. Pierce, M. Marengo, and A. Amirfazli. General methodology for evaluating the adhesion force of drops and bubbles on solid surfaces. *Langmuir*, 25(11):6143–6154, 2009.

[51] F. Celestini and R. Kofman. Vibration of submillimeter-size supported droplets. *Physical Review*, 73(1), 2006.

[52] Energy Systems Design Laboratory (ESDLab), University of Alberta. `http://www.esdlab.mece.ualberta.ca/`.

[53] F.M. White. *Viscous Fluid Flow*. McGraw-Hill, 2nd edition, 1991.

[54] P. Dadvand, R. Rossi, and E. Oñate. An object-oriented environment for developing finite element codes for multi-disciplinary applications. *Archieves of Computational Methods in Engineering*, 17/3:253–297, 2010.

[55] V.R. Gopala and G.M. van Wachem. Volume of fluid methods for immiscible-fluid and free-surface flows. *Chemical Engineering Journal*, 141:204–221, 2008.

[56] S. Hysing. A new implicit surface tension implementation for interfacial flows. *International Journal of Numerical Methods in Fluids*, 6(51):659–672, 2006.

[57] P. H. Saksono and D. Perić. On finite element modelling of surface tension. Variational formulations and applications - Part I: Quasistatic problems. *Computational Mechanics*, 38:265–281, 2006.

[58] P. H. Saksono and D. Perić. On finite element modelling of surface tension. Variational formulations and applications - Part II: Dynamic problems. *Computational Mechanics*, 38:251–263, 2006.

[59] S.D. Hong, M.Y. Ha, and S. Balachandar. Static and dynamic contact angles of water droplet on a solid surface using molecular dynamics simulation. *Journal of Colloid and Interface Science*, 339:187–195, 2009.

[60] V. Cristini and Y. C. Tan. Theory and numerical simulation of droplet dynamics in complex flows - a review. *Lab on a Chip*, 4:257–264, 2004.

[61] M. Sussman and M. Ohta. A stable and efficient method for treating surface tension in incompressible two-phase flow. *SIAM Journal on Scientific Computing*, 31:2447–2471, 2009.

[62] R. Bird, W. Stewart, and E. Lightfoot. *Transport Phenomena*. John Wiley and Sons, 2nd edition, 2002.

[63] J. Donea and A. Huerta. *Finite Element Methods for Flow Problems*. John Wiley & Sons, 1st edition, 2003.

[64] J. N. Reddy. *An introduction to the finite element method*, volume 2. McGraw-Hill New York, 1993.

[65] P.B. Ryzhakov, E. Oñate, R. Rossi, and S.R. Idelsohn. Improving mass conservation in simulation of incompressible flows. *International Journal for Numerical Methods in Engineering*, 90:1435–1451, 2012.

[66] P.B. Ryzhakov, R. Rossi, S.R. Idelsohn, and E. Oñate. A monolithic Lagrangian approach for fluid-structure interaction problems. *Computational Mechanics*, 46:883–899, 2010.

[67] T. J. R. Hughes, L. P. Franca, and G. M. Hulbert. A new finite element formulation for computational fluid dynamics: VIII. the Galerkin/least-squares method for advective-diffusive equations. *Computer Methods in Applied Mechanics and Engineering*, 73(2):173–189, 1989.

[68] R. Codina. A stabilized finite element method for generalized stationary incompressible flows. *Computer Methods in Applied Mechanics and Engineering*, 190(20-21):2681 – 2706, 2001.

[69] R. Codina. Stabilization of incompressibility and convection through orthogonal sub-scales in finite element methods. *Computer Methods in Applied Mechanics and Engineering*, 190:1579–1599, 2000.

[70] E. Oñate. A stabilized finite element method for incompressible viscous flows using a finite increment calculus formulation. *Computer methods in applied mechanics and engineering*, 182(3):355–370, 2000.

[71] P. Ryzhakov, J. Cotela, R. Rossi, and E. Oñate. A two-step monolithic method for the efficient simulation of incompressible flows. *International Journal for Numerical Methods in Fluids*, 74(12):919–934, 2014.

[72] A. J. Chorin. A numerical method for solving incompressible viscous problems. *Journal of Computational Physics*, 2:12–26, 1967.

[73] R. Temam. Sur lapproximation de la solution des equations de Navier-Stokes par la methode des pase fractionaires. *Archives for Rational Mechanics and Analysis*, 32:135–153, 1969.

[74] R. Codina. Pressure stability in fractional step finite element method for incompressible flows. *Journal of Computational Physics*, 170:112–140, 2001.

[75] P. B. Ryzhakov and A. Jarauta. An embedded approach for immiscible multi-fluid problems. *International Journal of Numerical Methods in Fluids*, 2015. DOI: 10.1002/fld.4190.

[76] I. V. M. Tasso, S. S. Rodrigues, and G. C. Buscaglia. Assessment of curvature approximation methods in the simulation of viscous biological membranes.

[77] M. Meyer, M. Desbrun, P. Schröder, and A. H. Barr. Discrete differential-geometry operators for triangulated 2-manifolds. *Visualization and Math. III*, pages 35–57, 2003.

[78] P. J. Slikkerveer, E. P. Van Lohuizen, and S. B. G. O'Brien. An implicit surface tension algorithm for Picard solvers of surface-tension-dominated free and moving boundary problems. *Int. Journal for Numerical Methods in Fluids*, 22:851–865, 1996.

[79] H. Lamb. *Hydrodynamics*. Cambridge University Press: Cambridge, 4th edition, 1916.

[80] F. Denner and B.G.M. van Wachem. Numerical time-step restrictions as a result of capillary waves. *Journal of Computational Physics*, 285:24–40, 2015.

[81] E. Bänsch. Finite element discretization of the Navier–Stokes equations with a free capillary surface. *Numerische Mathematik*, 88(2):203–235, 2001.

[82] C.E. Weatherburn. *Differential Geometry of Three Dimensions*. Cambridge University Press, 4th edition, 1955.

[83] A.J.B. Milne and A. Amirfazli. The Cassie equation: How it is meant to be used. *Advances in colloid and interface science*, 170(1):48–55, 2012.

[84] S.F. Chini, V. Bertola, and A. Amirfazli. A methodology to determine the adhesion force of arbitrarily shaped drops with convex contact lines. *Colloids and Surfaces A: Physicochemical and Engineering Aspects*, 436:425–433, 2013.

[85] W. Bouwhuis, K. G. Winkels, I. R. Peters, P. Brunet, D. van der Meer, and J. H. Snoeijer. Oscillating and star-shaped drops levitated by an airflow. *Physical Review E*, 88:023017, 2013.

[86] P. R. Waghmare and S. K. Mitra. Contact angle hysteresis of microbead suspensions. *Langmuir*, 26(22):17082–17089, 2010.

[87] ImageJ, Image Processing and Analysis in Java. `http://imagej.nih.gov/ij/`. Accessed: 2015-03-16.

[88] A.F. Stalder, G. Kulik, D. Sage, L. Barbieri, and P. Hoffmann. A snake-based approach to accurate determination of both contact points and contact angles. *Colloids And Surfaces A: Physicochemical And Engineering Aspects*, 286(1-3):92–103, 2006.

[89] G. N. Doku, W. Verboom, D. N. Reinhoudt, and A. van der Berg. On microchip multiphase chemistry - a review of microreactor design principles and reagent contacting modes. *Tetrahedron*, 61(11):2733–2742, 2005.

[90] F. A. Gomez. *Biological applications of microfluidics*. Wiley, Hoboken, 1st edition, 2008.

[91] M. Wörner. Numerical modeling of multiphase flows in microfluidics and micro process engineering: a review of methods and applications. *Microfluid Nanofluid*, 12:841–886, 2012.

[92] C. E. Brennen. *Fundamentals of Multiphase Flow*. Cambridge University Press, 1st edition, 2005.

[93] C. T. Crowe. *Multiphase Flow Handbook*. Taylor & Francis, 1st edition, 2006.

[94] D. L. Youngs. Time-dependent multi-material flow with large fluid distortion. *Numerical methods for fluid dynamics*, 24:273–285, 1982.

[95] D. Gueyffier, J. Li, A. Nadim, R. Scardovelli, and S. Zaleski. Volume-of-Fluid interface tracking with smoothed surface stress methods for three dimensional flows. *Journal of Computational Physics*, 152:423–456, 1999.

[96] S. Osher and J.A. Sethian. Fronts propagating with curvature dependent speed: algorithms based on Hamilton-Jacobi formulations. *Journal of Computational Physics*, 79:12–49, 1988.

[97] S. J. Osher and R. P. Fedkiw. *Level Set Methods and Dynamic Implicit Surfaces*. Springer, 2006.

[98] R. Rossi, A. Larese, P. Dadvand, and E. Oñate. An efficient edge-based level set finite element method for free surface flow problems. *International Journal for Numerical Methods in Fluids*, 71(6):687–716, 2013.

[99] P. T. Barton, B. Obadia, and D. Drikakis. A conservative level-set method for compressible solid/fluid problems on fixed grids. *Journal of Computational Physics*, 230:7867–7890, 2011.

[100] P. D. M. Spelt. A level-set approach for simulations of flows with multiple moving contact lines with hysteresis. *Journal of Computational Physics*, 207(2):389–404, 2005.

[101] Y. L. Zhang, Q. P. Zou, and D. Greaves. Numerical simulation of free-surface flow using the level-set method with global mass correction. *International Journal of Numerical Methods in Fluids*, 63(6):366–396, 2010.

[102] R. F. Ausas, E. A. Dari, and G. C. Buscaglia. A geometric mass-preservating redistancing scheme for the level set function. *International Journal of Numerical Methods in Fluids*, 65(8):989–1010, 2011.

[103] M. Cruchaga, E. Oñate, and S. Idelsohn. On the pseudomaterial approach for the analysis of transient forming processes. *Communications in numerical methods in engineering*, 11(2):137–148, 1995.

[104] C.S. Peskin. The immersed boundary method. *Acta Numerica*, pages 479–517, 2002.

[105] S. Idelsohn, M. Mier-Torrecilla, and E. Oñate. Multi-fluid flows with the particle finite element method. *Computer Methods in Applied Mechanics and Engineering*, 198(33):2750–2767, 2009.

[106] K. Kamran, R. Rossi, E. Onate, and S.R. Idelsohn. A compressible Lagrangian framework for the simulation of the underwater implosion of large air bubbles. *Computer Methods in Applied Mechanics and Engineering*, 255:210–225, 2013.

[107] S. Chen and G.D. Doolen. Lattice Boltzmann method for fluid flows. *Annual Review of Fluid Mechanics*, 30:329–364, 1998.

[108] D. M. Heyes, J. Baxter, U. Tüzün, and R. S. Qin. Discrete-element method simulations: from micro to macro scales. *Phil. Trans. R. Soc. Lond. A*, 362:1853–1865, 2004.

[109] R. A. Gingold and J. J. Monaghan. Smoothed particle hydrodynamics: theory and application to non-spherical stars. *Monthly Notices of the Royal Astronomical Society*, 181:375–389, 1977.

[110] O. Kum, W.G. Hoover, and C.G. Hoover. Smooth-particle boundary conditions. *Physical Review E*, 68:017701–4, 2003.

[111] E. Oñate, S. Idelsohn, F. del Pin, and R. Aubry. The Particle Finite Element Method: an overview. *International Journal of Computational Methods*, 1:267–307, 2004.

[112] S. Idelsohn, E. Oñate, and F. del Pin. The particle finite element method: a powerful tool to solve incompressible flows with free-surfaces and breaking waves. *International Journal for Numerical Methods in Engineering*, 61:964–989, 2004.

[113] B. Delaunay. Sur la sphre vide. *Izvestia Akademii Nauk SSSR, Otdelenie Matematicheskikh i Estestvennykh Nauk*, 7:793–800, 1934.

[114] A. Gerstenberger and W.A. Wall. An eXtended Finite Element/Lagrange multiplier based approach for fluid-structure interaction. *Computer Methods in Applied Mechanics and Engineering*, 197:1699–1714, 2008.

[115] U. Küttler and W.A. Wall. Vector extrapolation for strong coupling fluid-structure interaction solvers. *Journal of Applied Mechanics*, 76(2):021205, 2009.

[116] A. Gerstenberger and W.A. Wall. An embedded Dirichlet formulation for 3D continua. *International Journal for Numerical Methods in Engineering*, 82(5):537–563, 2010.

[117] P. Ryzhakov, E. Oñate, R. Rossi, and S. Idelsohn. *Lagrangian FE methods for coupled problems in fluid mechanics.* CIMNE, 2010. ISBN: 978-84-96736-97-9.

[118] J. Marti, P. Ryzhakov, S. Idelsohn, and E. Oñate. Combined Eulerian-PFEM approach for analysis of polymers in fire situations. *International Journal for Numerical Methods in Engineering*, 92:782–801, 2012.

[119] J.L. Guermond, P. Minev, and J. Shen. An overview of projection methods for incompressible flows. *Computer Methods in Applied Mechanics and Engineering*, 195:6011–6045, 2006.

[120] R. Codina, G. Houzeaux, H. Coppola-Owen, and J. Baiges. The fixed-mesh ALE approach for the numerical approximation of flows in moving domains. *Journal of Computational Physics*, 228(5):1591 – 1611, 2009.

[121] T. Tezduyar, M. Behr, S. Mittal, and J. Liou. A new strategy for finite element computations involving moving boundaries and interfacesthe deforming-spatial-domain/space-time procedure: II. computation of free-surface flows, two-liquid flows, and flows with drifting cylinders. *Computer methods in applied mechanics and engineering*, 94(3):353–371, 1992.

[122] M. Cruchaga and E. Oñate. A generalized streamline finite element approach for the analysis of incompressible flow problems including moving surfaces. *Computer Methods in Applied Mechanics and Engineering*, 173(1):241–255, 1999.

[123] S. Idelsohn, N. Nigro, J. M. Gimenez, R. Rossi, and J. Marti. A fast and accurate method to solve the incompressible Navier-Stokes equations. *Engineering Computations*, 30(2):197–222, 2013.

[124] G. Minor. *Experimental study of water droplet flows in a model PEM fuel cell gas microchannel*. PhD thesis, University of Victoria, 2007.

Appendix A

Area ratio deduction

The droplet in its static configuration it's supposed to have the shape of a spherical cap, as shown on Figure A.1.

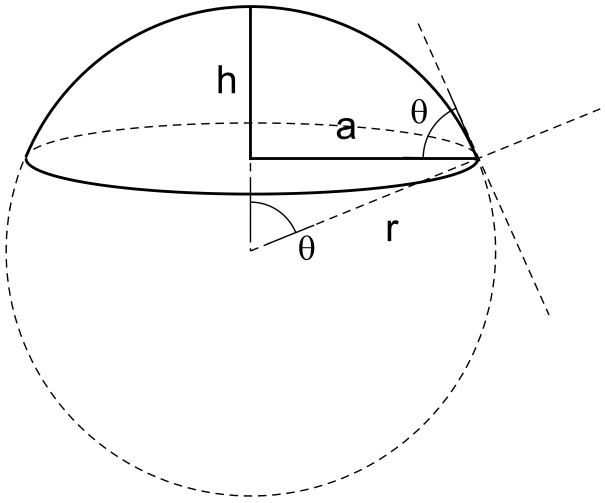

Figure A.1: Characterization of a droplet with a spherical cap shape

According to the considered geometry, the aforementioned areas can be described with equations (A.1) and (A.2), respectively.

$$A_{\mathrm{f}} = \pi a^2 = \pi \left(r\sin\theta\right)^2 = \pi r^2 \sin^2\theta \tag{A.1}$$

$$A_{\mathrm{c}} = 2\pi r h = 2\pi r \left(r - r\cos\theta\right) = 2\pi r^2 \left(1 - \cos\theta\right) \tag{A.2}$$

At equilibrium, equation (2.7) becomes (A.3)

$$\gamma_{LV} \left(dA_{\mathrm{c}} + dA_{\mathrm{f}}\right) - W_{\mathrm{SVL}} dA_{\mathrm{f}} = 0 \tag{A.3}$$

The expression in equation (A.3) can be divided by dA_{f}, giving the following equation:

$$\gamma_{LV} \left(\frac{dA_{\mathrm{c}}}{dA_{\mathrm{f}}} + 1\right) - W_{\mathrm{SVL}} = 0 \tag{A.4}$$

The derivative of A_c with respect A_f can be easily transformed using the chain rule:

$$\frac{dA_c}{dA_f} = \frac{dA_c}{d\theta}\frac{d\theta}{dA_f} = \frac{\frac{dA_c}{d\theta}}{\frac{dA_f}{d\theta}} \tag{A.5}$$

For a droplet of constant volume these derivatives can be found deriving the area expressions with respect to θ. According to equations (A.1) and (A.2), both areas depend on the radius of the sphere and the contact angle θ. However, the radius may depend on the angle. The volume of a spherical cap has the following expression:

$$V_{cap} = \frac{\pi h}{6}\left(3a^2 + h^2\right) \tag{A.6}$$

where a and h are the flat area radius and the cap height, respectively (Figure A.1). This equation can be expressed as a function of r and θ:

$$V_{cap} = \frac{\pi\left(r - r\cos\theta\right)}{6}\left(3\left(r\sin\theta\right)^2 + \left(r - r\cos\theta\right)^2\right) =$$

$$= \frac{\pi r\left(1 - \cos\theta\right)}{6}\left(3r^2\sin^2\theta + r^2\left(1 - \cos\theta\right)^2\right) =$$

$$= \frac{\pi}{6}r^3\left(1 - \cos\theta\right)\left(3\sin^2\theta + \left(1 - \cos\theta\right)^2\right) =$$

$$= \frac{\pi}{6}r^3\left(1 - \cos\theta\right)\left(2\sin^2\theta + \sin^2\theta + \cos^2\theta - 2\cos\theta + 1\right) =$$

$$= \frac{\pi}{6}r^3\left(1 - \cos\theta\right)\left(2\sin^2\theta + 1 - 2\cos\theta + 1\right) =$$

$$= \frac{\pi}{3}r^3\left(1 - \cos\theta\right)\left(\sin^2\theta + 1 - \cos\theta\right) =$$

$$= \frac{\pi}{3}r^3\left(1 - \cos\theta\right)\left(\left(1 - \cos^2\theta\right) + 1 - \cos\theta\right) =$$

$$= \frac{\pi}{3}r^3\left(1 - \cos\theta\right)\left(2 - \cos\theta - \cos^2\theta\right) =$$

$$= \frac{\pi}{3}r^3\left(2 - \cos^2\theta - \cos\theta - 2\cos\theta + \cos^3\theta + \cos^2\theta\right) =$$

$$= \frac{\pi}{3}r^3\left(2 - 3\cos\theta + \cos^3\theta\right) \tag{A.7}$$

Thus, for a spherical cap of constant volume, the radius depends on θ:

$$r = \left(\frac{V_{cap}}{\frac{\pi}{3}\left(2 - 3\cos\theta + \cos^3\theta\right)}\right)^{\frac{1}{3}} \tag{A.8}$$

Substituting the radius in equations (A.1) and (A.2) and deriving them with respect to θ, one obtains the following relationship:

$$\frac{dA_{\mathrm{c}}}{dA_{\mathrm{f}}} = \cos\theta \tag{A.9}$$

Conclusively, equation (A.4) becomes:

$$\gamma_{LV}\left(\cos\theta + 1\right) = W_{\mathrm{SVL}} \tag{A.10}$$

Appendix B

Droplet Geometry Model

The first step in the development of the droplet model is the full characterization of its geometry. The geometry model is based on the one developed by Esposito et al. [24] but with several corrections and improvements, which will be discussed in the following sections. The middle section of the deformed droplet is shown in Figure B.1. It is important to note that point A is the reference for the coordinate system used in the whole study (Figure 2.7).

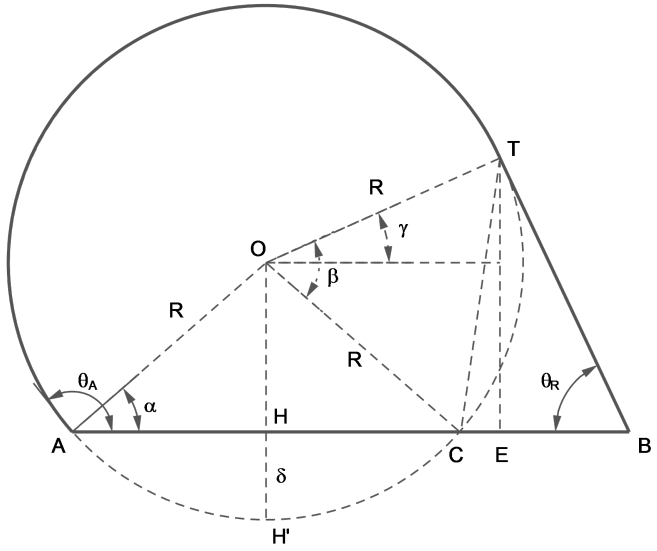

Figure B.1: Deformed droplet geometry. Air flows from right to left

The main points and angles have been labeled in order to follow better the explanation of each formula found. The first task is to characterize every distance and angle, before finding the area of every sector in the droplet.

B.1 Angles and distances

According to Figure B.1, the angle α is:

$$\theta_{\mathrm{A}} = \frac{\pi}{2} + \alpha \qquad \longrightarrow \qquad \alpha = \theta_{\mathrm{A}} - \frac{\pi}{2} \tag{B.1}$$

The first hypothesis used in the present model is that the segment $\bar{OT}$ is perpendicular to the segment $\bar{TB}$, hence the angle $\widehat{ETB}$ is equal to γ. Therefore:

$$\pi = \frac{\pi}{2} + \theta_{\mathrm{R}} + \gamma \qquad \longrightarrow \qquad \gamma = \frac{\pi}{2} - \theta_{\mathrm{R}} \tag{B.2}$$

The angle β can be found at point O, knowing that the angle $\widehat{HOC}$ is equal to $\frac{\pi}{2} - \alpha$:

$$\widehat{HOC} + (\beta - \gamma) = \frac{\pi}{2} \qquad \longrightarrow \qquad \frac{\pi}{2} - \alpha + \beta - \left(\frac{\pi}{2} - \theta_{\mathrm{R}}\right) = \frac{\pi}{2}$$

$$\frac{\pi}{2} - \left(\theta_{\mathrm{A}} - \frac{\pi}{2}\right) + \beta - \frac{\pi}{2} + \theta_{\mathrm{R}} = \frac{\pi}{2} \qquad \longrightarrow \qquad \frac{\pi}{2} - \theta_{\mathrm{A}} + \frac{\pi}{2} + \beta + \theta_{\mathrm{R}} = \pi$$

$$\beta = \theta_{\mathrm{A}} - \theta_{\mathrm{R}} \tag{B.3}$$

Once the angles have been characterized, the different distances are found. Distance $\bar{OH}$ can be found using:

$$\mathrm{sin}\alpha = \frac{\bar{OH}}{R} \qquad \longrightarrow \qquad \mathrm{sin}\left(\theta_{\mathrm{A}} - \frac{\pi}{2}\right) = \mathrm{sin}\theta_{\mathrm{A}}\mathrm{cos}\frac{\pi}{2} - \mathrm{cos}\theta_{\mathrm{A}}\mathrm{sin}\frac{\pi}{2} = -\mathrm{cos}\theta_{\mathrm{A}} = \frac{\bar{OH}}{R}$$

Therefore:

$$\bar{OH} = -R\mathrm{cos}\theta_{\mathrm{A}} \tag{B.4}$$

The distance δ can be found using the distance $\bar{OH}$:

$$R = \bar{OH} + \delta \qquad \longrightarrow \qquad \delta = R - \bar{OH} = R - (-R\mathrm{cos}\theta_{\mathrm{A}}) = R\,(1 + \mathrm{cos}\theta_{\mathrm{A}}) \tag{B.5}$$

$\bar{TC}$ is given by:

$$\frac{\bar{TC}}{2} = R\mathrm{sin}\frac{\beta}{2} \qquad \longrightarrow \qquad \bar{TC} = 2R\mathrm{sin}\frac{\beta}{2} \tag{B.6}$$

$\bar{AC}$ is obtained from geometrical arguments as:

$$\bar{AC} = 2\bar{AH} = 2R\mathrm{cos}\alpha = 2R\left(\mathrm{cos}\theta_{\mathrm{A}} - \frac{\pi}{2}\right) = 2R\left(\mathrm{cos}\theta_{\mathrm{A}}\mathrm{cos}\frac{\pi}{2} + \mathrm{sin}\theta_{\mathrm{A}}\mathrm{sin}\frac{\pi}{2}\right)$$

$$\bar{AC} = 2R\mathrm{sin}\theta_{\mathrm{A}} \tag{B.7}$$

Also, $\bar{CB}$ can be obtained using the the sine theorem applied in the triangle CTB. However, the angle $\widehat{CTB}$ has to be found first. In the triangle COT:

$$\beta + 2\widehat{OTC} = \pi \qquad \longrightarrow \qquad \widehat{OTC} = \frac{\pi}{2} - \frac{\beta}{2}$$

Knowing that the angle $\widehat{OTB}$ is equal to $\frac{\pi}{2}$:

$$\widehat{OTC} + \widehat{CTB} = \frac{\pi}{2} \qquad \longrightarrow \qquad \frac{\pi}{2} - \frac{\beta}{2} + \widehat{CTB} = \frac{\pi}{2}$$

Thus:

$$\widehat{CTB} = \frac{\beta}{2} \tag{B.8}$$

Applying the sine theorem in the triangle CTB:

$$\bar{CB} = \bar{TC}\frac{\sin\frac{\beta}{2}}{\sin\theta_{\mathrm{R}}} = 2R\frac{\sin^2\frac{\beta}{2}}{\sin\theta_{\mathrm{R}}} \tag{B.9}$$

B.1.1 Chord and height

The previous distances enable to find an expression for both the chord and the droplet height:

$$c = \bar{AC} + \bar{CB} = 2R\sin\theta_{\mathrm{A}} + 2R\frac{\sin^2\frac{\beta}{2}}{\sin\theta_{\mathrm{R}}} = 2R\left(\sin\theta_{\mathrm{A}} + \frac{\sin^2\frac{\beta}{2}}{\sin\theta_{\mathrm{R}}}\right)$$

However, this equation can be further simplified:

$$c = 2R\left(\sin\theta_{\mathrm{A}} + \frac{\sin^2\frac{\beta}{2}}{\sin\theta_{\mathrm{R}}}\right) = 2R\left(\sin\theta_{\mathrm{A}} + \frac{1-\cos\beta}{2\sin\theta_{\mathrm{R}}}\right) =$$

$$= R\left(2\sin\theta_{\mathrm{A}} + \frac{1-\cos\left(\theta_{\mathrm{A}}-\theta_{\mathrm{R}}\right)}{\sin\theta_{\mathrm{R}}}\right) =$$

$$= \frac{R}{\sin\theta_{\mathrm{R}}}\left(2\sin\theta_{\mathrm{A}}\sin\theta_{\mathrm{R}} + 1 - \left(\cos\theta_{\mathrm{A}}\cos\theta_{\mathrm{R}} + \sin\theta_{\mathrm{A}}\sin\theta_{\mathrm{R}}\right)\right) =$$

$$= \frac{R}{\sin\theta_{\mathrm{R}}}\left(2\sin\theta_{\mathrm{A}}\sin\theta_{\mathrm{R}} + 1 - \cos\theta_{\mathrm{A}}\cos\theta_{\mathrm{R}} - \sin\theta_{\mathrm{A}}\sin\theta_{\mathrm{R}}\right)$$

$$c = \frac{R}{\sin\theta_{\mathrm{R}}}\left(1 + \sin\theta_{\mathrm{A}}\sin\theta_{\mathrm{R}} - \cos\theta_{\mathrm{A}}\cos\theta_{\mathrm{R}}\right) \tag{B.10}$$

The droplet height can be easily found:

$$h = R + \bar{OH} = R - R\cos\theta_{\mathrm{A}} = R\left(1 - \cos\theta_{\mathrm{A}}\right) \tag{B.11}$$

The rest of the distances can be found using the previous relationships. Distance $\bar{TB}$ is found using again the sine theorem on the CTB triangle:

$$\frac{\bar{TB}}{\sin\widehat{TCB}} = \frac{\bar{TC}}{\sin\theta_{\mathrm{R}}} \qquad \longrightarrow \qquad \bar{TB} = \frac{2R\sin\frac{\beta}{2}}{\sin\theta_{\mathrm{R}}}\sin\widehat{TCB}$$

The angle $\widehat{TCB}$ equals to:

$$\widehat{TCB} + \theta_{\mathrm{R}} + \frac{\beta}{2} = \pi \qquad \longrightarrow \qquad \widehat{TCB} = \pi - \theta_{\mathrm{R}} - \frac{\beta}{2}$$

Then, the distance $\bar{TB}$ is:

$$\bar{TB} = \frac{2R\sin\frac{\beta}{2}}{\sin\theta_{\mathrm{R}}}\sin\left(\pi - \left(\theta_{\mathrm{R}} + \frac{\beta}{2}\right)\right) =$$

$$= \frac{2R\sin\frac{\beta}{2}}{\sin\theta_{\mathrm{R}}}\left(\sin\pi \cdot \cos\left(\theta_{\mathrm{R}} + \frac{\beta}{2}\right) - \cos\pi \cdot \sin\left(\theta_{\mathrm{R}} + \frac{\beta}{2}\right)\right)$$

$$\bar{TB} = \frac{2R\sin\frac{\beta}{2}}{\sin\theta_{\mathrm{R}}}\sin\left(\theta_{\mathrm{R}} + \frac{\beta}{2}\right) \tag{B.12}$$

Distance $\bar{TE}$ can be found using equation (B.12):

$$\sin\theta_{\mathrm{R}} = \frac{\bar{TE}}{\bar{TB}} \qquad \longrightarrow \qquad \bar{TE} = \bar{TB} \cdot \sin\theta_{\mathrm{R}} = \left(\frac{2R\sin\frac{\beta}{2}}{\sin\theta_{\mathrm{R}}}\sin\left(\theta_{\mathrm{R}} + \frac{\beta}{2}\right)\right)\sin\theta_{\mathrm{R}}$$

$$\bar{TE} = 2R\sin\left(\frac{\beta}{2}\right)\sin\left(\theta_{\mathrm{R}} + \frac{\beta}{2}\right) \tag{B.13}$$

Equivalently, the distance $\bar{EB}$ is equal to:

$$\cos\theta_{\mathrm{R}} = \frac{\bar{EB}}{\bar{TB}} \qquad \longrightarrow \qquad \bar{EB} = \bar{TB} \cdot \cos\theta_{\mathrm{R}} = \left(\frac{2R\sin\frac{\beta}{2}}{\sin\theta_{\mathrm{R}}}\sin\left(\theta_{\mathrm{R}} + \frac{\beta}{2}\right)\right)\cos\theta_{\mathrm{R}}$$

$$\bar{EB} = 2R\sin\left(\frac{\beta}{2}\right)\sin\left(\theta_{\mathrm{R}} + \frac{\beta}{2}\right)\mathrm{cotan}\theta_{\mathrm{R}} \tag{B.14}$$

It is important to note that this distance is negative for $\theta_{\mathrm{R}} > \frac{\pi}{2}$. The last distance to be characterized is $\bar{CE}$:

$$\bar{CE} = \bar{CB} - \bar{EB} = 2R\frac{\sin^2\frac{\beta}{2}}{\sin\theta_{\mathrm{R}}} - 2R\sin\left(\frac{\beta}{2}\right)\sin\left(\theta_{\mathrm{R}} + \frac{\beta}{2}\right)\mathrm{cotan}\theta_{\mathrm{R}}$$

$$\bar{CE} = 2R\frac{\sin\frac{\beta}{2}}{\sin\theta_{\mathrm{R}}}\left(\sin\frac{\beta}{2} - \sin\left(\theta_{\mathrm{R}} + \frac{\beta}{2}\right)\cos\theta_{\mathrm{R}}\right) \tag{B.15}$$

B.1.2 Perimeter

Once all the distances have been characterized, the perimeter is computed as follows:

$$P = \widehat{AT} + \bar{TB} = R\left(2\pi - \left(\beta + 2\left(\frac{\pi}{2} - \alpha\right)\right)\right) + \frac{2R\sin\frac{\beta}{2}}{\sin\theta_{\mathrm{R}}}\sin\left(\theta_{\mathrm{R}} + \frac{\beta}{2}\right)$$

The first term of the previous expression can be simplified:

$$2\pi - \left(\beta + 2\left(\frac{\pi}{2} - \alpha\right)\right) = 2\pi - \left(\theta_{\mathrm{A}} - \theta_{\mathrm{R}} + \pi - 2\left(\theta_{\mathrm{A}} - \frac{\pi}{2}\right)\right) =$$

$$= 2\pi - (\theta_A - \theta_R + \pi - 2\theta_A + \pi) = 2\pi - (2\pi - \theta_A - \theta_R) = \theta_A + \theta_R$$

Therefore:

$$P = R\left(\theta_A + \theta_R\right) + \frac{2R\sin\frac{\beta}{2}}{\sin\theta_R}\sin\left(\theta_R + \frac{\beta}{2}\right) \tag{B.16}$$

B.2 Area

The area of the middle section of the droplet can be calculated as:

$$A = A_{\text{circ}} - A_{\widehat{AH'C}} - A_{\widehat{CT}} + A_{\text{CTB}} \tag{B.17}$$

The areas of the different sectors are found in the following sections. The area of the circle is:

$$A_{\text{circ}} = \pi R^2 \tag{B.18}$$

On the other hand, the area of the sector $A_{\widehat{AH'C}}$ is:

$$A_{\widehat{AH'C}} = \frac{R^2}{2}\left(2\left(\frac{\pi}{2} - \alpha\right) - \sin\left(2\left(\frac{\pi}{2} - \alpha\right)\right)\right) = \frac{R^2}{2}\left(\pi - 2\alpha - \sin\left(\pi - 2\alpha\right)\right) \tag{B.19}$$

This expression can be simplified knowing that:

$$\pi - 2\alpha = \pi - 2\left(\theta_A - \frac{\pi}{2}\right) = \pi - 2\theta_A + \pi = 2\pi - 2\theta_A \tag{B.20}$$

and

$$\sin\left(\pi - 2\alpha\right) = \sin\left(2\pi - 2\theta_A\right) = \sin 2\pi \cdot \cos 2\theta_A - \cos 2\pi \cdot \sin 2\theta_A = -\sin 2\theta_A \tag{B.21}$$

Using equations (B.20) and (B.21) in (B.19), it yields:

$$A_{\widehat{AH'C}} = \frac{R^2}{2}\left(2\pi - 2\theta_A + \sin 2\theta_A\right) \tag{B.22}$$

The area of $A_{\widehat{CT}}$ is characterized as follows:

$$A_{\widehat{CT}} = \frac{R^2}{2}\left(\beta - \sin\beta\right) \tag{B.23}$$

The area of the triangle CTB can be easily found since distances $\bar{CB}$ and $\bar{TE}$ are already known:

$$A_{\text{CTB}} = \frac{1}{2}\bar{CB} \cdot \bar{TE} = \frac{1}{2}\left(2R\frac{\sin^2\frac{\beta}{2}}{\sin\theta_R}\right)\left(2R\sin\left(\frac{\beta}{2}\right)\sin\left(\theta_R + \frac{\beta}{2}\right)\right)$$

$$A_{\text{CTB}} = \frac{2R^2}{\sin\theta_R}\sin^3\left(\frac{\beta}{2}\right) \cdot \sin\left(\theta_R + \frac{\beta}{2}\right) \tag{B.24}$$

B.2.1 Droplet area

Considering the equations for the different sections of the area, equation (B.17) becomes:

$$A = \pi R^2 - \frac{R^2}{2}\left(2\pi - 2\theta_{\mathrm{A}} + \sin 2\theta_{\mathrm{A}}\right) - \frac{R^2}{2}\left(\beta - \sin\beta\right) + \frac{2R^2}{\sin\theta_{\mathrm{R}}}\sin^3\left(\frac{\beta}{2}\right)\cdot\sin\left(\theta_{\mathrm{R}} + \frac{\beta}{2}\right) \tag{B.25}$$

This equation can be further simplified using the known expression for β and simplifying some terms:

$$A = \frac{R^2}{2}\left(\theta_{\mathrm{A}} + \theta_{\mathrm{R}} - \sin 2\theta_{\mathrm{A}} + \sin\left(\theta_{\mathrm{A}} - \theta_{\mathrm{R}}\right) + \frac{4\sin^3\left(\frac{\theta_{\mathrm{A}} - \theta_{\mathrm{R}}}{2}\right)\sin\left(\frac{\theta_{\mathrm{A}} + \theta_{\mathrm{R}}}{2}\right)}{\sin\theta_{\mathrm{R}}}\right) \tag{B.26}$$

Finally, the equation for the droplet area in any configuration yields:

$$A = \frac{R^2}{2\sin\theta_{\mathrm{R}}}\left(\left[\theta_{\mathrm{A}} + \theta_{\mathrm{R}} - \sin 2\theta_{\mathrm{A}} + \sin\left(\theta_{\mathrm{A}} - \theta_{\mathrm{R}}\right)\right]\sin\theta_{\mathrm{R}} + \right.$$
$$\left. + 4\sin^3\left(\frac{\theta_{\mathrm{A}} - \theta_{\mathrm{R}}}{2}\right)\sin\left(\frac{\theta_{\mathrm{A}} + \theta_{\mathrm{R}}}{2}\right)\right) \tag{B.27}$$

B.3 Equation to solve

With all the distances and areas defined, the relationship between the advancing and receding angles can be found. When there is no force acting on the droplet, it can be considered as static with the geometry in Figure B.2.

The area of the static droplet is the following:

$$A_{\mathrm{S}} = R_{\mathrm{S}}^2\left(\theta_{\mathrm{S}} - \frac{\sin 2\theta_{\mathrm{S}}}{2}\right) \tag{B.28}$$

where the static radius R_{S} can be found using the following equation:

$$c_{\mathrm{S}} = 2R_{\mathrm{S}}\sin\theta_{\mathrm{S}} \longrightarrow R_{\mathrm{S}} = \frac{c_{\mathrm{S}}}{2\sin\theta_{\mathrm{S}}} \tag{B.29}$$

Therefore, the area of the static droplet can be written as follows:

$$A_{\mathrm{S}} = \left(\frac{c_{\mathrm{S}}}{2\sin\theta_{\mathrm{S}}}\right)^2\left(\theta_{\mathrm{S}} - \frac{\sin 2\theta_{\mathrm{S}}}{2}\right) = \frac{c_{\mathrm{S}}^2}{4\sin^2\theta_{\mathrm{S}}}\left(\theta_{\mathrm{S}} - \frac{\sin 2\theta_{\mathrm{S}}}{2}\right) = \frac{c_{\mathrm{S}}^2}{4}\cdot K_3 \tag{B.30}$$

Using the hypothesis of small deformations, the area of the middle section of the droplet can be supposed constant. Therefore, using both equations (B.27) and (B.30):

$$\frac{c_{\mathrm{S}}^2}{4}\cdot K_3 =$$

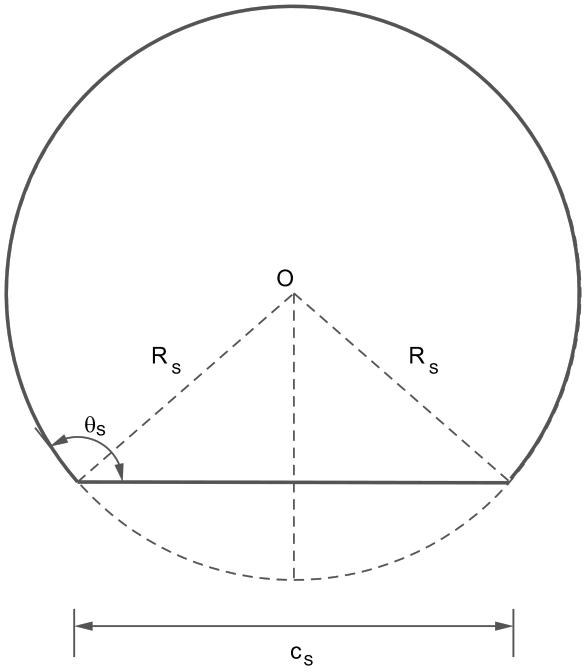

Figure B.2: Static droplet geometry

$$= \frac{R^2}{2\sin\theta_R}\left(\left[\theta_A + \theta_R - \sin 2\theta_A + \sin\left(\theta_A - \theta_R\right)\right]\sin\theta_R + 4\sin^3\left(\frac{\theta_A - \theta_R}{2}\right)\sin\left(\frac{\theta_A + \theta_R}{2}\right)\right) \tag{B.31}$$

The radius R can be substituted using the equation (B.10), and the previous equation yields:

$$\frac{c_S^2}{4}\cdot K_3 =$$

$$= \frac{1}{2\sin\theta_R}\left(\frac{c\cdot\sin\theta_R}{(1+\sin\theta_A\sin\theta_R - \cos\theta_A\cos\theta_R)}\right)^2 (\theta_A + \theta_R - \sin 2\theta_A + \sin\left(\theta_A - \theta_R\right) + \cdots) \tag{B.32}$$

The r.h.s. term can be further simplified and written in a more compact form:

$$\frac{c_S^2}{4}\cdot K_3 = \frac{c^2\cdot\sin\theta_R}{2K_2^2}\cdot K_1 \tag{B.33}$$

From equation (B.33), it can be seen that both terms in each side have the chord squared. It has been observed in some experiments that the chord length doesn't chance from the static droplet to the deformed one [24]. Therefore, both chord terms can be cancelled, giving the following equation in compact form:

$$\frac{K_3}{4} = \frac{\sin\theta_R}{2K_2^2}\cdot K_1 \qquad \longrightarrow \qquad K_2^2\cdot K_3 - 2\sin\theta_R\cdot K_1 = 0 \tag{B.34}$$

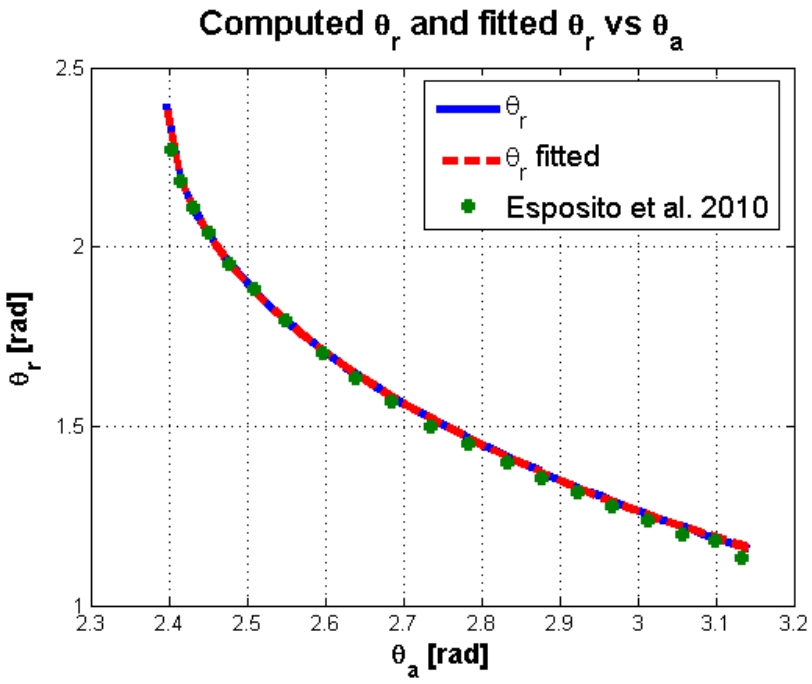

Figure B.3: Computed θ_R versus fitted θ_R

where:

$$K_1 = \left((\theta_A + \theta_R - \sin 2\theta_A + \sin(\theta_A - \theta_R)) \sin\theta_R + 4\sin^3 \left(\frac{\theta_A - \theta_R}{2} \right) \sin \left(\frac{\theta_A + \theta_R}{2} \right) \right) \tag{B.35}$$

$$K_2 = 1 + \sin\theta_A \sin\theta_R - \cos\theta_A \cos\theta_R \tag{B.36}$$

$$K_3 = \frac{1}{\sin^2\theta_S} \left(\theta_S - \frac{\sin 2\theta_S}{2} \right) \tag{B.37}$$

Equation (B.34) is solved in MATLAB for θ_R, and in each step a different value of θ_A is given, varying from θ_S to π. It is very important to note that the only two variables in this equation are the angles, which means that their relationship is the same regardless the size of the droplet. The result can be plotted in order to find a relationship between the advancing and receding angles.

Since it is impossible to find an explicit equation for the receding angle, a fitting function needs to be found in order to have an expression for this magnitude. Figure B.3 shows the computed values for the receding angle and a fitting curve, compared to the fitting curve found by the study of Esposito et al. [24]. From the yielding plot, one can observe two clearly different parts: from $\theta_A = 2.39$ to 2.43 rad, the receding angle drops quickly, whereas from 2.43 to π θ_R decreases almost linearly. Therefore, two different equations are proposed for the two parts of the curve. Using the free software CurveFit, the best curve for both cases is:

$$\theta_R = \frac{a + b\theta_A}{1 + c\theta_A + d\theta_A^2} \tag{B.38}$$

where the constants a, b, c and d have the values shown in Table 2.1.

B.4 Center of Mass

In this section, the expressions for both coordinates of the droplet center of mass are developed.

B.4.1 Circle

The center of mass coordinates are the same than the point O:

$$x_{\text{circ}} = R\sin\theta_{\text{A}} \tag{B.39}$$

$$y_{\text{circ}} = -R\cos\theta_{\text{A}} \tag{B.40}$$

The center of mass x-coordinate of the sector $\widehat{AHC}$ is the same than the circle:

$$x_{\widehat{AHC}} = \bar{AH} = R\sin\theta_{\text{A}} \tag{B.41}$$

On the other hand, the y-coordinate has to be computed using some known relationships. For a circular sector as the one shown on the following Figure B.4, the x-coordinate of the center of mass is:

$$x_{\widehat{AHCO}} = \frac{2R\sin\alpha_2}{3\alpha_2} \tag{B.42}$$

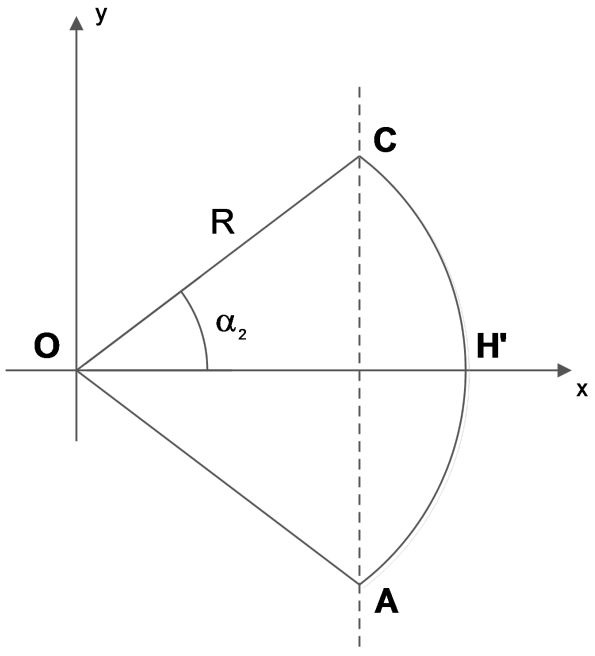

Figure B.4: Center of mass of a circular sector

Since the geometry is symmetric with respect the x axis, the y-coordinate of the center of mass is 0. Thus, the center of mass of the sector AH'C can be computed as the difference between the circular sector AH'CO and the triangle ACO:

$$x_{\widehat{AHC}} = \frac{x_{\widehat{AHCO}} A_{\widehat{AHCO}} - x_{\mathrm{ACO}} A_{\mathrm{ACO}}}{A_{\mathrm{AHC}}} \tag{B.43}$$

where

$$A_{\widehat{AHCO}} = \frac{1}{2} R^2 2\alpha_2 = R^2 \alpha_2 \tag{B.44}$$

$$x_{\mathrm{ACO}} = \frac{2R\mathrm{cos}\alpha_2}{3} \tag{B.45}$$

$$A_{\mathrm{ACO}} = 2 \cdot \frac{1}{2} R\mathrm{sin}\alpha_2 R\mathrm{cos}\alpha_2 = R^2 \mathrm{sin}\alpha_2 \mathrm{cos}\alpha_2 = R^2 \frac{\mathrm{sin}2\alpha_2}{2} \tag{B.46}$$

$$A_{\mathrm{AHC}} = A_{\widehat{AHCO}} - A_{\mathrm{ACO}} = R^2 \alpha_2 - R^2 \frac{\mathrm{sin}2\alpha_2}{2} \tag{B.47}$$

Therefore, equation (B.43) becomes:

$$x_{\widehat{AHC}} = \frac{\frac{2R\mathrm{sin}\alpha_2}{3\alpha_2} R^2 \alpha_2 - \frac{2R\mathrm{cos}\alpha_2}{3} R^2 \frac{\mathrm{sin}2\alpha_2}{2}}{R^2 \alpha_2 - R^2 \frac{\mathrm{sin}2\alpha_2}{2}} \tag{B.48}$$

Simplifying terms, the previous expression yields:

$$x_{\widehat{AHC}} = \frac{\frac{2R\mathrm{sin}\alpha_2}{3} \left(1 - \mathrm{cos}^2\alpha_2\right)}{\alpha_2 - \frac{\mathrm{sin}2\alpha_2}{2}} = \frac{\frac{2R\mathrm{sin}\alpha_2}{3} \left(\mathrm{sin}^2\alpha_2\right)}{\alpha_2 - \frac{\mathrm{sin}2\alpha_2}{2}} = \frac{\frac{2R\mathrm{sin}^3\alpha_2}{3}}{\alpha_2 - \frac{\mathrm{sin}2\alpha_2}{2}} \tag{B.49}$$

In this case, the angle α_2 is:

$$\alpha_2 = \frac{\pi}{2} - \alpha = \frac{\pi}{2} - \left(\theta_{\mathrm{A}} - \frac{\pi}{2}\right) = \pi - \theta_{\mathrm{A}} \tag{B.50}$$

The expressions with the sine of α_2 can be simplified:

$$\mathrm{sin}\alpha_2 = \mathrm{sin}\left(\pi - \theta_{\mathrm{A}}\right) = \mathrm{sin}\pi \cdot \mathrm{cos}\theta_{\mathrm{A}} - \mathrm{cos}\pi \cdot \mathrm{sin}\theta_{\mathrm{A}} = \mathrm{sin}\theta_{\mathrm{A}} \tag{B.51}$$

$$\mathrm{sin}2\alpha_2 = \mathrm{sin}\left(2\pi - 2\theta_{\mathrm{A}}\right) = \mathrm{sin}2\pi \cdot \mathrm{cos}2\theta_{\mathrm{A}} - \mathrm{cos}2\pi \cdot \mathrm{sin}2\theta_{\mathrm{A}} = -\mathrm{sin}2\theta_{\mathrm{A}} \tag{B.52}$$

Then, equation (B.49) becomes:

$$x_{\widehat{AHC}} = \frac{\frac{2}{3} R\mathrm{sin}^3\theta_{\mathrm{A}}}{\left(\pi - \theta_{\mathrm{A}}\right) + \frac{\mathrm{sin}2\theta_{\mathrm{A}}}{2}} \tag{B.53}$$

However, this expression is based on the system of coordinates shown in Figure B.4. The coordinates in the global system of coordinates are:

$$y_{\widehat{AHC}} = -\frac{\frac{2}{3} R\mathrm{sin}^3\theta_{\mathrm{A}}}{\left(\pi - \theta_{\mathrm{A}}\right) - \frac{\mathrm{sin}2\theta_{\mathrm{A}}}{2}} + R\mathrm{sin}\alpha = -\frac{\frac{2}{3} R\mathrm{sin}^3\theta_{\mathrm{A}}}{\left(\pi - \theta_{\mathrm{A}}\right) + \frac{\mathrm{sin}2\theta_{\mathrm{A}}}{2}} - R\mathrm{cos}\theta_{\mathrm{A}} \tag{B.54}$$

Both equations (B.41) and (B.54) give an expression for the $\widehat{AHC}$ center of mass.

The equations used for $\widehat{CT}$ sector are the same than the ones for the $\widehat{AHC}$ sector, but this one is rotated with an angle α_3 (Figure B.5). Using the relationships in the previous section, but substituting the angle α_2 by $\frac{\beta}{2}$:

$$x_{\widehat{CT}} = \frac{\frac{2}{3}R\sin^3\frac{\beta}{2}}{\frac{\beta}{2} - \frac{\sin 2\frac{\beta}{2}}{2}} \tag{B.55}$$

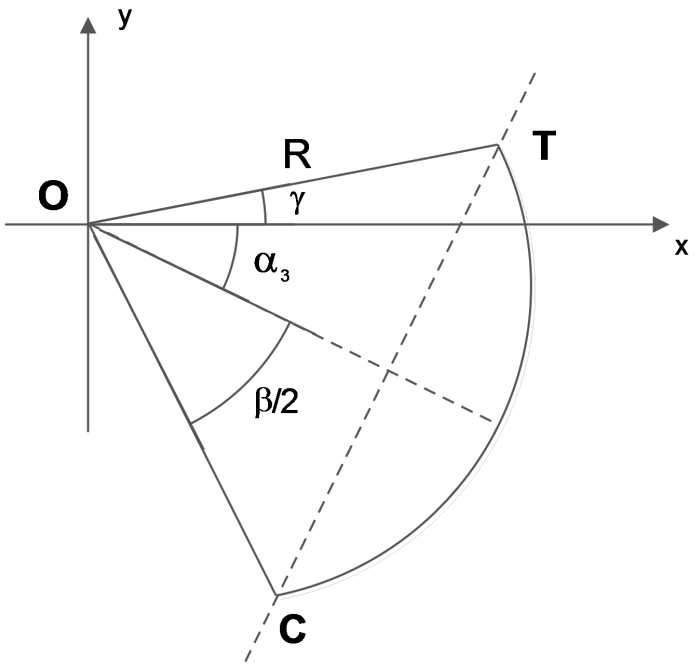

Figure B.5: Center of mass of the sector CT

This expression is for the sector before the rotation. The global coordinates of the center of mass can be found with the projection of this distance using the angle α_3:

$$x_{\widehat{CT}} = \left(\frac{\frac{2}{3}R\sin^3\frac{\beta}{2}}{\frac{\beta}{2} - \frac{\sin 2\frac{\beta}{2}}{2}}\right) \cdot \cos\alpha_3 \tag{B.56}$$

$$y_{\widehat{CT}} = -\left(\frac{\frac{2}{3}R\sin^3\frac{\beta}{2}}{\frac{\beta}{2} - \frac{\sin 2\frac{\beta}{2}}{2}}\right) \cdot \sin\alpha_3 \tag{B.57}$$

Taking into account the coordinates of the point O in the global coordinates, the final expressions yield:

$$x_{\widehat{CT}} = R\sin\theta_{\mathrm{A}} + \left(\frac{\frac{2}{3}R\sin^3\frac{\beta}{2}}{\frac{\beta}{2} - \frac{\sin\beta}{2}}\right) \cdot \cos\alpha_3 \tag{B.58}$$

$$y_{\widehat{CT}} = -R\cos\theta_{\mathrm{A}} - \left(\frac{\frac{2}{3}R\sin^3\frac{\beta}{2}}{\frac{\beta}{2} - \frac{\sin\beta}{2}} \right) \cdot \sin\alpha_3 \tag{B.59}$$

The angle α_3 can be easily computed as:

$$\frac{\beta}{2} + \alpha_3 + \gamma = \beta \qquad \longrightarrow \qquad \alpha_3 = \frac{\beta}{2} - \gamma \tag{B.60}$$

Using both relationships expressed in (B.3) and (B.2), the previous expression yields:

$$\alpha_3 = \frac{\theta_{\mathrm{A}} - \theta_{\mathrm{R}}}{2} - \left(\frac{\pi}{2} - \theta_{\mathrm{R}}\right) = \frac{\theta_{\mathrm{A}}}{2} - \frac{\theta_{\mathrm{R}}}{2} - \frac{\pi}{2} + \theta_{\mathrm{R}} = \frac{\theta_{\mathrm{A}} + \theta_{\mathrm{R}}}{2} - \frac{\pi}{2} \tag{B.61}$$

The sine and cosine of α_3 yield:

$$\sin\alpha_3 = \sin\left(\frac{\theta_{\mathrm{A}} + \theta_{\mathrm{R}}}{2} - \frac{\pi}{2}\right) = \sin\frac{\theta_{\mathrm{A}} + \theta_{\mathrm{R}}}{2} \cdot \cos\frac{\pi}{2} - \cos\frac{\theta_{\mathrm{A}} + \theta_{\mathrm{R}}}{2} \cdot \sin\frac{\pi}{2} = -\cos\frac{\theta_{\mathrm{A}} + \theta_{\mathrm{R}}}{2} \tag{B.62}$$

$$\cos\alpha_3 = \cos\left(\frac{\theta_{\mathrm{A}} + \theta_{\mathrm{R}}}{2} - \frac{\pi}{2}\right) = \cos\frac{\theta_{\mathrm{A}} + \theta_{\mathrm{R}}}{2} \cdot \cos\frac{\pi}{2} + \sin\frac{\theta_{\mathrm{A}} + \theta_{\mathrm{R}}}{2} \cdot \sin\frac{\pi}{2} = \sin\frac{\theta_{\mathrm{A}} + \theta_{\mathrm{R}}}{2} \tag{B.63}$$

Finally, the expressions (B.58) and (B.59) yield:

$$x_{\widehat{CT}} = R\sin\theta_{\mathrm{A}} + \left(\frac{\frac{2}{3}R\sin^3\frac{\beta}{2}}{\frac{\beta}{2} - \frac{\sin\beta}{2}} \right) \cdot \sin\frac{\theta_{\mathrm{A}} + \theta_{\mathrm{R}}}{2} \tag{B.64}$$

$$y_{\widehat{CT}} = -R\cos\theta_{\mathrm{A}} + \left(\frac{\frac{2}{3}R\sin^3\frac{\beta}{2}}{\frac{\beta}{2} - \frac{\sin\beta}{2}} \right) \cdot \cos\frac{\theta_{\mathrm{A}} + \theta_{\mathrm{R}}}{2} \tag{B.65}$$

The center of mass of CTE triangle can be easily found with the following relationships:

$$x_{CTE} = \bar{AC} + \frac{2}{3}\bar{CE} = 2R\sin\theta_{\mathrm{A}} + \frac{2}{3}\left(2R\frac{\sin\frac{\beta}{2}}{\sin\theta_{\mathrm{R}}}\left(\sin\frac{\beta}{2} - \sin\left(\theta_{\mathrm{R}} + \frac{\beta}{2}\right)\cos\theta_{\mathrm{R}}\right)\right) \tag{B.66}$$

$$y_{CTE} = \frac{1}{3}\bar{TE} = \frac{2R}{3}\sin\left(\frac{\beta}{2}\right)\sin\left(\theta_{\mathrm{R}} + \frac{\beta}{2}\right) \tag{B.67}$$

The center of mass of ETB triangle depends on the value of θ_{R} since, according to equation (B.14), the distance $\bar{EB}$ is negative or positive for certain values of the receding angle. Therefore, the area of this triangle becomes negative when $\theta_{\mathrm{R}} > \frac{\pi}{2}$, whereas it is positive when $\theta_{\mathrm{R}} < \frac{\pi}{2}$ as shown in Figure B.6. Notice that the area is exactly 0 when $\theta_{\mathrm{R}} = \frac{\pi}{2}$.

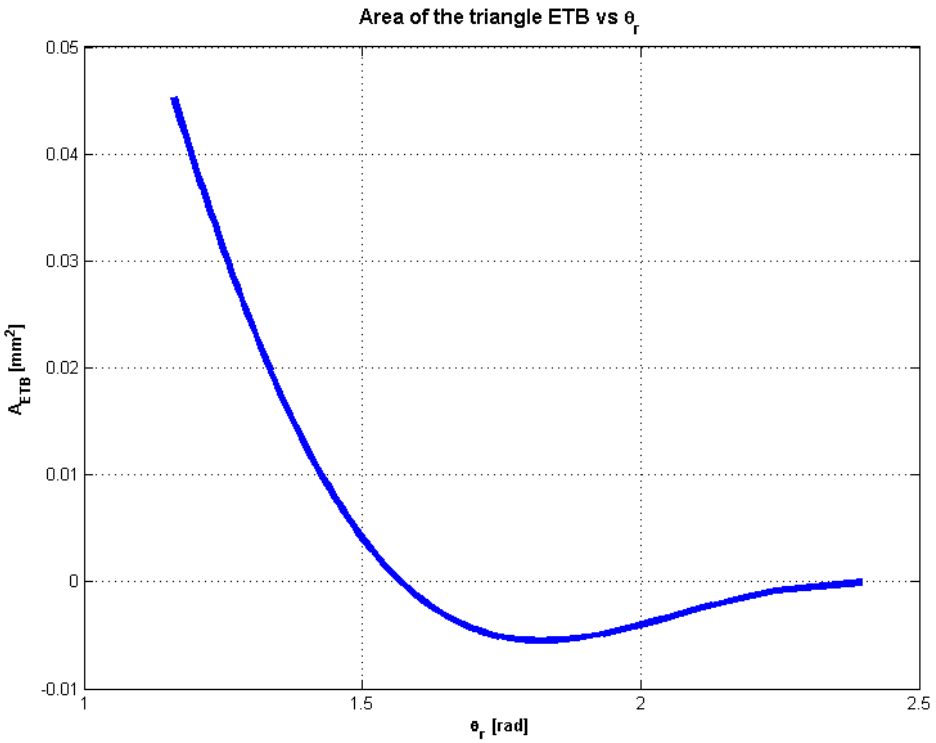

Figure B.6: Area of the ETB triangle depending on θ_{R}

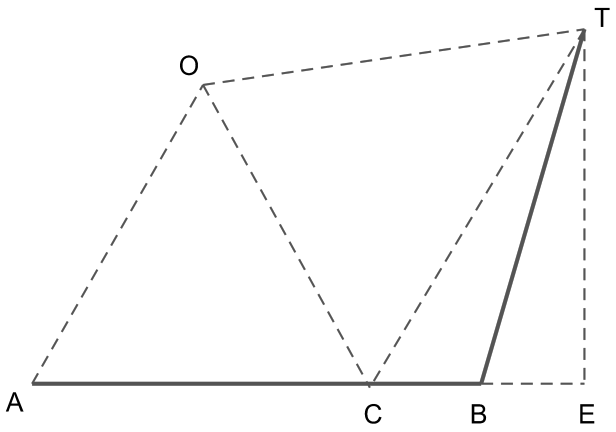

Figure B.7: Triangle ETB for values of $\theta_{\mathrm{R}} > \frac{\pi}{2}$

Due to the change in the sign, two possible situations are studied depending on the value of the receding angle in order to see if there is any difference in the computation.

Figure B.7 shows the shape of triangle ETB when $\theta_{\mathrm{R}} > \frac{\pi}{2}$. Therefore, the x coordinate of the center of mass can be computed as follows:

$$x_{ETB} = \bar{AC} + \bar{CB} + \frac{2}{3}\bar{EB} =$$

$$= 2R\mathrm{sin}\theta_{\mathrm{A}} + 2R\frac{\mathrm{sin}^2\frac{\beta}{2}}{\mathrm{sin}\theta_{\mathrm{R}}} + \left|\frac{4}{3}R\mathrm{sin}\left(\frac{\beta}{2}\right)\mathrm{sin}\left(\theta_{\mathrm{R}} + \frac{\beta}{2}\right)\mathrm{cotan}\theta_{\mathrm{R}}\right| \tag{B.68}$$

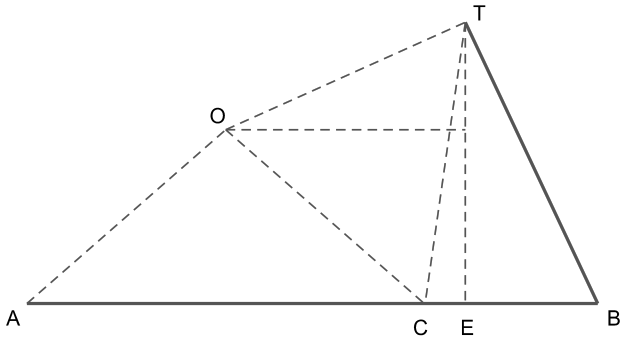

Figure B.8: Triangle ETB for values of $\theta_{\mathrm{R}} < \frac{\pi}{2}$

On the other hand, when $\theta_{\mathrm{R}} < \frac{\pi}{2}$ as shown in Figure B.8, the x coordinate of the center of mass can be computed as follows:

$$x_{ETB} = \bar{AC} + \bar{CE} + \frac{1}{3}\bar{EB} = \bar{AC} + \bar{CB} - \bar{EB} + \frac{1}{3}\bar{EB} = \bar{AC} + \bar{CB} - \frac{2}{3}\bar{EB}$$

$$= 2R\mathrm{sin}\theta_{\mathrm{A}} + 2R\frac{\mathrm{sin}^2\frac{\beta}{2}}{\mathrm{sin}\theta_{\mathrm{R}}} - \frac{4}{3}R\mathrm{sin}\left(\frac{\beta}{2}\right)\mathrm{sin}\left(\theta_{\mathrm{R}} + \frac{\beta}{2}\right)\mathrm{cotan}\theta_{\mathrm{R}} \tag{B.69}$$

$$y_{ETB} = \frac{1}{3}\bar{TE} = \frac{2R}{3}\mathrm{sin}\frac{\beta}{2}\mathrm{sin}\left(\theta_{\mathrm{R}} + \frac{\beta}{2}\right) \tag{B.70}$$

Looking at equations (B.68) and (B.69) it can be concluded that the same equation works for any value of the receding angle. It is important to note that this result does not agree with the one shown by Esposito et al. [24]. The results found in that study state that there is indeed a difference on the x_{ETB} equation depending on the value of θ_{R}. When $\theta_{\mathrm{R}} > \frac{\pi}{2}$, the equation is the same that equation (B.68):

$$x_{ETB} = 2R\mathrm{sin}\theta_{\mathrm{A}} + 2R\frac{\mathrm{sin}^2\frac{\beta}{2}}{\mathrm{sin}\theta_{\mathrm{R}}} - \frac{4}{3}R\mathrm{sin}\left(\frac{\beta}{2}\right)\mathrm{sin}\left(\theta_{\mathrm{R}} + \frac{\beta}{2}\right)\mathrm{cotan}\theta_{\mathrm{R}}$$

Nonetheless, the equation for $\theta_{\mathrm{R}} < \frac{\pi}{2}$ is the following:

$$x_{ETB} = 2R\mathrm{sin}\theta_{\mathrm{A}} + 2R\frac{\mathrm{sin}^2\frac{\beta}{2}}{\mathrm{sin}\theta_{\mathrm{R}}} + \frac{2}{3}R\mathrm{sin}\left(\frac{\beta}{2}\right)\mathrm{sin}\left(\theta_{\mathrm{R}} + \frac{\beta}{2}\right)\mathrm{cotan}\theta_{\mathrm{R}}$$

The easiest way to see which formula makes sense is to plot both equations in the same chart. Figure B.9 shows the difference between the previous expressions. Before reaching any conclusion, it is worth mentioning that the plot has been obtained using a droplet of a fixed chord, in this case 0.5mm. Therefore, according to Esposito et al., the center of mass x-coordinate of the ETB triangle is always greater than the chord. This result is not physical.

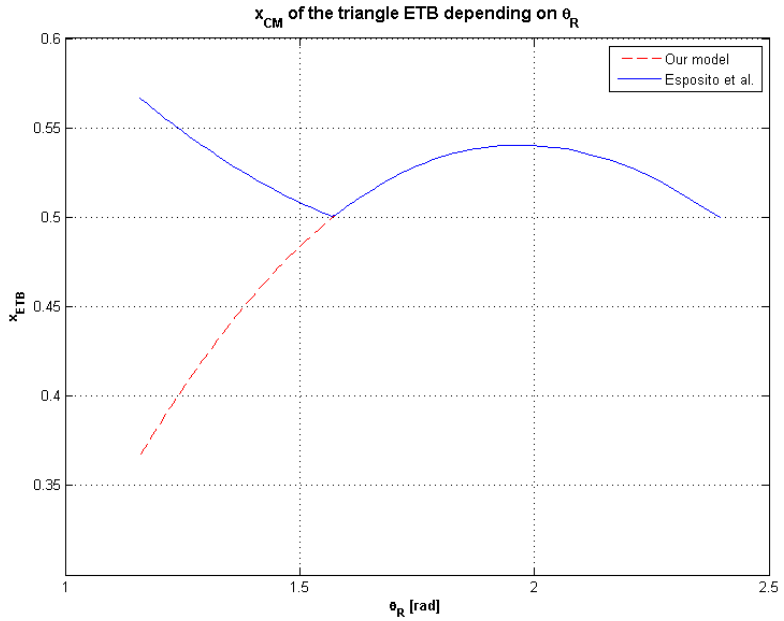

Figure B.9: Center of mass coordinates depending on θ_{A}

Alternatively, the present model uses the same formula for both cases and the result makes sense: when $\theta_{\mathrm{R}} > \frac{\pi}{2}$, the center of mass of the ETB triangle is outside the droplet and is greater than the chord. On the other hand, when $\theta_{\mathrm{R}} < \frac{\pi}{2}$ the center of mass of the aforementioned triangle is inside the droplet, which means that its x-coordinate has to be less than the chord.

Finally, the center of mass of the droplet can be computed using the different equations displayed in the previous sections:

$$x_{\mathrm{drop}} = \frac{x_{\mathrm{circ}}A_{\mathrm{circ}} - x_{\widehat{AHC}}A_{\widehat{AHC}} - x_{\widehat{CT}}A_{\widehat{AHC}} + x_{\mathrm{CTE}}A_{\mathrm{CTE}} + x_{\mathrm{ETB}}A_{\mathrm{ETB}}}{A} \tag{B.71}$$

$$y_{\mathrm{drop}} = \frac{y_{\mathrm{circ}}A_{\mathrm{circ}} - y_{\widehat{AHC}}A_{\widehat{AHC}} - y_{\widehat{CT}}A_{\widehat{AHC}} + y_{\mathrm{CTE}}A_{\mathrm{CTE}} + y_{\mathrm{ETB}}A_{\mathrm{ETB}}}{A} \tag{B.72}$$

Having the center of mass well characterized, the previous equations are implemented in MATLAB, and the relationship of both coordinates of the center of mass with the advancing angle can be seen in Figure B.10. Additionally, the results obtained by Esposito et al. [24] are displayed as well, proving that there is a good agreement between both results.

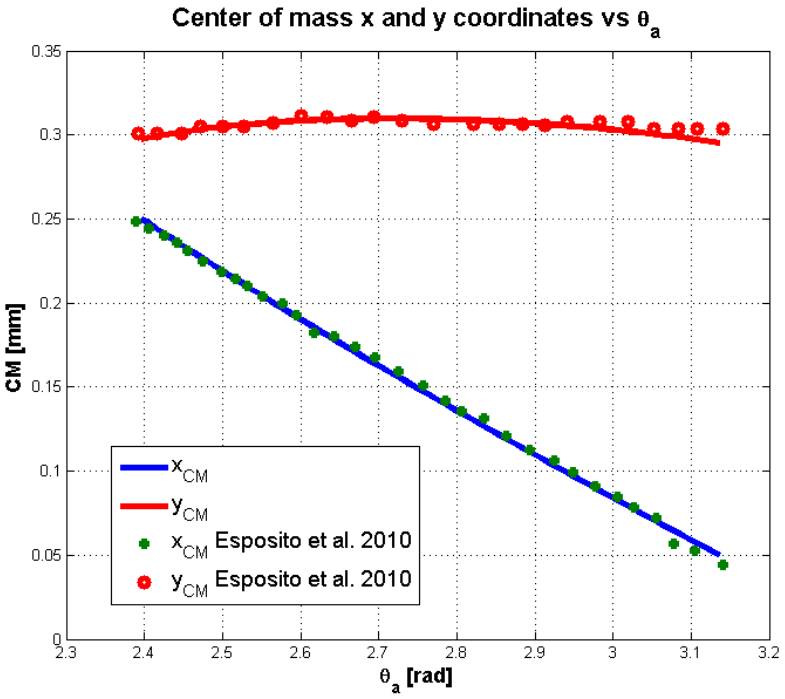

Figure B.10: Center of mass coordinates depending on θ_A

Two conclusions can be extracted from Figure B.10. Firstly, the y-coordinate of the mass center is fairly constant with respect the advancing angle. In addition, the relationship between the x-coordinate and θ_A is linear, so a fitting curve can be obtained. This means that if one can find an explicit relationship between the x-coordinate and the advancing angle, it is also possible to find its relationship with the radius, the height and the perimeter of the droplet.

B.5 Volume of the droplet

Another important variable that needs to be parameterized is the droplet volume. Figure B.2 shows the geometry of a static droplet laying on a horizontal surface. Its volume can be computed as the difference between the volume of the sphere of radius R_s minus the volume of the spherical cap:

$$V_{drop} = V_{sphere} - V_{cap} \tag{B.73}$$

B.5.1 Volume of the sphere

The equation for the sphere volume is well-known. For a sphere of radius R_s:

$$V_{sphere} = \frac{4}{3}\pi R_s^3 \tag{B.74}$$

B.5.2 Volume of the spherical cap

The volume of a spherical cap (Figure A.1 in Appendix A is computed according to the following equation:

$$V_{cap} = \frac{\pi\delta_s}{6}\left(3\left(\frac{c_s}{2}\right)^2 + \delta_s^2\right) \tag{B.75}$$

where c_s is the droplet chord, which is computed using equation (B.29), and the distance δ (Figure B.1) can be computed using equation (B.5):

$$\delta_s = R_s\left(1 + \cos\theta_s\right) \tag{B.76}$$

Thus, using equations (B.29) and (B.76), equation (B.75) yields:

$$V_{cap} = \frac{\pi R_s\left(1+\cos\theta_s\right)}{6}\left(3\left(R_s\sin\theta_s\right)^2 + R_s^2\left(1+\cos\theta_s\right)^2\right) =$$

$$= \frac{\pi}{6}R_s^3\left(1+\cos\theta_s\right)\left[3\sin^2\theta_s + 1 + 2\cos\theta_s + \cos^2\theta_s\right] \tag{B.77}$$

The term between brackets in equation (B.77) can be further simplified:

$$3\sin^2\theta_s + 1 + 2\cos\theta_s + \cos^2\theta_s = 2\sin^2\theta_s + \sin^2\theta_s + 1 + 2\cos\theta_s + \cos^2\theta_s =$$

$$= 2\sin^2\theta_s + 1 + 2\cos\theta_s + 1 = 2\left(\sin^2\theta_s + 1 + \cos\theta_s\right) \tag{B.78}$$

On the other hand:

$$\sin^2\theta_s = 1 - \cos^2\theta_s = \left(1-\cos\theta_s\right)\left(1+\cos\theta_s\right) \tag{B.79}$$

Substituting the term $\sin^2\theta_s$ in equation (B.78), it yields:

$$2\left(\sin^2\theta_s + 1 + \cos\theta_s\right) = 2\left[\left(1-\cos\theta_s\right)\left(1+\cos\theta_s\right) + 1 + \cos\theta_s\right] =$$

$$= 2\left(1+\cos\theta_s\right)\left[\left(1-\cos\theta_s\right) + 1\right] = 2\left(1+\cos\theta_s\right)\left(2-\cos\theta_s\right) \tag{B.80}$$

Getting back to equation (B.77), the term between brackets is substituted by the simplified term in equation (B.80):

$$V_{cap} = \frac{\pi}{6}R_s^3\left(1+\cos\theta_s\right)2\left(1+\cos\theta_s\right)\left(2-\cos\theta_s\right) = \frac{\pi}{3}R_s^3\left(1+\cos\theta_s\right)^2\left(2-\cos\theta_s\right) \tag{B.81}$$

B.5.3 Volume of the droplet

Finally, according to equations (B.73), (B.74) and (B.81), the volume of the droplet is expressed by the following equation:

$$V_{drop} = \frac{4}{3}\pi R_s^3 - \frac{\pi}{3}R_s^3\left(1+\cos\theta_s\right)^2\left(2-\cos\theta_s\right) = R_s^3\left[\frac{4}{3}\pi - \frac{\pi}{3}\left(1+\cos\theta_s\right)^2\left(2-\cos\theta_s\right)\right] \tag{B.82}$$

Equation (B.82) can be used to have an explicit relationship between the droplet chord and its volume:

$$c_s = 2R_s\sin\theta_s = 2\sin\theta_s\left[\frac{V_{\text{drop}}}{\frac{4}{3}\pi - \frac{\pi}{3}\left(1+\cos\theta_s\right)^2\left(2-\cos\theta_s\right)}\right]^{\frac{1}{3}} \tag{B.83}$$

It is worth mentioning that this equation is different than the one proposed by Esposito et al. [24]:

$$c_s = 2\sin\theta_s\left[\frac{V_{\text{drop}}}{\frac{4}{3}\pi - \pi\left(1+\cos\theta_s\right)^2\cos\theta_s}\right]^{\frac{1}{3}} \tag{B.84}$$

B.5.4 Contact line

The surface tension force is a force that acts along the droplet contact line [43]. However, this line has not been characterized yet. In order to simplify the computation of the surface tension force, the contact line will be considered rectangular. Since the volume and the area are already described by equations (B.82) and (B.28) respectively, the thickness of the cylinder can be found as follows:

$$\begin{aligned} t_d = \frac{V}{A} &= \frac{R_{\text{S}}^3\left[\frac{4}{3}\pi - \frac{\pi}{3}\left(1+\cos\theta_{\text{S}}\right)^2\left(2-\cos\theta_{\text{S}}\right)\right]}{R_{\text{S}}^2\left(\theta_{\text{S}} - \frac{\sin 2\theta_{\text{S}}}{2}\right)} = \\ &= R_{\text{S}}\frac{\left[\frac{4}{3}\pi - \frac{\pi}{3}\left(1+\cos\theta_{\text{S}}\right)^2\left(2-\cos\theta_{\text{S}}\right)\right]}{\left(\theta_{\text{S}} - \frac{\sin 2\theta_{\text{S}}}{2}\right)} \end{aligned} \tag{B.85}$$

Of course, this is a coarse approximation of the actual geometry of the contact line, but future works will include a parametrization of the contact line depending on the droplet deformation. As shown in [43], as soon as the droplet deforms, the contact line deforms as well, from a circular shape to a less intuitive shape, formed by half a circle and half an ellipse (Figure B.11).

This shape is closer to the actual one due to the effect of pinning [24], [43].

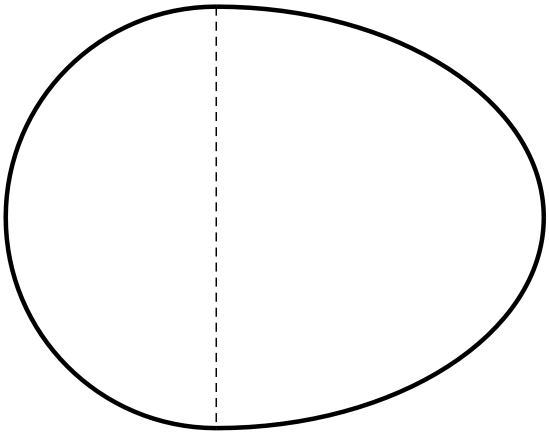

Figure B.11: Droplet contact line once it is deformed

Appendix C

Newmark-Bossak integration scheme

The Newmark-Bossak method is a modification of the Newmark method to improve the solution of highly geometrically non-linear problems. The original Newmark algorithm is an unconditionally stable time integration scheme with second-order accuracy. Bossak scheme introduces numerical dissipation, thus damping the high frequencies. The Newmark-Bossak formulae for the acceleration and velocity read:

$$\bar{\mathbf{v}}_{n+1} = \frac{\gamma}{\beta}\left(\frac{\bar{\mathbf{u}}_{n+1} - \bar{\mathbf{u}}_n}{\delta t}\right) - \left(\frac{\gamma}{\beta} - 1\right)\bar{\mathbf{v}}_n - \frac{\delta t}{2}\left(\frac{\gamma}{\beta} - 2\right)\bar{\mathbf{a}}_n \tag{C.1}$$

$$\bar{\mathbf{a}}_{n+1} = \frac{\bar{\mathbf{u}}_{n+1} - \bar{\mathbf{u}}_n}{\beta \delta t^2} - \frac{1}{\beta \delta t}\bar{\mathbf{v}}_n - \left(\frac{1 - 2\beta}{2\beta}\right)\bar{\mathbf{a}}_n \tag{C.2}$$

where

$$\gamma = \frac{1}{2} - \alpha^B \tag{C.3}$$

and

$$\beta = \frac{\left(1 - \alpha^B\right)^2}{4} \tag{C.4}$$

with $\alpha^B > 0$. If $\alpha^B = 0$ we obtain the standard Newmark scheme at its optimal, without any numerical dissipation. Numerical dissipation control is obtained by varying the coefficient α^B [66].